NOVEL CONFIGURATIONS FOR PULSED OPTICAL PARAMETRIC OSCILLATORS AND THEIR PUMP SOURCES

Cameron Francis Rae

A Thesis Submitted for the Degree of PhD
at the
University of St Andrews

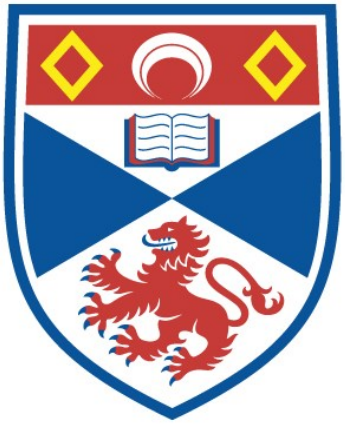

1998

Full metadata for this item is available in
St Andrews Research Repository
at:
http://research-repository.st-andrews.ac.uk/

Please use this identifier to cite or link to this item:
http://hdl.handle.net/10023/14948

This item is protected by original copyright

Novel Configurations for Pulsed Optical Parametric Oscillators and their Pump Sources

A thesis presented to the University of St Andrews
in application for the degree of Doctor of Philosophy

by

CAMERON FRANCIS RAE, B.Sc., M.Sc.

February 1998

BIBLIOTHECA UNIVERSITATIS ANDREANÆ

University of St Andrews
School of Physics and Astronomy
North Haugh
St Andrews, Fife
Scotland
KY16 9SS

ProQuest Number: 10166483

All rights reserved

INFORMATION TO ALL USERS
The quality of this reproduction is dependent upon the quality of the copy submitted.

In the unlikely event that the author did not send a complete manuscript
and there are missing pages, these will be noted. Also, if material had to be removed,
a note will indicate the deletion.

ProQuest 10166483

Published by ProQuest LLC (2017). Copyright of the Dissertation is held by the Author.

All rights reserved.
This work is protected against unauthorized copying under Title 17, United States Code
Microform Edition © ProQuest LLC.

ProQuest LLC.
789 East Eisenhower Parkway
P.O. Box 1346
Ann Arbor, MI 48106 – 1346

TL D 19

Declarations

I, Cameron Francis Rae, hereby certify that this thesis, which is approximately 75000 words in length, has been written by me, that it is a record of work carried out by me and that it has not been submitted in any previous application for a higher degree.

Date: 4 March 1998 Signature of candidate:.....

I was admitted as a research student in October, 1990 and as a candidate for the degree of Doctor of Philosophy in October 1990; the higher study for which this is a record was carried out in the University of St Andrews between 1990 and 1997.

Date: 4 March 1998 Signature of candidate:.....

I hereby certify that the candidate has fulfilled the conditions of the Resolution and Regulations appropriate for the degree of Doctor of Philosophy in the University of St Andrews and that the candidate is qualified to submit this thesis in application for that degree.

Date: 4 March 1998 Signature of supervisor:.....

In submitting this thesis to the University of St Andrews I understand that I am giving permission for it to be made available for use in accordance with the regulations of the University Library for the time being in force, subject to any copyright vested in the work not being affected thereby. I also understand that the title and abstract will be published, and that a copy of the work may be made and supplied to any bona fide library or research worker.

Date: 4 March 1998 Signature of candidate:.....

Publications

C. F. Rae, J. A. C. Terry, B. D. Sinclair, M. H. Dunn and W. Sibbett *"Single Frequency, End-Pumped Nd:YLF Laser Excited by a 12-mJ Diode-Laser Array"* Opt. Lett. 17 (23) pp.1673-1675, 1992.

Y. Cui, Dominic E. Withers, **Cameron F. Rae**, Callum J. Norrie, Y. Tang, Bruce D. Sinclair, Wilson Sibbett and Malcolm, H. Dunn *"Widely Tunable All-Solid-State Optical Parametric Oscillator for the Visible and Near Infrared"* Opt. Lett. 18 (2) pp.122-124, 1993.

Malcolm H. Dunn, Miles J. Padgett, **Cameron F. Rae**, Wilson Sibbett, Bruce D. Sinclair, Dominic E. Withers and Yong Cui *"New Solid-State, Variable-Colour Lasers"* The Royal Society Summer Exhibition, 1993.

J. A. C. Terry, **C. F. Rae** and M. H. Dunn *"Low Threshold Operation of an All Solid State KTP-OPO"* Quantum Electronics Conference No.11 - Queens University Belfast, Technical Digest p.133, 1993.

G. R. Morrison, M. Ebrahimzadeh, **C. F. Rae** and M. H. Dunn *"All-Solid-State Gain-Switched Cr:LiSAF Laser"* Paper CMD1 CLEO®/QELS '95 - Baltimore Maryland, 1995.

Jian Wang, Malcolm H. Dunn and **Cameron F. Rae** *"Polychromatic Optical Parametric Generation by Simultaneous Phase Matching over a Large spectral Bandwidth"* Postdeadline Paper CPD1.1 CLEO®-Europe/EQEC '96 - Hamburg Germany, 1996.

Jian Wang, Malcolm H. Dunn and **Cameron F. Rae** *"Polychromatic Optical Parametric Generation by Simultaneous Phase Matching over a Large spectral Bandwidth"* Opt. Lett. 22 (11) pp.763-765, 1997.

Yan Tang, **Cameron F. Rae**, Christian Rahlff and Malcolm H. Dunn *"Low Threshold, High Efficiency and Widely Tunable Infrared Source from a KTP based OPO"* J. Opt. Soc. B 14 (12) pp.3442-3451, 1997.

Yan Tang, **Cameron F. Rae** and Malcolm H. Dunn *"Temperature-Tuned Phase-Matching Properties of LiB_3O_5 for Sum-Frequency Generation"* in preparation.

Acknowledgements

It is my pleasure to acknowledge and thank a number of people for their assistance and support throughout the duration of these studies.

First and foremost I extend my sincere thanks to Professor Malcolm H. Dunn, for his guidance, encouragement and advice, as my research supervisor during the course of this project. To work with and learn from a person possessing such great enthusiasm and physical insight into his research field has been an inspiration and a privilege for which I am truly grateful. I am grateful also to Professor Wilson Sibbett, who in a co-supervisory role has expressed a constant interest in this work and been keen to offer his support and encouragement throughout.

I thank also my many colleagues with whom I have interacted, or whose good humour have made this School such a pleasurable place to work. In particular, Bill Sleat, whose electronics expertise has been invaluable and yarns about sailing exploits a constant source of amusement. Also, Dom Withers and Jian Wang, who have contributed significantly to these projects, Bruce Sinclair, Christian Rahlff, and from the 'Old School' Callum Norrie, Angus Henderson, Finlay Colville, Jonny Terry, Sara Shepherd and Yong Cui.

I wish to take this opportunity to say special thanks to Yan Tang and Garry Morrison, not just for the many worthwhile discussions and collaborations over the last few years, but also for their good friendship.

This project has benefited greatly from the technical support provided by the School. Thanks therefore are also due to the Mechanical Workshop under the supervision of Jim Clark and more recently George Radley, and to the Electronics Workshop under the supervision of Jim Park.

Finally, I have to thank my family. It is difficult to suitably express my gratitude to Karen for her patience and support in raising and caring for our wonderful children, Jennifer and Stewart, over the last few years and providing me with the time and opportunity to complete this thesis. Simply, my heartfelt thanks. Also, to my parents, thank you for your constant and invaluable support, not only now, but over many years of learning.

To my family

Abstract

The development of all-solid-state, diode-laser pumped neodymium (Nd) lasers and optical parametric oscillators (OPOs) is described, which realise practical sources of coherent radiation with a high degree of frequency agility, are efficient, reliable and potentially compact.

A comparison of various neodymium doped host materials reveals yttrium lithium fluoride (YLF) to be an appropriate replacement for the more widely known host yttrium aluminium garnet (YAG) in diode-laser pumped devices. The development of an end-pumped Nd:YLF laser that utilises a 12-mJ, 60W, quasi-CW diode-laser bar is initially described. Multilongitudinal-mode, TEM_{00} pulse energies of greater than 2 mJ have been observed, with corresponding peak output powers in excess of 118 kW. The incorporation of a novel pre-lase Q-switching technique has realised single-longitudinal-mode peak powers in excess of 90 kW continuing to be achieved. Further, the development of a more powerful end-pumped Nd:YLF laser utilising 2, 3-bar diode-laser arrays, each providing 72-mJ of pump energy is described. In this case, Q-switched, multilongitudinal-mode, TEM_{00} pulse energies of greater than 11 mJ are reported, with the clear potential for increasing this to greater than 20 mJ, based on measured fixed-Q pulse energies of greater than 30 mJ.

Complementing the development of these diode-laser pumped solid-state lasers is the development of optical parametric oscillators based on the nonlinear materials lithium triborate (LBO) and beta-barium borate (β-BBO). Pumped by the frequency up-converted (third harmonic) output of the Nd laser, such optical parametric oscillators introduce extensive frequency agility spanning a spectral range from the deep blue (0.4 μm) to the mid-infrared (2.5 μm). Initially, the development of an LBO based device is reported, which in a type I critical phase-match (CPM) geometry has a measured oscillation threshold of <0.3 mJ, when pumped by the frequency tripled output of the 144-mJ diode-laser pumped Nd:YLF

laser at 0.349 μm. Observed pump depletions are as high as 35%. A similar CPM geometry is reported in β-BBO, in this case pumped by the frequency tripled and amplified output of a diode-laser pumped Nd:YAG laser at 0.355 μm. This is a more energetic device with thresholds of >5 mJ, but through the introduction of interferometric, dispersive and injection seeding techniques made to operate on a single axial mode. Near transform limited linewidths are reported in devices which continue to have modest pump thresholds and broad tunability.

The parametric generation of broad spectral bandwidths (polychromatic) by the use of suitable phase-matching geometries is also reported. Greater than 100 nm simultaneous bandwidth in the visible spectrum is generated in a collimated signal-wave from a novel, noncollinear phase-matching geometry in a β-BBO optical parametric oscillator, which is pumped by the collimated output of frequency tripled diode-laser pumped Nd:YAG laser. The device is demonstrated to be efficient, having a similar pump threshold and efficiency to that of the well known collinear phase-matched tunable device, and to continue to encompass a degree of tunability allowing the large simultaneous bandwidth to be tuned across the entire visible spectrum. Dispersive cavity tuning of the optical parametric oscillator by the use of a Littrow-mounted grating or acousto-optic tuning filter, with a static crystal and pump configuration, is also described.

Contents

Chapter 1
Introduction

Since the first demonstration of Light Amplification by Stimulated Emission of Radiation (LASER) in 1960 [1] progress in the field of laser physics has been rapid. While during the first decade this can be largely attributed to interest in the academic world, during later years advances have been seen to be driven jointly by academia keen to research and demonstrate the versatility of this relatively new tool, and by the demands of end users eager to exploit its advantages in such diverse applications as industrial machining, medical physics, communications and defence.

Instrumental to the development of solid-state lasers in recent years has been the technological advancement in high-power semiconductor diode-lasers, used as an optical pump source in place of conventional xenon or krypton flashlamps. These diode-lasers used as pumps have brought about the development of solid-state lasers which are more efficient, more compact, have improved reliability and are more stable than their flashlamp pumped counterparts.

In parallel with the development of the solid-state laser has been the devotion of considerable effort to the development of tunable sources of coherent radiation. Many applications which use narrowband coherent sources of radiation are benefited by the introduction of frequency agility, such as in spectroscopic applications including long-path LIDAR, diagnostic and therapeutic medical techniques and industrial machining and marking. Since the first demonstration of second harmonic generation of laser radiation in a nonlinear crystal by Franken *et al.* [2] in 1961, much progress has been made, not least in recent years through the development of new nonlinear materials, opening up opportunities for parametric-wave devices providing frequency agility across the ultraviolet, visible and infrared spectra. Compared to established sources of tunable coherent radiation, e.g. colour centre lasers, dye lasers, semiconductor lasers and vibronic lasers, these optical parametric generators offer exceptionally broad tuning

bandwidths, even from a single device, and like their solid-state laser pump sources may be made highly efficient, reliable and compact.

1.1 Diode-Laser Pumping of Solid-State Lasers

The first allusion as to the possibility of using semiconductor sources to optically excite solid-state lasers was made not long after the first demonstration of the laser itself by Newman in 1963 [3]; it being suggested that GaAs light emitting diodes could be used to pump neodymium tungstate lasers. In fact, the first demonstration came less than one year later when Keyes and Quist [4] used five GaAs diode-lasers to pump uranium doped calcium fluoride (U^{3+}:CaF_2). While at this first stage of development severe technical difficulties were faced, including operating at liquid helium temperatures, the potential advantages to be gained from diode-laser pumping were clearly identified;

> "The potential advantages of this type of pumping source for a laser are several. The small size and simple structure of the diodes will make possible a direct coupling of the pumping radiation to the laser without any complex optics. This in turn will greatly reduce the size and cost of functional devices. The efficiency of conversion of input pump power to output power, both as regards the pump source and the internal conversion of energy within the laser, may permit continuous power output several orders of magnitude higher than presently possible" (Keyes and Quist, 1964).

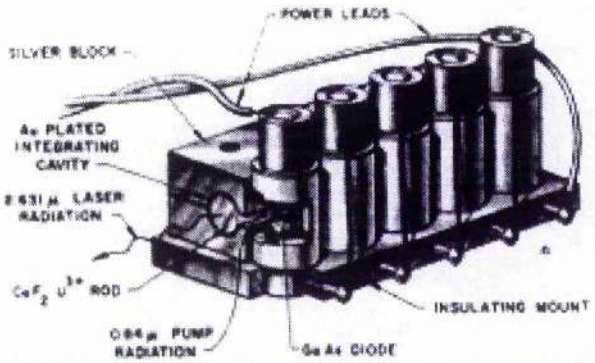

Figure 1.1: Artists representation of the first diode-laser pumped solid-state laser [4].

Throughout the next decade progress in diode-laser pumping was slow, constrained by the low-power of diode-lasers available and their poor reliability. None the less, the first demonstration of diode-laser pumping of Nd:YAG came in 1968 when Ross [5] used a single GaAs diode laser, cooled to 170 K to match its wavelength to the Nd absorption band at 867 nm, to transversely pump a Nd:YAG laser. In his work it was clearly recognised that the use of diode-lasers as pump sources have several advantages over the use of diode-lasers directly. It was noted that the solid-state laser can act as a temporary energy storage medium, having a long upper state lifetime, to combine the output of several diode-lasers and then release the combined energy in a short energetic and high peak power pulse. Also, the solid-state laser had a narrower emission solid angle, so providing an enhanced brightness compared to the diode-laser, and the spectral bandwidth was narrower. Even with the improvements in diode-laser technology today these advantageous generally still apply, although certainly narrow-linewidth devices are now commercially available [6].

Later, the potential for higher power operation was demonstrated by Conant and Reno [7] when they achieved 120 mW of average output power for an absorbed diode-laser power of 1.3 W. This work studied the use of bursts of short diode-laser pulses to excite Nd:YAG in a transversely pumped and quasi-CW mode. Like all studies at this time true CW operation could not be obtained due to limitations associated with the diode-lasers. In other transverse pump geometries Jackson and Rice [8] reported low ripple output from a Nd:YAG laser by quasi-CW pumping with diode-lasers at repetition rates of up to 1 MHz, while many other workers continued to explore the use of LED's [9-12].

Complementing the studies of transverse pump geometries was the investigation of longitudinal pumping schemes, which advantageously offered the possibility of improving the overlap between the pumped volume and the lowest order transverse mode of the solid-state laser resonator. Disadvantageously however, this approach limited the number of diode-lasers which could be used in the absence of elaborate coupling schemes. The first reported pulsed operation of a diode-laser pumped Nd:YAG laser with a longitudinal pumping scheme was in 1973 by Rosenkrantz [13]. In addition to the improved spatial overlap, he also noted that longer absorption path lengths could be

obtained in longitudinal pumping schemes, and thus a greater fraction of the pump light absorbed, so further improving the overall efficiency. Other reports of longitudinal pumping using LEDs and superluminescent diodes are contained in ref's. [14-17].

Throughout the 1980's and 1990's, diode-laser pumped solid-state laser technology has progressed rapidly as a result of the development of high-power and reliable semiconductor diode-lasers, and in particular AlGaAs devices operating around the 0.81 μm wavelength region [18,19] which are suitable for pumping Nd^{3+} doped gain media. During this time the possibility of pumping Nd doped gain media other than YAG was also explored. Among the most important studies were for example by, Fan *et al.* [20] who first demonstrated diode-laser pumping of Nd:yttrium lithium fluoride (YLF), a material of interest because of its long upper state lifetime and thus high energy storage capability for Q-switched applications. Nd:glass was investigated by Kozlovsky *et al.* [21], who demonstrated that while the emission cross-section was an order of magnitude lower than that of Nd in YAG, low threshold devices could still be developed due to the materials high optical quality and low loss. It was also noted that the broad absorption bandwidth of Nd in glass around the pump wavelength was beneficial in reducing the temperature control requirements normally imposed on the diode-lasers. A more extensive list of material and device development can be found in for example the review articles of; Fan and Byer, 1988 [22] and Hughes and Barr, 1992 [23].

Q-switching of diode-laser pumped solid-state lasers has also been considered by many groups and covers devices producing pulse energies of less than a millijoule with a peak power of tens of kilowatts and at repetition rates of up to tens of kilohertz, to devices of much higher peak powers, typically megawatts, but at repetition rates of perhaps only tens of pulses per second. In the former case Burnham and Hayes [24] have pumped a Nd:YAG rod at some 20 W CW to produce over 3 W average output at 1.06 μm and at 10 kHz, while in more recent work Rahlff [25] has demonstrated around 8 W average output from a Nd:YLF slab laser pumped by 25 W at 20 kHz. In a high peak power system Beach *et al.* [26] have demonstrated pulse energies of greater than 100 mJ from again a Nd:YLF laser but pumped by quasi-CW diode-lasers at 30 Hz and delivering 1 J per pulse in a transverse pumping geometry. Through industrial and

defence collaborations, output powers in excess of 1 J from various Nd doped gain media have now been achieved from slab based devices and again in transverse pump geometries.

1.2: Extension to Frequency Agile Devices

Nonlinear optical techniques have been used to extend the spectral coverage of solid-state lasers and provide efficient, compact and reliable sources of coherent radiation over a spectral range extending from the ultraviolet to mid-infrared.

The first demonstration of such techniques was the frequency doubling of a ruby laser by Franken [2] in 1961, however, it was four years later and the first demonstration of frequency down-conversion in an optical parametric oscillator (OPO), by Giordmaine and Miller [27], which brought about the advent of truly frequency agile nonlinear devices. In their work a $LiNbO_3$ based OPO was pumped by the second harmonic of a Nd:$CaWO_4$ laser at a wavelength of 0.529 μm, resulting in a tunable output extending over the range 0.97 μm to 1.16 μm. In much of this early work the full potential of the OPO, in respect of the very large phase-matchable bandwidths available, could not be exploited however, due to a number of physical limitations; the nonlinear materials used had either a low nonlinear coefficient or a low damage threshold while for the visible region of the spectrum nonlinear materials for frequency up-conversion of the pump source to the UV were not readily available.

Much effort has since been expended on the development of new nonlinear materials and in improving growth techniques, resulting in the ready supply of high quality crystals which have a high nonlinearity and high damage threshold. Such materials include; potassium titanyl phosphate/arsenate (KTP/KTA), β-barium borate (BBO), lithium triborate (LBO), potassium niobate ($KNbO_3$), doped lithium niobate and silver gallium selenide/sulphide ($AgGaSe_2$/$AgGaS_2$). Optical parametric oscillators based on these materials have been substantially investigated and tuning bandwidths demonstrated which far exceed the accessible wavelength regions of other tunable lasers, as indicated in Fig. 1.2.

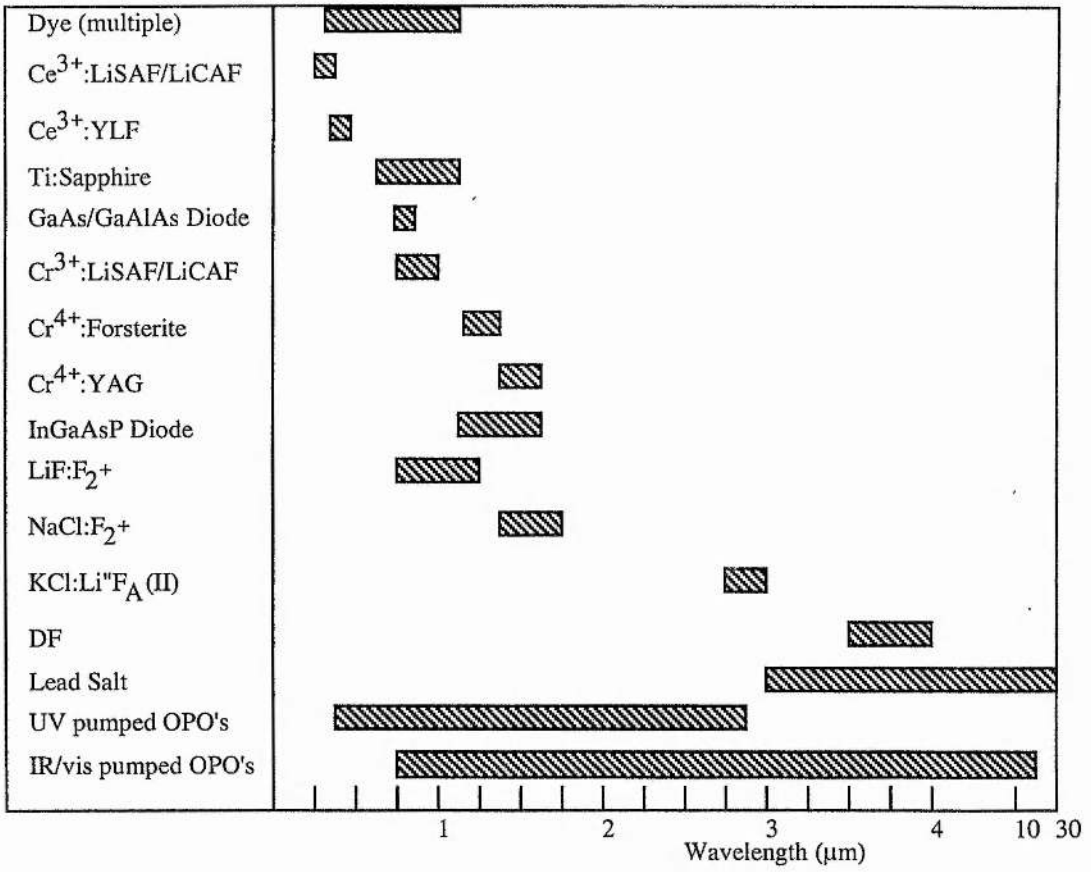

Figure 1.2: Comparative wavelength ranges of various tunable laser sources.

The chronological development of OPOs based on these and other materials is illustrated in Table 1.1, which summarises the main operating characteristics of some of the most notable pulsed devices demonstrated.

Pump source	Material	Tuning range	Output	Efficiency	Ref.
0.530 μm Nd:glass SH	KDP	0.96-1.18 μm	5 kW		[28]
0.529 μm Nd:$CaWO_4$ SH	$LiNbO_3$	0.73-1.93 μm	1 kW	1 %	[29]
0.694 μm Ruby	$LiNbO_3$	1-1.08 1.94-2.27	38 kW	1.2 %	[30]
0.530 μm Nd:glass SH	$LiNbO_3$	0.96 μm 1.18 μm		36%	[31]
0.694 μm Ruby	$LiNbO_3$	0.98-1.04 μm 2.08-2.38 μm	250 kW	28 %	[32]
0.530 μm Nd:glass SH	ADP		100 kW	1 %	[33]
0.694 μm Ruby	$LiNbO_3$	1.05-1.19 μm 1.67-2.05 μm	340 kW	45 %	[34]

1.064 μm Nd:YAG	$LiNbO_3$	1.95-2.35 μm	170 W	8.5 %	[35]
0.530 μm Nd:glass SH	KDP		5 MW	7%	[36]
0.514 μm Argon ion	$LiNbO_3$	0.66-0.7 μm 1.93-2.32 μm		60%	[37]
0.532 μm Nd:YAG SH	$LiNbO_3$	0.55-3.65 μm		67 %	[38]
1.064 μm Nd:YAG	$LiNbO_3$	~2 μm		75 %	[39]
1.833 μm Nd:YAG	CdSe	2.23-2.25 μm 9.8-10.4 μm		40 %	[40]
0.694 μm Ruby	$LiIO_3$	1.12-1.83 μm	100 kW	10 %	[41]
0.347 μm Ruby SH	$LiIO_3$	0.415-2.1 μm	10 kW	8 %	[42]
2.87 μm HF	CdSe	4.3-4.5 μm 8.1-8.3 μm	800 W	15 %	[43]
1.064 μm Nd:YAG	$LiNbO_3$	1.4-4.4 μm	1 mJ	15 %	[44]
0.355 μm Nd:YAG TH	RD*A	0.65-0.8 μm	1.2 MW	17 %	[45]
0.532 μm Nd:YAG SH	$LiIO_3$	0.63-3.4 μm	160 kW		[46]
0.532 μm Nd:YAG SH	$KNbO_3$	0.88-1.35 μm	12 MW	32 %	[47]
1.064 μm Nd:YAG	$AgGaS_2$	1.4-4.0 μm	0.5 mJ	16 %	[48]
1.064 μm Nd:YAG	$LiIO_3$	2.5-3.2 μm 1.59-1.85 μm	100 mJ	10 %	[49]
0.355 μm Nd:YAG TH	Urea	0.5-0.64 μm 0.79-1.23 μm		23 %	[50]
0.355 μm Nd:YAG TH	β-BBO	0.45-1.68 μm	1.4 mJ	9.4 %	[51]
0.355 μm Nd:YAG TH	β-BBO Type I	0.412-2.55 μm	4.7 mJ	24 %	[52]
0.308 μm XeCl	β–BBO Type I	0.354-2.37 μm	2 mJ	10 %	[53]
0.266 μm Nd:YAG FH	β-BBO Type I	0.33-1.37 μm			[54]
0.355 μm Nd:YAG TH	LBO Type II NCPM	0.46-0.48 μm 1.35-1.59 μm	42 kW	50 %	[55]
0.355 μm Nd:YAG TH	LBO Type I	0.46-0.67 μm 0.77-1.59 μm	30 kW	35 %	[56]
0.355 μm Nd:YAG TH	β-BBO	~0.62/0.83 μm line-narrowed		30 %	[57]

Table 1.1: Chronological development of pulsed optical parametric oscillators.

Interest here lies in particular in the operation of pulsed OPOs in the visible and near-infrared regions of the spectrum. While visible operation had been demonstrated using both frequency doubled Nd:YAG [46] and ruby [42] lasers as the pump source, it was in 1984 that Donaldson and Tang [58] were the first to demonstrate the potential for broad tunability from an OPO based on the organic crystal urea and pumped by the third harmonic of a Nd:YAG laser at 0.355 μm; potential which was to be realised shortly afterwards by Rosker and Tang [50], who demonstrated tunability in the range 0.498 μm to 0.64 μm for the visible signal-wave with a corresponding idler-wave range of 0.79 μm to 1.23 μm in the near-infrared. Later, and using the then new and more desirable nonlinear materials β-BBO and LBO, this tunability was further extended for OPOs continuing to be pumped by the third harmonic of Nd:YAG lasers. Initially by Cheng *et al.* [51] an OPO based on β-BBO was demonstrated which was tunable about degeneracy and had a combined signal and idler wavelength range of 0.45 μm to 1.68 μm. This range was further extended by Fan *et al.* [52] to 0.412 μm to 2.55 μm and more recently in our own work to 0.406 μm to 2.75 μm. Pumped by the fourth harmonic of a Nd:YAG laser deeper blue and ultraviolet operation of a β-BBO OPO has been demonstrated by Bosenberg *et al.* [54] at wavelengths as short as 0.33 μm.

1.3: Diode-Laser Pumped Nd Lasers and All-Solid-State Optical Parametric Oscillators

While in recent years OPOs operating in the visible and near-infrared spectral regions and pumped by the harmonics of Nd lasers have been widely reported, these devices have largely been based on inefficient flashlamp pumped Nd lasers, and so detract from the high nonlinear conversion efficiencies noted in published work as being achievable. In contrast, the diode-laser pumped Nd laser can provide a pump source which is highly efficient, reliable and may be made compact.

In this thesis, and firstly in Chapter 3, a comparison is made of the most notable neodymium doped gain media available, with particular regard being given to the relative merits of each for diode-laser pumping. The development of two diode-laser pumped

Nd:YLF lasers is then described in Chapter 4, each of which provide high quality radiation in the form of near diffraction limited spatial characteristics and relatively narrow linewidth. In low or moderate power devices, the highest overall laser efficiencies are achieved from longitudinal pumping geometries due to the excellent overlap achievable between the pumped volume and TEM_{00} mode of the laser resonator. However, the collection and focusing of the highly asymmetric diode-laser pump beam, in such a way as to match the normally circular resonator mode, is not trivial. One solution to this was proposed by Berger *et al.* [59], who collected the light from each emitter of a diode-laser bar into individual fibre cables and then collected the individual fibres into a circularly symmetric bundle to launch the diode light through circular focusing optics and into the Nd gain element. While successful in generating a circularly symmetric pumped volume, the overall efficiency of the laser was not good due to a high coupling loss at the fibres. More recently Shannon and Wallace [60] longitudinally pumped an Nd:YAG laser using a 1 cm wide 10 W diode-laser bar. In their work it was accepted that an elliptical pumped volume would be generated, however, the laser resonator was designed such that an elliptical TEM_{00} mode existed within the gain medium which matched well the pumped volume. In a similar vein here, again it is accepted that the pumped volume generated in each of the lasers developed will be asymmetric, however, by the application of different techniques high quality circularly symmetric outputs are still achieved.

In Chapter 5 the excellent temporal qualities of one of the lasers developed is seen to be exploited in the generation of single axial mode and near transform limited pulses. Through the application of a novel line-narrowing technique based on slow-Q-switching, the already relatively narrow linewidth found to exist in this type of longitudinally pumped Nd:YLF laser is further reduced to the point of single axial mode operation, while maintaining a high overall efficiency and introducing little additional complexity into the optical arrangement.

The use of the other of the Nd:YLF lasers developed as a pump source for a broadly tunable, low threshold and high efficiency optical parametric oscillator based on the nonlinear material LBO is described in Chapter 7. Although LBO has a lower

nonlinear coefficient than β-BBO, the material has certain characteristics which make it preferable in low power applications. For example, the birefringence of LBO is somewhat smaller, resulting in a slower tuning rate. As a consequence the angular acceptance bandwidth and pump bandwidth are larger than for β-BBO, beneficial in devices operated at the modest pump energies available from diode-laser pumped solid-state lasers with tight focusing. Further, LBO has a damage threshold at least a factor of two times greater than that of β-BBO, again benefiting tight focusing geometries and in some way compensating for the lower nonlinear coefficient of LBO by allowing operation at higher pump and parametric wave intensities.

With many applications benefiting from broadly tunable but narrow-linewidth radiation, Chapter 7 goes on to describe the development of narrow linewidth optical parametric oscillators based on the nonlinear material β-BBO. Again it is noted that much of the work published to date has concentrated on devices pumped by flashlamp pumped Nd lasers [57,61] where large pump pulse powers are available. Through the application of dispersive, interferometric and injection seeding techniques a variety of line-narrowing options are presented which demonstrate the possibility of obtaining narrow-linewidth, broadly tunable pulses from all-solid-state systems. The not widely recognised appearance of a pedestal in the spectrum of the injection seeded OPO, possibly arising as a result of operation at low or modest pump energies, is also reported.

Finally, in Chapter 8 a novel noncollinear optical parametric generation phase-matching condition is described which results in the observation of extremely broad-bandwidth radiation. Denoted 'polychromatic' phase-matching, it is found that for a particular pair of pump- and signal-wave directions, if a phase-match curve is plotted for signal wavelength vs. signal-wave direction, then over a range of wavelengths the curve is substantially parallel to the wavelength axis, i.e. a broad phase-matchable bandwidth. A polychromatic condition in β-BBO is identified and investigated and results presented in Chapter 8. As well as being of use in generating broad-bandwidth radiation, such a phase-match condition may also be of benefit in narrow-linewidth devices. In, for example, a device employing dispersive line-narrowing means, it is usual to have to accurately rotate both the nonlinear crystal and dispersive components simultaneously

[62,63] to ensure the resonated wavelength matches the phase-matched wavelength. In this polychromatic geometry the need to rotate the nonlinear element is removed. Again such a device is demonstrated and characterised.

In completing this thesis, Chapters 2 and 6 present respectively the theory relevant to the solid-state lasers and nonlinear optics described in this work. In conclusion Chapter 9 briefly summarises the principal achievements realised and points toward possible future investigations.

Chapter 1 References:

1. T. H. Maiman *"Stimulated Optical Radiation in Ruby"* Nature 187 p.493, 1960.

2. P. A. Franken, A. E. Hill, C. W. Peters and G. Weinreich *"Generation of optical harmonics"* Phys. Rev. Lett. 7 (4) pp118-119, 1961.

3. R. Newman *"Excitation of the Nd^{3+} fluorescence in $CaWO_4$ by recombination radiation in GaAs"* J. Appl. Phys. 34 (2) p.437, 1963.

4. R. J. Keyes and T. M. Quist *"Injection luminescent pumping of $CaF_2:U^{3+}$ with GaAs diode lasers"* Appl. Phys. Lett. 4 (3) pp.50-52, 1964.

5. M. Ross *"YAG laser operation by semiconductor laser pumping"* Proc. IEEE 56 () pp.196-197, 1968.

6. K. Kobayashi and I. Mito *"Single frequency and tunable laser diodes"* J. Lightwave Tech. 6 (11) pp.1623-1633, 1988.

7. L. C. Conant and C. W. Reno *"GaAs laser diode pumped Nd:YAG laser"* Appl. Opt. 13 (11) pp.2457-2458, 1974.

8. J. E. Jackson and R. R. Rice *"Output fluctuations of high-frequency pulse-pumped Nd:YAG laser"* J. Appl. Phys. 45 (5) pp.2353-2355, 1974.

9. G. I. Farmer and Y. C. Kiang *"Low-current-density LED-pumped Nd:YAG laser using solid cylindrical reflector"* J. Appl. Phys. 45 (3) pp.1356-1371, 1974.

10. A. L. Zakgeim, Yu. M. Makushenko, V. M. Marakhonov, S. A. Nikishin and R. P. Seisyan *"Enhanced output of an Nd^{3+}:YAG laser with a semiconductor pump system"* Sov. Tech. Phys. Lett. 4 pp.281-282, 1978.

11. V. I. Bilak, I. S. Goldobin, G. M. Zverev, I. I. Kuratev, V. A. Pashkov, M. F. Stel'makh, Yu. V. Tsvetkov and N. M. Solev'eva *"Neodymium YAG laser pumped by light-emitting-diodes"* Sov. J. Quant. Elect. 11 (11) pp.1471-1476, 1981.

12. F. W. Ostermayer, Jr. *"GaAsP diode pumped YAG:Nd lasers"* Appl. Phys. Lett. 18 (3) pp.93-96, 1971.

13. L. J. Rosenkrantz *"GaAs diode-pumped Nd:YAG laser"* J. Appl. Phys. 43 (11) pp.4603-4605, 1972.

14. R. B. Chesler and D. A. Draegert *"Miniature diode-pumped Nd:YAlG lasers"* Appl. Phys. Lett. 23 (5) pp.235-236, 1973.

15. D. A. Draegert *"Single-diode end-pumped Nd:YAG laser"* IEEE J. Quant. Elect. QE-9 (12) pp.1146-1149, 1973.

16. K. Iwamoto, I. Hino, S. Matsumoto and K. Inoue *"Room temperature CW operated superluminescent diodes for optical pumping of Nd:YAG laser"* Japan J. Appl. Phys. 15 pp.2191-2194, 1976.

17. F. W. Ostermayer, Jr. *"LED end-pumped Nd:YAG lasers"* IEEE J. Quant. Elect. QE-13 (1) pp.1-6, 1977.

18. W. Streifer, D. R. Scifres, G. L. Haragel, D. F. Welch, J. Berger and M. Sakamoto *"Advances in diode laser pumps"* IEEE J. Quant. Elect. QE-24 (6) pp.883-893, 1988.

19. J. G. Endriz, M. Vakili, G. S. Browder, M. DeVito, J. M. Haden, G. L. Harnagel, W. E. Plano, M. Sakamoto, D. F. Welch, S. Willing, D. P. Worland and H. C. Yao *"High power diode laser arrays"* IEEE J. Quant. Elect. QE-28 (4) pp.952-965, 1992.

20. T. Y. Fan and R. L. Byer *"Semiconductor diode-laser pumping of Nd:$LiYF_4$"* J. Opt. Soc. Am. A 2 (13) p.44, 1985.

21. W. J. Kozlovsky, T. Y. Fan and R. L. Byer *"Diode-pumped continuous-wave Nd:glass laser"* Opt. Lett. 11 (12) pp.788-790, 1986.

22. T. Y. Fan and R. L. Byer *"Diode laser-pumped solid-state lasers"* IEEE J. Quant. Elect. QE-24 (6) pp.893-912, 1988.

23. D. W. Hughes and J. R. M. Barr *"Laser diode pumped solid state lasers"* J. Phys. D: Appl. Phys. 25 pp.563-586, 1992.

24. R. Burnham and A. D. Hays *"High-power diode-array-pumped frequency-doubled cw Nd:YAG laser"* Opt. Lett. 14 (1) pp.27-29, 1989.

25. C. P. Rahlff, M. H. Dunn, B. D. Sinclair and W. Sibbett *"High-power, end-pumped effects and applications in Nd:YLF at 1047 and 1321 nm"* Conference on Lasers and Electro-Optics, (1994 Technical Digest Series 8, Optical Society of America, Washington, USA), Paper CThG4, 1994.

26. R. Beach, P. Reichert, W. Benett, B. Freitas, S. Mitchell, A. Velsko, J. Davin and R. Solarz *"Scalable diode-end-pumping technology applied to a 100-mJ Q-switched Nd^{3+}:YLF laser oscillator"* Opt. Lett. 18 (16) pp.1326-1328, 1993.

27. J. A. Giordmaine and R. C. Miller *"Tunable coherent parametric oscillation in $LiNbO_3$ at optical frequencies"* Phys. Rev. Lett. 14 (24) pp.973-976, 1965.

28. S. A. Akhmanov, A. I. Kovrigin, V. A. Kolosov, A. S. Piskarskas, V. V. Fadeev and R. V. KhoKhlov *"Tunable parametric light generator with KDP crystal"* JETP Lett. 3 p.241, 1966.

29. J. A. Giordmaine and R. C. Miller *"Optical parametric oscillation in the visible spectrum"* Appl. Phys. Lett. 9 (8) pp.298-300, 1966.

30. L. B. Kreuzer *"Ruby-laser-pumped optical parametric oscillator with electro-optic effect tuning"* Appl. Phys. Lett. 10 (12) pp.336-338, 1967.

31. L. B. Kreuzer *"High-efficiency optical parametric oscillation and power limiting in $LiNbO_3$"* Appl. Phys. Lett. 13 (2) pp.57-59, 1968.

32. J. E. Bjorkholm *"Some spectral properties of doubly and singly resonant pulsed optical parametric oscillators"* Appl. Phys. Lett. 13 (12) pp.399-401, 1968.

33. A. G. Akmanov, S. A. Akhmanov, R. V. Vokhlov, A. I. Kovrigin, A. S. Piskarskas and A. P. Sukhorukov *"Parametric interactions in optics and tunable light oscillators"* IEEE J. Quant. Elect. QE-4 (11) pp.828-831, 1968.

34. J. Falk and J. E. Murray *"Single-cavity noncollinear optical parametric oscillation"* Appl. Phys. Lett. 14 (8) pp.245-247, 1969.

35. E. O. Ammann, M. K. Oshman, J. D. Foster and J. M. Yarborough *"Repetitively pumped optical parametric oscillator at 2.13 μm"* Appl. Phys. Lett. 15 (5) pp.131-133, 1969.

36. Yu. N. Belyaev, A. M. Kiselev and J. R. Freidman *"Investigation of parametric generator with feedback in only one of the waves"* JETP Lett. 9 p.263, 1969.

37. R. L. Byer, A. Kovrigin and J. F. Young *"A cw ring-cavity parametric oscillator"* Appl. Phys. Lett. 15 (5) pp.136-137, 1969.

38. R. W. Wallace *"Stable, efficient, optical parametric oscillators pumped with a doubled Nd:YAG"* Appl. Phys. Lett. 17 (11) pp.497-499, 1970.

39. E. O. Ammann, J. D. Foster, M. K. Oshman and J. M. Yarborough *"Repetitively pulsed 2.13-μm internal optical parametric oscillator"* J. Opt. Soc. Amer. 60 p.717, 1970.

40. R. L. Herbst and R. L. Byer *"Singly resonant CdSe infrared parametric oscillator"* Appl. Phys. Lett. 21 (5) pp.189-191, 1972.

41. A. J. Campillo *"Properties of pulsed $LiIO_3$ doubly resonant parametric oscillator"* IEEE J. Quant. Elect. QE-8 (10) pp.809-811, 1972.

42. G. Nath and G. Pauli *"Efficient pulsed optical parametric oscillator with a tuning range from 0.415 to 2.1 μm"* Appl. Phys. Lett. 22 (2) pp.75-76, 1973.

43. J. A. Weiss and L. S. Goldberg *"Singly resonant CdSe parametric oscillator pumped by an HF laser"* Appl. Phys. Lett. 24 (8) pp.389-391, 1974.

44. R. L. Herbst, R. N. Fleming and R. L. Byer *"A 1.4 - 4-μm high-energy angle-tuned $LiNbO_3$ parametric oscillator"* Appl. Phys. Lett. 25 (9) pp.520-522, 1974.

45. K. Kato *"3547-Å pumped parametric oscillation in RD*A"* IEEE J. Quant. Elect. QE-11 (12) pp.939-941, 1975.

46. S. A. Akhmanov, B. V. Zhdanov, A. I. Kovrigin, V. I. Kuznetsov, S. M. Pershin and A. I. Kholodnykh *"Pulse-periodic tunable (0.63-3.4 μm) optical parametric oscillator for nonlinear spectroscopy"* Sov. J. Quant. Elect. 7 (10) pp.1271-1276, 1977.

47. K. Kato *"High-efficiency high-power parametric oscillation in $KNbO_3$"* IEEE J. Quant. Elect. QE-18 (4) pp.451-452, 1982.

48. Y. X. Fan, R. C. Eckardt, R. L. Byer, R. K. Route and R. S. Feigelson *"$AgGaAs_2$ infrared parametric oscillator"* Appl. Phys. Lett. 45 (4) pp.313-315, 1984.

49. I. I. Ashmarin, Yu. A. Bykovskii, V. A. Ukraintsev, A. A. Chistyakov and L. V. Shishonkov *"High-power $LiIO_3$ optical parametric oscillator for infrared laser chemistry applications"* Sov. J. Quant. Elect. 14 (9) pp.1237-1239, 1984.

50. M. J. Rosker and C. L. Tang *"Widely tunable optical parametric oscillator using urea"* J. Opt. Soc. Amer. B 2 (5) pp.691-696, 1985

51. L. K. Cheng, W. R. Bosenberg and C. L. Tang *"Broadly tunable optical parametric oscillation in β-BaB_2O_4"* Appl. Phys. Lett. 53 (3) pp.175-177, 1988.

52. Y. X. Fan, R. C. Eckardt, R. L. Byer, J. Nolting and R. Wallenstein *"Visible BaB_2O_4 optical parametric oscillator pumped at 355 nm by a single-axial-mode pulsed source"* Appl. Phys. Lett. 53 (21) pp.2014-2016, 1988.

53. M. Ebrahimzadeh, F. Akerboom and M. H. Dunn *"Highly efficient visible urea optical parametric oscillator pumped by a XeCl excimer laser"* Opt. Lett. 14 (11) pp.560-562, 1989.

54. W. R. Bosenberg, L. K. Cheng and C. L. Tang *"Ultraviolet optical parametric oscillation in β-BaB_2O_4"* Appl. Phys. Lett. 54 (1) pp.13-15, 1989.

55. Y. Cui, M. H. Dunn, C. J. Norrie, W. Sibbett, B. D. Sinclair, Y. Tang and J. A. C. Terry *"All-solid-state optical parametric oscillator for the visible"* Opt. Lett. 17 (9) pp.646-648, 1992.

56. Y. Cui, D. E. Withers, C. F. Rae, C. J. Norrie, Y. Tang, B. D. Sinclair, W. Sibbett and M. H. Dunn *"Widely tunable all-solid-state optical parametric oscillator for the visible and near infrared"* Opt. Lett. 18 (2) pp.122-124, 1993.

57. J. M. Boon-Engering, W. E. van der Veer, J. W. Gerritsen and W. Hogervorst *"Bandwidth studies of an injection-seeded β-barium borate optical parametric oscillator"* Opt. Lett. 20 (4) pp.380-382, 1994.

58. W. R. Donaldson and C. L. Tang *"Urea optical parametric oscillator"* Appl. Phys. Lett. 44 (1) pp.25-27, 1984.

59. J. Berger, D. F. Welch, W. Streifer, D. R. Scifres, N. J. Hoffman, J. J. Smith and D. Radecki *"Fibre-bundle coupled, diode end-pumped Nd:YAG laser"* Opt. Lett. 13 (4) pp.306-308, 1988.

60. D. C. Shannon and R. W. Wallace *"High-power Nd:YAG laser end-pumped by a cw, 10 mm x 1 μm aperture, 10-W laser-diode bar"* Opt. Lett. 16 (5) pp.318-320, 1991.

61. P. Bourdon, M. Pealat and V. I. Fabelinski *"Continuous-wave diode-laser injection-seeded β-barium borate optical parametric oscillator: a reliable source for spectroscopic studies"* Opt. Lett. 20 (5) pp.474-476, 1995.

62. W. R. Bosenberg and D. R. Guyer *"Broadly tunable, single-frequency optical parametric frequency-conversion system"* J. Opt. Soc. Amer. B 10 (9) pp.1716-1722, 1993.

63. I. Paiss, S. Festig and R. Lavi *"Narrow-linewidth optical parametric oscillator with an intracavity laser gain element"* Opt. Lett. 21 (20) pp.1652-1654, 1996.

Chapter 2
Background LASER Theory

In this chapter the basic principles of operation of the laser shall be introduced. The discussion will lead to a more detailed look at laser theory, with a particular view to optical pumping. An introduction to the Fabry-Perot resonator follows which includes both a description of the spatial modes it will support, through consideration of Gaussian beam optics, and the axial mode structure of such a resonator. A brief review of how the formation of these modes may be controlled is also provided.

2.1: Basic Principles

While over the last two decades numerous and varied laser devices have been developed, a number of features common to all can be identified; Firstly the medium in which the laser light is generated - the gain medium, where energy in some form is absorbed and through the stimulated emission processes turned into monochromatic radiation. This may take the form of a gas, as in the argon ion or carbon dioxide laser, a liquid as in dye lasers, or solid as for example in doped insulator and semiconductor diode-lasers. Secondly, and as alluded to above, we find also in each a process by which the atomic medium is excited. This may be by electrical discharge, arc-lamp, rf excitation or indeed another laser and more recently the semiconductor diode-laser. The third common feature to each is the optical resonator, the means by which light is fed back to the amplifying medium to maintain the stimulated emission process and generate high spatial quality beams. These fundamental concepts are depicted in Fig. 2.1.

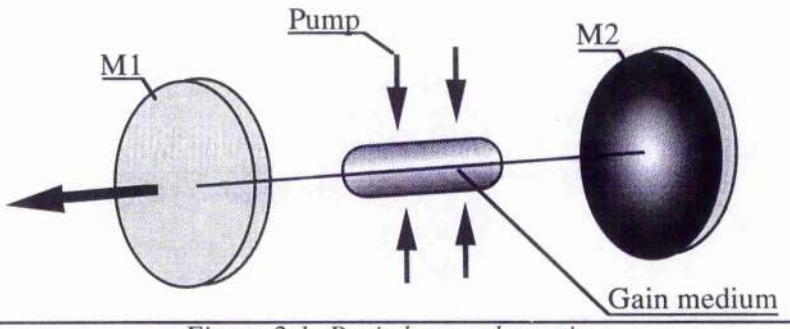

Figure 2.1: Basic laser schematic.

The optical resonator is formed by mirrors M1 and M2. As radiation is reflected back and forth it undergoes amplification in the gain medium, previously excited by the often incoherent pump source. Useful output from the laser is then in this case obtained by making one of the mirrors only partially reflecting (M1) and hence coupling out a fraction of the circulating field.

Assuming that the gain experienced by the circulating radiation in transiting the amplifying medium, while making one round trip of the cavity, exceeds the loss incurred by the reduced reflectivity of M1 and any other parasitic losses, then the lasing process will be sustained and a continuous output will be observed. In fact, while the *small signal* or *unsaturated* gain exceeds the loss the intra-cavity and hence extracted power will naturally continue to grow. This process does not continue indefinitely however; due to saturation effects as the optical field within the resonator grows the gain decreases to a point where the *saturated gain* just equals the cavity loss and a steady state mode of operation is reached.

The basic principles of operation of the laser are therefore straightforward, however, to understand more fully the physical processes involved requires a more rigorous analysis.

2.2: Electron Transition Concepts

2.2.1: The Electron Transition

Solid-state physics shows that bound electrons can occupy only discrete energy levels associated with a particular atom and can undergo transitions between these levels through phonon and photon interactions. Let us consider three such photon interactions between two energy levels (E_1,E_2) of a hypothetical atom as depicted in Fig's 2.2a,b and c. Through Planck's relationship, the photon involved in such a transition can be described by a wave of frequency υ_{12}, where $\Delta E=h\upsilon_{12}$ and ΔE is the energy difference between E_2 and E_1. If the electron exists initially in the lower energy level then through the absorption of a photon of energy ΔE it may be excited to the higher level. Conversely, if the electron is initially to be found in the higher level it may, through a

downward transition of one of two forms, return to the lower state; by the random or spontaneous emission of a photon of energy ΔE or, in the presence of radiation of frequency υ_{12} the transition may be triggered resulting in the stimulated emission of a photon of energy ΔE.

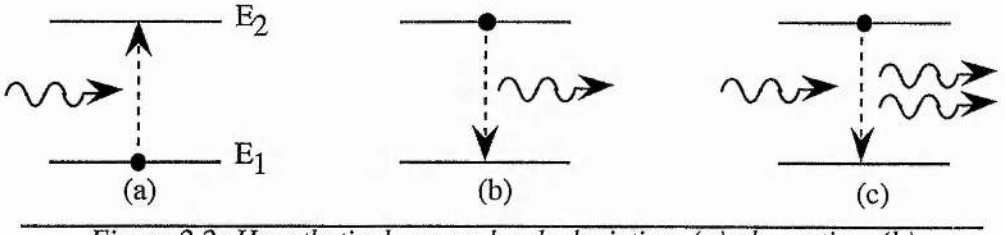

Figure 2.2: Hypothetical energy levels depicting; (a) absorption, (b) spontaneous emission and (c) stimulated emission.

These three processes were first described quantitatively by Einstein [1] in 1917 when he was the first to demonstrate mathematically that the process of stimulated emission must exist. Before discussing the concept of the Einstein A and B coefficients however, it is necessary to introduce some fundamentals of the interaction of radiation with matter.

When a collection of atoms are in thermal equilibrium the resultant radiation field must follow the distribution described by Planck a decade prior to Einstein's hypothesis. This says that the radiation density is given by

$$\rho(\upsilon)d\upsilon = \frac{8\pi\upsilon^2}{c^3}\frac{h\upsilon}{\exp(h\upsilon/kT)-1}d\upsilon \ , \qquad (2.1)$$

where $\rho(\upsilon)$ is the radiation density per unit frequency and unit volume, T the absolute temperature of the body and all other symbols have their usual meaning. Likewise, and again for a system in thermal equilibrium, the number of upward transitions between two levels must equal the number of downward transitions, where the steady-state populations of each level are described by Boltzmann statistics and given by

$$N_j = \frac{g_j N_0 \exp(-E_j/kT)}{\sum_i g_i \exp(-E_i/kT)} \ , \qquad (2.2)$$

and thus,

$$\frac{N_1}{N_2} = \frac{g_1}{g_2}\exp\left(\frac{-h\upsilon}{kT}\right) , \qquad (2.3)$$

where g_i is the degeneracy of the i^{th} level, N_0 the total number of atoms and $h\upsilon$ given by the energy difference between levels 1 and 2.

Returning then to the hypothetical two level atom described earlier, consider for the moment the system to exist in a state of thermal equilibrium and how the three transitions fit into this model. The number of upward transitions must be proportional to both the number of atoms in the lower state N_1 and the intensity of the radiation field at the frequency υ_{12}. So then the upward transition rate can be written as $N_1\rho(\upsilon_{12})B_{12}$, where B_{12} is the first of the Einstein coefficients and a constant. Similarly the stimulated emission process is also proportional to the radiation field intensity at υ_{12} and now the number of atoms in the excited state N_2 and so described by $N_2\rho(\upsilon_{12})B_{21}$, where again B_{21} is a constant. The final transition rate, that of spontaneous emission, is related to the average time τ_{21} the atom spends in the excited state prior to spontaneously returning to the lower energy state, and is described by the third Einstein coefficient A_{21} and given by $1/\tau_{21}$. The rate of change of population density N_2 due to spontaneous emission is then described by

$$\frac{dN_2}{dt} = -A_{21}N_2(t) \ , \tag{2.4}$$

and so integrating to express N_2 in terms of N_2 at time zero gives

$$N_2(t) = N_2(0)\exp\left(\frac{-t}{\tau_{21}}\right) . \tag{2.5}$$

The system in thermal equilibrium may then be described by

$$N_1\rho(\upsilon_{12})B_{12} = N_2\rho(\upsilon_{12})B_{21} + N_2A_{21} \ . \tag{2.6}$$

By re-arranging this equation and introducing the Boltzmann ratio described by equ. (2.3) an expression for $\rho(\upsilon)$ is obtained which when compared to Planck's distribution, equ. (2.1), gives the relationship between the Einstein coefficients as;

$$B_{12} = \frac{g_2}{g_1}B_{21} \ , \tag{2.7a}$$

$$B_{21} = \frac{c^3}{8\pi h\upsilon_{21}^3}A_{21} \ . \tag{2.7b}$$

It has been seen already that A_{21} is essentially the probability per unit time of an electron making a spontaneous downward transition, independent of any radiation field, and thus a property of the atom itself derivable from a quantum mechanical analysis of the atomic levels. From this starting point it is then possible to evaluate the Einstein B coefficients, describing the processes of absorption and stimulated emission. Furthermore, from the arguments given above it is also possible to derive the ratio of stimulated to spontaneous emission under this restrictive view of assuming a black-body problem. This then gives

$$\frac{Stim.rate}{Spon.rate} = \frac{B_{21}\rho(\upsilon_{12})}{A_{21}} = \left\{\exp\left(\frac{h\upsilon_{12}}{kT}\right) - 1\right\}^{-1} . \qquad (2.8)$$

Solving this equation reveals that under these conditions, for the stimulated emission rate to exceed the spontaneous emission rate in the optical regime requires black-body temperatures in the range of 10^4 - 10^5 degrees! As the spontaneously emitted photons take no part in the lasing process and are uncorrelated they are essentially a loss mechanism affecting the spectral purity of the laser. It is therefore important that the stimulated emission process dominate over the spontaneous process. This is achieved in the presence of a non-thermal monochromatic field.

In the presence of a monochromatic field it is further important that the process of stimulated emission dominates also over that of absorption, which involves the absorption of a photon of frequency υ_{12} and is hence another loss mechanism, if optical gain is to be observed. It is obvious, however, that under steady state conditions, and ignoring for the moment spontaneous emission, that for this two level system the condition

$$N_1\rho(\upsilon_{12})B_{12} = N_2\rho(\upsilon_{12})B_{21} , \qquad (2.9)$$

must also be satisfied. It will be seen shortly that by extending the model to include additional levels, the requirement for the downward transition rate between levels 1 and 2 to exceed the upward rate can be satisfied.

It is the case that the stimulated emission process provides a means by which the incident radiation field undergoes amplification in such a way that the amplified field is

indistinguishable from the incident field. That is the amplified signal is in-phase, has the same polarisation and has the same spectral and directional properties of the applied field. A simple qualitative description of this interaction is given by the classical electron-oscillator model. That is to say, when an electric field is applied to matter, a displacement of the electrons and nuclei from their equilibrium positions takes place, and consequently where the applied field takes the form of an electromagnetic wave oscillatory motion of the charged particles is observed. Such an oscillatory charge will then act as an electric dipole and radiate away energy in the form of an electromagnetic wave which is indistinguishable from the applied field.

2.2.2: Line Broadening Processes

Before going on to discuss in more detail induced transitions in the presence of a field on monochromatic radiation, the concept of lineshape functions is introduced and for now with particular reference to spontaneous transitions. It is clear that as the transition has associated with it a finite time, then the wavetrain is of finite extent. Consequently, a spectral analysis of the wavetrain will show it not to be truly monochromatic, but to have a finite spectral bandwidth. A lineshape function $g(\upsilon)$ describing the distribution of the emitted radiation is then introduced, such that $g(\upsilon)d\upsilon$ is the probability of the resultant photon from any spontaneous transition lying between υ and $\upsilon+d\upsilon$. i.e.

$$\int_{-\infty}^{\infty} g(\upsilon)d\upsilon = 1 \ . \qquad (2.10)$$

It was shown in equ. (2.5) that the population of the upper level displays exponential decay in time and so it would seem reasonable that the emitted wavetrain might take the form of a harmonic wave of frequency υ_{12}, but exponentially damped. The Fourier analysis of such a wavetrain gives, after squaring for the intensity rather than amplitude frequency spectrum,

$$|E(\upsilon)|^2 \propto \frac{1}{4\pi^2(\upsilon-\upsilon_{12})+(1/\tau)^2} \ . \qquad (2.11)$$

It is immediately apparent that this function has the form of a Lorentzian distribution and similar to the form one finds for many physical problems involving damped resonant behaviour. The distribution is characterised by a full width half maximum linewidth $\Delta\upsilon$ given by

$$\Delta\upsilon = \frac{1}{\pi\tau} \,. \tag{2.12}$$

The parameter τ in these expressions is not necessarily the upper level lifetime, but in fact the effective lifetime of the transition. This may be influenced by;

- The spontaneous lifetime of the upper state,
- Lower state lifetimes (usually insignificant if this is the ground or a metastable state),
- Collisional or Pressure broadening, particularly in gas lasers, where atomic collisions disrupt the wavetrain introducing random phase fluctuations,
- Thermal broadening due to the effect of thermal lattice vibrations in solid-state media on the atomic transition.

These broadening effects are characterised by each atom in the sample having the same resonant frequency perturbed in the same way and consequently having the same response function over the resulting frequency spread. As such they are classified as *homogeneous* broadening effects. Expressing then equ. (2.11) in terms of $\Delta\upsilon$, where now the origin of τ is understood, and normalising according to equ. (2.10), the normalised Lorentzian linewidth function is obtained;

$$g(\upsilon) = \frac{\Delta\upsilon}{2\pi\left[\left(\upsilon - \upsilon_{12}\right)^2 + \left(\Delta\upsilon/2\right)^2\right]} \,. \tag{2.13}$$

Other broadening factors exist which have a more localised effect on individual atoms or areas within a sample, generally resulting in a shift in the centre or resonant frequency of the atoms. These are then termed *inhomogeneous* effects and include such mechanisms as;

- Doppler broadening, where the random motions of atoms in gases results in an apparent shift in the resonant frequency of the atoms to the external observer due to Doppler shift,

• Irregular ionic field distributions in crystalline or amorphous media, resulting in small shifts in the energy level positions from one atom site to another,

• Inherent strain and lattice defects in crystalline media again causing shifts in atomic energy level positions.

In general inhomogeneous broadening effects can be described by a Gaussian frequency distribution. A good example of this is found in looking at the broadening due to the Doppler shift in gaseous media. The apparent resonant frequency of an atom in the laboratory frame of reference is given by

$$\upsilon_{12}^{'} = \upsilon_{12}(1 - v_z / c) \ , \tag{2.14}$$

where υ_{12} is the resonant frequency of an atom at rest and v_z the velocity component along say the laser resonator axis. Furthermore, the distribution of atoms having velocity components in the range v_z to $v_z + dv_z$ is given by the Maxwell-Boltzmann relationship from thermodynamics as

$$dN(v_z) = N\left(\frac{M}{2\pi kT}\right)^{\frac{1}{2}} \exp\left(\frac{-Mv_z^2}{2kT}\right) dv_z \ , \tag{2.15}$$

where N is the total number of atoms in the sample, M their atomic mass and T the absolute temperature of the sample. Combining then equ's. (2.14) and (2.15) it follows that the population density having apparent frequency υ' is described by

$$dN(\upsilon_{12}^{'}) = Nj(\upsilon_{12}^{'}) d\upsilon_{12}^{'} \ , \tag{2.16}$$

where $j(\upsilon_{12})$ is the normalised Gaussian distribution and given by

$$j(\upsilon_{12}^{'}) = \frac{2}{\Delta\upsilon}\left(\frac{\ln 2}{\pi}\right)^{\frac{1}{2}} \exp\left[-\left(\frac{\upsilon_{12}^{'} - \upsilon_{12}}{\Delta\upsilon / 2}\right)^2 \ln 2\right] \ , \tag{2.17}$$

and $\Delta\upsilon$ is the full width half maximum linewidth peculiar to each of the broadening mechanisms.

2.2.3 Induced Transitions and the Transition Cross-Section

Having introduced the concept of lineshape functions consider now how this is integrated into electron transition rates and where there is present a monochromatic field of radiation.

Under the restrictive conditions of sharp energy levels separated by υ_{21} and a monochromatic radiation field of photon energy $h\upsilon_{12}$ it has been shown, through a combination of equ's. (2.6) and (2.7), that the net rate of change in the population of the lower level in a two level system can be described by

$$-\frac{dN_1}{dt} = \rho(\upsilon_{12})B_{12}\left(\frac{g_2}{g_1}N_1 - N_2\right). \tag{2.18}$$

Consider this rate of change where the levels are broadened, having a centre transition frequency υ_0 and width $\Delta\upsilon$, and where the radiation field has a centre frequency υ_r and width $d\upsilon$, where $d\upsilon < \Delta\upsilon$. Furthermore, rather than expressing the rate of change in terms of number of atoms it is convenient to look at the change in radiation field or energy density $\rho(\upsilon)d\upsilon$. It is easily seen that this is no more than just $Nh\upsilon/V$, so multiplying each side of equ. (2.18) by $h\upsilon/V$ now gives

$$-\frac{d}{dt}[\rho(\upsilon_r)d\upsilon] = \rho(\upsilon_r)d\upsilon B_{12}h\upsilon g(\upsilon_r,\upsilon_0)\left(\frac{g_2}{g_1}n_1 - n_2\right), \tag{2.19}$$

where n_i are atomic densities. In fact, it is normal that $d\upsilon << \Delta\upsilon$, and so on integrating equ. (2.19) over the interval $d\upsilon$ one obtains the time rate of change of the radiation field as

$$-\frac{d\rho(\upsilon_r)}{dt} = \rho(\upsilon_r)B_{12}h\upsilon g(\upsilon_r,\upsilon_0)\left(\frac{g_2}{g_1}n_1 - n_2\right). \tag{2.20}$$

Rather than time rate of change it is also interesting to look at the path length rate of change, where naturally $dt = dx/c$. Substituting for dt in equ. (2.20) and integrating over the interval dx then gives one an expression describing the radiation field density at some point x along its propagation path relative to the initial field. That is

$$\rho(\upsilon_r) = \rho_0(\upsilon_r)\exp[-\alpha(\upsilon_r)x], \tag{2.21}$$

where

$$\alpha(\upsilon_r) = \left(\frac{g_2}{g_1} n_1 - n_2 \right) \sigma_{21}(\upsilon_r) \quad , \tag{2.22}$$

and

$$\sigma_{21}(\upsilon_r) = \frac{h\upsilon g(\upsilon_r, \upsilon_0) B_{21}}{c} \quad . \tag{2.23}$$

σ_{21} is the *transition cross-section* and an important parameter which will be referred back to often in the following chapters. Often more usefully, B_{21} is replaced by A_{21} using the Einstein relationship described in equ. (2.7), and $g(\upsilon_r,\upsilon_0)$ by the appropriate Lorentzian or Gaussian lineshape function of width $\Delta\upsilon$ peculiar to the sample in question.

It is clear from equ. (2.22) that for the isolated two level system, unless the upper level population exceeds that of the lower level then α will be positive and consequently in equ. (2.21) there will be a net absorption of the radiation field. It is important then to look at how such a population distribution or *population inversion* can be created.

2.2.4 The Population Inversion

It was stated earlier that the population inversion required for net gain to be observed in any laser can be generated through the introduction of additional energy levels to those of the lasing transition. Consider the four level energy diagram shown in Fig. 2.3.

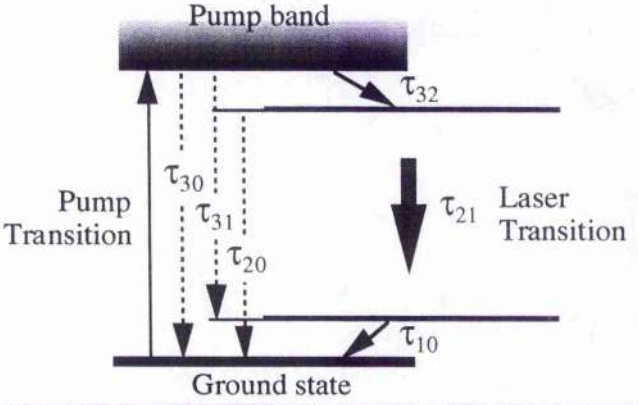

Figure 2.3: Simplified energy level diagram for a four level system.

Essentially pump energy is supplied to the system which is of an appropriate frequency to excite the electron from the ground state into the broad pump band. From here rapid non-radiative decay to the upper laser transition level takes place through phonon interactions with the crystal lattice. It is normal that this is a long-lived or

metastable state from where a radiative transition to the lower laser level takes place through either the process of spontaneous or stimulated emission. The electron then undergoes a further rapid non-radiative decay returning it to the ground state. Given then a sufficiently high pump rate and suitably timed decay rates, specifically $\tau_{10} < \tau_{32}$ and ideally also $\tau_{32} < \tau_{21}$(spontaneous), then a population inversion can be achieved.

Additional decay processes are also noted in Fig. 2.3, namely; τ_{30}, τ_{31} and τ_{20}. These may be regarded as loss mechanisms, reducing the number of electrons making the 2→1 laser transition. Fortunately, the frequencies of these transitions are too high to take place via single phonon interactions and consequently rely on either photon or multi-phonon processes. The decay times for such processes are generally at least three orders of magnitude longer than the single phonon interaction, ensuring small relaxation rates compared to that of the non-radiative decay to the upper laser level.

When evaluating the size of the population inversion it is necessary to include in the lower laser level population not only that population due to the laser transition but also any thermal population due to its proximity to the ground state. This equilibrium population is described in the usual way by the Boltzmann distribution

$$\frac{N_1}{N_0} = \exp\left(\frac{-\Delta E}{kT}\right). \qquad (2.24)$$

To place this in context, in a gain medium such as Neodymium doped Yttrium Aluminium Garnet (Nd:YAG) the lower laser level for the 1 μm laser transition is around 2000 cm^{-1} above the ground state. At room temperature equ. (2.24) then gives a population ratio of $7x10^{-5}$! In contrast, however, for the three level ruby laser the lower laser level is the ground state and consequently has a population near unity.

In the regime then where the equilibrium population of the lower laser level is very small and the level has a fast decay time, it becomes possible to create a population inversion even as the pump power approaches zero. However, as this lower state approaches the ground state thermal repopulation becomes a significant factor. In the extreme, lasers exist which operate on a three level basis where the ground and lower laser transition levels are the same state. In this instance it clearly becomes necessary to excite around one half the atoms from the ground state to create the population inversion.

Consequently such lasers are generally more difficult to operate, requiring considerably higher pump powers to attain threshold.

2.2.5 The Laser Rate Equations and Operation at Threshold

In the preceding sections the basic building blocks to laser theory have been discussed, including; spontaneous and induced electron transitions, transition broadening effects and the 3 or 4 state energy level diagram which provides a means of creating population inversions and consequently gain in a laser media. It is at this point that these concepts are now brought together to begin to form a model describing in practical terms the operation of lasers. In particular, the optical pumping of four level, rare earth ion, solid-state gain media is considered.

The gain experienced by a monochromatic radiation field as it transits the laser medium can be derived from the rate equations describing the populations of the upper and lower laser transition levels. These are;

$$\frac{dn_2}{dt} = \left(n_2 - \frac{g_2}{g_1} n_1 \right) c\phi\sigma + \frac{n_2}{\tau_{21}} - W_p n_1 \ , \tag{2.25a}$$

$$\frac{dn_1}{dt} = \left(n_2 - \frac{g_2}{g_1} n_1 \right) c\phi\sigma + \frac{n_2}{\tau_{21}} - \frac{n_1}{\tau_{10}} \ , \tag{2.25b}$$

$$n_{tot} = n_1 + n_2 + n_0 \ . \tag{2.25c}$$

Equations (2.25a,b) essentially bring together the spontaneous and stimulated transition rates described previously with the final parameter in each describing now also the pump rate and lower laser level decay rate for the four level system. Some reorganising of the stimulated transition rate has been done in order to express the $B_{21}\rho(\upsilon)$ product in terms the more useful stimulated emission cross-section and photon flux parameters, namely

$$B_{21} = \frac{c}{h\upsilon g(\upsilon)} \sigma_{21}(\upsilon) \quad \text{and} \quad \rho(\upsilon) = h\upsilon g(\upsilon)\phi \ , \tag{2.26}$$

so that

$$B_{21}\rho(\upsilon) = c\sigma_{21}(\upsilon)\phi \ . \qquad (2.27)$$

It is to be noted that in these expressions for the relative populations of each level, equ. (2.25), certain assumptions have been made: Firstly, that the pump transition is rapid and secondly that the nonradiative decay time from the pump band to the upper laser level is short. Consequently, the total number of atoms involved in the system is just the sum of those in the laser transition levels and the ground state as described by equ. (2.25c). Making the further assumption that the lower laser level population is zero, this being valid for when τ_{10} is small, gives the laser rate equation for the population inversion as

$$\frac{dn}{dt} = -n\sigma_{21}\phi c - \frac{n}{\tau_f} + W_p(n_{tot} - n) \ , \qquad (2.28)$$

where τ_f is the effective fluorescence lifetime of the upper laser level, taking into account all spontaneous decay transitions, and W_p is the effective pump rate, taking into account all spontaneous transitions from the pump band to energy levels other than the upper laser level.

Rather than looking at the time rate of change of population inversion, it can be useful to consider the time rate of change of photon density within the laser. This can by analogy to equ. (2.28) be seen to be given by

$$\frac{d\phi}{dt} = nc\sigma_{21}\phi\frac{l}{l'} - \frac{\phi}{\tau_c} + S \ . \qquad (2.29)$$

The change in photon number due to stimulated transitions is of course identical to the change in population inversion due to stimulated transitions, as is seen in the first factor on the right of equ's. (2.28) and (2.29). The factor l/l', where l is the gain length and l' the resonator length, must however be included as ϕ is a photon flux and the average flux in the resonator increases at a rate l/l' slower. The second factor in equ. (2.29) describes the reduction in the intra-cavity photon density due to cavity losses such as the reduced mirror reflectivity of a laser output coupler, parasitic losses from optical surfaces and absorption losses. For completeness an additional factor describing the contribution to the photon density from spontaneous emission is also included, but is generally much

smaller than either the stimulated emission or cavity loss components and so is henceforth neglected.

Under the conditions of either steady-state operation or radiation field growth, the time rate of change of photon density is respectively equal to or greater than zero. From equ. (2.29) one can then say that the required population inversion condition at threshold is

$$n_{th} = \frac{l'}{c\sigma_{21}\tau_c l} \ . \tag{2.30}$$

It has been shown earlier that σ_{21} is inversely proportional to the transition linewidth. Thus, in order to obtain a low lasing threshold a narrow transition linewidth and long cavity decay time τ_c are desirable, noting that the cavity decay time is determined by a combination of output coupling and parasitic losses. It is clear then that as one would expect losses should be kept to a minimum. However, increasing the output coupling reflectivity, while reducing threshold, will reduce the fraction of circulating power coupled out of the laser cavity and thus some trade off must be made to obtain the most efficient combination.

It can be useful to express the threshold conditions for operation described above in more measurable quantities. Consider the laser resonator depicted in Fig. 2.1, consisting of two mirrors of reflectivity R_1 and R_2, separated by some optical distance l' containing the gain medium of length l. Threshold is reached when the photon density after one round trip of the cavity just equals the photon density at the start of the round trip. For then a system in which the single pass gain of the medium is described by $\exp(g_0 l)$, at threshold

$$R_1 R_2 \exp(2g_0 l - 2\alpha l) = 1 \ , \tag{2.31}$$

where α describes the absorption and scatter losses in the gain medium, and R_2 is a modified reflectivity value for the normally highly reflecting M2, taking into account parasitic surface losses. The factor of 2 in the exponentiation function arises in considering a round trip of the resonator and hence double pass of the gain medium. Given the round trip time of the resonator is just 2l'/c and the fractional loss in power in each round trip is therefore just $2l'/c\tau_c$, then at threshold one can rewrite equ. (2.31) as

$$\tau_c = \frac{2l'}{c}\frac{1}{\left[\ln(R_1R_2)^{-1} + 2\alpha l\right]} . \qquad (2.32)$$

All of these factors are either known or reasonable estimates can be made, allowing one to predict with some accuracy cavity decay times and consequently, with the additional measurement of the spontaneous transition lineshape and decay time parameters, allow good estimates of threshold inversion conditions.

It is of interest of course to know how much pump power need be applied to the gain medium to sustain threshold operation. Under steady-state operating conditions dn/dt is zero and furthermore, at threshold the photon density is very small and can be ignored. Incorporating these assumptions into the four level laser rate equation described by equ. (2.28) gives

$$n_{th} = n_{tot}\frac{W_p\tau_f}{W_p\tau_f + 1} . \qquad (2.33)$$

Clearly then for the four level system described here any finite pump rate results in an inversion being created in the gain medium. The threshold inversion requires one to take into account cavity losses however, and so by equating equ. (2.33) to that given previously in equ. (2.30) one obtains the threshold inversion pump rate as

$$W_{p(th)} \approx \frac{l'}{c\sigma_{21}\tau_c\tau_f n_{tot} l} . \qquad (2.34)$$

This expression demonstrates clearly the desire to have a low loss cavity in the form of a high τ_c and a gain medium with large emission cross-section, long lived upper laser level and high active ion density. It will be discussed later however, how in the context of many solid-state gain media, increasing active ion densities can lead to an increase in threshold inversion due to increased scatter loss (so reducing τ_c) and a reduction in τ_f.

2.2.6 Operation above Threshold

In the preceding section operation near to threshold has been described, where it is assumed that the circulating photon density is small and indeed was ignored. Consider

now operation above threshold where this assumption is no longer valid, but where steady-state operation prevails such that $d\phi/dt$ and dn/dt are zero.

It is intuitively wrong to think that as the gain medium begins to be pumped at a rate above that required to reach threshold, then the radiation field should go on growing indefinitely. Clearly some steady-state condition must be reached where for some given pump rate the population inversion stabilises and the pump rate and the combined spontaneous and stimulated emission rates are balanced. It becomes immediately apparent then that at this stage some concept of gain saturation must be introduced. The mathematical description of this mechanism has in fact already been introduced in equ. (2.28), where now we can no longer ignore the significant photon density ϕ, as was the case when considering operation at threshold. In then the steady-state case, obtained from equ. (2.28) is the inversion density in the presence of a strong photon density described by

$$n = n_{tot} \frac{W_p \tau_f}{W_p \tau_f + 1 + c\sigma_{21}\phi\tau_f} . \qquad (2.35)$$

Clearly this just reduces to equ. (2.33) and the threshold condition when ϕ is negligible.

It is useful at this point to reintroduce a gain parameter g, previously identified in equ's. (2.21) and (2.22), where now $g = -\alpha$. The gain then is defined as just the emission cross-section x inversion density product. In the case of operation at threshold this gives from equ.(2.33) the *small signal gain coefficient*;

$$g_0 = \sigma_{21} n_{tot} \frac{W_p \tau_f}{W_p \tau_f + 1} , \qquad (2.36)$$

and in the case of a large photon density the *saturated gain coefficient*;

$$g = \sigma_{21} n_{tot} \frac{W_p \tau_f}{W_p \tau_f + 1 + c\sigma_{21}\phi\tau_f} . \qquad (2.37)$$

If now g is expressed in terms of g_0 and the photon density ϕ is replaced by the power density I, then with some rearranging

$$g = \frac{g_0}{1 + I / I_{sat}} , \qquad (2.38)$$

where

$$I = c\phi h\upsilon \quad \text{and} \quad I_{sat} = \left(W_p + \frac{1}{\tau_f} \right) \frac{h\upsilon}{\sigma_{21}} . \tag{2.39}$$

I_{sat} is the *saturated power density* and essentially the power density at which the small signal gain is reduced to one half its unsaturated value. The definition of I_{sat} is further simplified in the case of the four level laser where $W_p \ll 1/\tau_f$, so that

$$I_{sat} = \frac{h\upsilon}{\sigma_{21}\tau_f} . \tag{2.40}$$

2.2.7 Modelling of Laser Behaviour

In the preceding sections, the foundations have essentially been put in place to allow one to now go on and make reasonable predictions as to the operational characteristics of any laser, providing sufficient spectroscopic data for the gain medium, including emission cross-sections and laser level lifetimes are known and justifiable assumptions can be made as to such parameters as resonator losses and pumping efficiencies.

The most useful output of such a model lies in predicting such parameters as threshold pump power, output energy and optimum output coupling. In Section 2.3, when Q-switched operation of lasers is considered, the additional important parameter of pulse duration may be added to this list and indeed the model will be extended accordingly.

It has been noted previously that as the laser pulse builds up from noise it sees some gain value g_0 which, as the circulating field builds, reduces to the saturated gain level g, at which time the field intensity stabilises. Rearranging equ. (2.31) for g_0 and substituting in equ. (2.38) gives this circulating steady-state intensity as

$$I_{ss} = I_{sat}\left(\frac{2g_0 l}{2\alpha l - \ln R_1 R_2} - 1 \right) , \tag{2.41}$$

where R_1 and R_2 are known system parameters and the gain and losses must now in some way be determined. It is to be noted that this circulating intensity is, in the case of a standing wave resonator, the geometric mean of the intensities of the two counter propagating waves. That is

$$I = (I_i I_r)^{1/2} \ , \tag{2.42}$$

where I_i and I_r denote the intensities of the incident and reflected waves at the output coupling mirror of the resonator. Given some mirror reflectivity R, and using equ. (2.42) the intensities are related through

$$\frac{I_r}{I_i} = R \ \text{ and } \ I_i = \frac{I}{R^{1/2}} \ . \tag{2.43}$$

Taking into account the cross-sectional area of the beam A, then the output power from the resonator is just $P_{out} = A(I_i - I_r)$, and so on substitution from equ. (2.43) this gives

$$P_{out} = AI(1-R)R^{-1/2} \ . \tag{2.44}$$

Knowing then the circulating field it is a straightforward task to evaluate the output power of the laser.

The small signal gain as a function of the pump rate was given by equ. (2.36), which in the case of $W_p \tau_f \ll 1$ reduces to

$$g_o = \sigma_{21} n_{tot} W_p \tau_f \ . \tag{2.45}$$

Under the same conditions however equ. (2.33) tells us that $(n_{tot} W_p \tau_f)$ is just the inversion density n_{th}. At threshold therefore the inversion is just $n_{th} V$, where V is the pumped volume in the gain medium. Furthermore, the fluorescence power of the gain medium, again at threshold, is just the stored energy divided by the fluorescence decay time, where of course the stored energy is just the product of the threshold inversion and photon energy. That is

$$P_f = \frac{h\upsilon_{12} n_{th}}{\tau_f} \ . \tag{2.46}$$

Substituting for n_{th} in equ. (2.45) and expressing the fluorescence power in terms of the input power then gives for the small signal gain coefficient;

$$g_0 = \frac{\sigma_{21} \tau_f \eta_1 \eta_2 \eta_3 \eta_4 P_{th}}{h\upsilon_{12} V} \ , \tag{2.47}$$

where the efficiency factors η_i relate the input power at threshold (P_{th}) to the fluorescence power of the gain medium. They are defined as: η_1 includes the quantum defect between

the pump wavelength and emission wavelength and also the loss due to decay from the pump band to levels other than the upper laser level; η_2 is the efficiency of the pump source in converting electrical input to useful pump radiation; η_3 is the coupling efficiency between pump source and gain medium; and η_4 is the fraction of pump light entering the gain medium which is actually absorbed.

For then the single pass gain G_0 we have $G_0 = \exp(g_0 l)$, and thus $\ln(G_0) = g_0 l = KP_{th}$ where K is a dimensionless constant which, remembering equ. (2.40), may be regarded as a coefficient of pumping given by

$$K = \frac{\eta_1 \eta_2 \eta_3 \eta_4}{I_{sat} A} \ . \tag{2.48}$$

The significance in knowing the value of K lies in a series of rather simple expressions which may be used to predict such parameters as threshold pump power, the overall efficiency of the laser as a function of the output coupling mirror reflectivity and consequently the evaluation of the optimum output coupler reflectivity for some given set of pump and resonator parameters.

Using equ. (2.41) in (2.44) and remembering $g_0 l = KP_{in}$, then after some rearranging one obtains an expression for the output power

$$P_{out} = \sigma_s (P_{in} - P_{th}) \ . \tag{2.49}$$

This expression is intuitively obvious, it saying that the output power is just the difference in input power between threshold and the pump level times the slope of the input-output curve σ_s. Having made the above substitution however, it is possible to write down the factors in terms of known or measurable quantities, where the latter may be extracted from threshold measurements. These are;

$$P_{th} = \frac{L - \ln R}{2K} \ , \tag{2.50}$$

$$\sigma_s = K I_{sat} A \eta_5 \ , \tag{2.51}$$

$$\eta_5 = \frac{2(1-R)}{R^{1/2}(L - \ln R)} \ . \tag{2.52}$$

In these expressions R is the output coupling reflectivity only, the parasitic loss of the second resonator mirror being included in the loss term L and η_5 may be regarded as

an output coupling term. Substituting equ. (2.48) into (2.51) shows that the slope efficiency is as one would expect nothing more than the product of all the inefficiencies in the pumping to laser output chain.

Substituting these factors in equ. (2.49) and differentiating with respect to the output coupling reflectivity allows one, by finding a turning point, to obtain the optimum reflectivity for a given set of parameters. This is then

$$R_{opt} = 1 - \frac{(2KP_{in}L)^{1/2} - L}{1+L} \quad . \tag{2.53}$$

Until now, the models presented have incorporated parameters expressed in the dimensions of power, this being the more general case. The transition to pulsed operation and consequently energy is, however, a straightforward one and described in the subsequent section.

2.3: Q-switched Operation

In considering Q-switched operation of a laser it is desirable to extend the theory already presented to obtain such parameters as pulse energy and pulsewidth (and consequently peak power), and additionally information on the shape of the pulse, i.e. build up times and decay times. Such information can be obtained by making subtle changes to the theory already presented, starting with the laser rate equations.

Q-switched Laser Rate Equations

For a Q-switched mode of operation the fractional resonator loss per round trip ε becomes a time dependent variable of the form,

$$\varepsilon(t) = -\ln R_1 + L + \zeta(t) \quad , \tag{2.54}$$

where as before R_1 and L represent the output coupling and parasitic losses and $\zeta(t)$ represents the Q-switch induced cavity loss. Initially during the pump pulse, when the resonator loss is high and the photon flux negligible, the time rate of change of population inversion is described by pump and spontaneous decay mechanisms only, and so equ. (2.28) may be rewritten in the form

$$\frac{dn}{dt} = -\frac{n}{\tau_f} + W_p(n_{tot} - n) \ . \tag{2.55}$$

This expression may then be solved to obtain the population inversion density at the end of the pump pulse and consequently the unsaturated gain coefficient.

On switching from a low-Q to high-Q resonator state, which is assumed to be instantaneous i.e. $\zeta(t<0) = \zeta_{max}$ and $\zeta(t\geq 0) = 0$, and where the resulting laser pulse duration is short, the laser rate equations can be rewritten excluding the factors of spontaneous emission and optical pumping. It follows then from equ's. (2.28) and (2.29) that;

$$\frac{d\phi}{dt} = \phi\left(c\sigma_{21} n \frac{1}{l'} - \frac{\varepsilon}{t_R} \right) , \tag{2.56}$$

$$\frac{dn}{dt} = -n\phi\sigma_{21}c \ , \tag{2.57}$$

where the photon lifetime τ_c is expressed in terms of the round trip cavity time t_R and the fractional loss per round trip ε. The solution to equ. (2.57) is a monotonically decreasing function of time in which the inversion starts at some initial value n_i and decreases to a final value n_f. As the peak of the laser pulse occurs when the time rate of change of photon flux within the resonator is zero; and it can be readily seen by rewriting equ. (2.56) after the substitution of equ. (2.30), in the form

$$\frac{d\phi}{dt} = \phi\left(\frac{n}{n_{th}\tau_c} - \frac{1}{\tau_c} \right) , \tag{2.58}$$

that this will occur when $n = n_{th}$, the final inversion value n_f will be considerably less than n_{th} as dn/dt is still large in equ. (2.57) when $n = n_{th}$ due to the high photon flux. It is evident in these rate equations then that the Q-switched output will be in the form of single pulse, where additionally the continued depletion of the excited state atoms after the peak in the photon flux leads to a characteristic asymmetry in the temporal profile of the pulse as the pulse decay is not just the cavity decay rate.

Proceeding with the laser rate equations, time can be eliminated as a parameter by taking the quotient of equ's. (2.56) and (2.57) to obtain

$$\frac{d\phi}{dn} = -\frac{1}{l'}\left(1 - \frac{n_{th}}{n} \right) , \tag{2.59}$$

where the substitution $n_{th} = \varepsilon/2\sigma l$ is derived from equ. (2.30) and again $\varepsilon = t_R/\tau_c$ is the fractional loss per round trip. Integration of equ. (2.59) then gives the photon flux at some arbitrary time t after switching to a high-Q state as

$$\phi(t) = \frac{1}{l'}\left[n_{th} \ln\left(\frac{n(t)}{n_i}\right) + n_i - n(t) \right] . \qquad (2.60)$$

The maximum photon flux may then be found from equ. (2.60) by the substitution $n(t) = n_{th}$.

Q-switched Pulse Measurable Quantities

The output power in a Q-switched pulse can on substitution of equ. (2.39) into (2.44) be written as

$$P_{out} = \frac{Al'h\upsilon\phi}{t_R} \ln\left(\frac{1}{R_l}\right) , \qquad (2.61)$$

where the substitution $c = l'/t_R$ and approximation $(1-R)R^{1/2} \approx \ln(1/R)$ have been made. Substituting for ϕ from equ. (2.60) when $n(t) = n_{th}$ then gives the peak power of the laser as

$$P_{peak} = \frac{Vh\upsilon}{t_R} \ln\left(\frac{1}{R_l}\right)\left[n_{th} \ln\left(\frac{n_{th}}{n_i}\right) + n_i - n_{th} \right] , \qquad (2.62)$$

where V is the pumped volume in the gain medium. It is apparent then that it is desirable to keep the resonator round trip time as short as possible and to use the largest possible output coupling, without impacting overall efficiency, in order that the peak power be optimised.

Having a time variable expression, equ. (2.61), for the output power of the laser, it is possible to obtain the pulse energy by integrating this expression over an infinite time period, i.e.

$$E = \frac{Al'h\upsilon}{t_R} \ln\left(\frac{1}{R_l}\right) \int_0^\infty \phi(t)dt . \qquad (2.63)$$

Using equ. (2.57) to change the integration variable from time to population inversion and integrating over the range n_i to n_f, then the expression for laser pulse energy, equ. (2.63), becomes

$$E = \frac{A h\upsilon}{2\sigma_{21}} \ln\left(\frac{1}{R_1}\right) \ln\left(\frac{n_i}{n_f}\right). \tag{2.64}$$

It is notable from the above that the pulse energy is independent of the resonator length while as previously noted the peak power depends on the resonator length explicitly as one would expect. In order then to evaluate the pulse energy it is necessary to know the initial and final population inversions. n_i as previously noted is obtainable from equ. (2.55) or if K, as described in Section 2.2.7 and equ. (2.48), is known through the relationship

$$n_i = \eta_{st} \frac{KE_{in}}{\sigma_{21} l}, \tag{2.65}$$

where η_{st} is an efficiency term§ not previously included in K describing the loss in population inversion during the pump pulse due to spontaneous decay and E_{in} is the pump pulse energy. The final population inversion can be obtained from equ. (2.60) by setting the left hand side of the equation equal to zero, i.e. when there exists no circulating field within the resonator after the laser pulse has ended. The result is a transcendental expression for n_f which may be solved numerically;

$$n_i - n_f = n_{th} \ln\left(\frac{n_i}{n_f}\right). \tag{2.66}$$

A simple iterative technique for solving this equation makes the substitutions $y = n_f/n_{th}$ and $u = n_i/n_{th}$. Equation (2.66) may then be written in an iterative form as; $y_{i+1} = u\exp(y_i - u)$. Solving the equation in this way and plotting a graph of the final to initial inversions as a ratio of the threshold inversion produces the curve shown in Fig. 2.4.

§ $\eta_{st} = (\tau_f/\tau_p)[1-\exp(-\tau_p/\tau_f)]$

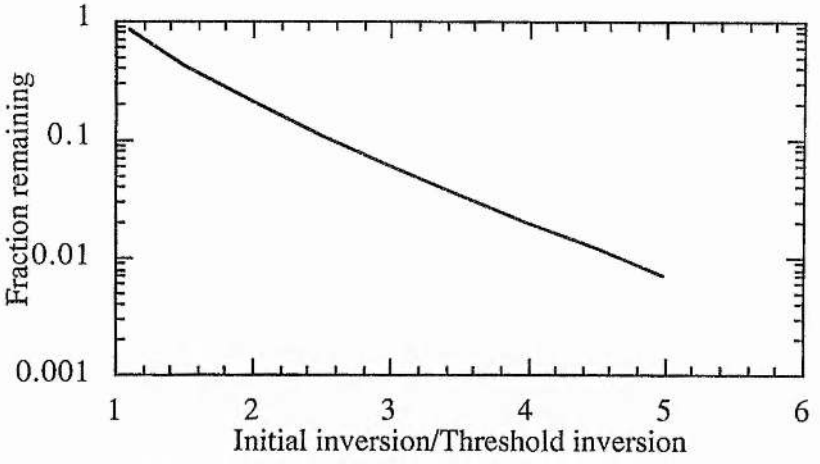

Figure 2.4: Fraction of the population inversion remaining as a function of the initial inversion.

It is evident that the higher the initial inversion ratio the greater the fraction of the inverted population that can be usefully extracted.

The final measurable quantities considered are those of pulse duration and pulse build up time. A good approximation to the pulse duration can be made through the relatively simple step of assuming the pulse to be triangular in shape, in which case the full width half maximum pulse duration is simply given by;

$$E = \frac{\Delta\tau_{base}}{2} P_{peak} \Rightarrow \Delta\tau_{fwhm} = \frac{E}{P_{peak}} = \tau_c \frac{n_i - n_f}{n_{th} \ln\left(\frac{n_{th}}{n_i}\right) + n_i - n_{th}}, \qquad (2.67)$$

where use has been made of equ's. (2.30) and (2.66).

The pulse build up time, which is the delay between the opening of the Q-switch and the first appearance of the laser pulse, can be appreciable. During this time the radiation density builds up exponentially from noise, however, since there is no appreciable density present the population inversion and hence gain may be regarded as constant. It is therefore reasonable to describe the growth of the photon flux according to

$$\phi(t) = \phi_i \exp(2g_o l - \varepsilon)\frac{t}{t_R}. \qquad (2.68)$$

Consequently, if one considers the build up time to be that required for the photon flux to build up to a level two orders of magnitude less than the peak photon flux then,

$$t_b = \frac{t_R \ln(\phi_{peak} / 100\phi_i)}{2g_o l - \varepsilon}. \qquad (2.69)$$

An initial value for ϕ_i has to be known to use this expression, however, this need not be an accurate value. The flux of spontaneously emitted photons into the solid angle of the laser beam is often used.

In Section 2.2 the theoretical description presented culminated in deriving an expression for the optimal output coupling necessary to optimise the performance of the essentially CW laser. The description of the Q-switched laser is now concluded in a similar way, by determining some optimal coupling level based on a dimensionless variable which is the ratio of the small signal gain to parasitic losses, parameters which are useful in a practical sense in the design of lasers. An optimally coupled theory was first presented by Degnan [2] using a method of Lagrange multipliers, however, optimised performance can also be obtained in a similar way to that presented in Section 2.2, by maximising the output energy expression, equ. (2.64), in respect of output coupling.

Making the substitution of equ. (2.66) into (2.64) and relating the logarithmic term in output coupling to the threshold population inversion through the cavity decay time[§§] gives

$$E = C\left(\frac{2g_0 l n_{th}}{n_i} - L\right)\left(\frac{n_i}{n_{th}} - \frac{n_f}{n_{th}}\right), \qquad (2.70)$$

where $C = Ah\upsilon/2\sigma_{21}$ and remembering $g_0 = \sigma_{21} n_i$. Making then the substitutions as before ($y = n_f/n_{th}$ and $u = n_i/n_{th}$) and setting $g = 2g_0 l$, then to optimise the energy requires

$$\frac{d}{du}\left[\left(\frac{g}{u} - L\right)(u - y)\right] = 0 . \qquad (2.71)$$

Performing the differentiation, one then obtains;

$$\frac{(u-y)}{u}\left[\frac{1}{(1-y)}\left(\frac{g}{u} - L\right) - \frac{g}{u}\right] = 0 . \qquad (2.72)$$

[§§] $\tau_c = t_R/\varepsilon = 2l'/[c(-\ln R + L)]$ and so from (2.30) $n_{th} = (-\ln R + L)/2\sigma_{21} l$

There are two solutions to this expression; the first is trivial and is that $n_i = n_f$ (u =y), the second is found by making the expression in square parenthesis equal to zero, which after rearranging gives the solution

$$\frac{u}{y} = \frac{g}{L} \Rightarrow \frac{n_i}{n_f} = \frac{2g_0 l}{L} \quad . \tag{2.73}$$

Substituting this solution into equ. (2.66) and remembering that $n_{th} = (-\ln R + L)/2\sigma_{21}l$ and using the simple rearrangement $n_f/n_i = (n_f/n_{th})(n_{th}/n_i)$, an expression for the optimum output coupling is obtained as;

$$R_{opt} = \exp\left[-L\left(\frac{z-1-\ln z}{\ln z}\right)\right], \tag{2.74}$$

where z is given by equ. (2.73) and is the dimensionless parameter describing the ratio of unsaturated gain to parasitic loss. Expanding g_0 in the form $\eta_{st}KE_{in}$ gives an expression for z which can be solved by the use of experimentally obtainable parameters K and L, through a Findlay-Clay [3] analysis of the laser.

With then an optimum output coupling expression derived, the optimum laser energy and pulsewidth can then be obtained by substitution of equ. (2.74) into (2.64) and (2.67).

2.4: The Laser Resonator

In the preceding sections the mechanisms by which one obtains light of high monochromaticity from a laser have been discussed. At this point it is useful to introduce issues relating to how the laser resonator influences that spectral purity of the laser output and also its other most important characteristic, that of directionality. This involves a discussion of the *longitudinal* and *transverse modes* of a laser resonator. For now only the basic concepts of mode structure shall be explained as a more detailed analysis will be performed in later chapters where the attainment of high spatial quality and line-narrowed operation of a laser will be considered.

2.4.1: Longitudinal modes

In its simplest form the laser resonator consists of two plane-parallel mirrors forming a resonant cavity in a fashion exactly analogous to the classical Fabry-Perot étalon. Such a resonator provides confinement of the light along one axis only, the so called resonator axis, and consequently through the characteristics of the stimulated emission processes previously described results in the generation of beams with high directionality. Furthermore, for a stable resonance to be observed it is important that the phase of the light after one round rip of the cavity reproduces itself. Any phase difference will result in the observation of destructive interference effects. This then requires that the round trip length of the cavity contain an integer number of optical cycles. i.e.

$$2nL = q\lambda \ , \tag{2.75}$$

where L is the physical length of the resonator, n the average refractive index and q an integer number of cycles.

This phase requirement places the constraint on the resonator that only well defined frequencies are allowed to oscillate, these frequencies separated by the resonator *free spectral range*, defined by

$$\Delta\upsilon = \frac{c}{2nL}(q+1) - \frac{c}{2nL}q = \frac{c}{2nL} \ . \tag{2.76}$$

In a typical laser resonator nL may be of the order of 0.5 m and so correspondingly $\Delta\upsilon \sim$ 300 MHz. To place this in context, the lasing transition linewidth of say a Neodymium Yttrium Aluminium Garnet (Nd:YAG) laser is around 100 GHz. There are then of the order of 300 resonator modes under the gain linewidth of the laser medium. Due to cavity losses and mode competition effects not all these modes would actually appear in the laser output, however, one might reasonably expect to see 10 - 30 simultaneous lasing modes.

These allowable frequencies are not delta functions in the frequency domain but have associated with them a finite width determined by the free spectral range of the resonator and its *finesse* and are further influenecd by such factors as; transient thermally and radiation field intensity induced fluctuations in refractive index during the emission of

a laser pulse, mechanical and acoustical vibrations, and power supply instabilities. Such factors may all be classed as environmental fluctuations and along with the design of the laser resonator determine the observed linewidth. Lower limits are placed on the linewidth achievable in pulsed and CW lasers by an intrinsic quantum mechanical limit in the form of the Schawlow-Townes limit and by the transform limit in the case of a short pulse or q-switched laser.

Finesse

The conventional Fabry-Perot interferometer has a bandwidth determined by a finesse

$$\mathcal{F} = \frac{\pi[\mathrm{Re}\,\mathrm{xp}(-\alpha L)]^{1/2}}{1-\mathrm{Re}\,\mathrm{xp}(-\alpha L)}\ , \qquad (2.77)$$

where $-\alpha$ is a power loss per unit length, R the geometric mean of the two mirror reflectivity's and the bandwidth $\delta\upsilon$ is given by $\Delta\upsilon/\mathcal{F}$. The effect of increasing the finesse of a resonator is suitably demonstrated graphically by considering the transmission of a Fabry-Perot étalon as a function of phase difference after one round trip of the étalon/resonator. This is shown in Fig. 2.5.

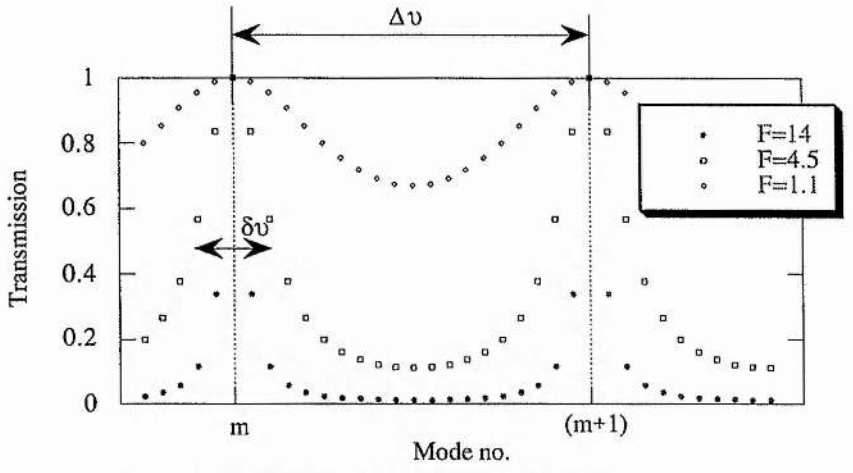

Figure 2.5: Intensity transmission of a general Fabry-Perot étalon as a function of phase mismatch and finesse.

Considering then steady-state operation of a laser where α is zero one obtains

$$\delta\upsilon = \frac{c(1-R)}{2nL\pi R^{1/2}}\ . \qquad (2.78)$$

In continuous wave systems a finesse of 10^8 can with some difficulty be attained with corresponding mode linewidths of 1 Hz or less. More typically however a finesse of 10 is readily achievable so providing individual mode linewidths of 10's of MHz or less.

Environmental Factors

The environmental factors noted above all have a similar manifestation in that in some way they all act so as to generate a random fluctuation in the length of the laser resonator. Consideration of equ. (2.75) shows the consequence of this action to be a shift in the resonant frequencies of the resonator and thus a broadening of the observed mode linewdiths. From equ (2.75), it is a simple task to show that the transient variation in mode frequency which occurs as a consequence of geometric length changes ($\Delta L(t)$) and refractive index changes ($\Delta n(t)$) is given by

$$\Delta\upsilon(t) = -\frac{\upsilon_0}{n_0 L_0}\left[n_0 \Delta L(t) + \Delta n(t) L_0\right]. \qquad (2.79)$$

where υ_0 is the mode frequency and n_0 and L_0 the refractive index and resonator length all at time zero.

Intrinsic Quantum Limits

Through the use of active and passive linewidth narrowing techniques, the environmentally broadened mode linewidth can be narrowed, but is ultimately restricted to a lower theoretical limit by the quantum nature of the radiation in the CW case and transform limit of a truncated wavepacket in the pulsed case. In the former of these, the limit is described by the well known Schawlow-Townes formula [4]

$$\Delta\upsilon_{ST} = \frac{h\upsilon}{2\pi\tau_c^2 P}, \qquad (2.80)$$

where τ_c is the cavity decay time and P is the laser output power. The dominant process in this limit is the frequency fluctuation caused by the random process of spontaneous decay of the upper laser level.

In the latter pulsed case, the transform limit is described by the well known Heisenberg uncertainty relationship

$$\Delta\upsilon\Delta\tau_p \approx 1, \tag{2.81}$$

where τ_p is the laser output pulse duration.

2.4.2: Transverse modes

It is also the case for an optical resonator that the spatial distribution of the phase and amplitude of an electromagnetic field must be reproduced after one round trip of the resonator if oscillation is to be sustained. This limits oscillation to well defined field distributions which are designated the *transverse electromagnetic modes* (TEM) of the resonator. Defined as TEM_{mn}, where m and n are integers denoting the number of nodes in the spatial distribution along orthogonal axes perpendicular to the resonator axis (p and l being used when working in cylindrical co-ordinates). The lowest order TEM_{00} mode has a Gaussian profile peaked on the beam axis. Higher order modes may be described using Hermite or Laguerre polynomials when working in rectangular or cylindrical frames of reference respectively. Before discussing in more detail the transverse mode structure of the laser resonator, however, it is desirable to first introduce some concepts of Gaussian beam propagation.

Properties of Gaussian Beams

The evolution of a Gaussian beam may be described by the field amplitude expression

$$E = \psi(r,z)\exp(-ikz) \ , \tag{2.79}$$

where ψ is some complex wave function describing the spatial distribution of the field and the exponential term a phase parameter. Bearing in mind that the electric field must satisfy Maxwell's scalar equation

$$\nabla^2 E + k^2 E = 0 \ , \tag{2.80}$$

where $k=2\pi n/\lambda$ and suitable boundary conditions are applied, namely that the beam take a spherical Gaussian spatial form, then it can be shown that [5] ψ has a solution of the form

$$\psi = \exp\left\{-i\left[P(z)+\frac{kr^2}{2q(z)}\right]\right\}, \tag{2.81}$$

where P(z) and 1/q(z) are given by

$$P(z) = -i\ln\left(1+\frac{z}{q_0}\right), \quad \frac{1}{q(z)} = \frac{1}{R(z)} - \frac{j\lambda}{\pi\omega^2(z)}. \tag{2.82 a,b}$$

This then gives an expanded form of equ. (2.81) as

$$\psi = \exp\left\{-j\left[P(z)+\frac{kr^2}{R(z)}\right]\right\}\exp\left[\frac{-r^2}{\omega^2(z)}\right]. \tag{2.83}$$

In this expansion the terms in P(z) and R(z) describe how the phase of the Gaussian propagating beam varies from an ideal plane wave; P(z) describing the longitudinal variation and R(z) the radial variation. The final non-oscillatory exponential term is just that which describes a Gaussian spatial distribution, where ω is a spot radius defined at the $1/e^2$ intensity point. Furthermore, when substituted into equ. (2.80), using (2.79), and assuming a transverse dependence only, one obtains

$$\frac{kr^2}{q^2}+\frac{2j}{q}+2\frac{\partial P}{\partial z}-\frac{kr^2}{q^2}\frac{\partial q}{\partial z}=0. \tag{2.84}$$

Given that equ. (2.84) must be satisfied for all r, then equating powers of r gives

$$\frac{\partial q}{\partial z}=1, \quad \frac{\partial P}{\partial z}=-\frac{j}{q}. \tag{2.85}$$

The *complex beam parameter* q(z) is then seen immediately to be given by the simple equation q(z) = q(0) + z. From equ. (2.82b), q(0) as defined at the point z=0, is then seen to be just

$$q(0)=\frac{j\pi\omega_0^2}{\lambda}, \tag{2.86}$$

where ω_0 is the beam waist size. Substituting this into the simple complex beam parameter equation, equ. (2.82b) ,and equating real and imaginary parts then gives two

equations describing the size and curvature of the wavefront as the beam propagates in the z-direction;

$$\omega(z) = \omega_0 \left[1 + \left(\frac{\lambda z}{\pi \omega_0^2} \right)^2 \right]^{1/2} , \tag{2.87}$$

$$R(z) = z \left[1 + \left(\frac{\pi \omega_0^2}{\lambda z} \right)^2 \right] . \tag{2.88}$$

The parameter $\lambda/\pi\omega_0^2$, known as the *Rayleigh range* and denoted z_r, is significant as it is the distance from the beam waist at which the beam area has doubled. When considering Gaussian beam focusing, the range $-z_r$ to z_r is taken to be the distance over which the beam is approximately collimated; this length often being denoted the *confocal parameter*. Further significance lies in the Rayleigh range in that when substituted in equ. (2.88) and then after differentiation one obtains

$$\frac{dR(z)}{dz} = 1 - \frac{z_r^2}{z^2} . \tag{2.89}$$

Clearly then R(z) goes through a minimum when $z = z_r$ and consequently it is at this point the wavefront has a maximum curvature of $2z_r$. Furthermore, from equ. (2.87), when $z \gg z_r$ then $\omega(z) \approx \omega_0 z/z_r$ and so the *far-field* half-angle divergence of the beam θ_d, given by $\omega(z)/z$, is just ω_0/z_r. Conversely, the region $z \ll z_r$ is denoted as the *near-field*. These parameters are shown schematically in Fig. 2.6.

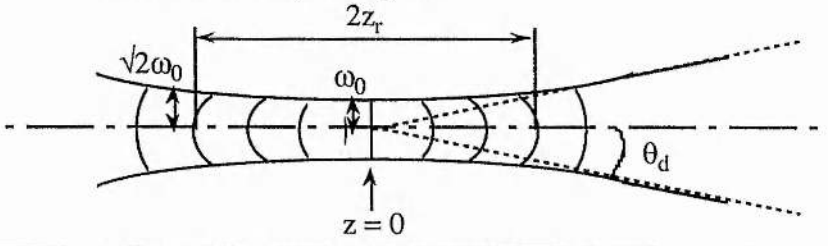

Figure 2.6: Gaussian Beam Parameters.

Focusing of Gaussian Beams

Making a similar substitution to the derivation of equ's. (2.87) and (2.88) one obtains a pair of equations describing the size and distance to a beam waist, given the size and radius of curvature of the beam at some point z along the beam propagation axis, as;

$$z = R(z)\left[1+\left(\frac{\lambda R(z)}{\pi\omega(z)^2}\right)^2\right]^{-1}, \tag{2.90}$$

$$\omega_0 = \omega(z)\left[1+\left(\frac{\pi\omega(z)^2}{\lambda R(z)}\right)^2\right]^{-1/2}. \tag{2.91}$$

The effect of passing the beam through a thin lens of focal length f is such as to modify the complex beam parameter according to

$$\frac{1}{q'(z)} = \frac{1}{q(z)} - \frac{1}{f}. \tag{2.92}$$

In fact, by assuming the lens to be thin the matter is somewhat simplified in that the spot size can be assumed to be unchanged by the lens and consequently q may be replaced by just the radius of curvature R. Knowing then the spot size at the lens and evaluating the transformed radius of curvature, equ's. (2.90) and (2.91) may be used to evaluate the new waist location and size. Expressing the input beam to the lens in terms of the measurable parameters ω_1 and θ_d then gives after some simplification the general expression for the new waist size as

$$\omega_0' = \frac{\lambda}{\pi}\left\{\theta_d^2 + \left(\frac{\omega_1}{f}\right)^2 - \frac{2\lambda}{f\pi}\left[\left(\frac{\pi\omega_1\theta_d}{\lambda}\right)^2 - 1\right]^{1/2}\right\}^{-1/2}. \tag{2.93}$$

Further simplification of equ. (2.93) may be made under particular conditions; namely when the lens is placed in the near or far field of the original waist. In the former case one may assume $\omega_1 \approx \omega_0$, while in the latter one may assume in its derivation $z \gg z_r$. Having evaluated the new waist size, and knowing ω_1 and the transformed radius of curvature, one may substitute in equ. (2.90) to evaluate the new waist position.

Lowest Order Mode of Passive Laser Resonators

It has been noted that the stable modes of a laser resonator are those where the spatial distribution of the phase and amplitude repeat themselves after one round trip of the resonator. Such a condition can be established by applying the boundary condition that at the point a resonator mirror is inserted its curvature must match that of the mode, so that the mode simply retraces its path upon reflection. In reality, it is of course the

mode that forms to match the curvature of the two resonator mirrors, which are separated by some distance L, where the position of the waist and waist size adjust themselves accordingly to allow such a coincidence. A stable resonator mode then exists when such a solution can be found.

For the stable two mirror resonator, shown in Fig. 2.7, Kogelnik and Li [6] derived a set of formulae relating the mirror curvatures and resonator length to the beam size at relevant points within the resonator, by applying the above boundary condition to the Gaussian beam propagation formulae derived previously.

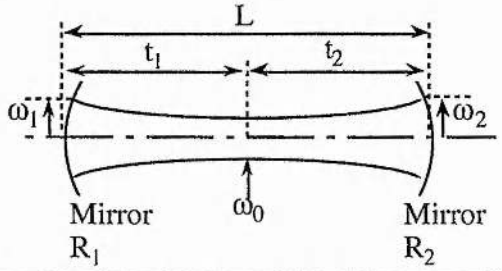

Figure. 2.7: Resonator Mode Parameters.

The mode size at the mirrors is found to be given by

$$\omega_i^4 = \left(\frac{\lambda R_i}{\pi}\right)^2 \frac{R_j - L}{R_i - L}\left(\frac{L}{R_1 + R_2 - L}\right), \tag{2.94}$$

where i and j denote the two mirrors, while the waist size ω_0 and its position, which may be formed within or outwith the resonator itself, are given by;

$$\omega_0^4 = \left(\frac{\lambda}{\pi}\right)^2 \frac{L(R_1 - L)(R_2 - L)(R_1 + R_2 - L)}{(R_1 + R_2 - L)^2}, \tag{2.95}$$

$$t_i = \frac{L(R_j - L)}{R_1 + R_2 - 2L}. \tag{2.96}$$

Equations (2.94-96) are then the general set of equations describing a two mirror resonator formed by mirrors of unequal curvature. Often they may be simplified through the choice of resonator configuration. Some examples of special resonator configurations are tabulated below.

Geometry	ω_1	ω_2	ω_0
Equal ROC $R_1 = R_2$	$=\left(\frac{\lambda R}{\pi}\right)^{1/2}\left(\frac{L}{2R-L}\right)^{1/4}$	$=\omega_1$	$=\left(\frac{\lambda}{2\pi}\right)^{1/2}[L(2R-L)]^{1/4}$
Large ROC $R \gg L$	$=\left(\frac{\lambda}{\pi}\right)^{1/2}\left(\frac{RL}{2}\right)^{1/4}$	$=\omega_1$	$=\omega_1$
Confocal $R_1=R_2=L$	$=\left(\frac{\lambda R}{\pi}\right)^{1/2}$	$=\omega_1$	$=\left(\frac{\lambda R}{2\pi}\right)^{1/2}$
Spherical $R_1=R_2=L/2$	$\to \infty$	$=\omega_1$	diffraction limited
Pl.-Parallel $R_1=R_2=\infty$	$\to \infty$	$=\omega_1$	$< \omega_1$
Pl.-Concave $R_1=\infty$	$=\left(\frac{\lambda}{\pi}\right)^{1/2}[L(R_2-L)]^{1/4}$	$=\left(\frac{\lambda}{\pi}\right)^{1/2}R_2\left(\frac{L}{R_2-L}\right)^{1/4}$	$=\omega_1$

Table 2.1: Summary of resonator mode sizes.

It should be noted in the case of the plane-parallel resonator that in practice the mode is not a plane-parallel wavefront. Due to diffraction losses at the edges of the finite sized resonator mirrors a phase lag is introduced to the wavefront which imparts on it a slight curvature [7]. Further, one may expect to observe a high power loss due to diffraction, however, the mode tends to propagate as a truncated Gaussian and consequently a lower than expected loss is observed.

For the above, and indeed any type of resonator it has been noted that a stable resonator mode exists when after successive round trips of the resonator it continues to retrace its path due to the periodic focusing of the mirrors or any other element in the resonator, and not in such a way that the rays become more dispersed. A useful means of expressing this condition in terms of mirror curvature and resonator length is to use the g-product . It is found that a stable mode exists when the stability criteria

$$0<\left(1-\frac{L}{R_1}\right)\left(1-\frac{L}{R_2}\right)<1 \qquad (2.97)$$

is satisfied. In g-factor notation that is $0 < g_1 g_2 < 1$, where

$$g_i = 1-\frac{L}{R_i}\,. \qquad (2.98)$$

The graphical representation of this condition is shown in Figure 2.8, where stable solutions may be found in the area bounded by the two hyperbola and the plot axes. The location of a number of the special resonator cases is also noted.

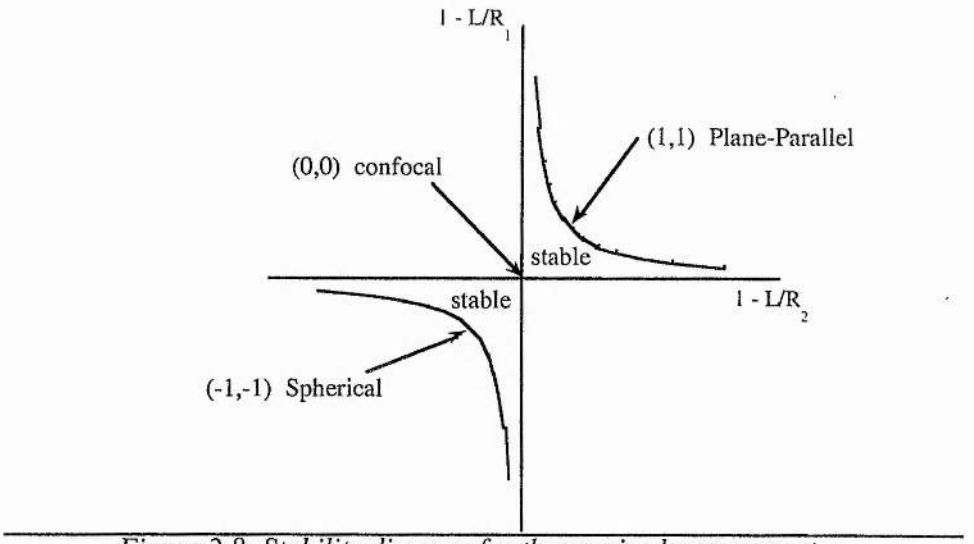

Figure 2.8: Stability diagram for the passive laser resonator.

Diffraction Losses

It was noted earlier that a stable mode is found to exist in a plane-parallel resonator due to diffraction effects at the boundary of the resonator mirrors. More generally diffraction effects are prevalent in all resonator geometries as the Gaussian mode always extends to infinity, however, in general has the effect of only introducing a small power loss due to the mode overspilling the finite mirror diameter. Clearly the loss is then a function of the mode size, this being defined by the resonator parameters R_1, R_2, and L and the beam parameters λ, m and n, and the limiting aperture radius (a) which may be a mirror diameter or gain element radius or other element within the resonator.

In discussing the diffraction loss of a resonator a useful parameter to introduce is the Fresnel number (N) given by

$$N = \frac{a^2}{\lambda L} . \qquad (2.99)$$

This may be regarded as just the ratio of the angle subtended by a mirror of radius a when viewed from the centre of the opposing mirror (a/L), to the approximate diffraction angle of the beam (λ/a). Clearly, the larger the Fresnel number the more of the beam will be accepted by the limiting aperture and the lower the loss.

Diffraction losses for resonators with circular mirrors were first studied by Li [8], who solved numerically the loss for various resonator geometries defined by some Fresnel number N and g-factor, where $g_1 = g_2 = g$. It is of note that any two resonators having the same Fresnel number and g-values will have the same diffraction loss. In practice it is found that a Fresnel number of greater than around 2 is adequate for the loss to become negligible in all resonators ranging from near plane-parallel to near concentric ($|g| < 0.9$).

Higher Order Modes

This work is predominantly concerned with the development of lasers producing beams of a high spatial and temporal quality and as such concentrates on the formation of lowest order TEM modes. For completeness however, the existence of higher order modes should be recognised. Presented here are only the more salient features of higher order modes, a more detailed analysis being found in for example ref. [6].

The TEM_{00} field distribution is just one solution to the general equations describing the passive modes of a laser resonator [9] namely;

$$I_{pl}(r,\phi,z) = I_0 \rho^l \left[L_p^l(\rho)\right]^2 \cos^2(l\phi)\exp(-\rho) \ , \tag{2.100}$$

$$I_{mn}(x,y,z) = I_0 \left[H_m(\sigma)\exp\left(\frac{-x^2}{\omega^2(z)}\right)\right]^2 * \left[H_n(\kappa)\exp\left(\frac{-y^2}{\omega^2(z)}\right)\right]^2 , \tag{2.101}$$

where in equ. (2.100) $\rho = 2r^2/\omega^2$, in equ. (2.101) $\sigma = \sqrt{2}x/\omega(z)$ and $\kappa = \sqrt{2}y/\omega(z)$ and z is the propagation direction of the beam.

These two equations describe in cylindrical and rectangular co-ordinates respectively the allowable TEM modes of a laser resonator. In the former case p and l refer to the number of nodes in radial and angular field distribution, while in the later case

m and n again refer to the number of nodes but now in orthogonal directions normal to the beam axis. L and H are the Laguerre and Hermite polynomials used to describe the detailed spatial distribution of the field.

In equ. (2.100) one sees that the centre of the beam will be bright only when $l = 0$, due to the ρ^l term. In this case the cosine term drops out and the pattern consists of a set of angularly symmetric concentric rings, the number determined by the order of the Laguerre polynomial, the intensity of which diminish with increasing radius through the exponential term. Similarly in equ. (2.101) the number of nodes are again determined by the order of the now Hermite polynomials with again the intensity of the bright lobes diminishing with transverse distance. Given that in the case of the lowest order mode $L(\rho) = 1$ and $H_m(\sigma) = H_n(\kappa) = 1$ then equ's. (2.100) and (2.101) become identical and just describe the Gaussian profile of the TEM_{00} mode considered previously.

Higher order modes, while having the same wavefront curvature to the lowest order mode, as required by the same boundary conditions being imposed by the resonator mirrors, have a larger cross sectional area than the lowest order mode. In considering modes with cylindrical symmetry it remains a straightforward task to define some mode radius, that typically being the radius at which the intensity of the outermost lobe has fallen to e^{-2} its peak value. For example, the TEM_{01} mode is 1.5 times larger than the lowest order mode, while the TEM_{10} and TEM_{11} are factors of 1.9 and 2.15 larger respectively. The divergence of the mode scales in a similar way. For modes with rectangular symmetry it is more difficult to define a mode radius and for practical purposes one defines a radius through which some fractional power of the beam is transmitted.

Given the larger mode size and greater divergence of these higher order modes, the desire to develop sources in this work with optimal brightness and spatially smooth profiles leads us to actively suppress such modes. Spatial and temporal coherence are also enhanced through their suppression; adjacent lobes have a π phase difference between them resulting in a non-uniform phasefront across the beam and degraded spatial coherence, while the transverse mode frequencies are not degenerate, due to differing phase velocities, and consequently the temporal coherence is affected when there is

simultaneous operation on more than one transverse mode. The mode separation in the frequency domain including both longitudinal and transverse mode structure is found to be given by [6];

$$\Delta\nu = \left(\frac{c}{2nL}\right)\left[\Delta q + \left(\frac{1}{\pi}\right)\Delta(m+n)\cos^{-1}\left(g_1 g_2\right)^{1/2}\right], \qquad (2.102)$$

where q refers to the longitudinal mode number and $\Delta(m+n)$ is replaced by $\Delta(2p+l)$ when working in cylindrical co-ordinates.

Active Laser Resonators

In concluding this description of the transverse mode properties of the laser resonator, it has to be noted that the discussion so far has dealt only with passive resonators consisting of two mirrors separated by some distance. In practice the laser resonator of course contains several other elements all of which distort in some way the mode of the resonator. For example, a non-uniform gain and gain saturation effects lead to normally a flattening of the Gaussian mode profile, and also introduce such effects as thermal lensing and thermal birefringence. It is often the case that additional focusing or refractive elements will also be included in the resonator which expand or reduce the mode size as necessary.

The general theory used to describe such real resonators was developed by Kogelnik [10], in which the passage of beams through lenses and lenslike media has been studied. In this work the concept of geometric ray analysis applied to optical resonators was introduced through the ray transfer matrix or ABCD notation. In this description the lateral position and angle of a paraxial ray is specified in some input plane along the beam axis and a ray transfer matrix, specific to the element being traversed, used to evaluate the new lateral position and angle at the exit plane of the element. That is

$$\begin{vmatrix} s' \\ \theta' \end{vmatrix} = \begin{vmatrix} A & B \\ C & D \end{vmatrix} \begin{vmatrix} s \\ \theta \end{vmatrix}, \qquad (2.103)$$

where s is the lateral displacement and θ the paraxial ray angle.

Rather than discussing the mode in terms of ray position and angle in the foregoing discussions, it has been expressed in terms of a mode size ω and wavefront curvature R.

These parameters were seen to be related through the complex beam parameter q using equ. (2.82b). It is found that the transformed beam parameter can also be evaluated using the ray matrix through the relationship

$$q' = \frac{Aq + B}{Cq + D} \ . \tag{2.104}$$

It is to be noted that the matrix coefficients A through D need not be those describing only a single element, but can, through matrix multiplication of the individual element matrices, be those coefficients describing an entire optical chain. It has been noted earlier that for a stable resonator mode the mode parameter q must reproduce itself after one round trip of the resonator, i.e. $q' = q$, and so it follows from equ. (2.104) that the mode parameter q is that satisfying the quadratic equation

$$Cq^2 + (D - A)q - B = 0 \ . \tag{2.105}$$

Use will be made of the ray matrix transformation notation in Chapter 4 when developing the design of optical resonators used in this work.

2.5: Line-Narrowing Techniques

Previously in this chapter the origin of multi-longitudinal mode operation of the laser resonator was introduced and seen to be a consequence of the large spectral linewidth of a lasing transition when compared to the frequency separation of the allowable modes of a laser resonator. Clearly then to obtain single longitudinal mode (SLM) operation, it is necessary to either reduce the linewidth of the lasing transition to a point at which it is comparable to the free spectral range of the laser resonator, or conversely decrease the length of the laser resonator until its free spectral range is larger than the transition linewidth, or restrict in some way the number of allowable modes supported by the resonator.

In the case of rare-earth ion doped crystalline laser media, the principal factors involved in determining the transition linewidth are; the transition lifetime, an irregular ionic field, lattice strain and thermal lattice vibrations. The former of these parameters are largely intrinsic to the particular medium chosen and it is only the latter, the thermal lattice

vibrations, that one may significantly influence. Unfortunately, however, the contribution toward the lasing transition linewidth from thermal lattice vibrations compared to the other parameters noted is small. For example, the effective transition lifetime for the $^4F_{3/2}$ to $^4I_{11/2}$ transition in Nd:YAG is around 550 μsec [11], giving a corresponding frequency bandwidth of 0.3 kHz. Contrast this with the thermal lattice vibration bandwidth of 264 GHz at 300 °K [12].

Decreasing the resonator length to the point of obtaining single axial mode operation is only practical in certain cases. The gain linewidth of a typical solid-state ion laser is of the order of 300 GHz. The equivalent resonator length for a free spectral range of this order is 500 μm. This approach has been shown to be successful in mini-lasers and microchip devices [13], but is not appropriate for high-power Q-switched lasers like those investigated here.

As then longitudinal mode selection cannot be adequately controlled through narrowing the transition linewidth or cavity shortening alone, one must look toward controlling the mode development within the resonator itself. This can be achieved through the application of one or both of the techniques of interferometric selection and injection seeding. In the former a Fabry-Perot type element is inserted into the resonator causing a strong amplitude modulation of the closely spaced modes of the laser resonator, preventing all but one mode from reaching threshold. In the latter a small SLM source is used to seed a more powerful slave oscillator, the slave oscillator mode being that mode having its frequency nearest that of the seed source. It should be noted also, however, that while the techniques noted above may have the effect of reducing the linewidth of the laser resonator at some instance in time to that of a single longitudinal mode, they do not necessarily control the absolute stability of the laser in terms of its central frequency over prolonged periods of operation. To do so requires the additional feature of locking the resonator frequency to some stable external reference, this being for example a highly stable interferometer or atomic source.

2.5.1: Interferometric Mode Selection

Two types of interferometric mode selection are commonly used, both being based on the principals of operation of the Fabry-Perot cavity. These are resonant reflectors and tilted intra-cavity étalons. In the case of the resonant reflector, the element replaces one of the laser resonator mirrors and mode selectivity is obtained through the reflectors sharp reflection peaks in the frequency domain. For the intra-cavity étalon the requirement is for sharp transmission peaks in the frequency domain and a large power loss off-resonance. In either case the element is suitably designed so that the bandwidth of its modulation peaks are sufficiently narrow as to encompass only one longitudinal mode of the laser resonator, while having a large enough free spectral range to suppress all other modes.

For some pair of plane-parallel surfaces, light undergoing multiple reflections between these surfaces will experience constructive or destructive interference effects depending on their optical separation. For each round trip of the Fabry-Perot cavity the phase difference between successive reflected or transmitted components is clearly seen from Fig. 2.9 to be just

$$\delta = \left(\frac{2\pi}{\lambda}\right) 2nd\cos\phi \ . \tag{2.106}$$

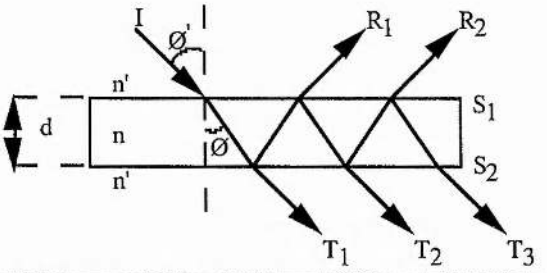

Figure 2.9: Multiple reflections in a plane-parallel plate.

By adding together the complex amplitudes of the transmitted or reflected components and multiplying by the complex conjugate to obtain an irradiance, one obtains the total transmission of the Fabry-Perot étalon as

$$\frac{I_t}{I_i} = \left(\frac{t}{1-r}\right)^2 \frac{1}{1+[4r/(1-r)^2]\sin^2(\delta/2)} \ . \tag{2.107}$$

It is noted that as $\delta \rightarrow 0$ then equ. (2.107) tends to 1 for a lossless media, or accordingly for any real étalon where $t \neq (1-r)$ to some value given by

$$\frac{I_{t.max}}{I_i} = \left[1 - \frac{a}{(1-r)}\right]^2 , \tag{2.108}$$

where a is the combined scatter and absorption component loss. For some intra-cavity étalon it is clearly desirable to have a parasitic loss approaching zero as at this point the étalon transmission becomes independent of the surface reflectivity, so aiding the use of high finesse devices.

In a similar way, the reflected component from a Fabry-Perot étalon is given by

$$\frac{I_r}{I_i} = \frac{1}{1 + [(1-r)^2 / (4r\sin^2(\delta/2))]} . \tag{2.109}$$

It is noted now that as $\delta \rightarrow 0$ the reflected component goes to zero and that the peaks in reflectivity occur when $\delta \rightarrow n\pi$, where n is an odd integer. The maximum reflectivity of a single element is then

$$R_{max} = \frac{4r}{(1+r^2)} . \tag{2.110}$$

Equations (2.107) and (2.109) describe the transmission and reflectivity characteristics within the frequency domain of the single element Fabry-Perot étalon and provide the basis for the design of such elements. For convenience they are often expressed in a more simplified form, by substituting a coefficient of finesse

$$F = \left(\frac{2r^{1/2}}{1-r}\right)^2 . \tag{2.111}$$

As has been previously noted, the finesse of an étalon is just the ratio of its free spectral range to the width of its passband, defined at the 50% power transmission points. For then some lossless element at normal incidence, combining equ's. (2.106) and (2.107) gives a finesse

$$\mathcal{F} = \pi\left[2\arcsin\left(\frac{(1-r)^2}{4r}\right)^{1/2}\right]^{-1} . \tag{2.112}$$

For values of $r > 0.5$ this expression can be simplified and shown to be just $\pi\sqrt{F}/2$. Including some absorption or gain coefficient α gives the more general expression noted in equ. (2.77) for some real Fabry-Perot element.

Resonant Reflectors

The most simple form of resonant reflector is that resulting from a three mirror cavity design originally proposed by Kleinmen [14]. A third reflecting surface located in a linear two mirror resonator, usually near to one of the existing mirrors, and aligned parallel to the existing mirrors will form a secondary cavity with high finesse and large free spectral range.

A particularly simple form of this is created by aligning a surface of an already existing optical element in the laser resonator to that of a cavity mirror and so forming a secondary cavity in this way. While the reflectivity of this additional surface may be low, perhaps less than 0.25% for an anti-reflection coated surface, if the secondary cavity contains the gain element then for operation above threshold a useful finesse may still be obtained†. Such a reflector was demonstrated successfully by Bua *et al.* [15] who generated temporally smooth, SLM, Q-switched pulses of 5 nsec duration from a Nd:YAG laser.

Two element reflectors have also been usefully employed, notably by Voss and Goldberg [16], who again in Nd:YAG obtained single longitudinal mode operation of a Q-switched resonator with the insertion of a third mirror with 85% reflectivity. With the addition of slow-Q-switching pulse duration's in the range 10 - 300 nsec were obtained, all the time being of a single longitudinal mode. Previously observed problems in the degradation of spatial beam quality through the use of resonant reflectors was in this work noted to have been minimised through the careful alignment of the third reflector and spatial mode matching of the two resonant cavities.

---

† For R=99.9% and 0.25%, gain coefficient 0.25 cm^{-1} and gain length of 10 cm then the effective finesse is 6.2. (Equ. 2.77)

Resonant reflectors comprising stacks of uncoated glass or sapphire plates have also been extensively studied. The maximum reflectivity of an uncoated flat, obtained by substituting the expression for the Fresnel reflectivity into equ. (2.110), is of course low, however, it can be shown that [17] the peak reflectivity of a multi-element reflector is considerably enhanced and given by

$$R_{max} = \left\{ \frac{1 - \left(\frac{1}{n}\right)^{2N}}{1 + \left(\frac{1}{n}\right)^{2N}} \right\}^2 , \qquad (2.113)$$

where N is the number of elements in the reflector and n their refractive index.

The periodicity of the resonance peaks of the multi-element device is determined by the product of the multiple resonance effects within the device. For the three element device six such resonances are identifiable, the shorter optical path length resonances being seen (see Fig. 2.10) to strongly amplitude modulate the closely spaced transmission peaks of the long optical path length resonanaces.

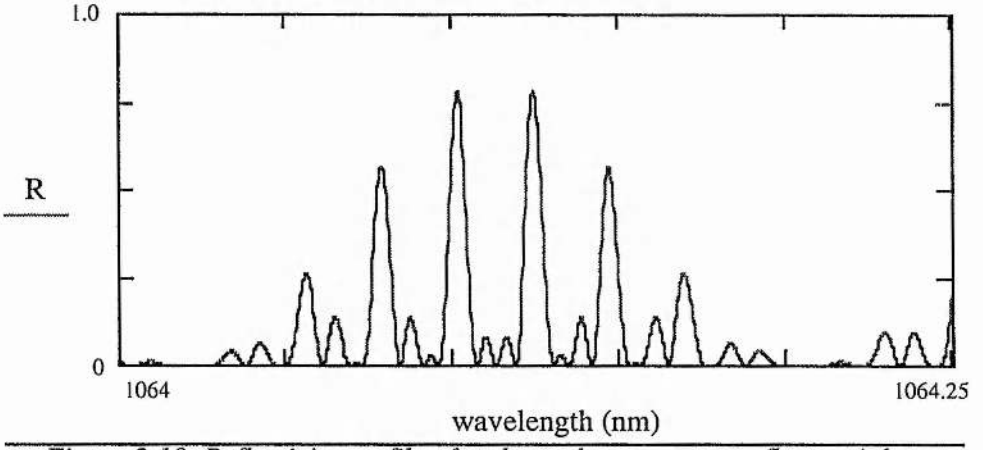

Figure 2.10: Reflectivity profile of a three plate resonant reflector (plate thickness = 2.0 mm, plate separation = 20 mm and n=1.5)

A more in-depth theoretical analysis of the resonant reflector, as performed by Watts [17], shows that plate thickness and plate separation tolerance is vital for optimising the reflectors peak reflectivity and periodicity. Typically errors should be no more than $\lambda/10$ in either case. Due to the relatively low peak reflectivity attainable these devices have been used predominantly in high gain Q-switched lasers. See for example [18-22].

Intra-cavity étalons

Historically resonant reflectors have been used as mode discrimination elements in high- power, Q-switched lasers as they may be fabricated from high damage threshold substrate materials and are typically uncoated, circumventing dielectric coating damage limitations. The intra-cavity étalon offers several advantages however, particularly in terms of simplicity of design, stability and versatility of use through tailoring the free spectral range and bandwidth to ones requirements by the application of dielectric coatings. Over the last decade high damage threshold coatings have been developed which now allow the potential advantages of the intra-cavity étalon to be exploited in both high-power pulsed and CW lasers [23-25].

Inserted at some angle in the laser resonator, to decouple it from the resonator mirrors and so avoid any spurious resonances, the étalon thickness and finesse are chosen so that its passband encompass only one mode of the laser resonator, while having a large enough free spectral range to preclude all other modes under the gain linewidth. This in fact is normally difficult to achieve with a single étalon and consequently 2 or 3 étalons of different thicknesses are often used simultaneously. As with the resonant reflector the periodicity of the line-narrowing element is then determined by the product of the transmission characteristics of the individual étalons.

While simple to use there are a number of practical considerations which should be taken in to account when using intra-cavity étalons. Firstly, in earlier theoretical discussions of étalons the passband was noted to be just the ratio of the étalons free spectral range to finesse. This resolution limit is in fact only achievable for a perfectly collimated beam and so in reality the inherent divergence of even a well collimated beam will reduce the spectral resolution attainable. Essentially, off-axis components, at some angle $\delta\theta$, and at some higher or lower frequency will still satisfy equ. (2.106) and consequently broaden the étalon passband. This results in an increased width to the passband given by

$$\delta\lambda = \lambda(\delta\theta)^2 \ . \qquad (2.114)$$

When $\delta\theta$ is defined by the diffraction of the laser beam it clearly becomes desirable to place the intra-cavity étalon at a point in the laser resonator where the mode size is maximised, at this point the diffraction angle being minimised.

Secondly, it has been noted that it is normal to insert an étalon in the resonator at some angle to decouple it from the resonator mirrors. Tilting the étalon, and so perturbing its effective optical thickness, also provides a convenient means by which its resonances may be tuned, to optimise overlap with a longitudinal mode of the resonator, or indeed to tune the resonator over some limited range. Tilting, however, results in some additional loss due to beam walk-off over successive round trips. Clearly, this loss is proportional to the degree of tilt angle, and inversely proportional to the beam size. More subtly it is also proportional to the finesse of the étalon; essentially the higher the finesse, the greater the number of round trips of the étalon occur and so the higher the loss. Consequently it is again desirable to locate the étalon in an area of the resonator where the mode is large and also to keep the finesse low. Restricting the finesse can preclude the use of only a single étalon in controlling the axial modes of the resonator and leads to the use of multiple étalons [25] as noted previously.

Enhancement of Interferometric Mode Selecting Techniques

Interferometric mode selection can be enhanced by making alterations to the laser resonator itself. Such modifications include; cavity length shortening, twisted mode resonators and extended pulse build-up times.

Cavity length shortening has already been discussed, and utilises the fact that the resonator is itself a mode selecting element. Shortening the resonator increases the longitudinal mode spacing and so places less demand on any intra-cavity étalons to have a large free spectral range and high finesse.

Single frequency operation is further aided by the elimination of spatial hole burning effects within the gain medium, arising due to the periodic waveform within a standing wave resonator. A common solution in many lasers, and especially where the gain bandwidth is very large such as in dye and vibronic lasers, is to adopt a unidirectional ring resonator structure. Another approach which is often used in Nd

lasers is to place the gain medium between properly orientated quarter-waveplates to create a twisted mode resonator in which the electric field between the waveplates is spatially uniform [26]. This technique has been shown to be generally applicable to most lasers, including polarisation coupled resonators similar to that which will be described in Chapter 4, where the polarisation state in the gain medium need not be circular but can be a more general elliptical state [27].

While interferometric techniques have then been successfully employed in line-narrowing, there are attendant difficulties associated with them, such as at times significant insertion losses and damage limitations. As an alternative which does not have such limitations, injection seeding can be considered.

2.5.2: Injection Seeding

By injecting the CW output from a small single-frequency oscillator into a more powerful slave oscillator, the slave oscillator can be forced to operate on a single longitudinal mode only, that being the slave resonator mode whose frequency is closest to, and preferably on-resonance with, the seed frequency.

The single-frequency master oscillator may take the form of a conventional two mirror resonator, narrow linewidth ring laser or, now more commonly, a monolithic ring resonator [28]. In the slave oscillator, the injected wave and noise grow simultaneously as the Q-switch is opened, the winner being that resonator mode which first saturates the gain medium. With a seed power of typically less than a few milliwatts and a near resonance condition this will be the seeded mode, resulting in a Q-switched output which reproduces the spectrum of the seed field.

This means of longitudinal mode selection provides probably the most reliable single frequency operation, the most significant limitation being the possible presence of spatial hole burning effects. This effect can be eliminated by introducing relative motion between the crystal atoms and the circulating electromagnetic field, often achieved through the use of either a twisted mode resonator or travelling wave ring resonator. It will be seen, however, that here neither is necessary, due in part to the short gain length associated with the end-pumped diode-laser pumped geometry used.

2.5.3: Slow Q-Switching

The technique of slow Q-switching, or pre-lase Q-switching, may be regarded as a special form of injection seeding, where the Q-switch pulse builds-up from a low level circulating field generated in the laser resonator itself. The technique involves increasing the resonator Q-factor during the pump cycle so that a low level field grows over many resonator round trips, preferentially selecting a single longitudinal mode of the resonator. Once established, the Q-switch is fully opened and the giant pulse seeded by the low level single axial mode circulating field.

The implementation of this technique is optically straightforward, necessarily requiring no additional elements beyond those of the Q-switched resonator, unlike dispersive or interferometric techniques, or the interfacing of an external seed source. Consequently, this may be a most efficient means of generating single-frequency radiation and is the approach adopted in this work.

Chapter 2 References:

1. A. Einstein *"Zur quantentheorie der strahlung"* Phys. Zeits. 18 pp.121-128, March 1917.

2. J. J. Degnan *"Theory of optimally coupled Q-switched lasers"* IEEE J. Quant. Elect. QE-25 (2) pp.214-220, 1989.

3. D. Findlay and R. A. Clay *"The measurement of internal losses in 4-level lasers"* Phys. Lett. 20 (3) pp.277-278, 1966.

4. A. L. Schawlow and C. H. Townes *"Infrared and optical masers"* Phys. Rev. 112 pp.1940-1949, 1958.

5. A. Yariv *"Optical Electronics - Fourth Edition"* (Harcourt Brace Jovanovich College Publishers, Orlando), 1991.

6. H. Kogelnik and T. Li *"Laser beams and resonators"* Appl. Opt. 5 (10) pp.1550-1567, 1966.

7. A. G. Fox and T. Li *"Resonant modes in a maser interferometer"* Bell Syst. Tech. J. 40 pp.453-488, 1961.

8. T. Li *"Diffraction loss and selection of modes in maser resonators with circular mirrors"* Bell Syst. Tech. J. 44 pp.917-932, 1965.

9. A. E. Seigman *"Lasers"* (University Science Books), 1986.

10. H. Kogelnik *"Imaging of optical modes - resonators with internal lenses"* Bell Syst. Tech. J. 44 pp.455-494, 1964.

11. T. Kushida, H. M. Marcos and J. E. Geusic *"Laser transition cross section and fluorescence branching ratio for Nd^{3+} in ytrrium aluminium garnet"* Phys. Rev. 167 (2) pp.289-291, 1968.

12. L. A. Riseberg and W. C. Holton *"Nd ion site distribution and spectral line broadening in YAlG:Lu, Nd laser materials"* J. Appl. Phys. 43 (4) pp.1876-1878, 1971.

13. H. Imai and M. Daimon *"Single-frequency laser using a 100 μm thick Nd:YVO_4 crystal in a 50 mm long cavity"* Optical Review 2 (3) pp.171-173, 1995.

14. D. A. Kleinman and P. P. Kisliuk *"Discrimination against unwanted orders in the Fabry-Perot resonator"* Bell Syst. Tech. J. 41 p.453, 1962.

15. D. Bua, D. Fradin and M. Bass *"A simple technique for longitudinal mode selection"* IEEE J. Quant. Elect. QE-8 (12) pp. 916-917, 1972.

16. D. F. Voss and L. S. Goldberg *"Simple single longitudinal mode Q-switched Nd:YAG oscillator"* IEEE J. Quant. Elect. QE-21 (2) pp. 106-107, 1985.

17. J. K. Watts *"Theory of multiplate resonant reflectors"* Appl. Opt. 7 (8) pp. 1621-16231623, 1968.

18. M. Hercher *"Single-mode operation of a Q-switched ruby laser"* Appl. Phys. Lett. 7 (2) pp. 39-41, 1965.

19. D. G. Peterson and A. Yariv *"Interferometry and laser control with solid Fabry-Perot etalons"* Appl. Opt. 5 (6) pp. 985-991, 1966.

20. M. Daehler, G. A. Sawyer and E. L. Zimmermann *"Mode control in a ruby laser"* J. Appl. Phys. 38 (4) p.1980, 1967.

21. M. M. Johnson and A.H. LaGrone *"Continuously tunable resonant ruby laser reflector"* Appl. Opt. 12 (3) pp. 510-518, 1973.

22. P. W. Smith *"Mode selection in lasers"* Proc. IEEE 60 (4) pp. 422-440, 1972.

23. E. Snitzer *"Frequency control of a Nd^{3+} glass laser"* Appl. Opt. 5 (1) pp. 121-125, 1966.

24. H. G. Danielmeyer and W. N. Leibolt *"Stable tunable single-frequency Nd:YAG laser"* J. Appl. Phys. 3 (3) pp.193-198, 1974.

25. W. Culshaw, J. Kannelaud and J. E. Peterson *"Efficient frequency-doubled single-frequency Nd:YAG laser"* IEEE J. Quant. Elect. QE-10 (2) pp. 253-263, 1974.

26. V. Evtuhov and A. E. Siegman *"A twisted-mode technique for obtaining axially uniform energy density in a laser cavity"* Appl. Opt. 4 (1) pp142-143, 1965.

27. E. S. Fry and S. W. Henderson *"Suppression of spatial hole burning in polarisation coupled resonators"* Appl. Opt. 25 (18) pp.3017-3018, 1986.

28. T. J. Kane and R. L. Byer *"Monolithic, unidirectional single-mode diode-pumped Nd:YAG ring laser"* Opt. Lett. 10 (2) pp.65-67, 1985.

Chapter 3
Diode-Laser Pumping of Nd Doped Gain Media

In the preceding chapter it was noted how one may create in atomic media a population inversion through optical excitation of the electron states. Most commonly such pump radiation is derived from arc lamps, filled with either krypton or xenon gas, and located close to the gain medium. Lamps and gain medium are then encapsulated in a pump chamber, normally incorporating reflective elements to help direct the randomly orientated lamp emission toward the gain element and so enhance the coupling efficiency. While high coupling efficiencies can be derived from such schemes, overall efficiency remains low due to much of the lamp radiation being of an inappropriate wavelength for excitation of the laser transition. As an alternative to the flashlamp, the first recorded allusion to the use of semiconductors in pumping solid-state gain media was then presented by Newman [1], who as early as 1963 recognised some of the possible advantages to be gained by replacing flashlamps with narrowband semiconductor diode sources. In his work GaAs diodes were observed to radiate in the range 0.865 μm to 0.9 μm, this wavelength range being recognised as suitable for pumping Nd:$CaWO_4$ (tungstate) at liquid nitrogen or room temperatures. At 77 °K strong fluorescence at 1.06 μm was observed from the Nd:$CaWO_4$ sample when pumped by Mn diffused GaAs diodes. The first actual pumping of a laser by GaAs diode-lasers was demonstrated by Keyes and Quist also in 1963 [2], shortly after the development of the diode-laser itself. In their work $CaF_2:U^{3+}$ was pumped at 0.84 μm and laser emission observed at 2.6 μm. Five diode-lasers were connected in series and illuminated transversely the laser gain medium. Illumination was via a slit in an integrating chamber surrounding the gain medium, incorporated to enhance pump coupling efficiency, as shown previously in Fig. 1.1.

In this chapter the advantages of diode-laser pumping solid-state lasers over flashlamp pumping are initially highlighted. A brief description then follows of the

fabrication and operating characteristics of semiconductor diode-lasers, with particular emphasis placed on quasi-CW devices and their use in pumping solid-state gain media. A comparison of end- and side-pump coupling geometries is then made, and finally a comparison of several neodymium:host laser materials is made, with particular regard being given to their suitability to diode-laser pumping.

3.1: The Advantages of Diode-Laser Pumping

Although having a lower radiative efficiency than the flashlamp (~50% compared to 90%) the diode-laser emits over a spectral range comparable to the absorption features of many solid-state gain media, as demonstrated in Fig. 3.1 for Nd:YAG.

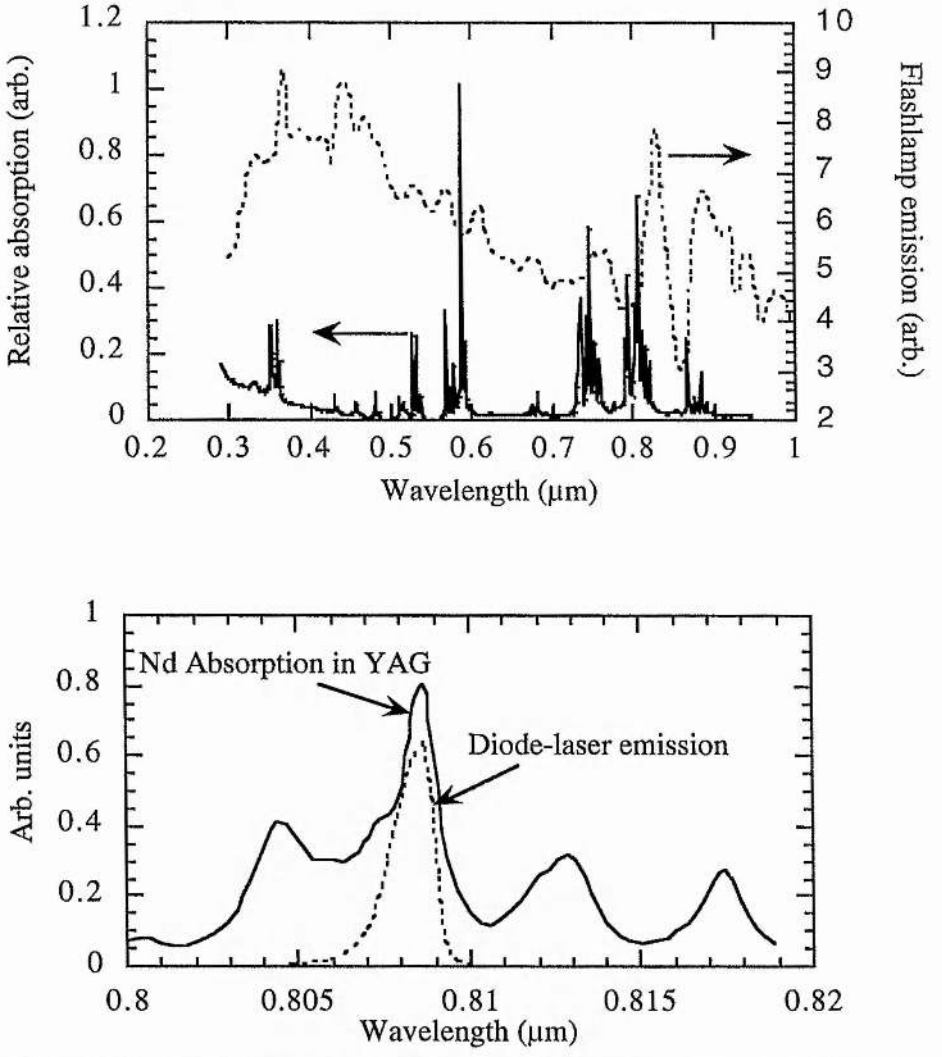

Figure 3.1: Comparison of lamp (upper) and diode-laser (lower) emissions with Nd:YAG absorption properties.

As a consequence of improving the overall system efficiency, due to all the pump radiation being potentially useful in pumping the lasing transition, diode-laser pumping leads to a lower thermal loading of the gain medium. Absorption of pump light radiation which results in an electron transition to some level other than the upper laser level, and which is followed by non-radiative decay, results in heating of the gain medium. This heating mechanism is clearly more pronounced in the case of flashlamp pumping where the majority of the lamp radiation lies outwith the absorption bands for the laser transition. Heating also occurs due to the quantum defect between the pump wavelength and laser emission wavelength. Although the same for that component of the lamp radiation lying in the same spectral range as the diode-laser pump wavelength, the laser transition in for example Nd:YAG can also be pumped through the absorption bands lying toward the blue end of the spectrum. Clearly this pump mechanism leads to additional heating due to a larger quantum defect.

Combined with the high spectral brightness of the diode-laser, the directional properties of it also lead to higher pumping densities being achieved. The diode-laser output can be focused into a small cross-sectional area, while the narrowband nature of the light allows the narrow absorption features of the gain medium to be fully exploited and consequently a short absorption depth realised. This enables the pumped volume to be minimised and consequently a high pumping density achieved with an associated increase in gain. Additionally, diode-laser pumping has enabled the demonstration of efficient quasi-three level lasers at room temperature, which had not been previously demonstrated in lamp pumped devices. These lasers require high pumping densities to elevate a large proportion of the ground state population into the upper laser level in order to achieve a population inversion and gain. High pumping densities have also facilitated the demonstration of up-conversion lasers, where the laser wavelength is longer than the excitation wavelength. Population in the upper laser level is generated through a multi-step excitation process, specifically excited state absorption. For this to be efficient, high pumping densities are required and ideally multiple pump sources used, each tuned to the specific excitation frequencies of the multi-step process. The ability to focus the diode-laser light into a small cross-section has obvious advantages

also in the pumping of fibre lasers and amplifiers. In this case the pump light can be efficiently coupled into the fibre, where it may be guided over long distances, efficiently pumping even low absorption media.

Diode-laser pumped lasers have been observed to have improved amplitude and frequency stability when compared to lamp pumped devices. This may be attributed to reduced amplitude instability in the output of the diode-laser compared to flashlamps, reduced heating of the gain medium and less mechanical noise. Heating of the gain medium results in localised variations in refractive index with consequential changes to the optical length of the laser resonator and thus its resonant frequencies, thus broadening the lasing linewidth. Additionally, vibrations and acoustic noise generated by flowing gas or liquid for lamp cooling again modify the optical path length and increase the linewidth. In contrast diode-lasers are typically conduction cooled and only high power devices require liquid or forced air cooling around the solid-state laser gain medium.

3.2 : Semiconductor Diode-Lasers

For some twenty years light emitting diodes, and then more recently laser-diodes, have been used to pump solid-state gain media, and in particular rare-earth ion doped insulator lasers. Development having been driven by the potentially dramatic increase in efficiency to be gained in such lasers and consequently the alleviation of problems associated with for example thermal loading and power consumption, has seen diode-laser powers increase from just μW's for small single stripe devices to 1 and 2D arrays producing 10's W CW and pulsed devices generating 1 - 2 kW peak powers.

3.2.1: Diode -Laser Fabrication

Based on Gallium Arsenide (GaAs) technology, stimulated emission was first observed in this semiconductor material simultaneously by three groups in 1962 [3-5]. Over the last thirty years these initially fragile devices with lifetimes of only a few

seconds and which required to be operated at cryogenic temperatures have been developed into robust and reliable devices suitable for a diverse range of applications.

Present-day diode-laser device types can be broadly divided into four categories: low power single stripe devices; large area 2D surface emitting arrays; multiple stripe CW devices; and quasi-CW pulsed laser-diodes. Each have found applications specific to their light emission characteristics, for example the former being used in such areas as compact disc players, laser printing, fibre communications and optical data storage. It is, however, the latter two which are of particular interest here, for the optical pumping of solid-state lasers. A schematic of these device types is shown in Fig. 3.2.

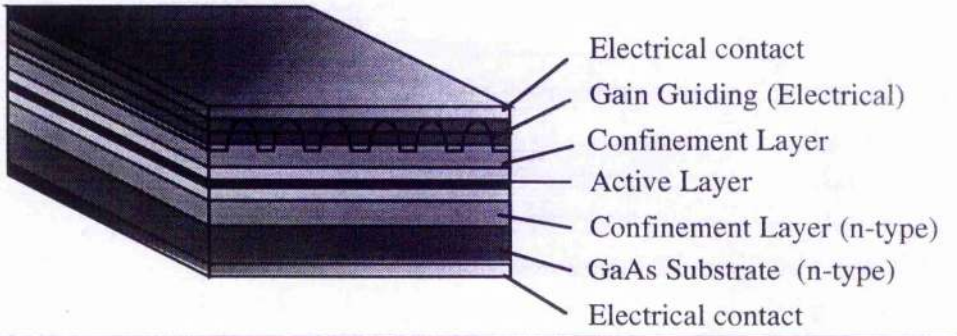

Figure 3.2: Multiple stripe, semiconductor diode-laser array construction.

The active layer is sandwiched between two confinement layers which have a higher aluminium doping level and consequently larger bandgap, so providing charge confinement, while the refractive index of these layers is also conveniently lower, providing optical confinement in a vertical plane through total internal reflection at the junction interface. Laser emission is confined laterally to a stripe through either fabricating the stripe from a different refractive index layer to the surrounding material, as with vertical confinement, or through gain guiding due to the profile of the electrical structure, as depicted in Fig. 3.2. Index guiding tends to be prevalent in low power devices and provides better confinement and consequently improved spatial beam quality compared to gain guiding. Typically found in high-power devices, gain guiding results in a more spatially dispersed beam, however, this is not necessarily detrimental in applications such as laser pumping and indeed is advantageous in reducing the power density on the diode-laser facet where there is a constant risk of optical damage. It is

important to preserve facet quality as it is the reflection from these surfaces that provides optical feedback in the laser-diode. Given the high refractive index of GaAs (~3.6) this leads to a Fresnel reflection at the diode facets of 30%, high enough to overcome losses and sustain laser oscillation without the addition of reflective coatings. Such coatings are at times applied, particularly to the rear facet of the diode, in which case efficiency can be improved and threshold reduced, however, one must again be aware of the potential risk of optical damage in high-power devices.

It has been noted that for efficient laser pumping one requires to match the spectral output of the diode-laser to absorption features within the laser gain medium. Diode-laser wavelengths are determined by the band gap of the active layer, in pure GaAs this being 1.35 eV (0.92 μm). It is found that doping with aluminium increases the bandgap energy, so reducing the emission wavelength, where over the range $0 < x < 0.45$, $Ga_{1-x}Al_xAs$ remains a direct bandgap material as necessary for lasing operation. For the maximum Al doping the bandgap energy is shifted to 2.0 eV or 0.62 μm. For some nominal doping level, wavelength tuning is at a rate of around 10 Å for a 1% change in Al doping. Bandgap energies for various III-V semiconductor compounds including GaAs and doped GaAs are shown in Fig. 3.3. GaAlAs laser-diodes can then be fabricated with emission wavelengths suitable for pumping the 1 μm and 1.3 μm transitions in neodymium doped laser crystals, typically pumped at around 800 nm, as well as other solid-state gain media. Notably, reliable diodes have recently been fabricated operating at the lower wavelength limits of the above range, which are suitable for the direct diode-laser pumping of new vibronic gain media such as Cr:LiSAF and Cr:LiCAF [6, 7].

The whole diode-laser structure is typically grown on a GaAs substrate, which is easier to produce in large wafer form than the Al doped material. The growth of bulk layers of high quality Al doped GaAs on the pure substrate is made possible by the close lattice match of GaAs (0.5653 nm) and AlAs (0.5662 nm), although more recently the advance of strained layered technologies have relaxed the requirement for excellent lattice matching. This relaxation also allows the growth of quaternary compounds on GaAs, so extending the spectral coverage further, as again depicted in Fig. 3.3.

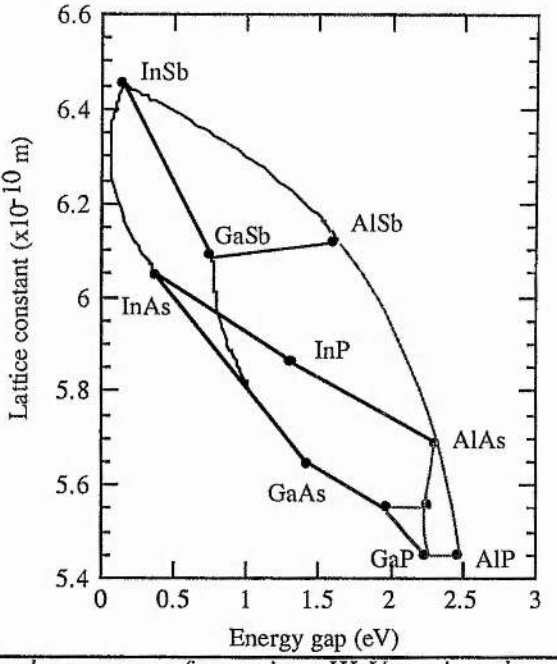

Figure 3.3: Bandgap energy for various III-V semiconductor compounds (after ref. [8]).

3.2.2: Diode-Laser Operating Characteristics

Having considered briefly the fabrication of diode-lasers, attention is now turned to the various operating parameters associated with these devices. Of particular interest is the efficiencies which can be achieved and the associated powers at which they may be operated along with their spectral characteristics. It is just these parameters which define the much improved radiation density of the diode-laser compared to the flashlamp, and which result in the considerable advantages offered in the pumping of lasers. The following discussion will concentrate on the operation of *quasi-CW* diode-lasers, that being diode-lasers which operate with pulse duration's exceeding several μsec's and at repetition rates of up to 100 Hz. Diode-lasers of this type are consistent with the pumping requirements of gain media such as Nd:YAG and Nd:YLF when operated in a Q-switched mode, where the fluorescence lifetime of the lasing transition is of the order of tens or hundreds of μsec's.

Efficiency and Output Energy

The output energy of the diode-laser is clearly determined by how efficient it is at turning the input electrical energy into useful radiation. This absolute efficiency is in turn determined by the threshold current required to drive the diode, its slope efficiency for drive currents above threshold and the operating point relative to threshold. One tends to find the slope efficiency to be constant over a large range of drive currents and consequently as the drive current is increased the absolute efficiency approaches the slope efficiency. Ultimately, however, the drive current is limited by the amount of waist heat that has to be dissipated in the device.

While heat dissipation limits the average power of the device, peak powers are limited by catastrophic facet degradation. Light absorbed near the facet of the diode results in localised heating and eventual thermal runaway, raising the temperature to melting point and irreversible failure. Thermal diffusion times within the diode are of the order of μsec's and consequently diodes operating with longer pulse duration's have similar drive current limitations to CW devices - hence the terminology of quasi-CW devices.

Maximum energy levels scale with the volume of the active layer, a single 100 μm wide and 1 μm high stripe generating pulse energies of typically around 1 mJ, in 400 μsec pulses. To increase pulse energies further the active layer is fabricated with many parallel stripes, a typical geometry now being a 1 cm wide bar containing 40 stripes and with a corresponding pulse energy of around 40 mJ [9]. Such bars may then be stacked into 2D arrays, as many as 50 bars being stacked in one package, with a corresponding output energy of 2 J or 5 kW peak power (SDL-3251-HK). Drive current threshold for this type of device is around 35 A and operating current at maximum output around 120 A. Single bar and devices comprising only a few stacked bars typically operate with drive currents of 70 - 80 A, depending on the particular device geometry, while slope efficiencies are in the range 30 - 50 %.

As previously noted the maximum average power which may be derived from the laser-diode is determined by the thermal loading on the package. This restricts the duty factor to typically 2 - 4 %, however, through the use of back surface impingement

coolers and by operating the diode in a longer pulse (1000 μsec), low peak power mode this can be extended to 20 %.

Spectral and Spatial Quality

The efficient pumping of lasers requires the spectral characteristics of the diode-laser to be well matched to the absorption features of the particular medium being pumped. This then places some constraint on the centre wavelength of the diode-laser and in turn its long term stability, as well as the spectral width of the emission.

Typically the absorption features in neodymium doped lasers have a bandwidth of ~2 nm, although this may be as high as 5 nm in for example Nd:YVO_4. Single element diode-lasers have a spectral width comparable to this (2 nm FWHM), however, in the case of arrays this is broadened due to slight compositional changes and temperature gradients across the bars. Consequently the spectral width of a 1 or 2D array is typically 2-4 nm. Further broadening of the spectral output occurs due to transient heating of the active layer during the emission of a pulse as demonstrated by the start of pulse and end of pulse spectra shown in Fig. 3.4 for a 25 W peak power quasi-CW diode-laser array.

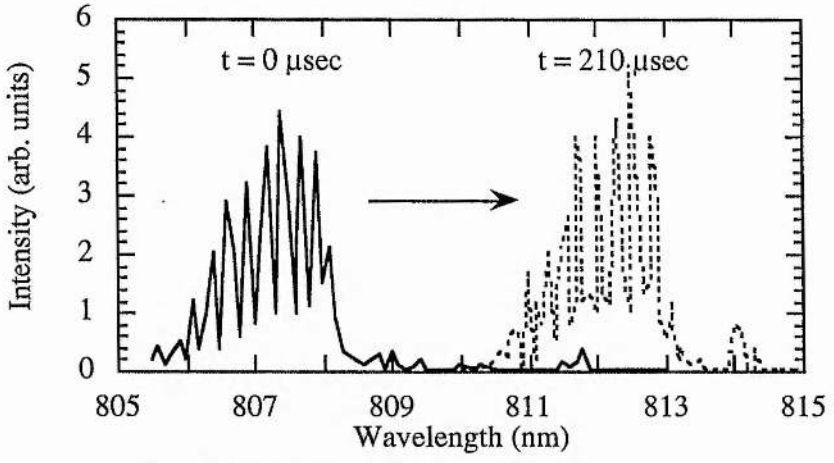

Figure 3.4: Transient spectral output of a diode-laser bar (after ref. [10]).

Lifetime/Reliability

Particularly outwith the laboratory environment, lifetime considerations are an important factor in the usefulness of any device, either through the desire to develop

reliable commercial devices or the practical difficulty that may arise in replacing failed components - for example in spaceborne applications. A further attractive feature of diode-lasers as a pump source for optically excited lasers is then their long lifetime when compared to flashlamps. Typical operating lifetimes for such pump sources are now in the range 5,000 to 30,000 hours when operated in either a CW or pulsed mode (up to 10^{10} pulses at 100 Hz continuous), and depending upon the operating point in relation to the maximum operating conditions of the diode. This should be contrasted with the best flashlamp lifetimes of < 1000 hours.

Diode-laser failure has been studied extensively in improving the reliability of early devices [11-13] and as a result failure mechanisms have been identified which may be broadly divided into three categories: facet damage; ohmic contact degradation; internal defects. Each of these mechanisms have associated with them both sudden, or catastrophic, and gradual failure scenarios as outlined below.

• Facet Damage

Catastrophic facet damage generally occurs when the power density exceeds the mechanical damage threshold of the device. Such damage results in a reduction of optical feedback and consequential increase in threshold current and reduced quantum efficiency. Damage threshold levels in the short pulse regime (< 1 μsec) have been seen to be dependent on the square root of the pulse length [14], while for pulses longer than this CW levels may be assumed. Typically, damage threshold in this regime is around 1.5 $MWcm^{-2}$.

Gradual facet degradation occurs due to facet erosion, resulting from the oxidation of the mirror facet in the vicinity of the emitting aperture. Degradation in only this vicinity indicates the process to be light activated. The consequences of facet erosion are similar to those of catastrophic failure, but also increases nonradiative recombination and thus thermal loading and may assist in the creation and migration of defects. The onset of such erosion can be circumvented by the application of coatings to the facet, so forming a moisture barrier.

• Ohmic contact degradation

The deterioration of ohmic contacts has been seen to result in increased electrical and thermal resistance within the diode-laser, particularly between the chip and heatsink [15]. Degradation is thought to be caused by one of two mechanisms: the formation of inter-metallic compounds involving gold and indium in the vicinity of the solder contacts, which have a high thermal resistivity compared to the semiconductor material; and indium migration into the semiconductor material. The increase in junction temperature due to thermal resistance at the heatsink boundary causes an increase in threshold current and consequential reduction in power conversion efficiency for some constant drive current. These parameters are linked through equ. 3.1, which describes the junction temperature rise as a function of the drive current (I), junction voltage drop (V_j), electrical resistance (R_s), conversion efficiency-(η_p), duty cycle (D) and thermal resistivity (φ);

$$\Delta T = \left(I^2 R_s + I V_j\right)\varphi\left(1-\eta_p\right)D \,. \qquad (3.1)$$

A gradual increase in electrical resistance has also been observed, however, this is not generally regarded as serious a problem as increased thermal resistance. The rate of deterioration is influenced by several factors, including solder types used, drive current and operating temperature. Typically however, increasing the operating temperature by a factor of 2 will reduce the gradual degradation lifetime by an order of magnitude.

• Internal defects

Internal defects within the active region of the diode-laser have been identified which reduce quantum efficiency and increase optical absorption. Visual observation of nonradiative regions, which are consequently denoted 'dark lines', in degraded diode-lasers indicated large areas of dislocations, which grew during device operation [16]. It is believed that the catalyst for multiplication of dislocations within the chip is nonradiative recombination of electron-hole pairs, the small amount of energy being released through this interaction being absorbed and easing the growth of dislocation networks [17].

Degradation in devices initially free from dislocations has also been observed, particularly in the form of 'dark points'. This may be attributed to low radiative efficiency regions migrating into the bulk material from the facet and other device surfaces [18]. This is similar to the damage mechanism previously noted in relation to facet damage, however, in some of the devices noted to have suffered from defect migration facet damage was not evident.

3.3: End- and Side-Pump Diode-Laser Pump Geometries

Having outlined the potential advantages in using diode-laser pump sources and their operational characteristics, attention must now be turned to what in the context of this work is the more important issue of their practical implementation. In general terms, arrangements for coupling the pump radiation from diode-lasers into a solid-state laser gain medium can be divided into two classes; longitudinally-pumped or so called end-pumped configurations; and transversely-pumped or so called side-pumped configurations. In the former case the geometry is such that the pump radiation is coupled into the gain medium co-axially with the solid-state laser resonator axis, while in the latter case the pump radiation propagates transversely to the resonator axis. End-pumping is generally regarded as the more efficient means of pumping, this technique affording the opportunity of minimising the pumped volume and simultaneously achieving an optimum overlap with the resonator mode. Limited potential exists for scaling however and thus side-pumping, although being less efficient, is more suited to high power devices where additional diode-laser pump modules may be added along or around the gain medium.

3.3.1: Transverse Pumping Schemes

To couple diode-laser radiation transversely into the laser gain medium, one of two schemes are generally invoked: simply locating the diode-laser arrays close to the laser gain medium, however this does not allow a great deal of flexibility in shaping the pump cross-section; or intervening optics may be placed between diode-laser and

gain medium, in which case the pump distribution may be modified, to be peaked on axis, providing a better overlap with the lowest order resonator mode. Coupling optics may take the form of focusing elements such as cylindrical lenses, elliptical or parabolic mirrors and refractive optics acting as beam shapers and concentrators.

The need for intervening optics is determined by the shape and size of the laser mode and the optical density of the gain medium at the pump wavelength. For example, it is easy to visualise that a large diameter laser rod with a high optical density will absorb most of the pump radiation in the vicinity of the rod barrel, resulting in a hole in the gain on axis. This will clearly couple poorly into the TEM_{00} mode of a laser resonator. It is often the case that low or intermediate power oscillators will utilise some form of coupling optic in order to facilitate the efficient extraction of power in a high quality spatial mode, while amplifiers will be directly pumped. Invariably direct diode-laser pumping is also found in slab lasers. Slab lasers are not considered here in any depth, however, before considering rod lasers in some detail their more salient features are noted.

Side-Pumped Slab Lasers

Side-pumped slab lasers are typically pumped from a single side by densely packed linear bars forming a 2-D array. As depicted in Fig. 3.5, the diodes are located in close proximity to the slab face with no coupling optics employed. The opposite face of the slab is bonded to a conductive heatsink incorporating a reflective coating to return pump light not absorbed in the first pass through the slab a second time.

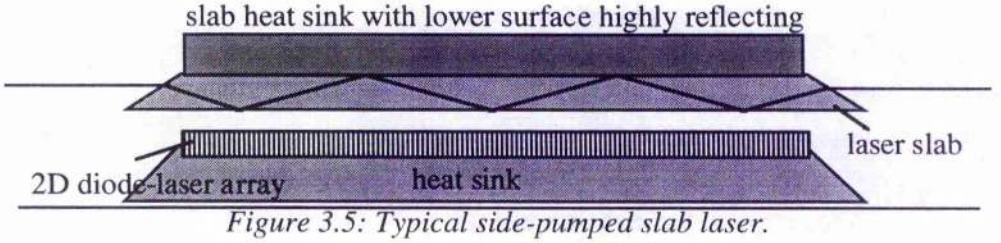

Figure 3.5: Typical side-pumped slab laser.

Such a pump geometry usually leads to a non-uniform gain profile, due to the exponential absorption of the pump light. Consequently a zig-zag resonator path is often employed, which geometrically averages the gain seen by the resonator mode

across its diameter. This type of slab geometry was first proposed by Martin [19], and is useful in that as well as providing a uniform gain cross-section, it also overcomes two thermal problems associated with rod lasers, namely; stress-induced birefringence and stress- or thermally-induced lensing. It is clear that as the pump light is preferentially concentrated toward the centre of a gain medium, for efficient coupling to the TEM_{00} resonator mode, then there will be a greater heat deposition in this area. This results in thermal lensing, due to the temperature dependence of the refractive index and stress induced changes in the refractive index, and also in thermal birefringence, as a radial and tangential refractive index variation is established in the laser rod. As the beam traverses the 1-dimensional thermal gradient set up in a slab laser geometry these effects can be nearly eliminated, there generally being some small effect present due to a thermal gradient orthogonal to the pumping and resonator mode directions due to imperfect insulation at the slab edges.

Thermal effects can often be adequately controlled in rod lasers and consequently slab laser design is most usually restricted to only the highest average power lasers. Average power limits of diode-laser pumped slab lasers have been addressed by several authors [20, 21]. Notably Basu et al. [22] have also developed means of extending the limitations of static slab geometries, by introducing moving slabs and discs. In such a device the pump density remains high, however, the moving gain medium allows heat to be dissipated over a larger area.

Side-Pumped Rod Lasers

Diode-laser side-pumping of solid-state gain media in general is made feasible by the relatively high absorption coefficient observed (typically > 5 cm^{-1}) for pump light within the pump spectral bandwidth of the gain media, so allowing a high level of pump light absorption in gain elements of only a few millimetres or less diameter. Such laser rod diameters are consistent with the aperture requirements for accommodating the lower order modes of typical laser resonators. To facilitate a good extraction efficiency however, it is also necessary to shape the pump light absorption profile to provide some optimum overlap with the resonator mode. While this is, and as will be demonstrated

later, relatively straightforward to achieve in low power end-pumped geometries, above certain power levels it becomes advantageous to adopt a side-pumped approach. Although pseudo-Gaussian pump profiles can be readily achieved in side-pumped geometries optimised for high average power operation, in which case several diode-arrays may be located symmetrically around the laser rod barrel, for moderate power devices which lie in the transition zone from end- to side-pumping, where for example only one high power diode-array may be used, it is more difficult to achieve the desired mode overlap.

A variety of side-pumping schemes have been demonstrated by several authors. Early work, for example by Hanson and Gerstenberger [23, 24], used simple close coupled geometries, as depicted in Fig. 3.6, where the barrel of the laser rod itself acted as a lens element to concentrate the highly divergent output of the diode-laser toward the centre of the rod. This work was successful in generating high optical conversion efficiencies in multi-transverse mode beams (~25-30%), however, due to the poor overlap between the pump cross-section and TEM_{00} mode only modest efficiencies could be achieved in generating near diffraction limited outputs (<5%).

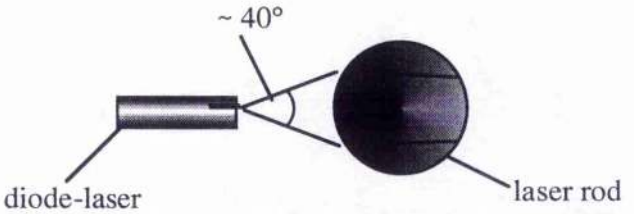

Figure 3.6: Close-coupled side-pumped laser rod geometry - Exponential absorption of the pump light results in a high deposition of pump power toward the entrance side of the laser rod and poor coupling to the TEM_{00} mode.

In later work the need to adapt coupling geometries to achieve high optical conversion efficiencies in low order modes was identified and schemes were employed to tailor pump light absorption profiles. Such schemes included the insertion of single or multiple lens elements between the diode-laser and laser rod [25, 26], as depicted in Fig. 3.7, resulting in an increase in optical conversion efficiencies to greater than 10%.

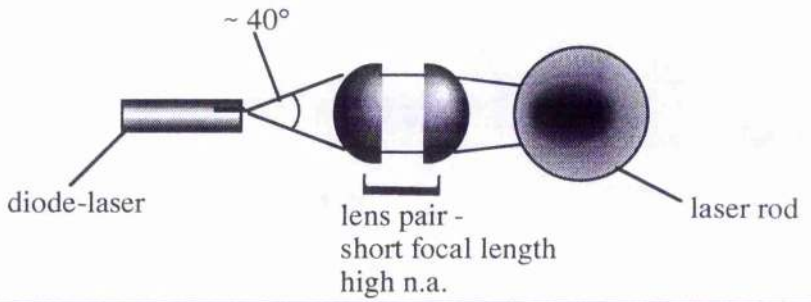

Figure 3.7: Lens-coupled side-pumped laser rod with the gain profile more circular and centred toward the rod axis.

Also, modifying the rod cross-section to form semi-circular or quadrant shaped apertures was conceived, with additionally reflective coatings being applied to the flat surfaces to return pump light not absorbed on a first pass through the gain medium for a second time [27, 28, 29], as depicted in Fig. 3.8. Again pseudo-Gaussian gain profiles could be generated and high optical conversion efficiencies achieved.

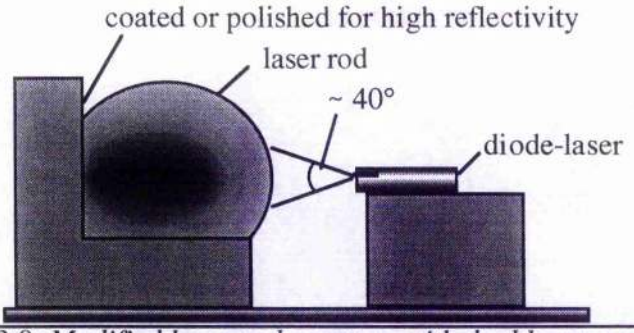

Figure 3.8: Modified laser rod aperture with double-pass reflector

3.3.2: Longitudinal Pumping Schemes

For the efficient generation of lowest-order transverse mode light, it has been previously noted that the most basic requirement is for a large proportion of the pump light to be absorbed along the axis of the laser resonator and within the mode volume of the resonator mode. This then requires that firstly, the pump light can be constrained to a radius less than that of the mode radius and secondly, that within this area the optical density of the gain medium at the pump wavelength be high enough to absorb a significant proportion of the pump light. Both of these requirements can be satisfied in properly designed focused end-pumped configurations.

One of the most simple means of achieving this was first demonstrated by Sipes [30]. A large numerical aperture lens is used to collect and collimate light from the

diode-laser, which emerges in a large cone angle, and then a second lens is used to focus the light to a small diameter spot in the gain medium. Such a scheme is depicted in Fig. 3.9.

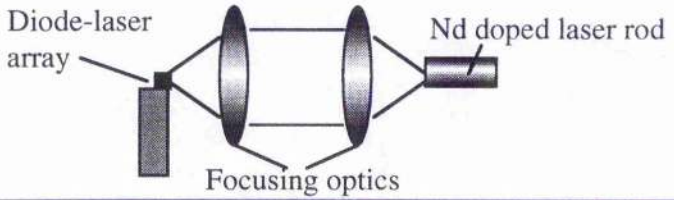

Figure 3.9: Schematic of a simple end-pumped laser system

In general, diode-lasers used as pump sources have associated with them a high degree of astigmatism in their output due to their rectangular emission apertures. Consequently, the focal spot generated in the simple coupling scheme outlined above will generally be elliptical in shape, detrimental to the spatial overlap with the normally circular resonator mode. In circumventing this deficiency options exist to reshape the resonator mode or introduce beam shaping optics into the coupling optic system. The latter of these options was for example employed by Berger [31] who used a x4 anamorphic prism pair to circularise the pumped volume in a Nd:YAG laser pumped by a diode-laser with a 100 μm by 1 μm emission cross-section (10° x 40° divergence), as depicted in Fig. 3.10.

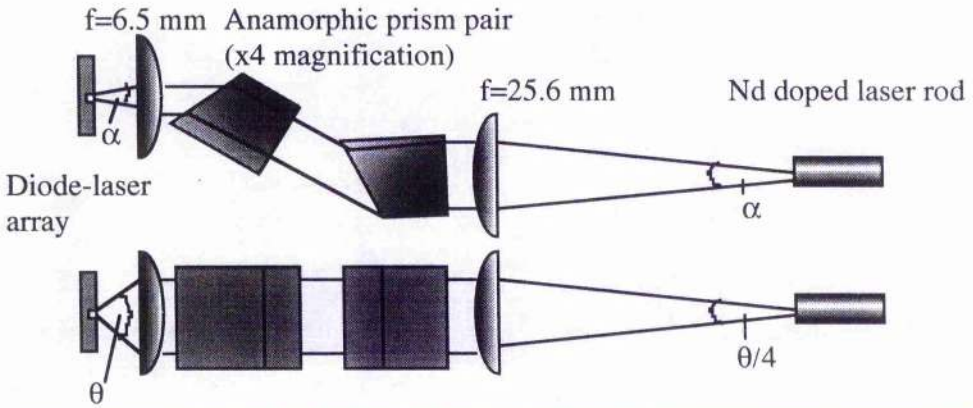

Figure 3.10: Schematic of anamorphic prism pair coupling [31].

While this type of beam shaping may be appropriate for diode-lasers with a single emitter, which may include several active stripes, other techniques have had to be developed for scaling end-pumped systems to higher powers and the use of diode-bars and diode-arrays.

In scaling to the use of single diode-bars, stringent focusing conditions are placed on the coupling optics if circular cross-section pumped volumes are to be obtained. Consequently, ensuring in some way that the TEM_{00} resonator mode fills a more easily controlled asymmetric pumped volume is often regarded as the preferred option in this case. One example of this was demonstrated by Baer [32] who proposed a quasi-longitudinal pumping scheme for a tightly folded laser resonator. As depicted in Fig. 3.11, this scheme relies on the resonator mode bouncing through the pumped volume of the gain medium, generated by a 1 cm wide, 10 W diode-laser bar which has been collimated in its high divergence plane. The technique is regarded as only a quasi-longitudinal scheme as not all the diode-laser light is launched along the resonator axis and in fact the scheme is somewhat similar to the transversely-pumped zig-zag slab laser where the angle of incidence of the resonator mode on the slab surface has been made more normal. The observed optical to optical slope efficiency in this case was 44%.

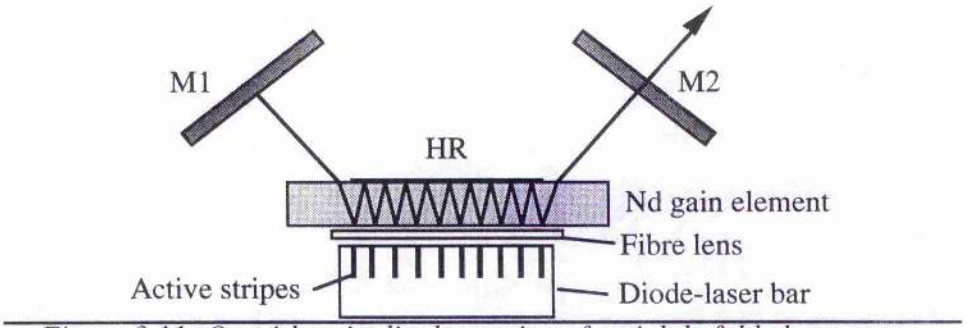

Figure 3.11: Quasi-longitudinal pumping of a tightly folded resonator. Each active area of the diode-laser bar is aligned to a resonator fold.

In a true end-pumped geometry Pfistner [33] utilised the astigmatism generated by an orthorhombic shaped slab of gain material located within the laser resonator, where the slab was designed to provide a resonator fold and the pump light was launched along the resonator path through the slab, to partially compensate for the ellipticity in the pumped volume cross-section, as shown in Fig. 3.12. Later Neuenschwander [34] stretched the slab to accommodate a second fold and increased the number of pump channels to eight. In both cases optical to optical slope efficiencies of greater than 40% were again observed.

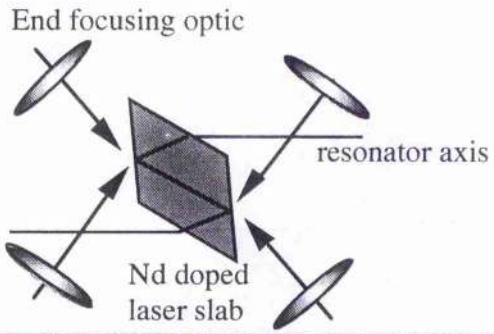

Figure 3.12: Multiple diode-laser longitudinal pumping of a folded resonator [33].

Improved spatial matching of the resonator mode and pump cross-section was demonstrated in an end-pumped geometry by Shannon [35] when an intra-cavity anamorphic prism pair was located in the laser resonator to expand the TEM_{00} resonator mode in the plane of the large pump cross-section dimension. Two SF-10 Brewster cut prisms in conjunction with a Brewster cut end to the gain medium were used to obtain a four times magnification in the desired plane and a good match to the pump cross-section, derived from a 1 cm wide 10 W diode-laser bar. Coupling between diode-laser and gain medium comprised a three element anamorphic lens system. This scheme, depicted in Fig. 3.13, allowed reliable TEM_{00} mode operation up to the maximum pump level available of 10 W with a slope efficiency of 44%. Inherent in the optical design of this type of resonator is, however, the generation of an astigmatic resonator mode and, consequently, laser output. Nonetheless the high coupling efficiency observed and reliable TEM_{00} mode of operation make this an attractive option and will be returned to later.

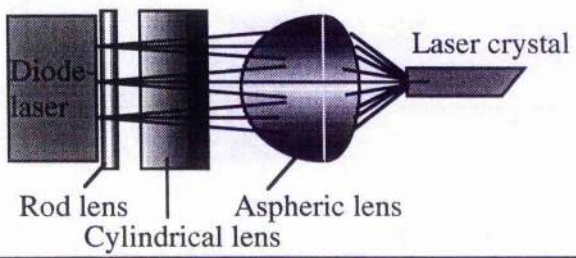

Figure 3.13: Anamorphic Coupling Lens System [35].

To scale end-pumped systems to higher powers and make use of multiple diode-laser bars, two options present themselves; firstly to use several discrete diode-bars or secondly to use diode-laser arrays incorporating several diode-bars in a single device

package. In using discrete bars, the normally polarised output from diode-lasers facilitates the polarisation coupling of a limited number of devices [36]. Alternatively, several fibre coupling schemes have been presented [37, 38], in which the light from many single stripe emitters or bars is coupled either directly into individual fibres by butting the fibre against the laser-diode or by using simple collimating and focusing optics. The use of large 2-D diode-laser arrays (typically > 5 bars) is limited, and most beneficial in the pumping of face pumped slab lasers.

3.4 Comparison of Neodymium Doped Laser Gain Media

Operation of common Nd lasers, such as Nd:YAG, Nd:YLF and Nd:glass, is well known, however, operation of Nd in other hosts such as LNP, GGG and BEL is less well documented. In particular, these less common hosts have historically been considered within the context of flashlamp pumping, for high peak power systems, and found generally to be less auspicious than their more common alternatives, however, many may have features well suited to diode-laser pumping. While then a particular wavelength requirement in this work makes the host choice restrictive (YLF or glass), it remains nonetheless of interest to compile some comparative study of other available hosts.

Facile performance estimates of the efficiency of the various Nd:host options considered can be made if sufficient spectroscopic data including absorption coefficient, effective stimulated emission cross-section and upper laser level lifetime are known. This data is shown in Table 3.3 for 11 hosts, while additional thermal and physical data pertaining to a number of these materials is given in Table 3.4. A qualitative description of these materials then follows and finally a comparison of relevant figures of merit made.

3.4.1: Spectroscopic and Physical Data

Host	λ (nm)	σ 10^{-19} cm^2	n (@ 1μm)	τ_u (μsec)	λ_{abs} (nm)	$\Delta\lambda_{abs}$ (nm)	α_p (cm^{-1})	β_{sc} (cm^{-1})
YAG [39]	1064.1	6.5	1.83	230	807.5	4.0	5.2	0.002
YLF [40]	1047 E||c 1053 E||a	3.7 2.6	1.45 1.47	480	792 E||c 797 E||a	3.5 3.0	11.5 5.0	0.007
Glass (LHG5)	1054	0.42	1.54	290	801.5	5.0	9.0	0.0005
LYAG [41]	1064	6.5	1.83	260	807.5	4.5	6.4	0.005
YALO [42,43]	1073 E||a 1064 E||b 1079 E||c	3.3	1.93	160	808	4.0	6.0	0.005
YVO_4 [44]	1064.3 E||c 1066 E||a	25 13	2.16 1.96	90	808.6	8.0	31.2	0.02
GSGG 2% Nd [45]	1061	1.3	1.94	250	805	4.5	12.0	0.01
LSB 10% Nd [46,47]	1062 E||x	1.3		118	808 E||a	3.0	36.0	
BZAG .2% Nd [48,49]	1055 E⊥c	1.03	1.74	280	806	4.0	2.6	
BEL [39]	1070 E||X 1079 E||Y 1079 E||Z	2.1 1.5 0.6	1.964 1.997 2.035	150	811	4.0 5.5 5.5	22.7	0.003
LNP [50,51, 52]	1048	3.2	1.61	120	800		40	.0004

λ - lasing wavelength, σ - stimulated emission cross-section, n - refractive index, τ_{up} - upper laser level lifetime, λ_{abs} - peak pump light absorption wavelength, $\Delta\lambda_{abs}$ - pump light absorption bandwidth (FWHM), α_p - absorption coefficient at λ_{abs}, β_{sc} - scatter loss coefficient at λ. Nominal 1% at. % Nd unless stated.

Table 3.3: Spectroscopic data for various Nd doped materials.

Host	dn/dt $x10^{-6}\ K^{-1}$	c $Jg^{-1}K^{-1}$	K $Wcm^{-1}K^{-1}$	α $x10^{-6}\ K^{-1}$	σ $(Kgcm^{-2})$	E $(Kgcm^{-2})$	γ (gcm^{-3})
YAG	7.3	0.59	0.13	7.5	2000	31	4.56
YLF	-4.3 E||c -2.0 E||a	0.79	0.06	13.0 a 8.0 c	330	7.5	3.95
Glass	8.6	0.71	0.012	8.6		6.9	2.68
YALO	8.1	0.42	0.11	9.5	3900	22	5.35
YVO_4	8.5 a 3.0 c		0.051 a 0.052 c	4.43 11.37			4.22
GSGG	10.1	0.448	0.07	7.5			6.46

dn/dt - refractive index temperature dependence, c - specific heat capacity, K - thermal conductivity, α - thermal expansion coefficient, σ - tensile strength, E - Youngs modulus, γ - density

Table 3.4: Thermo-mechanical data for various Nd doped materials.

3.4.2 : Review of Nd Doped Materials

Nd:YAG - Neodymium Yttrium Aluminium Garnet

Nd:YAG is by far the most commonly used solid-state laser material, combining spectroscopic properties attuned to efficient laser operation with physical properties that make it thermally and chemically stable, mechanically robust and relatively easy to grow, normally by the Czochralski technique, and fabricate.

The YAG crystal has a cubic structure similar to many garnets and is optically isotropic. First demonstrated as a laser crystal by Geusic [53] in 1964, the Nd laser transition linewidth around 1.064 μm is, as in most solid-state hosts, homogeneously broadened and, in the cubic lattice of YAG, relatively narrow (~9 cm^{-1}). Such conditions favour a high emission cross-section and consequential high gain and low threshold operation. The 1 μm laser transition in Nd represents a four level system as has been previously described, the lasing transition being $^4F_{3/2} \rightarrow {}^4I_{11/2}$, as shown in Fig. 3.14. Clearly, however, there exists considerable fine structure in the energy level structure, and indeed this is manifest in the observed fluorescence spectrum for Nd in YAG as shown in Fig. 3.15.

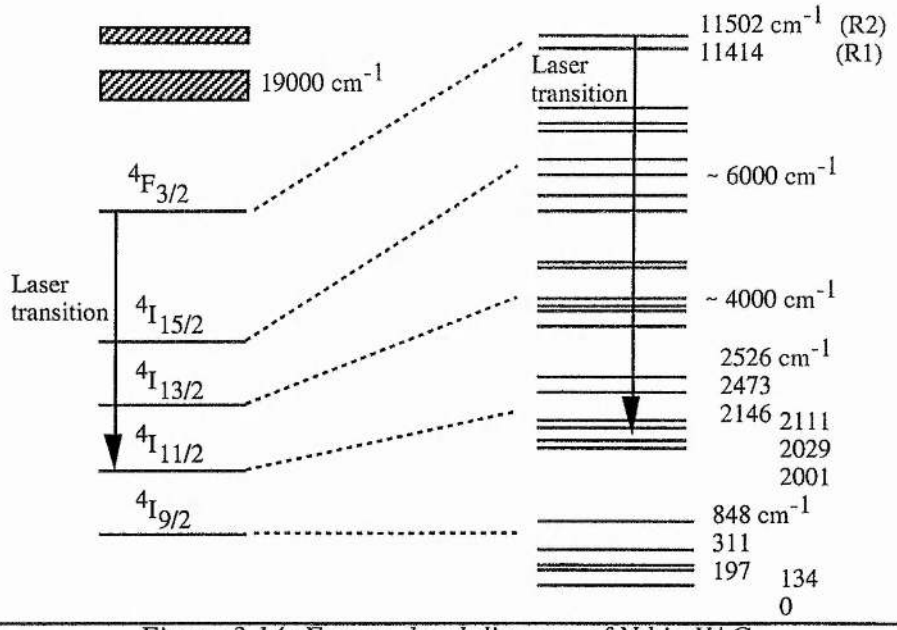

Figure 3.14: Energy level diagram of Nd in YAG.

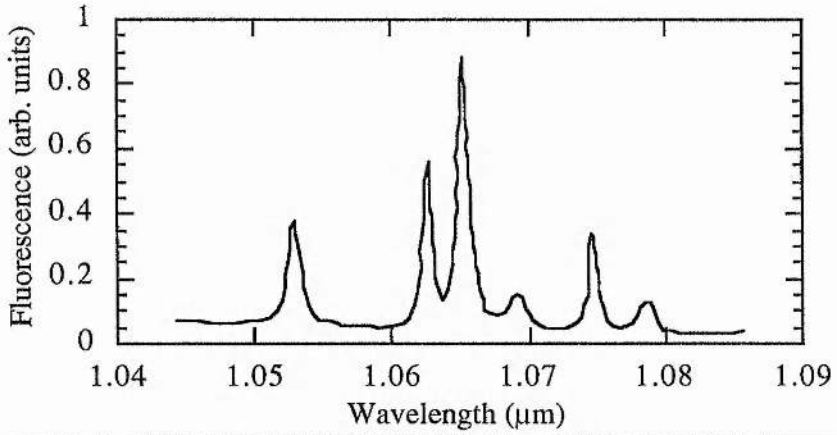

Figure 3.15: Fluorescence spectrum of Nd in YAG at 300°K around 1.06 μm.

Lasing takes place from either the R_1 or R_2 sublevels of the $^4F_{3/2}$ manifold, depending on which particular transition is considered. For the strongest 1.0641 μm transition, lasing is from the R_2 sublevel which according to Boltzmann statistics contains some 40% of the manifold population. The R_2 component is, however, rapidly repopulated from the R_1 sublevel through nonradiative thermal transitions. Additionally, radiative transitions can be made between the $^4F_{3/2}$ and $^4I_{13/2}$, $^4I_{9/2}$ and $^4I_{15/2}$ manifolds, providing spectral emissions at around 7500 cm^{-1} (1.3 μm), 10600 cm^{-1} (0.95 μm) and 5500 cm^{-1} (1.8 μm) respectively. The branching ratios of these various transitions have been ascertained [54] and found to be 0.14, 0.25 and < 0.01 respectively. The branching ratio for the $^4I_{11/2}$ transition is 0.6. Consequently, the

fluorescence efficiency of the combined transitions is greater than 99%, and without additional spectral selectivity the 1.06 μm transition will dominate.

Pumping of Nd:YAG is through broad and relatively strong absorption features at 0.75 μm and 0.8 μm, as shown in Fig. 3.16. The 0.8 μm feature is particularly well suited to diode-laser pumping, where it provides an excellent spectral match to high power GaAlAs diode-lasers. The weak absorption feature evident at around 0.88 μm ($^4I_{9/2} \rightarrow {}^4F_{5/2}$) was that exploited by Newman [1] when he was the first to demonstrate lasing in Nd doped tungstate pumped by GaAs diodes (LED's). The first diode-laser pumped Nd:YAG laser was also pumped through this $^4F_{5/2}$ manifold by Ross [55]. The laser was pumped by a single GaAs diode-laser in a transverse geometry, where the laser crystal was at room temperature, however, the diode-laser was cooled to 170 °K, to shift its wavelength to 0.867 μm. Nd:YAG is now almost exclusively pumped at 0.81 μm

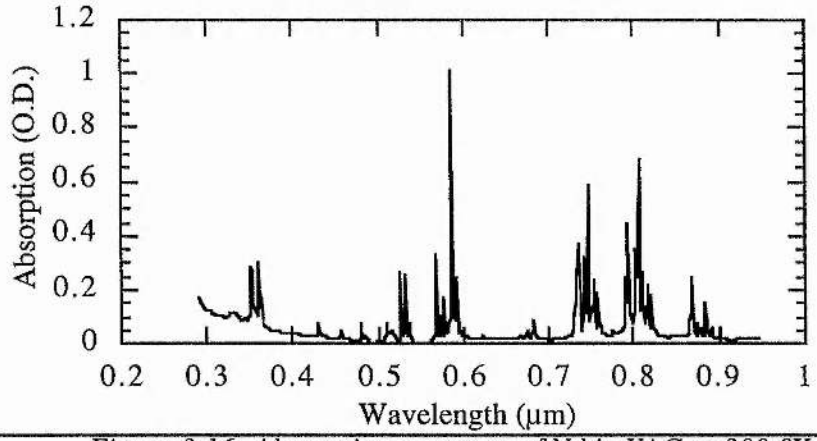

Figure 3.16: Absorption spectrum of Nd in YAG at 300 °K.

Nd:YLF - Neodymium Yttrium Lithium Fluoride

Nd:YLF is a crystal of the scheelite structure fluoride class, grown by a modified Czochralski method. The YLF lattice is isomorphous with tungstate ($CaWO_4$), introduced earlier as the first trivalent rare earth doped compound to be successfully pumped by semiconductor diodes. In the case of $CaWO_4$, the substitution of the Ca^{2+} ion with Nd^{3+} ion requires some form of charge compensation, resulting in a distorted ionic field around the Nd lattice site and consequently a shortened radiative lifetime, broader emission linewidth and additional lines in the fluorescence spectrum - all

effects detrimental to laser performance. These effects should, however, be absent in the Nd doped YLF lattice.

YLF is an negative uniaxial anisotropic host, resulting in strong polarised fluorescence peaks at 1.0471 μm (E||c, π-polarised) and 1.0530 μm (E⊥c, σ-polarised) for the $^4F_{3/2} \rightarrow {}^4I_{11/2}$ transition, as shown in Fig. 3.17 [40]. As with Nd:YAG, there are a plethora of transitions between the $^4F_{3/2}$ and $^4I_{11/2}$ manifolds, the transitions as noted above originating from the R1 and R2 sublevels of the $^4F_{3/2}$ manifold respectively and terminating on the level at 2042 cm^{-1}. Although the stronger of the two lines, with an emission cross-section ratio of between 1.5 and 2:1 [56, 57], the 1047 nm line can be suppressed, to allow lasing at 1053 nm, by restricting the lasing polarisation to be perpendicular to the crystallographic c-axis. As Nd:YLF is a uniaxial material and the crystallographic a and b axes are identical, then this can be achieved in an a-axis gain element by the introduction of polarisation selective elements, but also in a c-axis gain element without the need for any additional selectivity. Operation at 1.053 μm is of interest for use in conjunction with Nd doped phosphate glass amplifiers, to which it is well matched spectrally. Although the 1.052 μm line of Nd:YAG may be considered for this application, Nd:YLF offers certain advantages. Firstly, the $\sigma\tau_f$ product (where σ is the emission cross-section and τ_f the fluorescence lifetime) of the 1.053 μm Nd:YLF line is some three times higher than that of the 1.052 μm Nd:YAG line, and secondly precise frequency selectivity is required in the case of Nd:YAG to suppress the higher gain 1.064 μm lines.

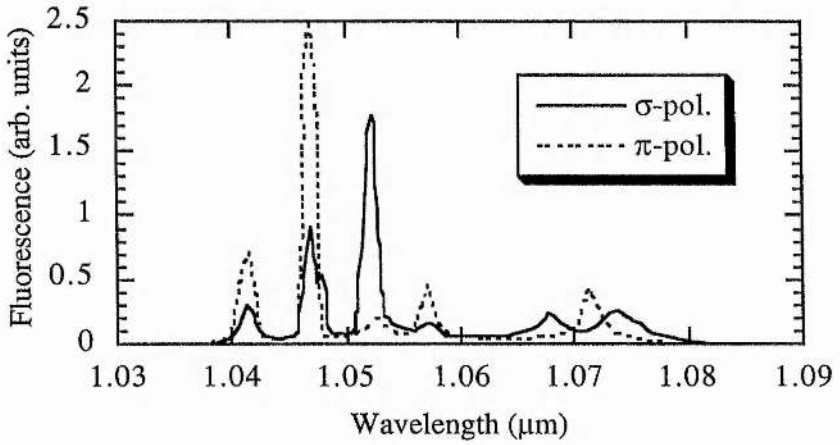

Figure 3.17: Fluorescence spectra of Nd in YLF at 300°K

Nd:YLF is well suited to moderate power oscillators and amplifiers. The maximum energy storage achievable in Q-switched oscillators and amplifiers is constrained by the onset of parasitic oscillations, a limit inversely proportional to the emission cross-section. The cross-section of Nd in YLF being a factor of 2 lower than in YAG therefore permits higher stored energy densities. The long upper laser level lifetime of Nd:YLF is also of some advantage when operating in a Q-switched mode, increasing the stored energy by around a factor of 2, when compared to Nd:YAG, for moderate frequency (<3 kHz) CW pumped devices. Also, the full potential of quasi-CW diode-lasers may be exploited, these diode types typically having pulse duration's of around 400 μsec.

Diode-laser pumping of Nd:YLF is further advantaged by the materials strong absorption peaks, shown in Fig. 3.18, which are broader than those of Nd in YAG.

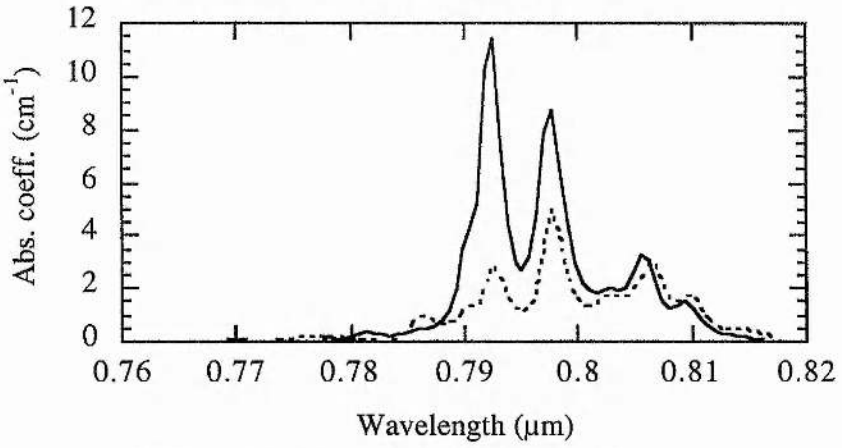

Figure 3.18: Absorption spectra of Nd in YLF at 300 °K (solid line - π polarised, dashed line - σ polarised).

Thermally YLF is similar to YAG as a host, having good thermal conduction properties and thus allowing efficient heat extraction and operation at high average powers [58, 59]. Unlike isotropic hosts such as YAG, the strong natural birefringence of YLF overwhelms any thermally induced birefringence, advantageously reducing thermal depolarisation to negligible amounts. The thermal lensing power of YLF is also weaker than in YAG due to the stress induced and material deformation contributions to the thermal lens power being compensated for by the materials negative refractive index variation with temperature.

Nd:Glass - Neodymium Phosphate/Silicate Glass

As an amorphous host, glass is characteristically isotropic and capable of being doped with large Nd ion concentrations without compromising quality in large substrate sizes. Restricted commercially to silicate (SiO_2based) and phosphate (P_2O_5 based) types, glass hosts are, however, distinctly different from crystalline materials in both their spectroscopic and physical parameters.

While spectral emission and absorption lines of the Nd ion doped into glass lie in the same areas as for crystalline hosts, as shown by a comparison of Fig's. 3.19 and 3.14, the features are generally broader. For diode-laser pumping the broad absorption lines, as shown in Fig. 3.20, offer advantages over crystalline counterparts, making diode-laser selection and wavelength control much less critical. A broader emission bandwidth has associated with it a lower gain ($\sigma \sim 4 \times 10^{-20}$ cm^2), resulting in a comparatively high lasing threshold. Nevertheless, the increased width can be advantageous in, for example, producing shorter mode-locked pulses, providing a higher saturation intensity and allowing the storage of larger amounts of energy before the onset of parasitic oscillations. It is evident then that Nd:glass is particularly well suited to high energy pulsed applications, as in large amplifier chains, however, a high saturation intensity may also be exploited in for example CW intra-cavity doubling arrangements where a high circulating intensity may be fully exploited.

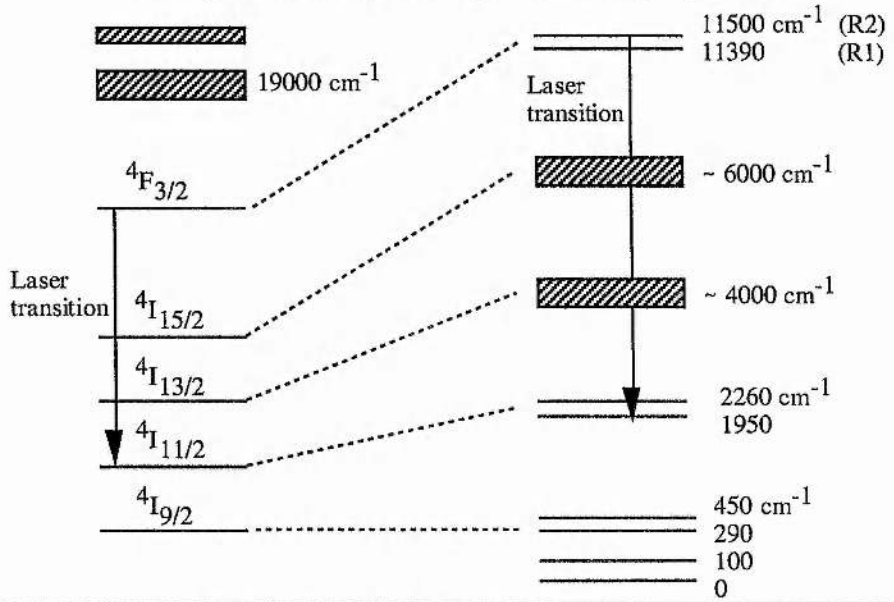

Figure 3.19: Partial energy level diagram of LHG-5 Nd:Phosphate Glass [60].

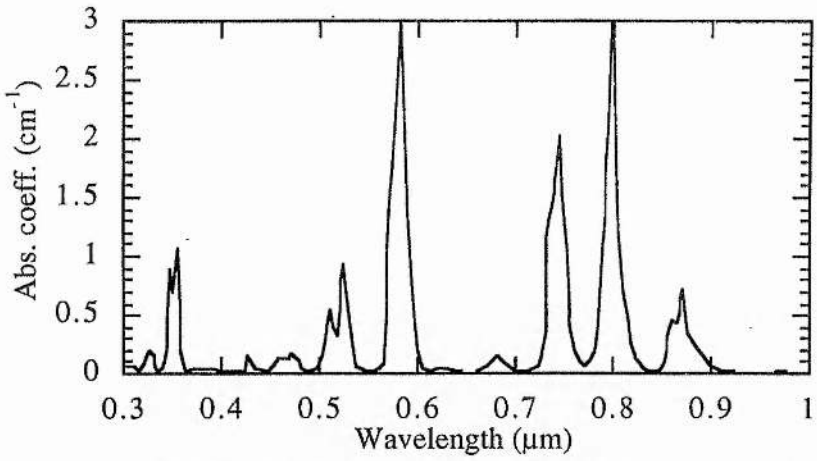

Figure 3.20: Absorption spectrum of Q-88 Nd:Phosphate Glass [61].

Physically, glass is generally regarded as being poorer than crystalline hosts, particularly with regard to its thermal properties. A low thermal conductivity results in excessive heating of the substrate at high average powers, resulting in astigmatic lensing, wedging and thermally induced birefringence effects which must be properly controlled.

Diode-laser pumping of Nd:glass was first reported by Kozlovsky [62] in 1986 when a Nd:glass laser was successfully pumped by a diode-laser array. Subsequently, more efficient performance was demonstrated by the same author [63] in which work the insensitivity to diode wavelength was also clearly demonstrated, by temperature tuning the diode wavelength over a range 803 nm to 809 nm with little affect being observed on the Nd:glass laser output. More recently, Nd:glass has been exploited in CW diode-laser pumped and mode-locked oscillators [64] where the large gain bandwidth results in the production of pulses of tens of picosecond duration; and also fabricated into nonplanar ring elements [65] for use in single frequency sources as seeders for 1.053 μm Nd:YLF and other Nd:glass oscillator/amplifier combinations.

Lu:Nd:YAG - Neodymium Lutetium Yttrium Aluminium Garnet

LYAG has been studied by a number of groups [41,66-69] with a view to developing high optical quality crystals, with high concentrations of Nd. Kestigian [66] was the first to demonstrate the use of Lu as a co-dopant with Nd to act as a size

compensator, the ionic radius of the Nd^{3+} ion being significantly larger than the Y^{3+} ion it replaces, therefore limiting the dopant level of Nd in YAG to around 1.5% in laser quality crystals. The introduction of Lu, being smaller than the Y ion, resulted in an increase in the possible level of Nd dopant to more than 3% while maintaining an excellent crystal quality.

While increasing the dopant density, and therefore the materials absorption coefficient, it was also observed that the fluorescence lifetime of Lu:Nd:YAG was some 10% longer than that of Nd:YAG. This would indicate an improved storage and consequential lasing efficiency to be achievable when operated in a Q-switched mode, as has been demonstrated for a flashlamp pumped system by Bass [67]. Improved lasing efficiency has also been reported in a diode-laser pumped scheme by Allik [41], however, in this case the relative improvement over Nd:YAG was attributed to a lower material scatter loss. Co-doping of Nd:YAG with Lu has been seen to have little effect on the spectral properties of the material at room-temperatures, and are generally as indicated in Fig's. 3.15 and 3.16 for emission and absorption in Nd:YAG. The emission linewidth of Nd in Lu:YAG is reported as being increased from 8.8 cm^{-1} to 9.6 cm^{-1} at 1.064 μm [69]. Studies in the same work at low temperatures (2°K) indicate, however, a degree of inhomogeneous line-broadening to take place, due to clustering effects of Nd and Lu: Nd sites within the YAG host. Advantageously, it has also been reported that the UV absorption of Lu:Nd:YAG is somewhat lower than in an equivalent Nd:YAG crystal [68]. Such an effect will, under conditions of flashlamp pumping, see a reduced thermal loading of the laser crystal and consequently reduced thermal birefringence and thermal lensing effects.

Nd:YVO_4 - Neodymium Yttrium Orthovanadate

Neodymium yttrium orthovanadate is a uniaxial material with various laser transitions lying close to 1.06 μm, as shown in Fig. 3.21 [70]. The material is well suited to CW or low threshold, high gain pulsed applications, as seen from a high figure of merit based on the $\sigma\tau$ product. It has an effective emission cross-section some 3

times larger than that of Nd:YAG [71], so that even in the presence of a short upper state lifetime, Nd:YVO_4 continues to exhibit a large gain coefficient.

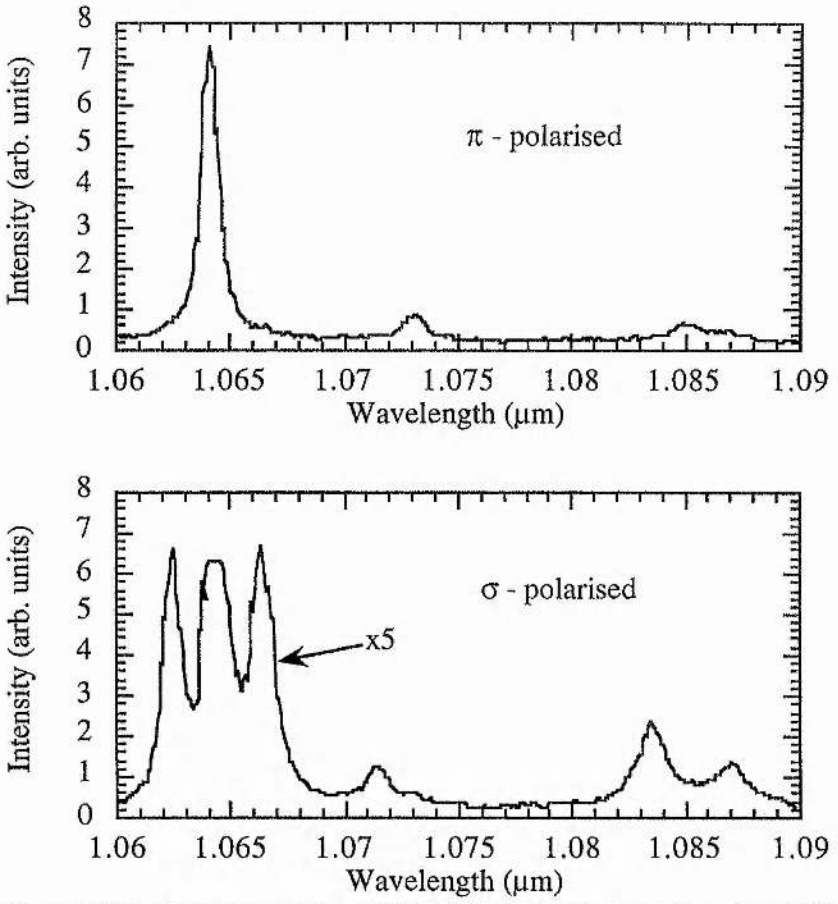

Figure 3.21: Fluorescence of Nd in YVO_4 (upper trace - π polarised, lower trace - σ polarised).

The pumping requirements of Nd:YVO_4 are similar to those of Nd:YAG, the absorption peak lying at 808.6 nm. However, the larger absorption bandwidth and coefficient, shown in Fig. 3.22, offer significant advantages in terms of a relaxation in diode-laser temperature stability and in facilitating the use of short gain length elements. This latter feature has been extremely significant in the development of moderate power mini- and microchip lasers [72, 73], where in particular short gain and cavity lengths can be usefully exploited in the development of single axial mode, narrow linewidth and compact lasers. The relaxation in diode-laser temperature stability was demonstrated well by Fields [74], where a direct comparison was made between Nd:YAG and Nd:YVO_4 of the effects of varying the diode temperature, as illustrated in Fig. 3.23.

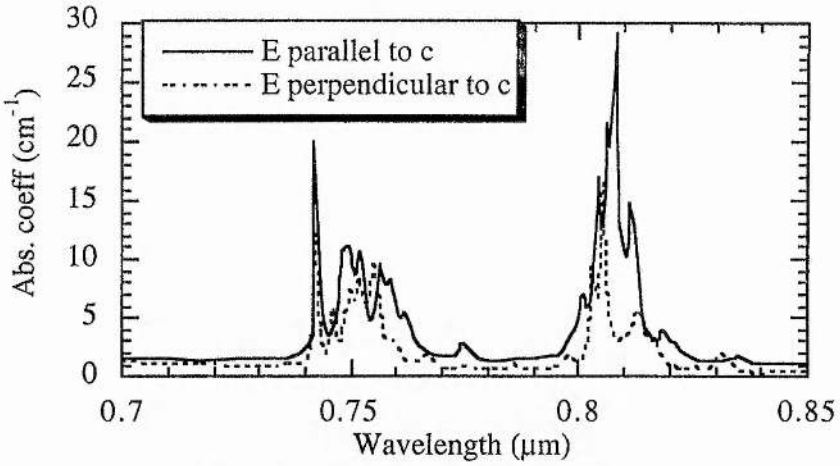

Figure 3.22: Absorption spectra of Nd in YVO_4

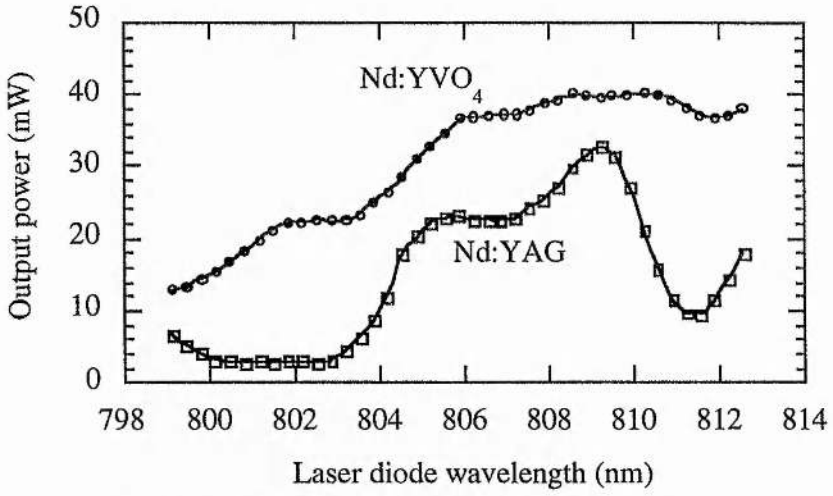

Figure 3.23: Comparison of Nd:YAG and Nd:YVO laser outputs as a function of diode-laser temperature (wavelength) [74].

The similarity in the pump requirements of Nd:YVO_4, when compared to Nd:YAG, offer further benefits in Nd:YVO_4 becoming a direct replacement for Nd:YAG in existing diode-laser pumped systems, this commonality being extended further to all other optics - linear or nonlinear, due to the similarity in emission wavelength.

Nd:$YAlO_3$ (YAP) - Neodymium Yttrium Orthoalluminate

Nd:$YAlO_3$ is an anisotropic crystal of the orthorhombic class and one of the few solid-state laser materials to rival the good thermal and physical properties of Nd:YAG.

First discovered by Weber [75] in 1969, excellent lasing properties [76] were observed a short time afterwards under conditions of flashlamp pumping.

YAlO is derived from the same Y_2O_3-Al_2O_3 system as YAG, YAlO being the 1:1 perovskite phase and YAG the 3:5 garnet phase. Rare earth ion doping is as with YAG through lattice substitution at the Y^{3+} site, and thus without charge compensation. It is however, noted that larger doping densities are achievable (up to 6%) [75] without deleterious effects on the crystal quality. Fluorescence is observed predominantly in four strong lines, as shown in Fig. 3.24, peaking at 1.0645 μm, 1.0729 μm and 1.0795. As with other anisotropic hosts the relative strengths of these lines are dependent on the field polarisation, in this case the 1.0795 μm line having the maximum gain for light polarised along the crystallographic c-axis, although the 1.0645 μm line is favoured for light polarised along the a- and b-axes [77]. In comparison to Nd in YAG, these lines are relatively broad, being around a factor of 3 greater, providing an opportunity for some degree of extended tunability, typically 3 nm in each wavelength band.

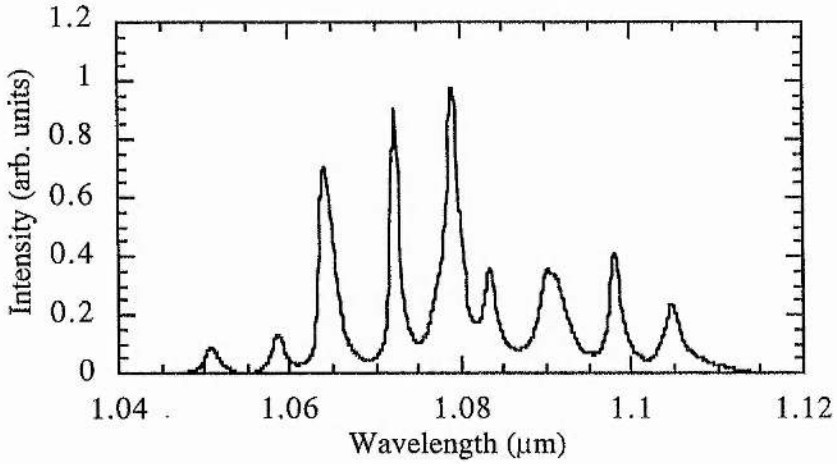

Figure 3.24: Fluorescence spectrum of Nd in YAlO for light polarised along the c-axis [42].

A broad absorption band well suited to diode-laser pumping is also found in Nd:$YAlO_3$, as shown in Fig. 3.25. The spectra for Nd in $YAlO_3$ are similar to those observed for Nd doped into other crystals, although the Stark splitting, relative line intensities and polarisation dependencies are, of course, specific to the material. Figure 3.25 shows the overall absorption spectrum for randomly polarised light. For diode-laser pumping the absorption coefficient is maximum at 813 nm when the pump light polarisation is parallel to the crystallographic a-axis.

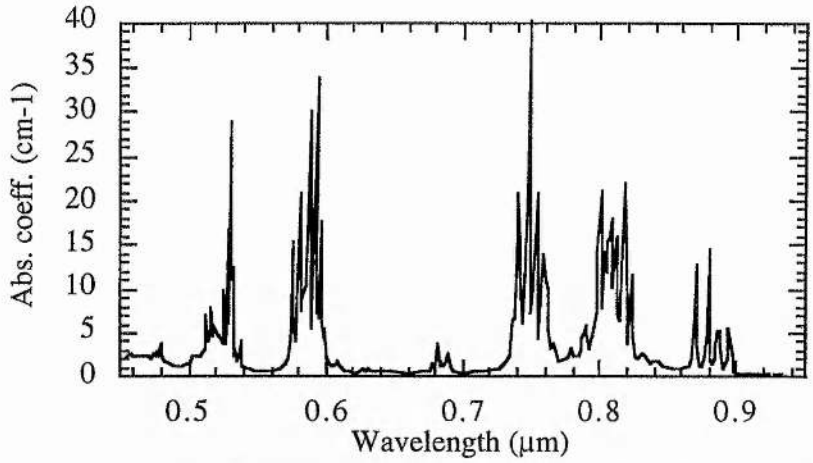

Figure 3.25: Absorption spectrum of Nd in $YAlO_3$ at 300 °K [42].

Despite the advantages of an anisotropic host in terms of a polarised output and negligible thermally induced birefringence and the good material characteristics of Nd:$YAlO_3$, it has never established itself as a popular laser material. This may be due in part to the quality of the material being initially poor, containing Fe^{3+} and OH^- impurities, and consequently having a high scatter loss. Additionally, however, strong fluorescence lifetime quenching is also observable for Nd doping densities exceeding 1 % at.wt.[75], as shown in Fig 3.26, reducing significantly the materials $\sigma\tau$ figure of merit.

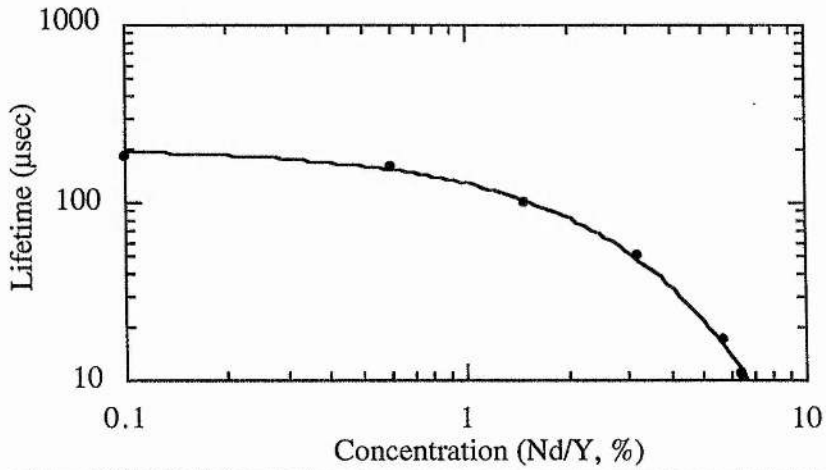

Fig. 3.26: Fluorescence lifetime quenching in Nd:$YAlO_3$.

Other Nd Doped Laser Crystals

The variety of crystals and glasses into which Nd has been doped is, to say the least, extensive and all have attributes which may be desirable for certain applications. In the preceding sections the most salient features of the more commonly used materials have been outlined, and may provide a useful guide toward the choice of material for a given application. This section is concluded by making mention of some other materials which show promise for the future or are important materials in the realm of diode-laser pumping but fall outwith the scope of this work.

$Nd:LaSc_3(BO_3)_4$ or Nd:LSB (Neodymium Lanthanum Scandium Borate) - This is a relatively new material which may prove to be an interesting contender to $Nd:YVO_4$ for applications in low and moderate power mini-lasers. The material can accept high Nd doping concentrations [46], providing a pump light absorption coefficient similar to $Nd:YVO_4$, but with a longer fluorescence lifetime (120 μsec).

$LiNd(PO_3)_4$ or LNP (Lithium Neodymium Tetraphosphate) - LNP is one of the stoichiometric neodymium class of laser crystals which have, as a result of the very high Nd concentrations, a large absorption coefficient (~40 cm^{-1} [51]) at 800 nm. This makes such materials attractive for compact and efficient miniature diode-laser pumped lasers, and particularly in end-pumped configurations where short absorption depths can lead to a well confined pumped volume for matching to low order resonator modes. Spectroscopically LNP offers wavelengths at around 1.05 μm and 1.32 μm. The στ product for the material is relatively good ($\sigma = 3.2 \times 10^{-19}$ cm^2, $\tau = 120$ μsec) and indeed has the lowest saturation parameter of all the known stoichiometric Nd crystals at 4.9 $kW.cm^{-2}$ [50].

$Nd^{3+}:Ba_2ZnGe_2O_7$ or Nd:BZAG (Neodymium) - Nd:BZAG has been seen to be a medium gain laser material with a stimulated emission cross-section, fluorescence linewidth and thermo-mechanical properties intermediate between those of Nd:YAG and Nd:Glasses [48, 49]. The material, however, possesses a longer upper-state

lifetime (330 μsec) than Nd:YAG and broader absorption features than Nd doped YAG, $YAlO_3$ and $YLiF_4$, making it an attractive host for diode-laser pumping and Q-switched applications. Performance to date has been limited by high material scattering losses [48], however, with improved crystal quality efficiency will be increased and contend with the observed performance of Nd:YAG.

3.4.3 : Figures of Merit for Nd Doped Materials

Some indication of the relative performance of the materials so far discussed can be obtained from consideration of a number of relevant figures of merit. In particular, a comparison is made here of 2 such figures; (i) the emission cross-section, upper-state lifetime product ($\sigma\tau$) and (ii) the saturated energy density ($h\upsilon/\sigma\tau$), as noted in Table 3.5.

Material	$\sigma\tau$ (x10^{-23} $cm^2.s$)	I_{sat} ($J.cm^{-2}.s^{-1}$)
Nd:YAG	14.9	1250
Nd:Glass	1.22	15493
Nd:YLF	17.8	1070
Nd:YVO_4	22.5	830
Nd:YAlO	5.28	3540
Nd:LSB	1.53	12209
Nd:BEL	3.15	5901
LNP	3.84	4942

Table 3.5: Comparison of figures of merit for various Nd doped host materials.

The relevance of the first of these figures can be seen by considering the equations describing the threshold inversion, equ. (2.33), and the small signal gain, equ. (2.37), of a laser. It is apparent in considering these equations that the laser gain is not solely dependent upon the emission cross-section, but in fact on its product with the upper-state lifetime of the material. As described in Chapter 2, when the photon density within a resonator becomes appreciable the small signal gain is reduced according to equ. (2.38). The saturated energy density is then the field density at which the small signal gain drops to one half its unsaturated level.

Chapter 3 References:

1. R. Newman *"Excitation of the Nd^{3+} fluorescence in $CaWO_4$ by recombination radiation in GaAs"* J. Appl. Phys. 34 (2) p.437, 1963.

2. R. J. Keyes and T. M. Quist *"Injection luminescent pumping of CaF_2:U^{3+} with GaAs diode lasers"* Appl. Phys. Lett. 4 (3) pp.50-52, 1964.

3. R. N. Hall, G. E. Fenner, J. D. Kingsley, T. J. Soltys and R. O. Carlson *"Coherent light emission from GaAs junctions"* Phys. Rev. Lett. 9 (9) pp.366-368, 1962.

4. M. I. Nathan, W. P. Dumke, G. Burns, F. H. Dill, Fr., and G. J. Lasher *"Stimulated emission of radiation from GaAs p-n junctions"* Appl. Phys. Lett. 1 (9) pp.62-64, 1962.

5. T. M. Quist, R. H. Rediker, R. J. Keyes, W. E. Krag, B. Lax, A. L. McWhorter and H. J. Zeiger *"Semiconductor maser of GaAs"* Appl. Phys. Lett. 1 (4) pp.91-92, 1962.

6. R. Scheps *"Cr:LiSAF$_6$ laser pumped by visible laser diodes"* IEEE J. Quant. Elect. QE-27 (8) pp.1968-1970, 1991.

7. R. Scheps, J. F. Meyers, H. Serreze, A. Rosenberg, R. C. Morris and M. Long *"Diode pumped Cr:LiSAF$_6$ laser"* Opt. Lett. 16 (11) pp.820-822, 1991.

8. J. Wilson and J. F. B. Hawkes *"Optoelectronics: An Introduction"* (Prentice Hall International Inc., London), 1983.

9. Spectra Diode Laboratories *"Product Catalogue"* (Spectra-Diode Laboratories, California, USA), 1995.

10. B. D. Sinclair, C. J. Norrie, N. Gallaher, J. Hong, W. Sibbett and M. H. Dunn *"Diode laser pumped solid state lasers"* (RARDE Progress Report, Univ. of St Andrews), June 1988.

11. M. Ettenberg and H. Kressel *"The reliability of (AlGa)As CW laser diodes"* IEEE J. Quant. Elect. 16 (2) pp.186-196, 1980.

12. I. Ladany and H. Kressel *"Influence of device fabrication parameters on gradual degradation of (AlGa)As cw diode lasers"* Appl. Phys. Lett. 25 (12) pp.708-710, 1974.

13. A. Thomson *"The reliability of practical $Ga_{1-x}Al_xAs$ laser devices"* IEEE J. Quant. Elect. 15 (1) pp.11-13, 1979.

14. H. Kressel, I. Ladany, M. Ettenberg and M. F. Lockwood *"Reliable semiconductor light sources for fiber optical communications"* Tech. Dig. Int. Elect. Devices Meeting pp.477-479, 1975.

15. S. Ritchie, R. F. Godfrey, B. Wakefield and D. H. Newman *"The temperature dependence of degradation mechanisms in long lived (AlGa)As DH lasers"* J. Appl. Phys. 49 (6) pp.3127-3132, 1978.

16. P. Petroff and R. L. Hartman *"Rapid degradation phenomenon in heterojunction GaAlAs-GaAs lasers"* J. Appl. Phys. 45 (9) pp.3899-3903, 1994.

17. D. V. Lang and L. C. Kimmerling *"Observation of recombination-enhanced defect reactions in semiconductors"* Phys. Rev. Lett. 33 (8) pp.489-492, 1974.

18. F. R. Nash, R. L. Hartman, N. M. Denkin and R. W. Dixon *"GaAs laser reliability and protective facet coatings"* J. Appl. Phys. 50 (5) pp.3123-3132, 1979.

19. W. S. Martin and J. P. Chernoch *"Multiple internal reflection face pumped laser"* US Patent 3,633,126, January 1994.

20. M. K. Reed, W. J. Kozlovsky, R. L. Byer, G. L. Harnagel and P. S. Cross *"Diode-laser-array-pumped neodymium slab oscillators"* Opt. Lett. 13 (3) pp.204-206, 1988.

21. S. Basu and R. L. Byer *"Average power limits of diode-laser-pumped solid state lasers"* Appl. Opt. 29 (12) pp.1756-1771, 1990.

22. S. Basu and R. L. Byer *"40-W average power, 30-Hz moving-slab Nd:Glass laser"* Opt. Lett 11 (10) pp.617-619, 1986.

23. F. Hanson and D. Haddock *"Laser diode side pumping of neodymium laser rods"* Appl. Opt 27 (1) pp.80-83, 1988.

24. D. C. Gerstenberger, A. Drobshoff and R. W. WAllace *"High-peak-power operation of a diode-pumped Q-switched Nd:YAG laser"* Opt. Lett. 15 (2) pp.124-126, 1990.

25. R. Burnham and A. D. Hays *"High-power diode-array-pumped frequency-doubled CW Nd:YAG laser"* Opt. Lett. 14 (1) pp.27-29, 1989.

26. M. D. Selker, R. S. Afzal and P. Reichert *"A pulse transmission mode Q-switched Nd:YLF laser pumped by cylindrical microlens-collimated diode bars"* IEEE J. Quant. Elect. 30 (7) pp.1616-1622, 1994.

27. R. Cunningham *"Diode array pumps Nd:YAG from side"* Lasers & Optronics p.17, May 1989.

28. D. Welford, D. M. Rines and B. J. Dinerman *"Efficient TEMoo-mode operation of a laser-diode side-pumped Nd:YAG laser"* Opt. Lett. 16 (23) pp.1850-1852, 1991.

29. H. Ajer, S. Landrø, G. Rustad and K. Stenersen *"Efficient diode-laser side-pumped TEMoo-mode Nd:YAG laser"* Opt. Lett. 17 (24) pp1785-1787, 1992.

30. D. L. Sipes *"Highly efficient neodymium:yttrium aluminium garnet laser end pumped by a semiconductor laser array"* Appl. Phys. Lett. 47 (2) pp.74-76, 1985.

31. J. Berger, D. F. Welch, D. R. Scifres, W. Streifer and P. S. Cross *"High power, high efficient neodymium:yttrium aluminium garnet laser end pumped by a laser diode array"* Appl. Phys. Lett 51 (16) pp.1212-1214, 1987..

32. T. M. Baer, D. F. Head, P. Gooding, G. J. Kintz and S. Hutchison *"Performance of diode-pumped Nd:YAG and Nd:YLF lasers in a tightly folded resonator geometry"* IEEE J. Quant. Elect 28 (4) pp.1131-1138, 1992.

33. C. Pfistner, P. Albers and H. P. Weber *"Efficient Nd:YAG slab longitudinally pumped by diode lasers"* IEEE J. Quant Elect. 26 (5) pp.827-829, 1990.

34. B. Neuenschwander, P. Albers and H. P. Weber *"Efficient multiple-longitudinally diode laser pumped Nd:YAG slab laser"* Opt. and Quant. Elect. 24 pp.363-370, 1991.

35. D. C. Shannon and R. W. Wallace *"High-power Nd:YAG laser end pumped by a cw, 10 mm x 1 mm aperture, 10-W laser-diode bar"* Opt. Lett 16 (5) pp.318-320, 1991.

36. G. P. A. Malcolm, M. A. Persaud and A. I. Ferguson *"Resonant frequency quadrupling of a mode-locked diode-pumped Nd:YLF laser"* Opt. Lett. 16 (13) pp.983-985, 1991.

37. J. Berger, D. F. Welch, W. Streifer, D. R. Scifres, N. J. Hoffman, J. J. Smith and D. Radecki *"Fiber-bundle coupled, diode end-pumped Nd:YAG laser"* Opt. Lett. 13 (4) pp.306-308, 1988.

38. D. Golla, M. Rode, S. Knoke, W. Schone and A. Tunnermann *"62-W cw TEM_{00} Nd:YAG laser side pumped by fibre-coupled diode lasers"* Opt. Lett. 21 (3) pp.210-212, 1996.

39. H. P. Jenssen, R. F. Begley, R. Webb and R. C. Morris *"Spectroscopic properties and laser performance of Nd^{3+} in lanthanum beryllate"* J. Appl. Phys. 47 (4) pp.1496-1500, 1976.

40. A. L. Harmer, A. Linz and D. R. Gabbe *"Fluorescence of Nd^{3+} in lithium yttrium fluoride"* J. Phys. Chem. Solids 30 pp.1483-1491, 1969.

41. T. H. Allik, W. W. Hovis, D. P. Caffey and V. King *"Efficient diode-array-pumped Nd:YAG and Nd:Lu:YAG lasers"* Opt. Lett. 14 (2) pp.116-118, 1989.

42. M. J. Weber and T. E. Varitimos *"Optical spectra and intensities of Nd^{3+} in $YAlO_3$"* J. Appl. Phys. 42 (12) pp.4996-5005, 1971.

43. Michael Bass and Marvin J. Weber *"Yalo: robust at age 2"* Laser Focus, September 1971.

44. Casix Optronics Inc. *"Crystals and Material Product Guide"* (Casix Inc., Fuzhou, P.R. China), 1996.

45. W. F. Krupke, M. D. Shinn, J. E. Marion, J. A. Caird and S. E. Stokowski *"Spectroscopic, optical, and thermomechanical properties of neodymium- and chromium-doped gadolinium scandium gallium garnet"* J. Opt. Soc. Am. B 3 (1) pp102-113, 1986.

46. J.-P. Meyn and G. Huber *"Intracavity frequency doubling of a continuous-wave, diode-laser-pumped neodymium lanthanum scandium borate laser"* Opt. Lett. 19 (18) pp.1436-1438, 1994.

47. B. Braun, C. Hönninger, G. Zhang, U. Keller, F. Heine, T. Kellner and G. Huber *"Efficient intracavity frequency doubling of a passively mode-locked diode-pumped nedymium lanthanum scandium borate laser"* Opy. Lett. 21 (19) pp.1567-1569, 1996.

48. T. H. Allik, M. J. Ferry, R. J. Reeves, R. C. Powell. W. W. Hovis, D. P. Caffey, R. A. Utano, L. Merkle and C. F. Campana *"Crystallography, spectroscopic analysis, and lasing properties of Nd^{3+}:$Ba_2ZnGe_2O_7$"* J. Opt. Soc. Am. B 7 (7) pp.1190-1197, 1990.

49. D. J. Horowitz, L. F. Gillespie, J. E. Miller and E. J. Sharp *"Laser action of Nd^{3+} in a crystal $Ba_2ZnGe_2O_7$"* J. Appl. Phys. 43 (8) pp.3527-3530, 1972.

50. K. Otsuka, T. Yamada, M. Saruwatari and T. Kimura *"Spectroscopy and laser oscillation properties of lithium neodymium tetraphosphate"* IEEE J. Quant. Elect. QE-11 (7) pp.330-335, 1975.

51. K. Kubodera and K. Otsuka *"Diode-pumped miniature solid-state laser: design considerations"* Appl. Opt. 16 (10) pp.2747-2752, 1977.

52. J. Nakano, K. Kubodera and S. Miyazawa *"Evaluation of scattering loss due to dislocations in $LiNdP_4O_{12}$ laser"* J. Appl. Phys. 52 (4) pp.3069-3070, 1981.

53. J. E. Geusic, H. M. Marcos and L. G. van Uitert *"Laser oscillation in Nd-doped yttrium aluminium garnet, yttrium gallium and gandolinium garnets"* Appl. Phys. Lett. 4 (10) pp.182-184, 1964.

54. T. Kushida, H. M. Marcos and J. E. Geusic *"Laser transition cross section and fluorescence branching ratio for Nd^{3+} in yttrium aluminium garnet"* Phys. Rev. 167 (2) pp.289-291, 1968.

55. M. Ross *"YAG laser operation by semiconductor laser pumping"* Proc. IEEE 56 pp.196-197, 1968.

56. J. E. Murray *"Pulsed gain and thermal lensing in Nd:YLF"* IEEE J. Quant. Elect. QE-19 (4) pp.488-491, 1983.

57. J. R. Ryan and R. Beach *"Optical absorption and stimulated emission of neodymium in yttrium lithium fluoride"* J. Opt. Soc. B 9 (10) pp.1883-1887, 1992.

58. G. Cerullo, S. de Silvestri and V. Magni *"High efficiency, 40W CW Nd:YLF laser with large TEM_{00} mode"* Opt. Comm. 93 (1,2) pp.77-81, 1992.

59. C. Rahlff, M. H. Dunn, B. D. Sinclair and W. Sibbett *"High-power , end-pumped effects and applications in Nd:YLF at 1047 and 1053 nm"* Conference on Lasers and Electro-Optics, (1994 Technical Digest Series 8, Optical Society of America, Washington, USA), Paper CThG4, 1994.

60. W. Koechner *"Solid-State Laser Engineering - 2nd Edition"* (Springer Verlag Series in Optical Science, New York), 1988.

61. S. E. Stokowski, R. A. Saroyan and M. J. Weber *"Nd-doped laser glass spectroscopic and physical properties"* Lawrence Livermore National Laboratory M-95, 1978.

62. W. J. Kozlovsky, T. Y. Fan and R. L. Byer *"Diode-pumped monolithic cw Nd:glass laser"* Conference on Lasers and Electro-Optics, (1986 Technical Digest Series , Optical Society of America, Washington, USA), Paper WG4, 1986.

63. W. J. Kozlovsky, T. Y. Fan and R. L. Byer *"Diode-pumped continuous-wave Nd:glass laser"* Opt. Lett. 11 (12) pp.788-790, 1986.

64. T. E. Dimmick *"Semiconductor-laser-pumped, CW mode-locked Nd:Phosphate Glass laser oscillator and regenerative amplifier"* Opt. Lett. 15 (3) pp.177-179, 1990.

65. E. C. Rea, D. Craven, A. C. Nillson and R. L. Byer *"Single frequency, unidirectional, monolithic Nd:Glass nonplanar ring laser"* Conference on Lasers and Electro-Optics, (1989 Technical Digest Series 11, Optical Society of America, Washington, USA), Paper WH4, 1989.

66. M. Kestigian and W. W. Holloway, Jr. *"Incorporation of increased concentrations of rare earth activator ions in optical quality single crystals of yttrium aluminium garnet"* J. Cryst. Growth 3 (4) pp.455-457, 1968.

67. M. Bass and M. J. Weber *"Nd,Cr:YALO$_3$ laser tailored for high-energy Q-switched operation"* Appl. Phys. Lett. 17 (9) pp.395-398, 1970.

68. J. W. Strozyk *"Lutetium effects on the UV absorption spectra of Nd:YAG"* IEEE J. Quant. Elect. QE-7 pp.467-469, 1971.

69. L. A. Riseberg and W. C. Holton *"Nd ion site distribution and spectral line broadening in YAlG:Lu,Nd laser materials"* J. Appl. Phys. 43 (4) pp.1876-1878, 1972.

70. P. P. Yaney and L . G. DeShazer *"Spectroscopic studies and analysis of the laser states of Nd^{3+} in YVO_4"* J. Opt. Soc. Am. 66 (12) pp.1405-1414, 1976.

71. A. W. Tucker, M. Birnbaum and C. L. Fincher *"Stimulated-emission cross section at 1064 and 1342 nm in Nd:YVO_4"* J. Appl. Phys. 48 (12) pp.4907-4911, 1977.

72. N. Mackinnon and B. D. Sinclair *"A laser-diode array pumped, Nd:YVO_4:KTP, composite-material microchip laser"* Opt. Comm. 105 (3,4) pp.183-187, 1994.

73. J. K. Jabczynski and W. Zendzian *"Free-running and electro-optically Q-Switched single-frequency generation of 1 cm quasi-CW diode-bar-end-pumped Nd:YVO_4 laser"* Optica Applicata 26 (1) pp.35-39, 1996.

74. R. A. Fields, M. Birbaum and C. L. Fincher *"Highly efficient Nd:YVO_4 diode-laser end-pumped laser"* Appl. Phys. Lett. 51 (23) pp.1885-1886, 1987.

75. M. J. Weber, M. Bass, K. Andringa, R. R. Monchamp and E. Comperchio *"Czochralski growth and properties of $YAlO_3$ laser crystals"* Appl. Phys. Lett. 15 (10) pp.342-345, 1969.

76. Laser Focus World 7 p.34, April 1971.

77. J. Liang, J. P. Rousseau, P. Maine and A. Migus *"Demonstration of a tuneable single longitudinal mode Q-switched solid-state source using injection seeded Nd:YAP"* Opt. Comm. 82 (5,6) pp.509-513, 1991.

Chapter 4
12 mJ- & 144 mJ-Diode-Laser Pumped Nd:YLF Lasers

In the preceding chapter it has been demonstrated that Nd:YLF is a promising material for use as the gain element in pulsed, diode-laser pumped solid-state lasers. In this chapter the design and both long-pulse and Q-switched operation of two diode-laser, end-pumped Nd:YLF lasers is described; Firstly a device pumped by a single 12 mJ-diode-laser bar and then a more powerful version based on a similar end-pumping theme, but pumped by 6, 24 mJ-diode-laser bars packaged into 2, 3 bar 2D arrays. It will be demonstrated that this type of laser can be made to operate with a high degree of spatial purity, and also that the temporal quality of these devices is inherently good. This will lead to the demonstration of reliable single axial mode operation of this type of laser in the next chapter.

4.1: 12 mJ-Diode-Laser Pumped Nd:YLF Laser

4.1.1: Design Background

The work described in this section was carried out within the confines of an industrially funded programme of work, a consequence of which being that specific specifications were laid out as to the expected performance of the laser source developed. This design specification is summarised in Table 4.1.

W'length	Energy	Repetition rate	Polarisation	Pulse duration	Transverse mode	Longitudinal mode
1.053 µm	30 mJ	< 30 Hz	> 100:1	20-30 nsec	TEM_{00}	SLM

Table 4.1: Design criteria.

As previously noted in Chapter 3, the requirement of an operational wavelength of 1.053 μm effectively restricts the choice of gain material to either Nd:glass or Nd:YLF. It was demonstrated in Section 3.4 that Nd:YLF is the much preferred choice in this case. While the overall goal is to obtain a pulse energy in excess of 30 mJ, this is to be achieved through a combination of a lower energy oscillator followed by a single or dual stage amplifier. It is generally less complicated to generate beams of high spatial (TEM_{00}) and temporal quality (SLM) in lower energy oscillators, and then to amplify this radiation in such a way as to impart minimal distortion on the spatial quality of the light through careful control of the gain profile, than it is to develop a single higher energy oscillator. It was thus decided that this would be the approach that would be adopted and consequently the principal aim of this work was to develop an oscillator producing pulse energies of ~ 2 mJ. It should be noted however that a high quality, higher energy oscillator has also been developed outwith the scope of the industrially funded programme of work and is described later in this chapter.

The gain material Nd:YLF has a naturally polarised output when used with the crystallographic a-axis parallel to laser resonator axis. An additional polarisation selective component is required to be inserted in the laser resonator however, to allow the laser to be Q-switched using established electro-optic techniques, and thus generate pulses of ten's of nanoseconds duration. The insertion of such a polarisation element will further ensure a linear polarisation of > 100:1.

Transverse mode control within the laser resonator is ideally achieved by matching the intra-cavity mode waist size to that of the pumped volume, the pumped volume therefore acting as soft aperture. The means of doing this will be discussed in Section 4.1.4. Longitudinal mode selection will be demonstrated to be inherently good but it is left to Chapter 5 for a full discussion of means of obtaining reliable SLM operation. Thermally induced noise, normally the largest contributory factor to beam pointing stability, is characteristically low in diode-laser pumped solid-state lasers of this nature. Consequently no additional design features are required to attain a stability of < 1/10th the beam divergence.

4.1.2: Diode-Laser Installation and Characterisation

A Spectra-Diode Laboratories SDL-3230-T quasi-CW diode-laser was procured as the pump source for the low energy Nd:YLF laser. This is a 60 W peak power device giving pulses of up to 200 μsec duration, with then a corresponding output energy of 12 mJ per pulse. The specified wavelength of operation of the device is 0.797 μm, to coincide with a strong absorption feature in Nd:YLF, however, this is subject to a manufacturers tolerance of ± 3 nm. The output wavelength of the device once characterised is temperature tuned to accurately match the Nd:YLF absorption line. The manufacturers recommended operating conditions and specified device characteristics for the diode-laser are summarised in Table 4.2.

Parameter	
Wavelength	0.797 μm ± 3 nm
Max. Peak Power	60 W
Max. Pulse Duration	200 μsec
Emitting Aperture	10 mm x 1 μm
Beam Divergence	40° (⊥) x 10° (∥)
Threshold Current	13 A
Operating Current	69.7 A
Operating Voltage	1.75 V
Spectral Width	1.8 nm
Max. Duty Factor	2.0 %

Table 4.2: Manufacturers data for the 12 mJ-diode-laser bar (SDL-3230-T).

The diode-laser was driven by a commercial high peak current supply also manufactured by Spectra Diode Laboratories (SDL-928). Designed for low impedance diode-laser arrays, the driver provides smooth high current pulses (up to 150 A) from a low inductance output stage. Flexibility is incorporated in terms of variable pulse width duration (50 μsec to 1 msec), variable repetition rate (14 Hz to 1 kHz) and variable compliance voltage.

Temperature control of the diode-laser was facilitated by mounting the device on a thermoelectric heat pump (Marlow Industries MI-1023) as shown in Fig. 4.1. The diode-laser was specified for operation at 0.797 μm at 22 °C, and consequently may

require to be operated at as low a temperature as 11 °C or as high as 33 °C, if supplied at an extreme of the manufacturers tolerance.

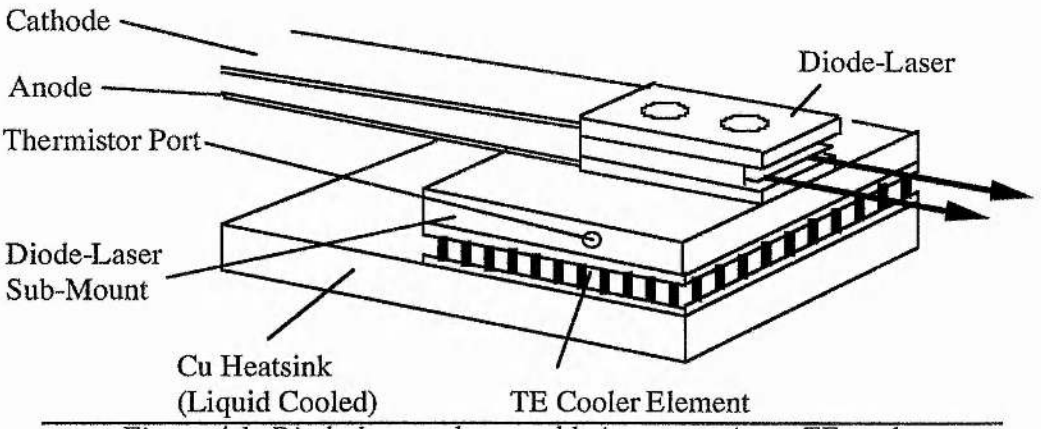

Figure 4.1: Diode-laser sub-assembly incorporating a TE cooler

Given the maximum operating conditions of the diode-laser as shown in Table 4.2, the device has a maximum peak power consumption of 122 W (70 A @ 1.75 V). The peak optical output power of the diode-laser is 60 W and thus there is some 375 mW of waist heat (62 W peak for 200 µsec @ 30 Hz) being generated by the device. The TE cooler heatsink is liquid cooled with water at room temperature (22 °C). The TE cooler is driven by a commercial temperature controller unit (Marlow Industries SE-5000), capable of delivering ± 2 A at ± 9 V. Temperature sensing for the unit is via a 10 kΩ NTC bead thermistor located in the diode-laser sub-mount.

Having established thermal control of the diode-laser, characterisation of the device was performed, with particular emphasis given to the power output as a function of drive current, the spectral output as a function of temperature and time, and the diode-laser spatial quality. These parameters are treated in turn below.

12 mJ-Diode-Laser Power Output

The diode-laser facet was placed in close proximity to a large area thermopile energy probe and the diode-laser pulse energy recorded as a function of the drive current. As shown in Fig. 4.2, the diode-laser has a threshold of around 18 A and slope efficiency of 1.02 $W.A^{-1}$ or 0.2 $mJ.A^{-1}$. This is in good agreement with the manufacturers specified data.

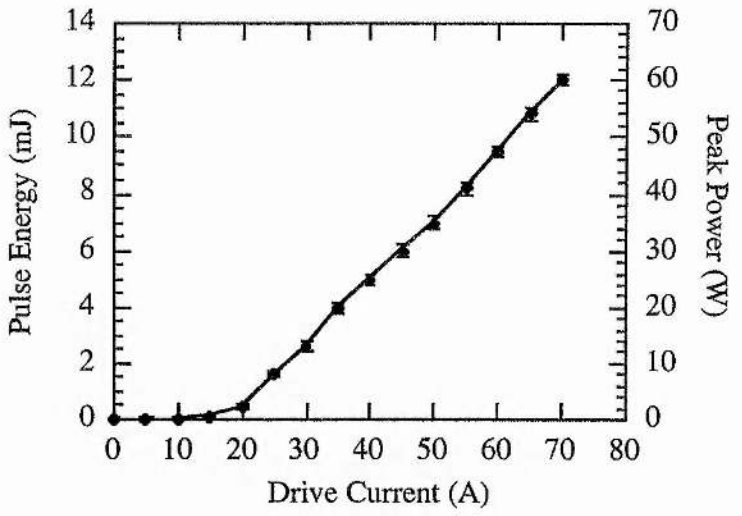

Figure 4.2: 12 mJ-diode-laser energy/power characteristics (SDL-3230-T).

12 mJ-Diode-Laser Spectral Output

It has been noted that it is generally desirable to match the diode-laser emission wavelength to a peak in the absorption profile of the Nd gain medium. The means of thermal control to facilitate this has been described earlier, however, this controls only the ambient surroundings of the diode-laser and not transient heating of the device during pulse emission. The choice of optimum set-point temperature for the diode-laser pumping of Nd is then further complicated by this transient behaviour and consequently will be determined by some combination of both factors.

Two relevant measurements are made to characterise the spectral emission of the diode-laser; (i) A measurement of the wavelength of the diode-laser as a function of the diode-laser sub-mount temperature, and (ii) a measurement of the transient wavelength shift during the diode-laser pulse emission.

The first of these measurements is straightforward to perform; the output from the diode-laser being imaged onto the input slit of a $^1/_4$ m monochromator and the transmission through the monochromator monitored on a photodiode. The emission wavelength at the centre of the pulse duration is then simply measured as a function of sub-mount temperature, resulting in the curve shown in Fig. 4.3.

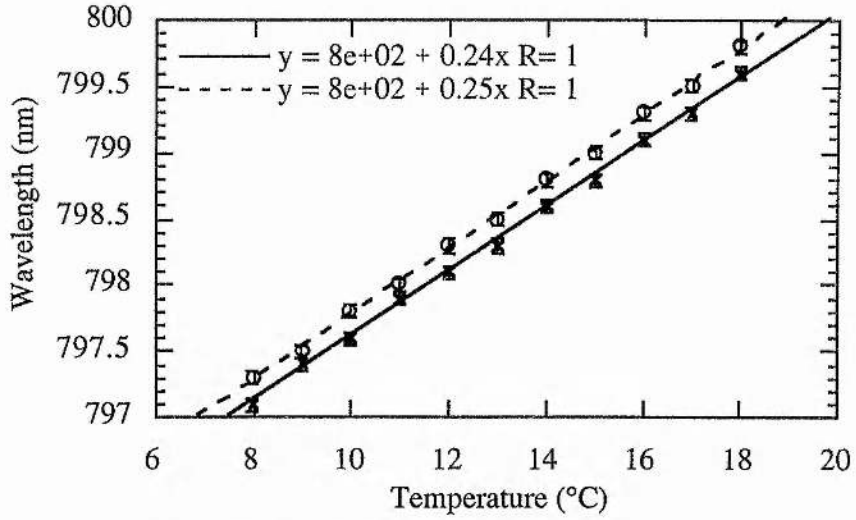

Figure 4.3: Emission wavelength of the 12 mJ-diode-laser as a function of sub-mount temperature at 14 Hz (solid line) and 30 Hz (dashed line).

The thermal loading on the diode-laser will increase as the pulse repetition rate is increased, and thus the central emission wavelength is also dependent upon the average power at which the device is being operated. It is shown by a comparison of the two curves in Fig. 4.3 that a central wavelength shift of 0.2 nm is observed for a change in average optical output power from 120 mW to 360 mW (10 Hz to 30 Hz). Given a wavelength gradient from Fig. 4.3 of 0.24 $nm°.C^{-1}$, the wavelength shift due to repetition rate variation is then indicative of an absolute rise in diode junction temperature of 0.83 °C or 0.05 $°C.Hz^{-1}$.

Measurement of the transient shift in emission wavelength is performed in a similar way, but using a fast photodiode (BPX65). The fast photodiode output is monitored simultaneously with the diode-laser current pulse, so that by varying the monochromator wavelength, the central wavelength of the diode-laser can be ascertained as a function of time. From this data the peak emission wavelength as a function of time can be extracted, as shown in Fig. 4.4.

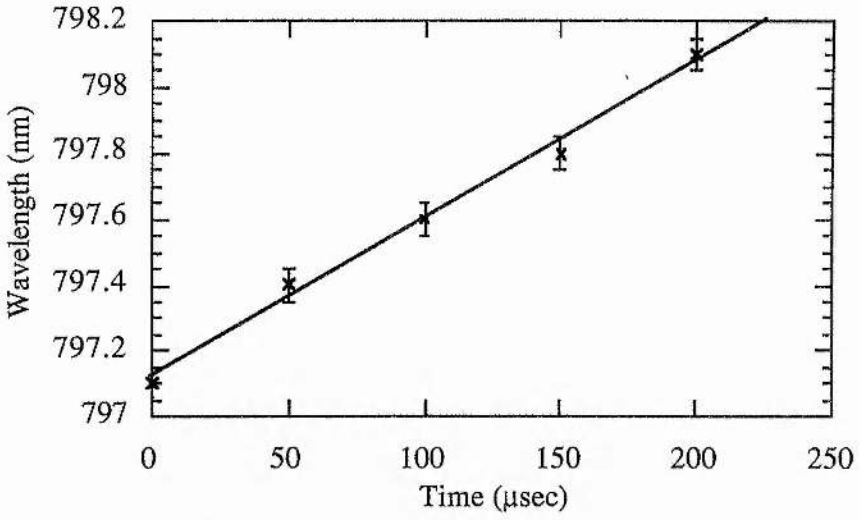

Fig. 4.4: Spectral output of the 12 mJ-diode-laser as a function of time (70 A diode-laser drive current and 14 Hz).

The transient shift in central wavelength of 1.0 nm corresponds to a 4.2 °C rise in the diode junction temperature during the current pulse. A more detailed spectral investigation of the diode-laser, using for example a higher resolution monochromator, can reveal additional detail in the diode-laser spectrum, and in particular longitudinal mode structure. Such an investigation has been performed by Norrie *et al.* [1] on a similar quasi-CW diode-laser bar to that used here, which revealed around 9 modes present, as previously shown in Fig. 3.4.

There will also be some change in emission wavelength across the 1 cm extent of the diode-laser facet, however, this is small (~0.5 nm) relative to the thermally induced variation and is not measured here.

12 mJ-Diode-Laser Spatial Quality

Diode-laser arrays such as that used here for optically pumping solid-state lasers are generally incoherent, i.e. there is no fixed phase relationship between the multiple gain stripes, although each stripe on its own operates on a single transverse mode. Diodes are manufactured in this way by including an optically isolating layer between each stripe of gain, in so doing allowing the fabrication of a large number of gain stripes on a single monolithic chip without incurring lateral lasing. Coherent arrays can be manufactured by omitting this isolating layer and having adjacent stripes sufficiently

close together such that each is evanescently coupled to the next and becomes phase-locked.

The far field energy distribution of the diode-laser used here has been measured parallel and perpendicular to the diode-laser bar using a simple scanning pinhole approach at two points distant from the source. The full width divergence angles at the FWHM energy distribution points are estimated to be around 36° perpendicular to the bar and 10° parallel to the bar, in good agreement with expected values.

4.1.3: Diode-Laser Coupling Optics Design

There are two requirements which must be met in the design of coupling optics for efficient lowest order mode, end-pumped lasers. Firstly, the cross sectional area of the pumped volume must be well matched to that of the resonator mode to avoid excitation of higher order modes, this in turn imposing the second requirement of the absorption depth being sufficiently short as to absorb the pump light within a short distance of the focal plane of the normally focused pump beam. As it is difficult to circularise the output of long-aperture-length diode-lasers similar to that used here, stringent focusing requirements have been relaxed by adopting an approach in which an elliptical shaped pumped volume is accepted and the resonator mode tailored to fit.

The diode-laser coupling scheme used is similar to that first described by Shannon and Wallace [2], and is as illustrated schematically in Fig. 4.5. The coupling scheme comprises initially a rod lens, located parallel and close to the diode-laser facet, to capture the light in its fast axis direction, followed by a cylindrical lens similarly orientated and which collimates the diode-laser output in this direction. A cylindrical lens pair is used to help reduce any spherical aberration arising in the collecting optics. The collecting optics are then followed by an aspheric condenser lens which focuses the pump light a short distance inside the Nd gain element.

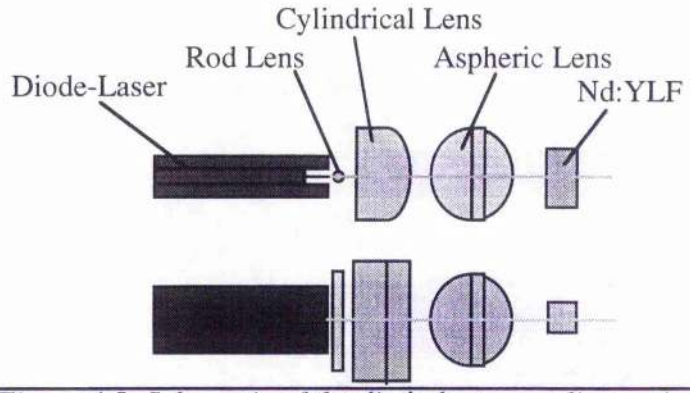

Figure 4.5: Schematic of the diode-laser coupling optics.

The particular lenses used in this case are summarised in Table 4.3, all of which are antireflection coated at 800 nm;

Lens Type	f (mm) @ 800 nm	Dimension (mm)	Material	Supplier Part no.
Rod	1.2	Ø1.6x20	BK7	Spindler & Hoyer 31 8303
Cylindrical	12.7	12.7x25.4 $t_c = 7.9$	BK7	Newport CKX012
Aspheric	8.5	Ø12.0 $t_c = 5.5$	Crown Glass	Melles Griot 01 LAG 000

Table 4.3: Coupling optic lens description

It has been found that the shape and size of the pumped volume within the Nd:YLF laser crystal is relatively insensitive to the positioning of the coupling optic components relative to one another, the main criticality arising in the positioning of the rod lens relative to the diode-laser bar. This lens must be aligned parallel to the bar and at a distance from it determined by the rod lens/cylindrical lens separation, so as to provide near collimation of the diode output in the fast axis direction. The pump beam propagation through the coupling optics is demonstrated in Fig. 4.6, which uses an ABCD formalisation to propagate a Gaussian type beam through the optical system. In the upper trace an on-axis element is modelled, i.e. light from a diode-laser stripe at the centre of the diode-laser bar, while the lower trace shows that for a gain stripe located at the end of the bar. Tight focusing in the Nd:YLF crystal in the plane of the diode-laser fast axis is clearly evident, and with the additional consideration of a finite absorption

depth of around 3 mm beyond this focal plane it is possible to visualise that an ellipticity will exist in the pumped cross-section.

In this case a small pumped cross-sectional area is desired and consequently optimal focusing in the fast axis plane is sought. However, it is notable that the pumped cross-section can be made more circular using this type of coupling scheme, by simply altering the diode-laser to rod lens separation so as to displace the focal plane corresponding to the fast axis direction of the diode-laser within the laser crystal, or indeed simply translate the laser crystal itself relative to the coupling optics. The penalty is a larger cross-sectional area being pumped resulting in a lower gain, however, as available diode-laser powers continue to increase this reduction may ultimately be recovered.

Using then the lens combination described above, 85% pump light transmission into an elliptical focal spot has been obtained. While, as is seen in Fig. 4.6, the focal spot is highly elliptical in the focal plane, it is as previously noted the ellipticity and dimension of the gain cross-section integrated along the extent of the absorption length within the laser crystal which is more relevant. Measurements of this size and details of the design of the laser resonator around the pumped Nd:YLF crystal are given in the next section.

4.1.4: Laser Resonator Design

The Nd:YLF laser crystal is cut in a b-axis orientation, so that the polarisation of the circulating field may be made parallel to either the crystallographic a-axis or c-axis. In this way operation at both 1.047 μm and 1.053 μm can be addressed, although principal concern here is with operation at 1053 nm as noted earlier. The YLF host is doped at a level of 1.0% Nd by atomic weight, and has dimensions Ø 3.3 mm x 12 mm long.

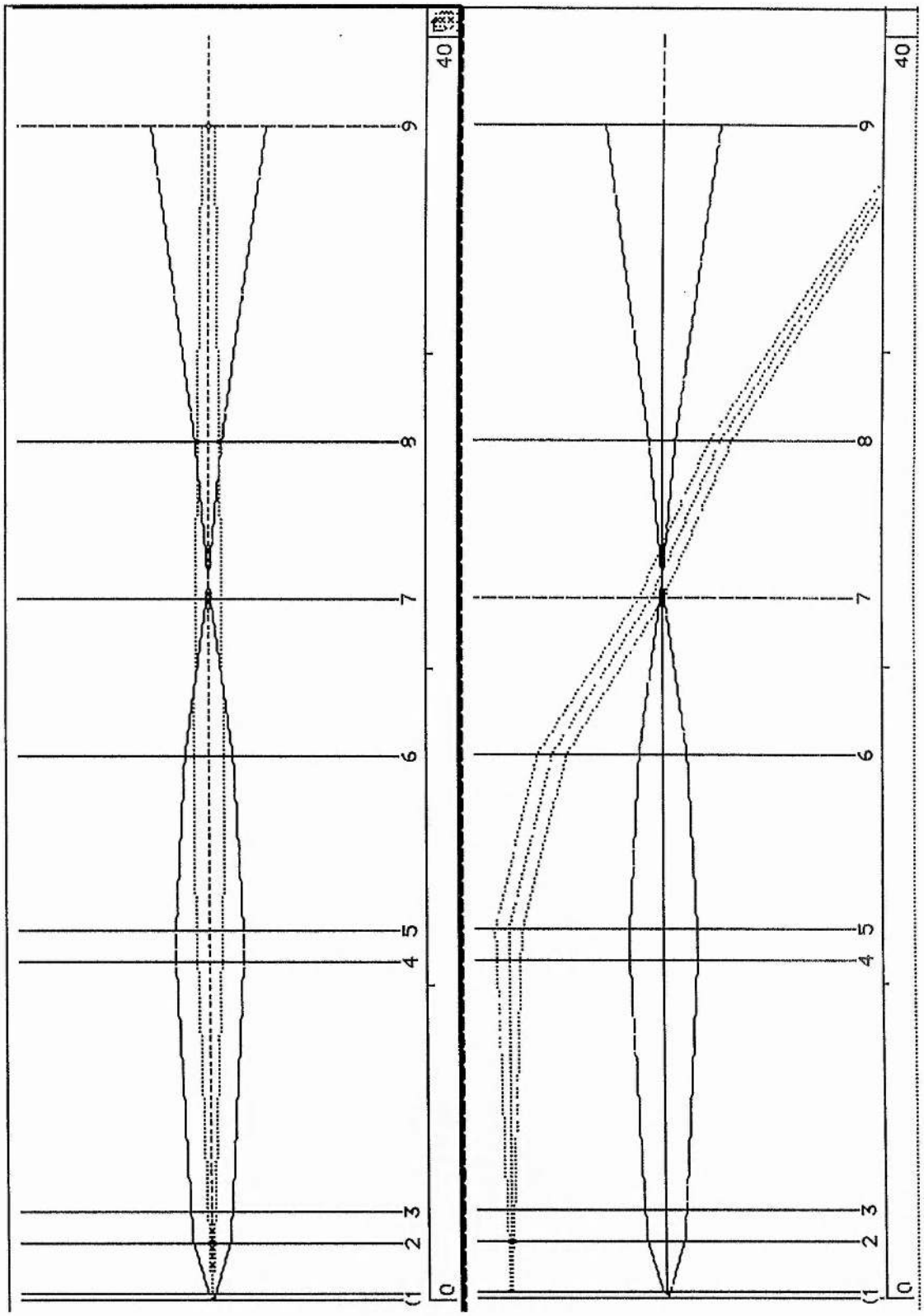

Figure 4.6: Diode-laser beam propagation through coupling optics; Surface 0 - Diode facet, Surface 1/2 - Rod lens, Surface 3/4 - Cylindrical lens, Surface 5/6 - Aspheric lens, Surface 7/8 - Nd:YLF rod. (Solid line - Diode-laser fast axis, Dotted line - Diode-laser slow axis).

Measurements of pump light absorption in this Nd:YLF sample are in good agreement with published values and are as shown in Fig. 4.7. The pump light polarisation has been chosen to be predominantly along the crystallographic c-axis, so exploiting the larger pump light absorption coefficients available in this orientation, although it is not possible to take advantage of the strongest feature at 0.792 μm due to the lack in availability availability of short wavelength diode-lasers at the time of this work. Manifest in the optimisation of the pump light absorption is the simultaneous minimisation of the pumped cross-section and absorption depth. The advantage derived from a shallow absorption depth will become clear in the discussion of longitudinal mode control in Chapter 5.

Measurements of the pumped volume have been made by observing the pumped rod fluorescence on a CCD camera as shown in Fig. 4.8. Using a simple set-up of a single lens located 2f from the centre of the pumped length in the Nd:YLF rod, a real sized image of the fluorescence profile is created on the CCD chip. Additional filters (RG850 and RG1000) are also used to reject any diode-laser light not absorbed in the Nd:YLF. Images are then captured by a frame grabber, after which line scans through the fluorescence profile can be performed and the extent of the pumped volume established. The pumped volume could be made as small as 1.12 mm x 250 μm (half-width at $1/e^2$ intensity), as shown by the false colour fluorescence intensity image - Fig. 4.8 where the 3.3 mm outer diameter of the laser rod is depicted by the inner (green) ring pattern. This results in an average pump energy density of 1.3 $kJ.cm^{-2}$, although this will be around a factor of 2 higher on-axis. It is notable that the gain profile is peaked on-axis, indicated by the blue colouring, and can be well matched to the TEM_{00} mode of a laser resonator. In contrast many transversely pumped systems have a dip in the centre of the gain profile [3], as shown by the false colour fluorescence intensity image in Fig. 4.9, where the on-axis intensity is approximately two thirds that of the peak near to the rod perimeter which is defined by the yellow/green ring pattern. Such a pump profile encourages the formation of higher order transverse modes (TEM_{p0}) which may have a better spatial overlap with the pumped volume.

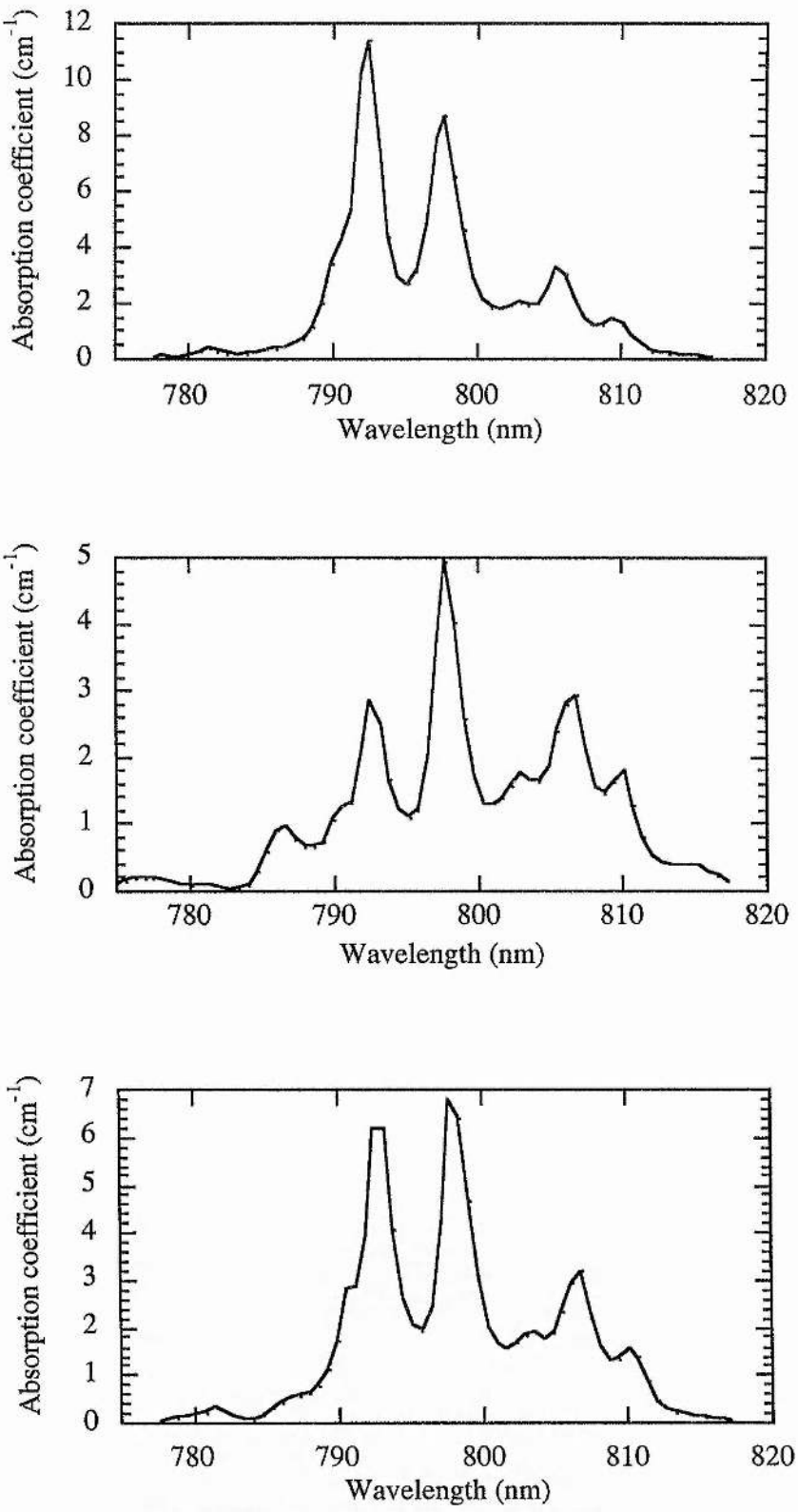

Figure 4.7: Absorption of Nd in YLF (1.0% at. wt.), (Upper trace - Field polarisation parallel to c-axis, Middle trace - Field polarisation perpendicular to c-axis, Lower trace - Field polarisation random).

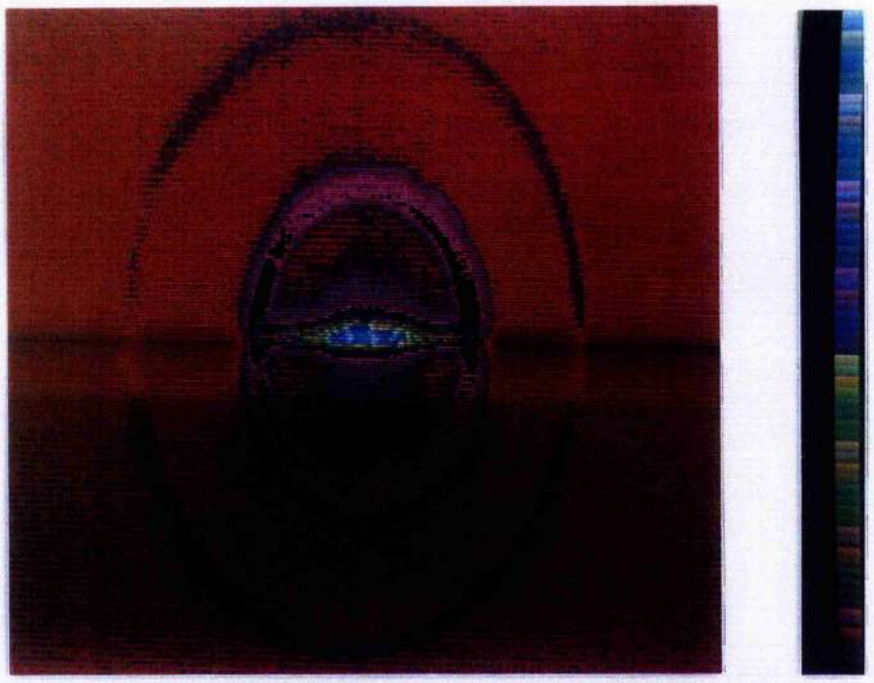

Figure 4.8: Fluorescence profile of the 12 mJ-diode-laser pumped end-pumped Nd:YLF rod looking along the rod axis.

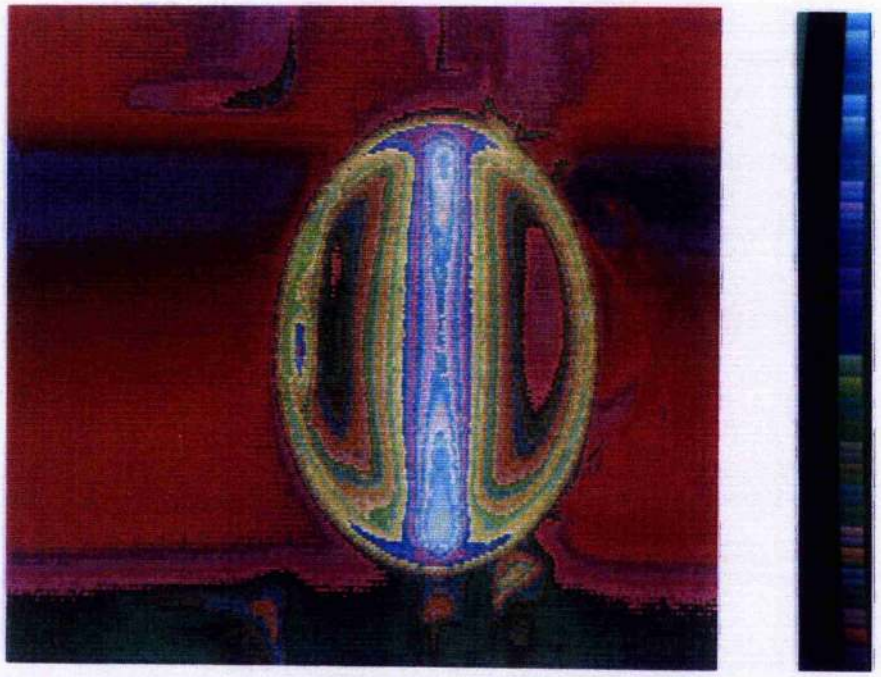

Figure 4.9: Fluorescence profile of a 24 mJ-diode-laser pumped side-pumped Nd:YLF rod looking along the rod axis.
(courtesy J. A. C. Terry, University of St Andrews)

A schematic of the complete laser resonator for long-pulse operation is shown in Fig. 4.10.

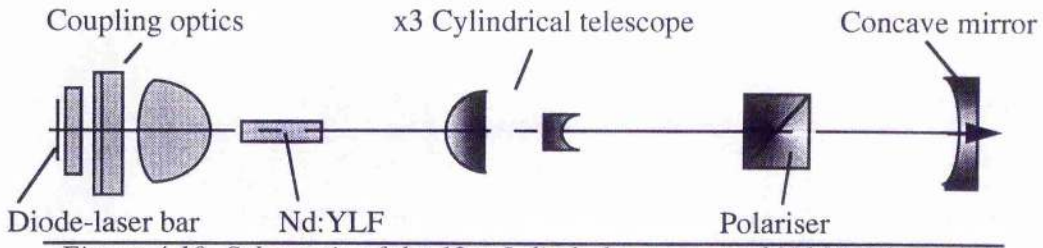

Figure 4.10: Schematic of the 12 mJ-diode-laser pumped Nd:YLF laser for long-pulse operation.

The resonator is formed by a plane high reflector, the high reflectivity dielectric coating being applied directly to the external surface of the Nd:YLF rod and which also has high transmission at the pump wavelength, and a concave partially reflecting output mirror. The radius of curvature (R) of this mirror is chosen so as to give an intra-cavity waist size (ω) at the plane mirror comparable to that of the small dimension of the pumped volume. Using the analysis given in Chapter 2.3 where the waist size at the plane mirror is given by;

$$\omega^2 = \left(\frac{\lambda}{\pi}\right)\left[L(R-L)\right]^{1/2} \qquad (4.1)$$

and for a resonator length (L) of 30 cm, this then predicts a mirror curvature of around 42 cm to give good matching of the resonator mode to the pumped volume, as shown in Fig. 4.11, for the otherwise empty resonator. In fact, we have chosen a mirror of slightly longer radius of curvature (50 cm), which results in a mode size slightly larger than the size of the pumped cross-section in the small dimension (287 μm compared to 250 μm). While this arrangement provides good overlap in one plane the mismatch in the other leads to the formation of a TEM_{p0} mode. To mitigate this effect a cylindrical telescope is introduced into the resonator, expanding the TEM_{00} mode to fill the pumped volume. A x3 expansion factor is used, formed by a 6.4 mm focal length plano-concave lens (Newport CKV006-AR.33) and 19.0 mm focal length plano-convex lens (Newport CKX019-AR.33), both being AR coated at 1.06 μm.

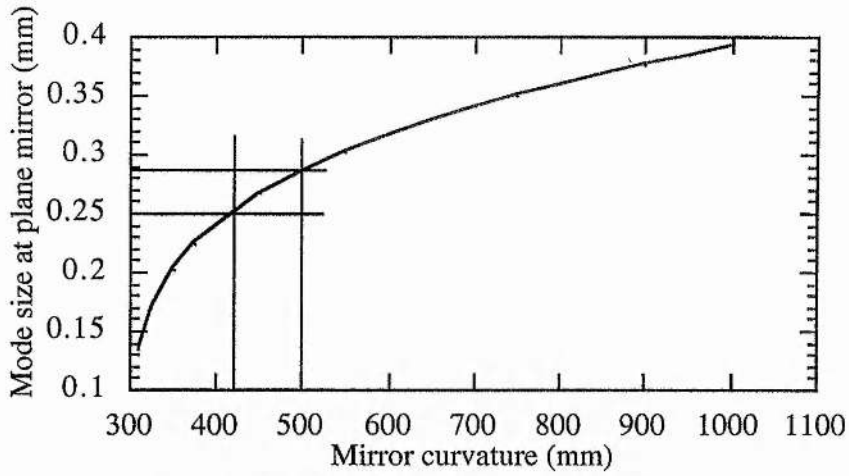

Figure 4.11: Resonator mode size at pumped volume as a function of mirror curvature (Cavity Length L = 30 cm).

Alternate techniques could be considered for controlling the transverse mode, however, these generally result in a high insertion loss and poorer coupling to the pumped volume.

Finally, a high damage threshold air-spaced cube polariser (supplied by Litton) is also inserted into the resonator to provide at this stage the opportunity to operate the laser on either of the orthogonally polarised laser lines, but also later to allow Q-switched operation.

To evaluate more accurately the mode size at various points within the resonator, now incorporating the elements described above, an ABCD analysis was performed. The results of this are shown in Fig. 4.12, which shows diagrammatically the mode shape, and Table 4.4 which lists the mode size at various relevant points within the resonator in the planes parallel and perpendicular to the diode-laser bar. The results given are for an optimal setting of the intra-cavity telescope, so as to provide the most circular and non-astigmatic output.

Position (surface no.)	‖-dimension (mm)	⊥-dimension (mm)
Plane mirror (1)	0.908	0.288
Telescope (3)	0.908	0.298
Telescope(6)	0.308	0.308
Concave mirror (10)	0.444	0.444

Table 4.4: 12 mJ-diode-laser pumped resonator mode sizes.

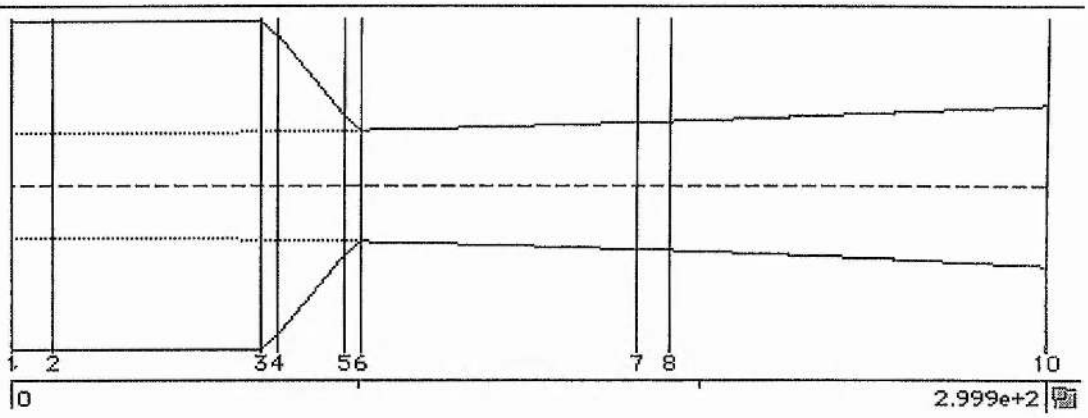

Figure 4.12: Intra-cavity mode shape of the 12 mJ-diode-laser pumped resonator (solid line - parallel to diode-laser bar, dotted line - orthogonal to diode-laser bar, long pulse)
Surface 1/2 - Nd:YLF rod, Surface 3/4 - Plano convex cylindrical lens, Surface 5/6 - Plano concave cylindrical lens, Surface 7/8 - Intra-cavity polariser, Surface 10 - Concave mirror.

4.1.5: Long Pulse Operation

With then the laser resonator set-up as described above, the 12 mJ-diode-laser pumped Nd:YLF laser is characterised initially for a long pulse mode of operation.

Diode-Laser Optimisation

While the diode-laser pump coupling scheme has been adjusted to provide what will be near to an optimum geometry, in the first instance pumping of the Nd:YLF gain element must be fully optimised through fine tweaking of the coupling optics positions and the diode-laser temperature. With the coupling optic position optimised the diode-laser temperature is varied and the operating point for maximum laser energy established. This is found to be near to the expected temperature for a diode-laser emission wavelength of 0.7975 μm, as shown in Fig. 4.13. It is to be noted that as the diode-laser is cooled its output energy increases due to a reduction in its threshold. The diode-laser drive current has therefore been adjusted at each temperature to give the same diode-laser pump energy.

The Nd:YLF laser pulse energy is observed to begin to increase again above diode-laser temperatures of 37 °C. The cause of this is the diode-laser wavelength approaching Nd:YLF absorption peaks above 0.803 μm.

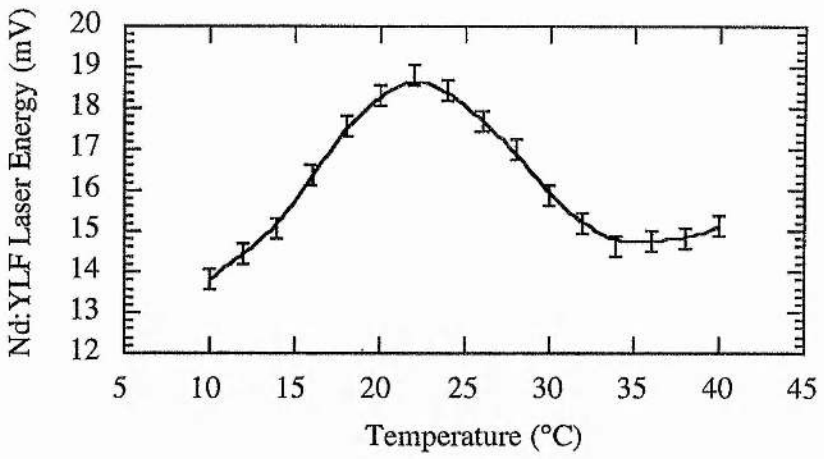

Figure 4.13: Nd:YLF laser output as a function of diode-laser heatsink temperature.

Small Signal Gain

For lasing to take place it has been shown that it is necessary for the relationship $2gl \geq \ln(R_1R_2)^{-1}$ to be satisfied (see Chapter 2.2.5), where 2gl is the round trip gain and the term on the right the total fractional loss per round trip. R_1 is the reflectivity of the output coupling mirror and R_2 the product of the reflectivity of mirror 2 and any other parasitic resonator losses. Setting R_1 equal to 1 and separating the parasitic loss L from the mirror reflectivity R_2 one obtains at threshold;

$$2gl - \left[2\ln\left(\frac{1}{T}\right) + \ln\left(\frac{1}{R}\right)\right] = 0 , \qquad (4.2)$$

where T = 1 - L.

It is then possible to ascertain the round trip small signal gain G_0 (=exp[$2g_0l$]) by increasing the parasitic loss within the laser resonator until lasing ceases. This is done in this case by the introduction of absorbing filters, with varying degrees of optical density, into the laser resonator so increasing the intrinsic parasitic loss of 8.5%. The small signal gains for this laser have then been established to be 3.6 at 1.047 μm and 2.12. at 1.053 μm. This ratio of gains is in good agreement with what is to be expected based on the published ratio of stimulated emission cross-sections for the two transitions (3.7:2.6).

From these measured gl values it is possible to predict the optimum output coupling reflectivity (see Chapter 2.2), through the relationship;

$$R_{opt} = 1 - \left[\frac{\sqrt{(2gl.L)} - L}{1 + L} \right]. \qquad (4.3)$$

Given L = 0.085, this then predicts an optimum reflectivity for 1.047 μm operation of 77.4% and for 1.053 μm operation 84.5%. An 80% reflecting output coupling mirror is used throughout these experiments.

Long-Pulse Energy

The useful output energy as a function of the pump pulse energy for this long pulse mode of operation is shown in Fig. 4.14.

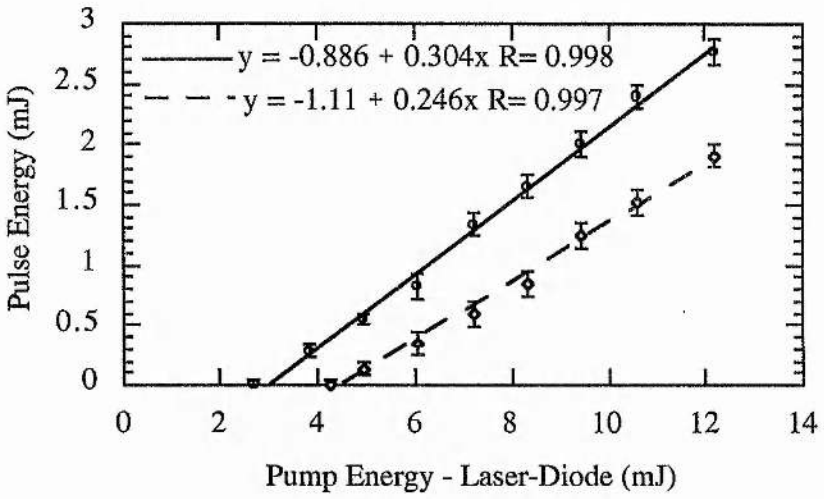

Figure 4.14: Nd:YLF laser output as a function of diode-laser pump energy - long pulse (o - 1.047 μm, ◊ - 1.053 μm).

These results equate to peak optical-optical conversion efficiencies of 22.7% and 15.7% for 1.047 μm and 1.053 μm operation respectively. Corresponding slope efficiencies are 30.4% and 24.6%. Taking into account the pump coupling efficiency, the laser output to pump light absorbed conversion efficiencies for 1.047 μm and 1.053 μm operation are 27.4% and 18.9% respectively, with corresponding slope efficiencies of 35.7% and 28.9%. The above and additionally wall plug efficiencies are summarised in Table 4.5.

Wavelength	Optical to Optical conversion efficiency	Absorbed pump light to Optical efficiency	Wall plug efficiency	Optical to Optical slope efficiency
1.047 μm	0.227	0.274	0.090	0.304
1.053 μm	0.157	0.189	0.063	0.246

Table 4.5: Summary of 12 mJ-diode-laser pumped Nd:YLF laser performance - long pulse (Coupling optic efficiency - 83%, Diode efficiency - 40%).

Spatial Quality

The spatial quality of the laser has been confirmed as being TEM_{00} at all operating powers. Measurements have been made of the full angle beam divergence.diameter product, which shows the beam to be near to diffraction limited (1.33 mm.mrad). Additionally, an rf spectrum analyser and fast response photodiode have been used to look for the beat frequency signal corresponding to the inter-transverse mode spacing, which will be contained in the beam if more than one transverse mode is oscillating. This mode spacing was shown by Kogelnik [4] to be given by;

$$\Delta\upsilon = \left(\frac{c}{2L}\right)\left[\Delta l + \left(\frac{1}{\pi}\right)\Delta(m+n)\arccos\sqrt{\left(1-\frac{L}{R_1}\right)\left(1-\frac{L}{R_2}\right)}\right], \qquad (4.4)$$

where L is the resonator length, l,m and n the longitudinal and transverse mode numbers and R_i the curvatures of the resonator mirrors. The first term in l is that which is familiar in describing the longitudinal mode spacing, while the second term in m and n describes the transverse mode spacing. In this case where L is 30 cm, $R_1 = \infty$ and R_2 = 50 cm, this transverse mode spacing is then 141 MHz. No beat signal around this frequency is evident in the output.

Temporal Quality

The temporal profile of the laser output in this long pulse mode of operation is as to be expected in the form of a damped train of relaxation oscillations as shown in Fig. 4.15.

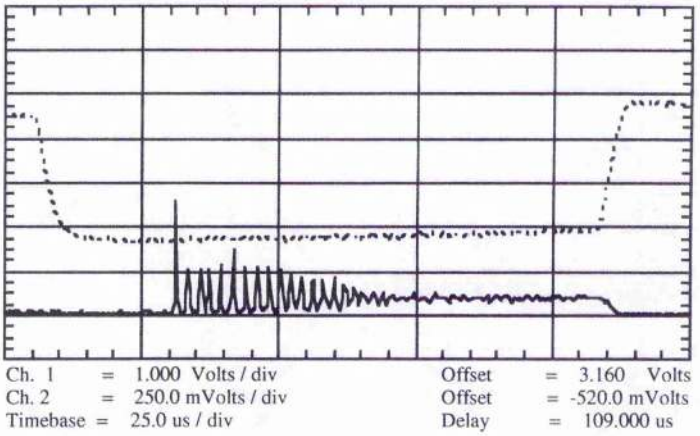

Figure 4.15: Temporal profile of long pulse 12 mJ-diode-laser pumped Nd:YLF laser (Upper trace - diode-laser current pulse, Lower trace - Nd:YLF laser pulse).

4.1.6: Q-switched Operation

Q-switch Description

Q-switched operation of the laser has been accomplished through the addition to the laser resonator of an electro-optic Q-switch or Pockels cell based on a z-cut lithium niobate ($LiNbO_3$) crystal, as shown in Fig. 4.16. This is an example of a transverse E-O modulator, wherein an electric field applied transversely to the crystal, and in this case parallel to the crystallographic x-axis, results in the formation of electro-optically induced birefringence in the crystal, the axis orientation being at 45° to the x- or y-axes, as depicted in Fig. 4.17.

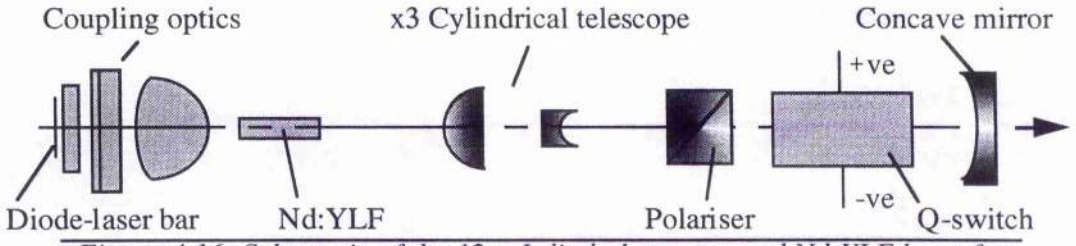

Figure 4.16: Schematic of the 12 mJ-diode-laser pumped Nd:YLF laser for Q-switched operation.

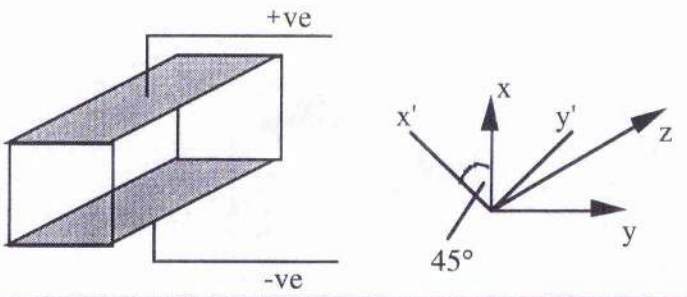

Figure 4.17: Electro-optic birefringence in $LiNbO_3$ (x,y and z - crystallographic axes, x' and y' E-O induced birefringence axes).

The magnitude of the refractive index change (Δn) between x' and y' is linearly proportional to the applied field and thus a Q-switch in the optical arrangement shown in Fig. 4.16 acts as a voltage dependent phase retarder, which in conjunction with the polariser provides a variable loss mechanism within the resonator. In theory, by applying a voltage to the $LiNbO_3$ crystal which results in a quarter-wave retardation between the resolved polarisation components along x' and y', for the initially linearly polarised right travelling wave, a half wave retardation is imparted on the left travelling wave after reflection by the resonator mirror and a second transit through the crystal, so resulting in an infinite resonator loss. In practice nonuniformities in the crystal and polariser limit the extinction ratio to greater than 100, however, this is normally adequate to prevent lasing and allow the build up of a high unsaturated gain level in the gain medium as the stored energy increases during the pump pulse.

The change in refractive index along x' and y' is given by

$$n_{x'} = n_0 + \frac{1}{2} n_0^3 r_{22} E_x \qquad n_{y'} = n_0 - \frac{1}{2} n_0^3 r_{22} E_x \ , \tag{4.5}$$

where n_0 is the ordinary index of refraction with no voltage applied, r_{22} is the relevant electro-optic coefficient and E_x the applied electric field. The phase difference δ ($=\Delta n l$) induced between the x' and y' resolved components over a crystal of length l and aperture d is then simply

$$\delta = \left(\frac{2\pi}{\lambda}\right) \frac{V_x n_0^3 r_{22} l}{d} \ . \tag{4.6}$$

For $LiNbO_3$, where the electro-optic coefficient $r_{22} = 6.5$ pm.V^{-1} [5], the ordinary refractive index $n_0 = 2.233$ [6] and the crystal used here is of size 9 mm square aperture and 25 mm length, the required dc. voltage for quarter-wave retardation is ~1.3 kV.

Q-switch Driver

Various Q-switch drivers have been used in conjunction with the Pockels cell during the course of this work. Initially a driver based on a krytron high voltage switching element (EG&G KN22) was used, the electronic circuit being shown in Fig. 4.18. Although reliable and convenient to use, the applied voltage being variable over a large range (400 - 3000 V) without the need for any alterations to the circuit, the krytron does have a limited pulse lifetime (10^6 pulses). Consequently, this driver was eventually replaced by one based on a transistor avalanche chain, shown in Fig. 4.19, which is again reliable but for practical purposes has no limited lifetime components. The applied voltage is still variable using this driver, however, large changes (> 250 V) in the operating voltage requires the removal or addition of transistors in the chain in order that they continue to operate near to their breakdown voltage. In this way the switching speed of the chain remains optimised.

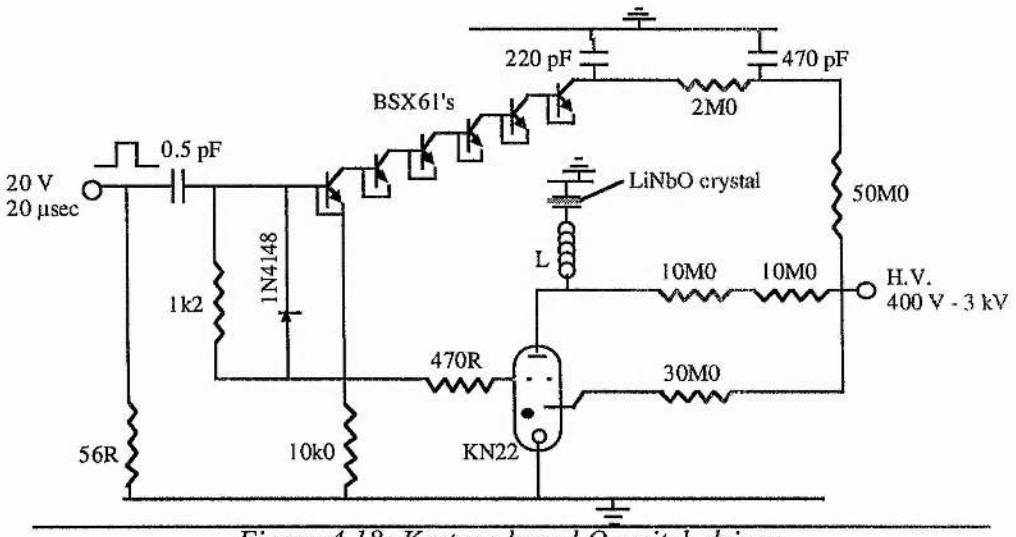

Figure 4.18: Krytron based Q-switch driver.

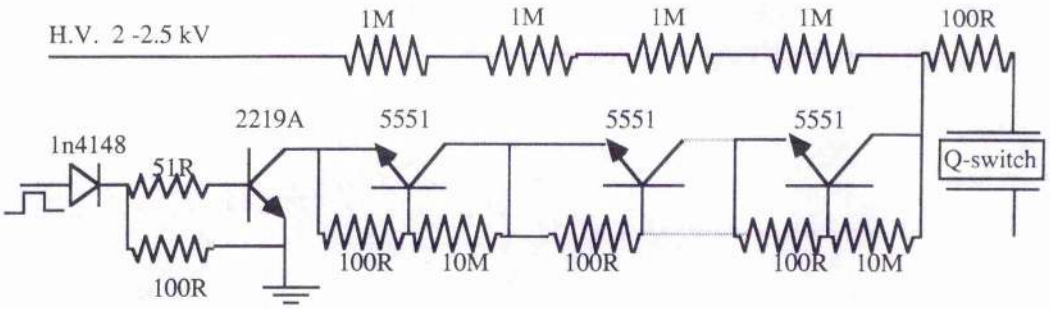

Figure 4.19: Transistor avalanche based Q-switch driver.

Operation of the Q-switched laser proved initially disappointing with only around 50% of the long pulse energy being observable in the Q-switched output and as much as 20% pulse to pulse instability. The source of this problem was found to lie in elasto-optic relaxation effects in the lithium niobate crystal.

Q-switch Optical Switching

When the applied voltage is removed from the Pockels cell the optical switching of the crystal is found to lag the electronic switching, resulting in a time varying loss on the microsecond timescale. The piezo-electric action of the applied voltage compresses the lithium niobate crystal and when this voltage is removed the crystal remains compressed for some finite length of time. This compression causes strain birefringence in the crystal, which in turn imparts a phase retardation on the optical wave [7, 8] and consequently a loss at the polariser. If then the pulse build up time from the time of switching is less than the crystal decompression time a loss will be experienced and the laser output reduced. The time varying loss was measured using the technique shown in Fig. 4.20.

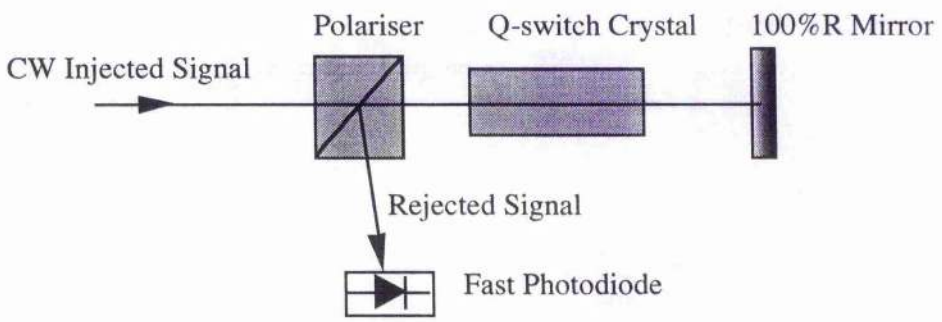

Figure 4.20: Experimental set-up for the measurement of the time varying Q-switch switching loss.

The set-up essentially mimics the output end of the laser resonator, except that for Q-switch evaluation purposes the normally partially reflecting output mirror is replaced by a plane high reflector. A polarised CW signal is initially injected into the set-up, this signal being transmitted by the polariser. With a quarter-wave voltage applied to the Pockels cell, the right travelling wave is made circularly polarised, which after being reflected by the mirror and a second pass through the Pockels cell is made linear again but orthogonal to the incident wave. This left travelling reflected wave is then rejected by the polariser and monitored on a photodiode. As the voltage is removed from the Pockels cell the time varying loss resulting from elasto-optic relaxation can then be monitored.

The result of this investigation is shown in Fig. 4.21, which clearly demonstrates the slow optical switching of the crystal, compared to an electronic switching time of less than 10 nsec.

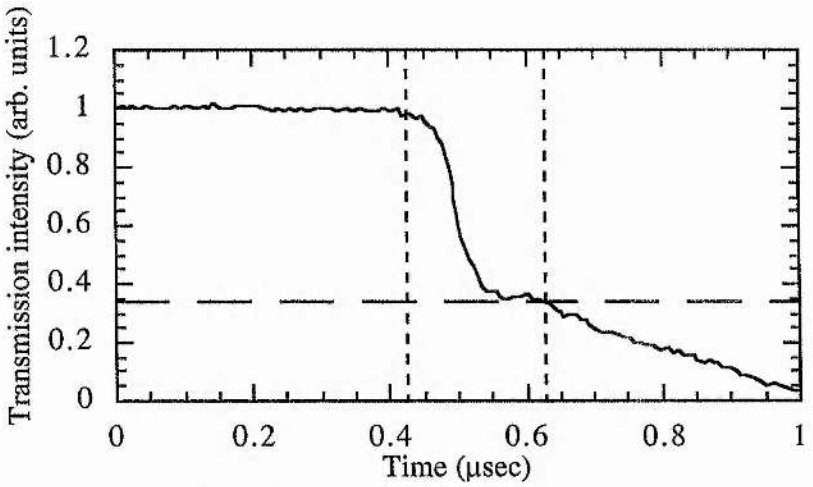

Figure 4.21: Optical switching of the $LiNbO_3$ Q-switch - normal operation.

During initial measurements of the Q-switched performance of the laser it was observed that the Q-switched laser pulse appears some 200 nsec after the electronic switching of the Pockels cell. From Fig. 4.21 it is readily established that the parasitic loss of the Pockels cell-polariser combination at this point is as high as 35%, which will clearly impact greatly the laser performance. As a means of circumventing this problem reverse biasing of the Pockels cell has been additionally included, as depicted in Fig. 4.22, and found to be a practical means of mitigating this effect.

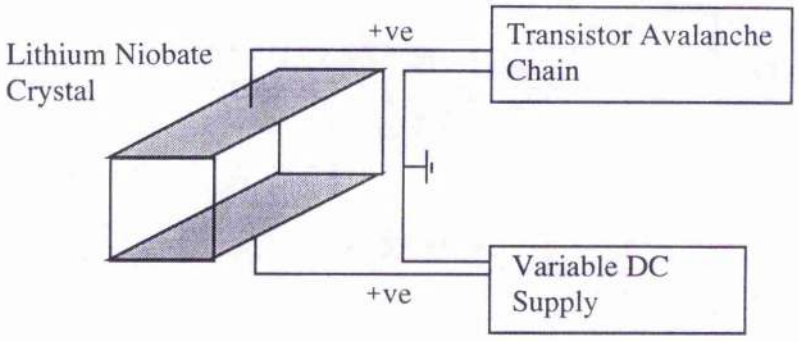

Figure 4.22: Reverse biased lithium niobate Q-switch.

By applying a reverse bias voltage of the same polarity to the opposite electrode of the Pockels cell while at the same time increasing the normally applied forward bias by an equal amount, so as to maintain optimum hold-off during the diode-laser pump pulse, the optical switching of the lithium niobate crystal can be improved by effectively over-switching the crystal. Previously, electrical switching of the Pockels cell switched the applied field from the quarter-wave voltage to zero volts, whereas now on switching the field is switched from the same net quarter-wave voltage, i.e. the difference between the forward and reverse bias voltages, to some reverse bias field. In this way the crystal is forced into a zero or lower birefringence state more quickly by the electro-optic effects generated by the reverse bias counteracting the elasto-optic relaxation of the crystal when the forward bias is removed.

Using the experimental set-up illustrated in Fig's. 4.20 and 4.21 and varying the applied reverse bias, the optimum biasing condition can be found. In so doing the optical switching form of the Pockels cell has been modified to that shown in Fig. 4.23, where a reverse bias voltage of 650 V is applied and complemented by an increase in the forward switchable bias voltage to 1.95 kV. The laser pulse now appears approximately 150 nsec after initiation of the electrical switching, at which time the parasitic loss can be seen to have been reduced to less than 5%.

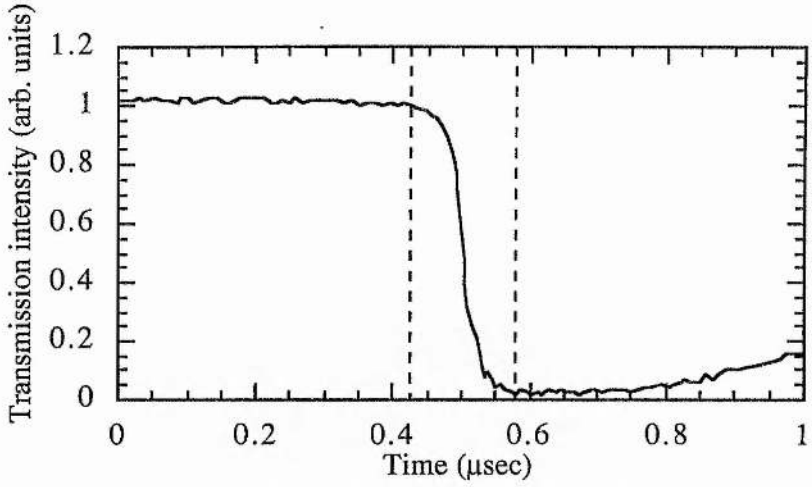

Figure 4.23: Optical switching of the $LiNbO_3$ Q-switch - reverse biased operation.

Q-switched Pulse Energy

With now the Pockels cell re-installed in the laser resonator and optimised for minimum loss at the time of appearance of the Q-switched laser pulse, the Q-switched laser pulse energy as a function of diode-laser pump energy can now be ascertained. Results are shown in Fig. 4.24, and represent a peak optical to optical conversion efficiency of 18.9% and 14.3% for 1.047 μm and 1.053 μm operation respectively. Corresponding slope efficiencies are 26.9% and 23.9%.

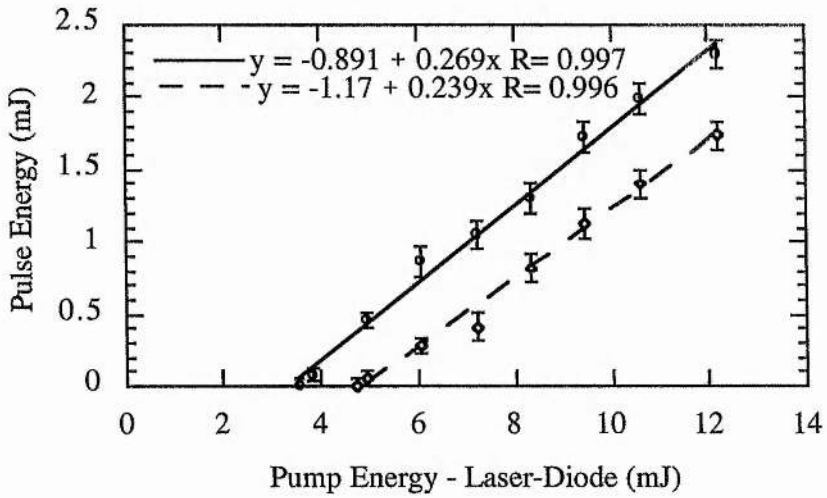

Figure 4.24: Nd:YLF laser output as a function of diode-laser pump energy - Q-switched (o - 1.047 μm, ◊ - 1.053 μm).

As for long pulse operation, taking into account coupling optic losses sees the peak conversion efficiencies increased to 22.8% and 17.2% again for 1.047 μm and 1.053 μm operation. Results are summarised in Table 4.6.

Wavelength	Optical to Optical conversion efficiency	Absorbed pump light to Optical efficiency	Wall plug efficiency	Optical to Optical slope efficiency
1.047 μm	0.189	0.228	0.076	0.269
1.053 μm	0.143	0.172	0.057	0.239

Table 4.6: Summary of 12 mJ-diode-laser pumped Nd:YLF laser performance - Q-switched (Coupling optic efficiency - 83%, Diode efficiency - 40%).

The efficiencies reported here compare favourably with those of others; Zbinden and Balmer [9] reported a 13% slope efficiency for Q-switched operation at 1.047 μm of their fibre bundle coupled diode-laser bar, and Mead *et al.* [10] reported a comparable 31% optical conversion efficiency in a long pulse mode of operation, but only 13% Q-switched, again at 1.047 μm.

Spatial Quality

During Q-switched operation the laser continues to operate on the lowest order transverse mode at all pump power levels. Shown in Fig's. 4.25 and 4.26 are the near- and far-field energy distributions respectively. A small degree of ellipticity is seen to exist in the near-field, the Gaussian fits being for 0.6 mm radius ($1/e^2$) and 0.48 mm radius beams in the two orthogonal directions. The beam propagates into a circularly symmetric mode in the far-field, the Gaussian fit being for a 0.6 mm radius ($1/e^2$) beam in each case. The far-field energy distribution is obtained by looking at the beam profile in the focal plane of a 1 m focal length lens.

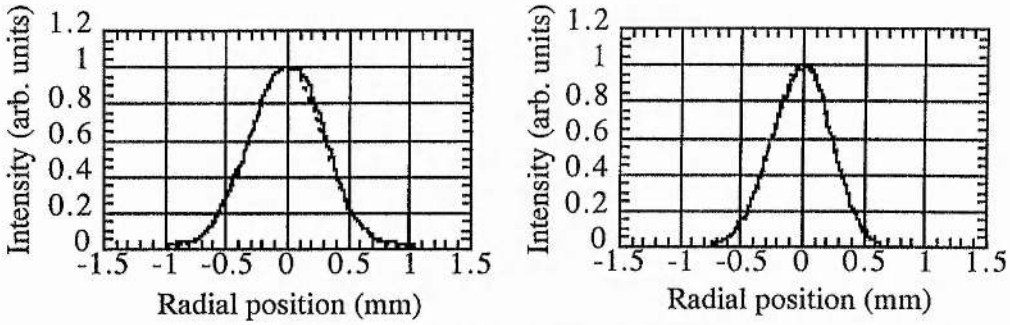

Figure 4.25: Near-field energy distribution in orthogonal planes (solid line - experimental, dashed line - Gaussian fit).

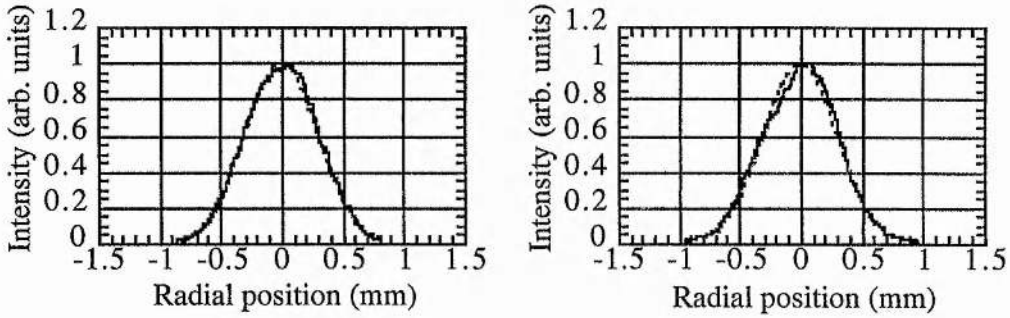

Figure 4.26: Far-field energy distribution in orthogonal planes (solid line - experimental, dashed line - Gaussian fit).

Temporal Quality

The temporal profile of the now Q-switched laser pulse is as expected a single giant pulse, shown in Fig. 4.27, having a duration (FWHM) of ~18 nsec for the 1.047 μm transition and ~31 nsec for 1.053 μm . Easily seen superimposed on the pulses is modulation arising from longitudinal mode beating, in this case measured to have a period of 2.4 nsec, corresponding to a mode beat frequency of 417 MHz and an optical resonator length of 36 cm. Such clearly evident mode beating is indicative of only a few longitudinal modes being present in the spectrum, a property to be exploited in single longitudinal mode operation of the laser, as will be described in detail in Chapter 5. Characteristic of a high initial inversion ratio is the asymmetry observable in a Q-switched pulse profile, particularly evident in this case for the 1.047 μm pulse.

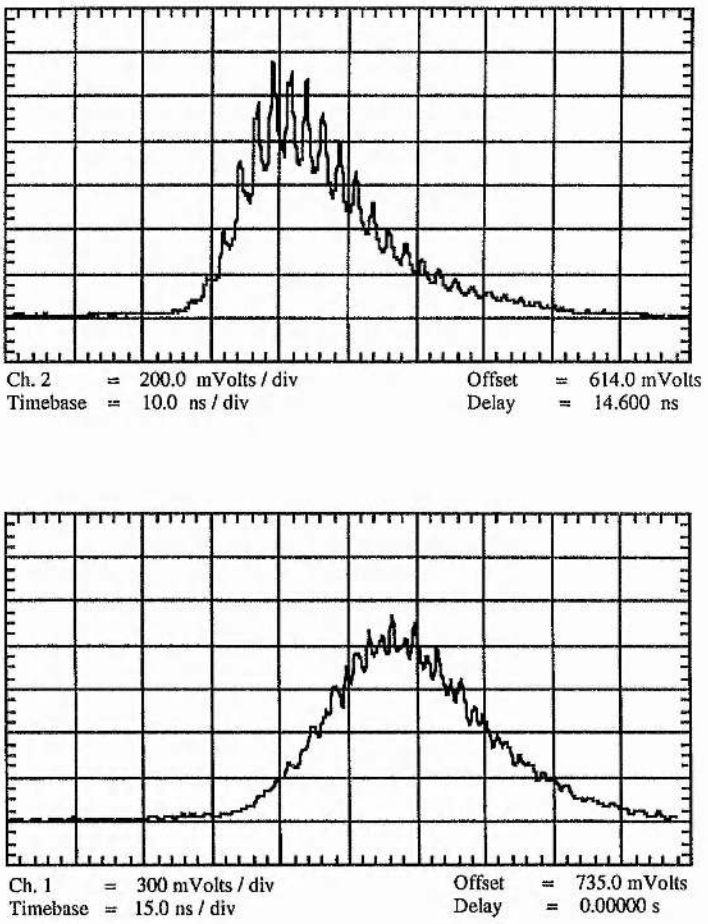

Figure 4.27: Q-switch pulse temporal profiles (Upper trace - 1.047 μm wavelength, Lower trace - 1.053 μm wavelength).

4.1.7: Addendum to the 12 mJ-Diode-Laser Pumped Device

It was noted in Section 4.1.1, that the desire was to develop an oscillator providing greater than 2 mJ per pulse at 1.053 μm. Results presented show that the 12-mJ diode-laser pumped device could provide up to only 1.75 mJ per pulse at this wavelength. Within the timeframe of this work, diode-laser bars of similar design to that described previously have become available which provide up to 24 mJ per pulse and which are suitable for pumping Nd:YLF. Such a diode-laser has since been installed in the Nd:YLF laser described here, where the coupling optic arrangement has been modified to provide a pumped volume which remains elliptical in form, but has an aspect ratio of now 1.5:1 (compared to 3:1 for the 12 mJ-diode-laser) and having the same large dimension as previously noted. Consequently, while the stored energy in

the gain medium is increased by around a factor of 2, the stored energy per unit volume is the same as before. To match the larger pumped volume, the concave resonator mirror curvature has been increased to 6 m, and the cylindrical telescope magnification reduced to 1.5.

The result of these modifications is a laser which provides a pulse energy of up to 3.2 mJ at 1.053 μm in a 28 nsec pulse, and in a beam which is again TEM_{00} with an M^2 value of < 1.1. The final device is shown in Fig. 4.28, which also incorporates the electro-optic phase-modulator for resonator length control and provides reliable SLM operation as will be discussed in Chapter 5.

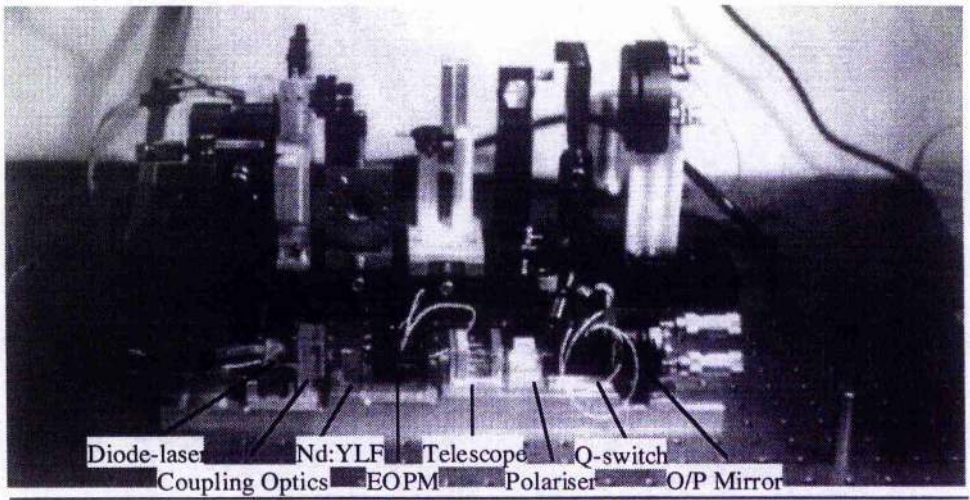

Figure 4.28: 24-mJ diode-laser pumped Nd:YLF laser with slow Q-switch and EOPM discussed in Chapter 5.

4.2: 144 mJ-Diode-Laser Pumped Nd:YLF Laser

4.2.1: Design Background

Described now is the design and characterisation of a higher power diode-laser pumped Nd:YLF laser. This device has a similar design basis to that described in Section 4.1, being based on an end-pumped geometry for efficient pump coupling while at the same time relying on the pumped cross-section to define a soft aperture and high quality spatial mode. Although generically similar, substantial resonator and pump configuration changes have been made in power scaling the laser. The single diode-laser bar used previously has been replaced by two, 3-bar-stack diode-laser arrays, one

located at each end of a linear resonator. Modifications have been made to the coupling optics to accommodate the 2-D diode-laser-arrays and output coupling is via the intra-cavity polariser, given that both resonator mirrors are obscured external to the resonator by pump modules. The detailed design and description of operation of the higher power laser is now presented, noting that interest now lies with predominantly 1.047 μm operation with a view to obtaining optimal performance.

4.2.2: Diode-Laser Installation and Characterisation

Two Spectra-Diode Laboratories SDL-3231-A3 quasi-CW diode-laser arrays were procured as the pump source for the high energy Nd:YLF laser. These, like the SDL-3230-T, are 60 W peak power bars, however, each array consists of 3-bars stacked vertically and can now be operated for a pulse duration of 400 μsec. Consequently, each array provides a maximum of 72 mJ per pulse, giving a total pump energy of 144 mJ. The manufacturers recommended operating conditions and device characteristics are summarised in Table 4.7.

Parameter	
Wavelength	0.797 μm ± 3 nm
Max. Peak Power	180 W (3 x 60 W)
Max. Pulse Duration	400 μsec
Emitting Aperture	10 mm x 1 μm
Diode Bar Pitch	0.4 mm
Beam Divergence	40° (⊥) x 10° (∥)
Threshold Current	13 A
Operating Current	69.7 A
Operating Voltage	5.25 V
Spectral Width	1.8 nm
Max. Duty Factor	4.0 %

Table 4.7: Manufacturers data for the 72 mJ-diode-laser array (SDL-3231-A3).

Both diode-laser arrays can be driven in series by a single high peak current supply, as before this being the Spectra-Diode Laboratories SDL-928.

Thermal control of the diode-laser arrays is established in exactly the same way as before, by mounting the arrays on a heatsink controlled by a thermoelectric heatpump. The physical separation of the diode-laser arrays in pumping either end of a linear resonator precludes the use of a single TE cooler, however, this would be possible in a folded resonator geometry where both diode-laser arrays have well matched spectral properties.

The maximum peak power consumption of each diode-laser array is 450 W (75 A @ 6V). The peak optical output power of each diode-laser array is 180 W and thus some 3.25 W of waist heat (270 W peak for 400 μsec @ 30 Hz) may be generated by the device.

72 mJ-Diode-Laser Array Power Outputs

In turn each of the diode-laser arrays is placed in close proximity to a thermopile energy probe and the diode-laser pulse energies measured as a function of drive current. The resulting curves are shown in Fig. 4.29.

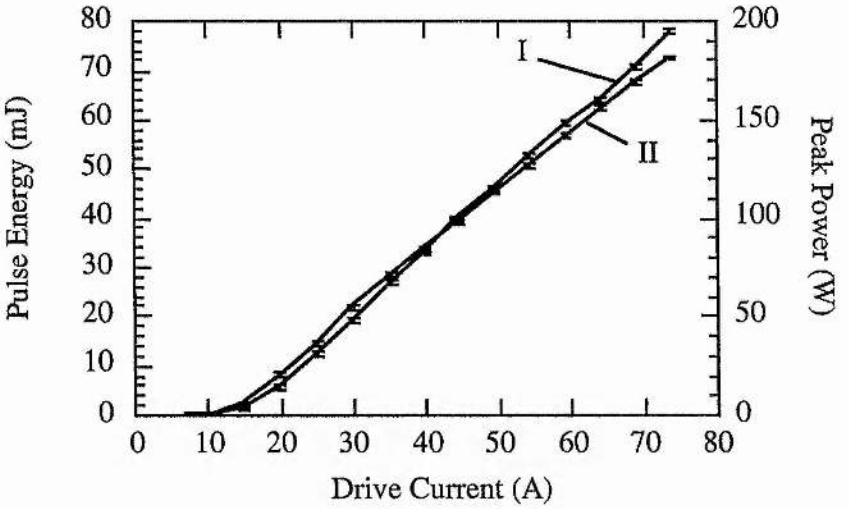

Figure 4.29: 72 mJ-diode-laser array pulse energies (I - Serial No. T353 , II - Serial No. T331).

Both diode-lasers have a threshold in the range 13 - 15 A, diode-laser (I) having the slightly higher threshold and slope of 3.29 $W.A^{-1}$ or 1.31 $mJ.A^{-1}$, compared to a slope of 2.98 $W.A^{-1}$ or 1.19 $mJ.A^{-1}$ for diode laser (II).

72 mJ-Diode-Laser Array Spectral Outputs

A detailed description of the spectral characteristics of the type of diode-laser bar used in this type of diode-laser array was presented in Section 4.1.2. In particular, it is necessary to establish the central wavelength of the arrays as a function of the diode-laser array sub-mount temperatures, in order that they may be tuned to the 0.797 μm absorption peak of Nd:YLF. Details of the measurement technique can again be found in Section 4.1.2. The resulting emission wavelength curves for the two diode-laser arrays are shown in Fig. 4.30.

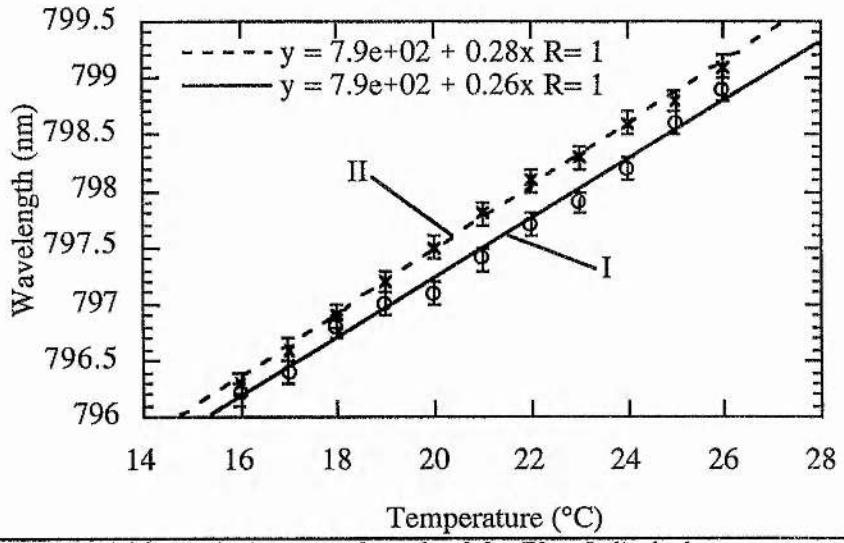

Figure 4.30: Emission wavelength of the 72 mJ-diode-laser arrays as a function of sub-mount temperatures at 14 Hz (I -Serial No. T 353 ,II - Serial No. T331).

As is to be expected, the wavelength gradient obtained from Fig. 4.30 is similar to that measured for the single diode-laser bar. However, given the additional thermal loading on the diode-laser array package it is also to be expected that the transient shift in wavelength during the current pulse will be somewhat greater. The transient response of the diode-laser arrays is measured as before and the observed spectral behaviour shown in Fig. 4.31.

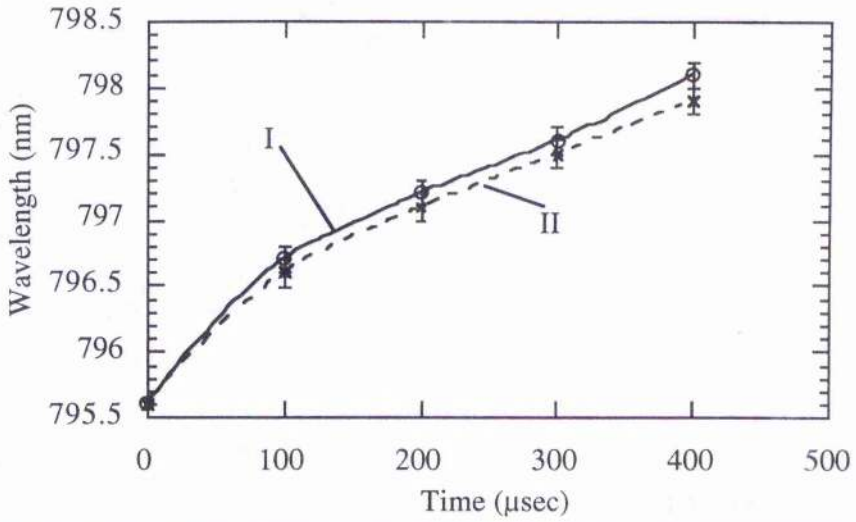

Figure 4.31: Spectral output of a 72 mJ-diode-laser array as a function of time (70 A diode-laser drive current and 15 Hz). (I -Serial No. T 353 , II - Serial No. T331).

Whereas before for the single diode-laser bar the transient change in emission wavelength over the pulse duration was 1.0 nm, this is now for the diode-laser array between 2.3 nm and 2.5 nm. This corresponds to a rise in junction temperature of between 8 °C and 10 °C over the pulse emission time. It is noteworthy that the broad absorption features found in Nd:YLF will minimise the impact of this large effective diode emission bandwidth.

4.2.3: Diode-Laser Coupling Optics Design

The diode-laser array coupling scheme is somewhat similar to that described previously in that a cylindrical lens pair is used to collimate the diode-laser output in the fast axis direction, followed in this case by a spherical lens and aspheric lens combination, used to focus the light into the Nd:YLF slabs used. The scheme is illustrated schematically in Fig. 4.32.

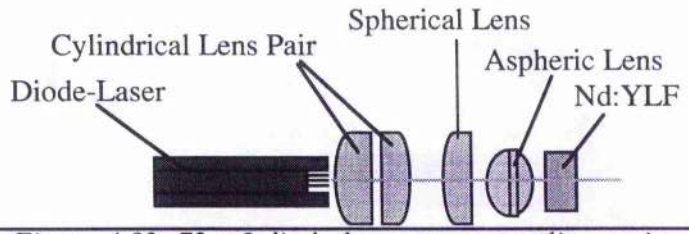

Figure 4.32: 72 mJ-diode-laser array coupling optics.

The particular lenses used are summarised in Table 4.8, again all of which are antireflection coated at 800 nm.

Lens Type	f (mm) @ 800 nm	Dimension (mm)	Material	Supplier Part no.
Cylindrical	12.7	12.7x25.4 $t_c = 7.9$	BK7	Newport CKX012
Cylindrical	19.0	12.7x25.4 $t_c = 5.33$	BK7	Newport CKX019
Spherical	31.7	Ø25.4 $t_c = 7.9$	BK7	Melles Griot 01LPX055
Aspheric	12.0	Ø17.0 $t_c = 8.0$	Crown Glass	Melles Griot 01 LAG 002

Table 4.8: Coupling optic lens description.

Propagation of the diode-laser pump beam through the coupling optics described above is illustrated in Fig. 4.33. In the upper trace an on-axis element is propagated, while the middle trace illustrates the effect of moving to the edge of a diode-laser bar, and is similar to the effect demonstrated in Fig. 4.7 for the rod lens coupling optic scheme. The lower trace illustrates the effect of moving from the central bar in the 3-bar stack to either of the outer bars, introducing an effective 400 μm displacement in the source relative to the coupling optic axis in a plane perpendicular to the diode-laser bars. As one would expect a clear displacement of the focal point in the fast-axis plane is observed at the Nd:YLF surface (9). In combining these effects it is expected that in practice the light from the three diode-laser bars in each array when imaged in the Nd:YLF slab will result in the formation of three discrete stripes of gain. This expectation will be seen to be borne out in the description of the laser resonator and pumped volume in the next section. The coupling optic transmission is measured to be 87%.

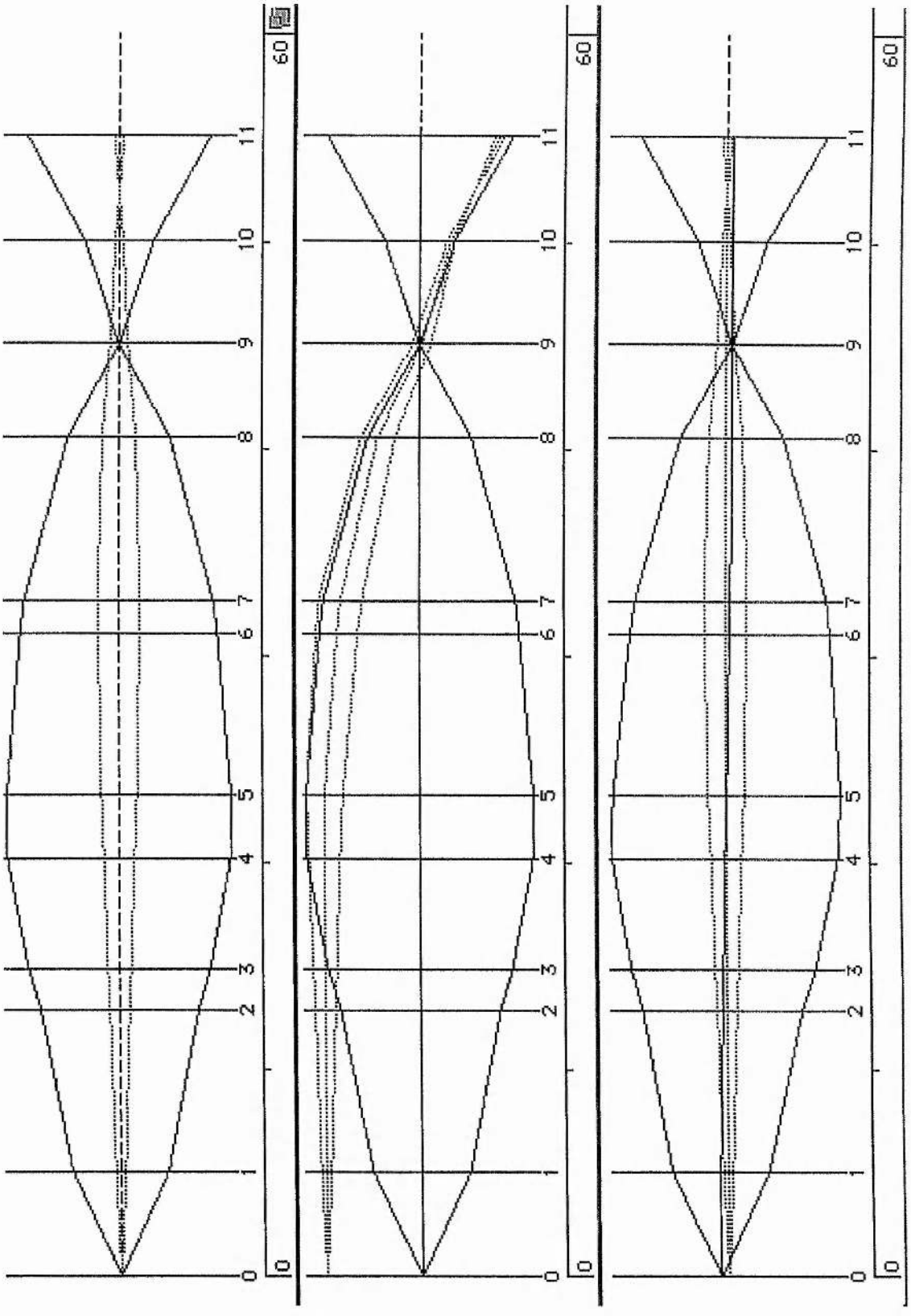

Figure 4.33: Diode-laser beam propagation ; Surface 0 - Diode facet, Surface 1/2 - Cylindrical lens, Surface 3/4 - Cylindrical lens, Surface 5/6 - Spherical lens, Surface 7/8 - Aspheric lens, Surface 9/10 - Nd:YLF Slab (Solid line - Diode-laser fast axis, Dotted line - Diode-laser slow axis).

4.2.4: Laser Resonator Design

The Nd:YLF crystals are cut in a b-axis orientation, so that the resonated wave may be made parallel to the crystallographic c-axis and 1.047 μm operation obtained. Also, in this orientation the pump light will be predominantly polarised along the c-axis, so optimising the pump light absorption coefficient. The YLF host is doped at a level of 1 % Nd by atomic weight and has dimensions 3 mm x 8 mm aperture and 4 mm length.

Observed fluorescence profiles of the pumped Nd:YLF slabs show a high degree of structure, attributable to the 3 diode-laser bars incorporated in each diode-laser array, as shown by the false colour fluorescence intensity image in Fig. 4.34 where the 3 mm slab width is defined by the vertical yellow/green features. Such structure being undesirable in generating high spatial quality laser modes, an effectively smoothly varying gain profile has been established by locating a pump module incorporating a diode-laser array, coupling optic set and Nd:YLF slab at either end of a linear resonator, where the pump modules are orientated orthogonal to each other through a 90 degree rotation about the resonator axis. In this way the round trip gain profile seen by the resonator mode will be near circularly symmetric. Measurements taken from the fluorescence profile shown in Fig. 4.34 indicate that the effective pumped volume cross section has dimension of 0.9 mm radius ($1/e^2$).

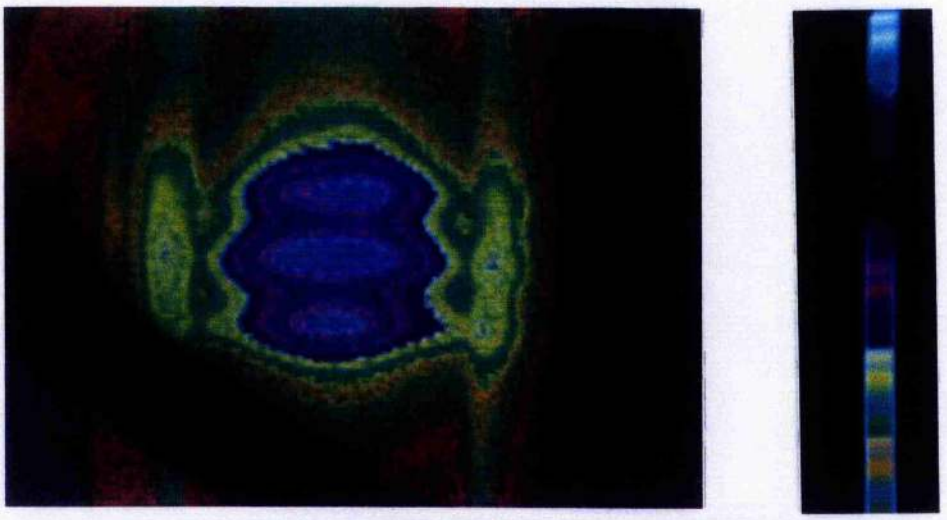

Figure 4.34: Fluorescence profile of the 72 mJ-diode-laser array pumped end-pumped Nd:YLF slab looking along the resonator axis.

A schematic of the complete laser resonator for long-pulse operation is shown in Fig. 4.35.

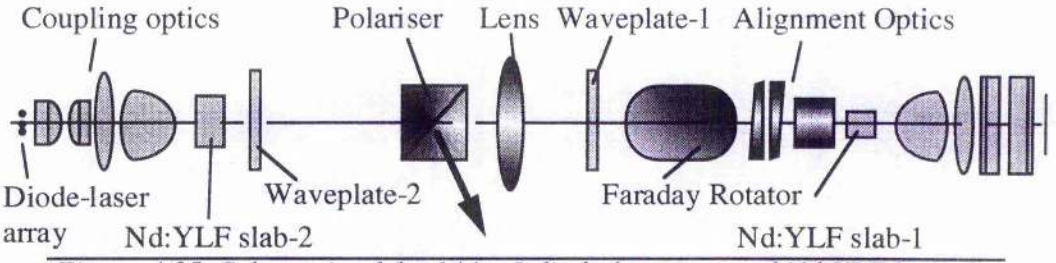

Figure 4.35: Schematic of the 144 mJ-diode-laser pumped Nd:YLF laser for long-pulse operation.

The resonator is formed by two plane high reflectors, the mirror coatings being evaporated directly onto the external surfaces of the Nd:YLF slabs, and which are also highly transmissive to the pump radiation at 0.797 μm. A 20 m focal length lens is placed central to the resonator to move the g_1g_2 product slightly away from a position of cavity instability, but continue to form a large size TEM_{00} mode which fills the relatively large pumped cross section.

Output coupling from the resonator is via the intra-cavity polariser, in combination with waveplate-1 and preferably a Faraday rotator. This set-up allows flexibility in the level of output coupling while at the same time maintaining an optimised polarisation state in the Nd:YLF slabs. After transmission by the polariser, the polarisation state of the right travelling wave experiences some degree of rotation by the λ/2 waveplate-1 and is then counter-rotated by the Faraday rotator to the same amount (the amount of rotation in the Faraday rotator is made to balance that of the waveplate by altering the position of the terbium gallium garnet (TGG) crystal relative to the magnetic field). In so doing the polarisation state of the wave remains parallel to the c-axis of the Nd:YLF slab-1 and consequently optimises the available gain. On reflection the left travelling wave then sees an additive rotation by the Faraday rotator and waveplate-1, resulting in some net rotation and a rejected component at the polariser, this forming the useful resonator output. Waveplate-2, also λ/2, is used to rotate the plane of polarisation of the left travelling wave by 90° in order that it be made parallel to the c-axis of the Nd:YLF slab-2, which as previously noted is orthogonal to

slab-1. After reflection the plane of polarisation is of course rotated through 90° by waveplate-2 once again for transmission back through the polariser.

As the resonator mirror coatings are applied directly to the Nd:YLF slabs, and the alignment of the slabs to the pump coupling optics should preferably remain fixed, it is undesirable in this case to align the resonator mirrors by tilting the Nd:YLF slabs. Additionally included in the resonator therefore are an optical wedge pair and optical micrometer. By using a wedge pair, the beam pointing direction can be steered in any direction within a cone angle derived from the wedge angle. Simple geometry shows that in the geometry used here where one surface of each wedge is normal to the resonator axis, the cone angle is just the wedge angle which in this case is 1°. Using initially an alignment laser it is straightforward to align the Nd:YLF slabs parallel to one another to within this tolerance. Any lateral displacement between the pumped regions of the Nd:YLF slabs at either end of the resonator can be accommodated for by the optical micrometer. This is a simple plane-parallel block of glass which may be tilted about orthogonal axes normal to the resonator axis and so introduce a beam displacement.

The mode size has been evaluated at various points within the resonator using an ABCD analysis. The resulting mode size at a number of relevant points is tabulated in Table 4.9.

Position (surface no.)	Size ($1/e^2$, mm)
Plane mirror (1)	0.888
Polariser (5)	0.889
Lens (8)	0.890
Plane mirror (14)	0.888

Table 4.9: 144 mJ-diode-laser pumped resonator mode sizes ($1/e^2$ radius, long pulse).

It is immediately evident that the resonator mode varies very little in size throughout the length of the resonator, but is well defined by the intra-cavity lens and of a size comparable to that of the pumped volume cross section.

4.2.5: Long Pulse Operation

With then the laser set-up as described above, it is first characterised in a long-pulse mode of operation.

Long-Pulse Energy

Having maximised the pulse energy at the maximum diode-laser drive current, the useful output energy is measured as a function of the pump energy as shown in Fig. 4.36.

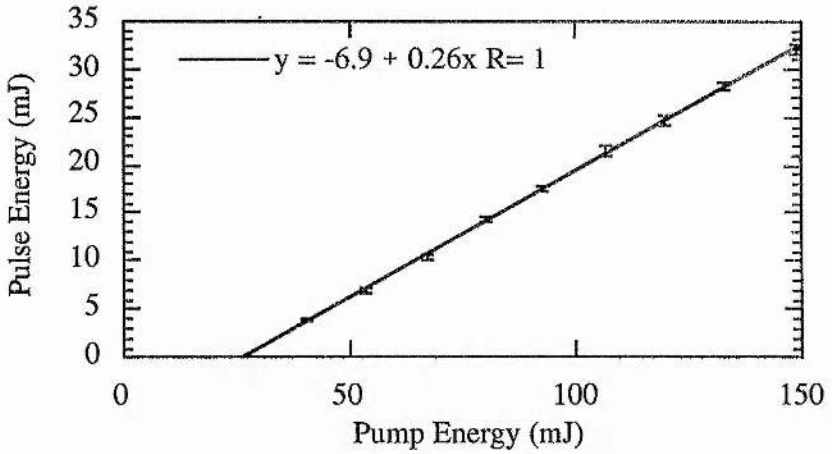

Figure 4.36: Nd:YLF laser output as a function of diode-laser pump energy - long pulse, 1.047 μm.

From Fig. 4.36, it is seen that the peak optical-optical conversion efficiency obtained is 21.6% and the slope efficiency is 26%. Taking into account the pump loss through the coupling optics (13%), the conversion efficiency is increased to 24.8% and the slope efficiency to 30.0%.

Spatial Quality

The transverse mode of the laser is TEM_{00} at all operating powers. Beam profiles and a quantitative description of the spatial quality is given in the ensuing section when considering Q-switched operation.

4.2.6: Q-Switched Operation

A schematic of the Q-switched laser resonator is shown in Fig. 4.37.

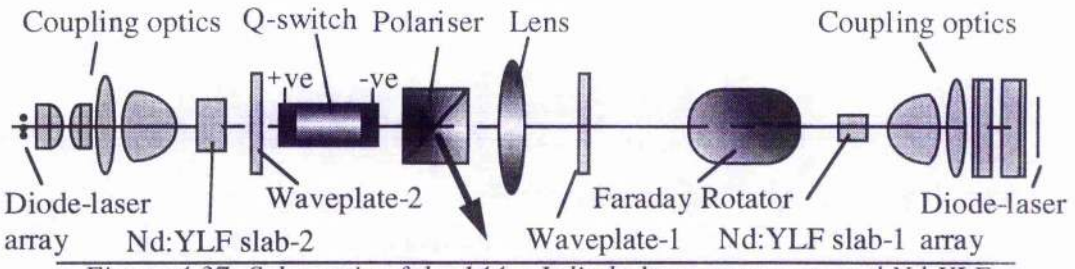

Figure 4.37: Schematic of the 144 mJ-diode-laser array pumped Nd:YLF laser for Q-switched operation.

Q-switch Description

If an output pulse energy of 75% of the long pulse energy is for the time being assumed, along with an output coupling of 30%T and intra-cavity mode size of 0.9 mm ($1/e^2$ radius), then the peak circulating intensity can be calculated from equ. (2.44) when assuming a Gaussian spatial profile to be 7 $J.cm^{-2}$. This is in excess of the material damage threshold of $LiNbO_3$ and consequently the Q-switch or Pockels cell used in the case of this higher power laser is based on the material Potassium Di-Hydrogen Phosphate (KD*P).

The KD*P Pockels cell operates in the same way as described previously for $LiNbO_3$, see Section 4.1.6, except that it is a longitudinal E-O modulator, that is the applied electric field is along the length of the crystal parallel to the resonator axis. The phase difference δ induced between the polarisation components of the wave resolved along the electro-optically induced x' and y' axes is then in this case given by

$$\delta = \frac{2\pi}{\lambda} n_0^3 r_{63} V_z , \qquad (4.7)$$

where r_{63} is the relevant electro-optic coefficient for KD*P. Note that this expression is now independent of both the crystal aperture and the crystal length. As the refractive index difference (Δn) between x' and y' is dependent on a longitudinal field E_z, i.e. $\Delta n = n^3 r_{63} E_z$ where $E_z = V_z/l$, then δ which is given by Δnl becomes length independent.

For then KD*P, where the electro-optic coefficient r_{63} = 26.4 $pm.V^{-1}$ and the ordinary refractive index n_0 = 1.47 [6], the required dc. voltage for quarter wave

retardation at 1.047 μm is ~ 3.1 kV. One disadvantage in the use of KD*P compared to $LiNbO_3$ is then the higher fields required for equivalent retardation. Additionally, KD*P cannot be readily AR coated, requiring then the use of an index matching cell to minimise the Fresnel loss from the crystal surfaces. Nonetheless, it is the preferred option in this case.

The Q-switch driver used for the KD*P Pockels cell is based on the transistor avalanche circuit shown in Fig. 4.19, with the addition of further transistor stages to accommodate the higher switching voltage.

Q-switched Pulse Energy

With the Pockels cell installed in the laser resonator the Q-switched laser pulse energy as a function of diode-laser pulse energy can now be ascertained. Results are shown in Fig. 4.38.

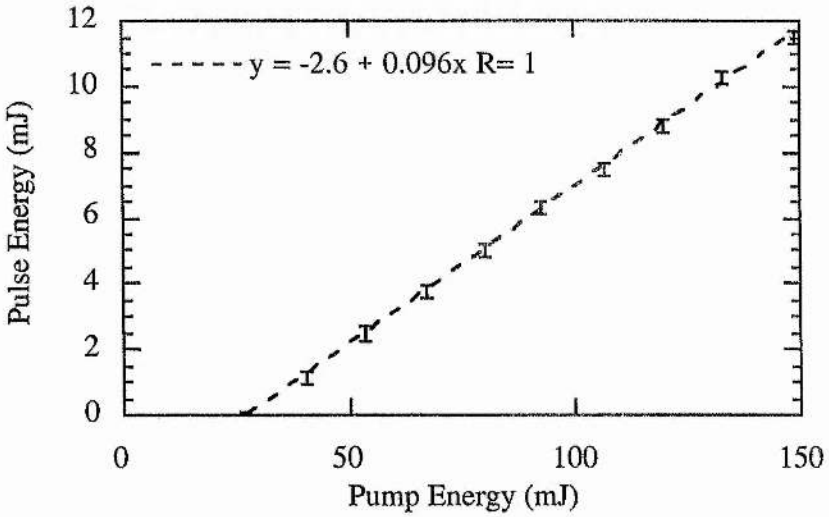

Figure 4.38: Nd:YLF laser output as a function of diode-laser pump energy - Q-switched 1.047 μm.

It is immediately evident that the pulse energy has been significantly reduced from the long pulse case (31 mJ), the maximum pulse energy now being measured to be 11.5 mJ. The cause of this is a high insertion loss related to the KD*P Q-switch crystal which reduces the long pulse energy with the crystal inserted to 14.1 mJ. The Q-switched pulse energy is therefore in fact 82% of the relevant long pulse energy.

Spatial Quality

The near- and far-field energy distributions for the Q-switched laser are shown in Fig's. 4.39 and 4.40 respectively. The beam is near circularly symmetric in the near field with an aspect ratio of <1.1:1, has a radius (20 cm from the output coupling polariser) of 0.8 mm ($1/e^2$) and is circularly symmetric in the far field. As shown by the curve fits, the beam is near Gaussian in profile in both the near- and far-field, the far-field distribution being obtained by looking in the focal plane of a 1 m focal length lens.

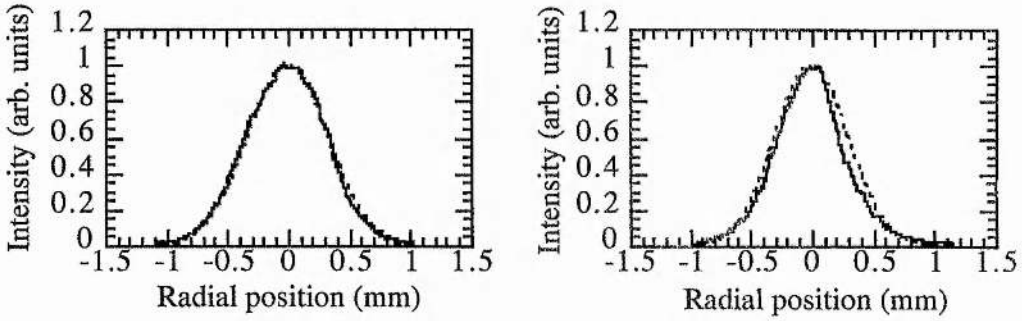

Figure 4.39: Near-field energy distribution in orthogonal planes (solid line - experimental, dashed line - Gaussian fit).

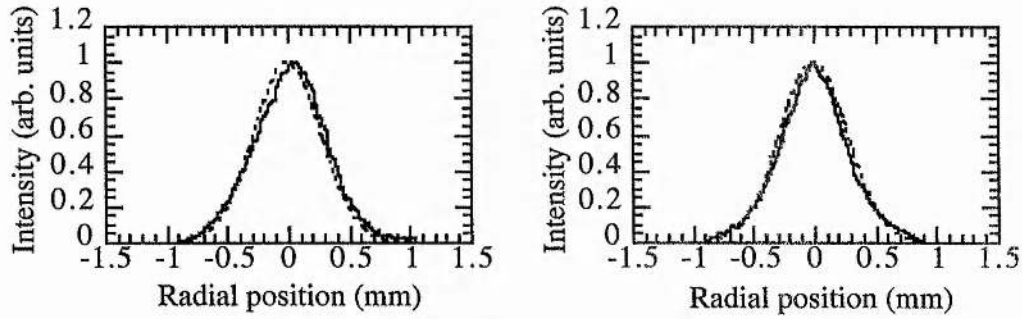

Figure 4.40: Far-field energy distribution in orthogonal planes (solid line - experimental, dashed line - Gaussian fit).

The M^2 factor for the beam has been measured to be <1.1.

Temporal Profile

The temporal output of the laser was found to consist of a single Q-switched pulse, as shown in Fig. 4.41. Mode beating effects are at times discernible, the beat period having been measured to be 2.3 nsec, corresponding to a frequency of 435 MHz and an optical resonator length of 34.5 cm.

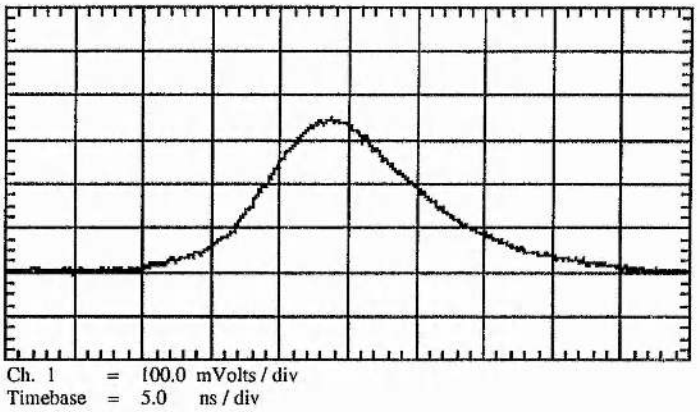

Figure 4.41: Temporal profile of the 144 mJ-diode-laser pumped Nd:YLF laser (45 A diode drive current).

The pulse duration is of course dependent on the pump level, and found to decrease from 17 nsec near to threshold to around 11 nsec at the maximum pump level, as shown in Fig. 4.42. Corresponding peak powers over the pump energy range are also shown on the second y-ordinate.

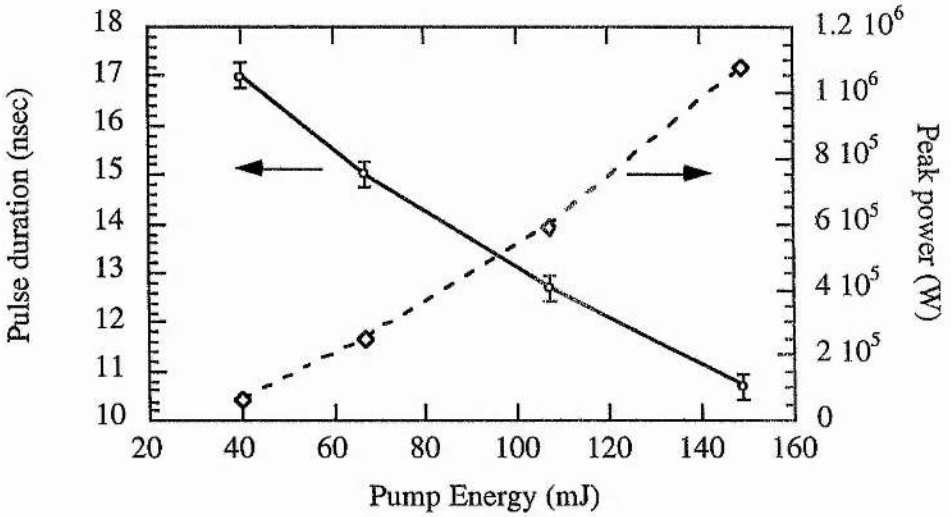

Figure 4.42: Pulse duration and peak power as a function of pump level for the 144-mJ-diode-laser pumped Nd:YLF laser.

A photograph of the complete laser is shown in Fig. 4.43, which also includes frequency up-conversion and an LBO optical parametric oscillator described later in Chapter 7.

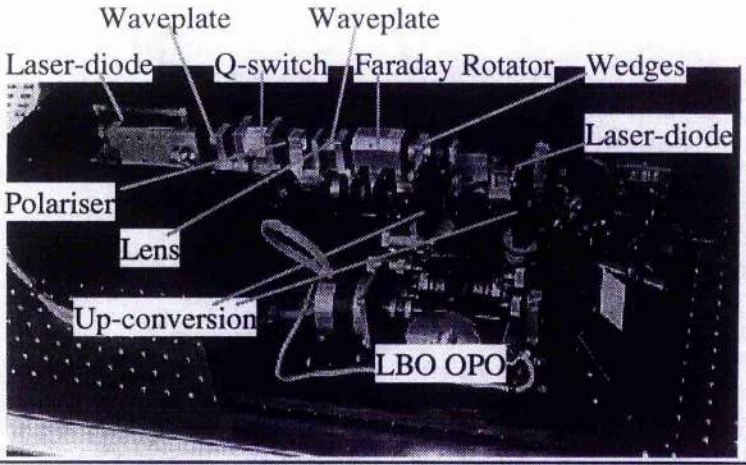

Figure 4.43: Photograph of the 144 mJ-diode-laser pumped Nd:YLF laser and frequency conversion addition.

Chapter 4 References:

1. C. J. Norrie, B. D. Sinclair, N. Gallaher, W. Sibbett and M. H. Dunn *"Measurement of frequency sweep in a quasi-CW diode-laser array, and its implication for pumping solid-state lasers"* J. of Modern Optics 36 (1) pp.1-6, 1989.

2. D. C. Shannon and R. W. Wallace *"High-power Nd:YAG laser end-pumped by a CW, 10 mm x 1 μm aperture, 10-W laser-diode bar"* Opt. Lett 16 (5) pp.318-320, 1991.

3. J. A. C. Terry *"An all-solid-state optical parametric oscillator for the infrared"* Ph.D. Thesis (Univ. of St Andrews, Scotland, UK), 1995.

4. H. Kogelnik and T. Li *"Laser beams and resonators"* Appl. Opt. 5 (10) pp.1550-1567, 1966.

5. A. S. Bebchuk, L. A. Kulevskiy, V. V. Smirnov and Yu. N. Solov'yeva *"Q-modulation of a ruby laser with a $LiNbO_3$ shutter"* Radio Eng. and Elect. Physics 14 (6) pp.919-921, 1969.

6. Casix Optronics Inc. *"Crystal Guide 1996"* (Casix Optronics Inc, Fuzhou, P.R. China), 1996.

7. P. Basséras, R. J. Dwayne Miller and S. M. Gracewski *"Theoretical analysis of acoustic transients in lithium niobate electr-optic modulators"* J. Appl. Phys. 69 (11) pp.7774-7781, 1991.

8. H. Veeser, U. Bogner and W. Eisenmenger *"Analysis of the acoustic transients in the pulse response of the linear electro-optic effect"* Phys. Stat. Sol. 37 pp.161-170, 1976.

9. H. Zbinden and J. E. Balmer *"Q-switched Nd:YLF laser end pumped by a diode-laser bar"* Opt. Lett. 15 (18) pp.1014-1016, 1990.

10. R. D. Mead, S. C. Tidwell, K. W. Kangas, A. J. W. Brown and D. D. Lowenthal *"Diode-end-pumped, Q-switched Nd:YLF laser"* Digest of Conference on Advanced Solid-State Lasers, Paper WA3, 1992.

Chapter 5
Single Frequency Operation of the 12 mJ-Diode-Laser Pumped Nd:YLF Laser

In Chapter 4 the development of two diode-laser pumped Nd:YLF lasers was described, where both have a high degree of spatial coherence, operating on a TEM_{00} mode, however, there being no restriction placed on their longitudinal mode of operation. It is of interest now to go on and develop these devices further to the point of obtaining single-frequency operation (single transverse and single longitudinal mode).

5.1: Implementation of a Pre-lase Q-switching Technique

As will be demonstrated in Section 5.2, the implementation of pre-lase Q-switching alone is sufficient to obtain SLM operation of the 12 mJ-diode-laser pumped laser described in Chapter 4 for most of the time, however, periods of operation exist during which 2 adjacent longitudinal modes of the laser resonator are observed to be present. The origin of this 2 mode operation lies in an uncontrolled drift in resonator length and hence mode frequencies, due to thermal fluctuations in the ambient surroundings. This leads to a condition where 2 modes are symmetric under the gain profile when insufficient mode discrimination exists to select only one mode. While thermal control of the surroundings and/or decreased sensitivity to any thermal fluctuations, for example through the choice of materials used, can be considered in circumventing this problem, these techniques are non-trivial and costly. A technique is therefore demonstrated here which relies on optoelectronic detection methods to monitor the mode position, via the detection of mode beating on a single pre-lase pulse, and then when necessary adjust the resonator length to disrupt the symmetric condition. Such techniques have been suggested before [1, 2], however, in these cases operation

relied upon passive resonator length changes due to pumping of the gain material. This consequently led to large pulse timing jitters (< 30 μsec); the length of time required to move away from the symmetric condition depending on how near to a position of exact symmetry the resonator is at the start of the train of pre-lase pulses generated and the thermal time constant associated with the gain medium.

5.1.1: Opto-Electronic Description

The frequency selectivity of the laser resonator is depicted schematically in Fig. 5.1, where frequency space is denoted on the x-ordinate and the net gain is denoted on the y-ordinate. As shown in Fig. 5.1a, the resonator modes (n-1, n and n+1) are separated by some frequency (c/2L), where L is the optical length of the resonator, and in the ideal case one mode is located in the centre of the gain profile so giving maximum mode discrimination. In Fig. 5.1b, the resonator length has changed and two modes now lie symmetric under the gain profile, resulting in two mode operation of the laser. As depicted in Fig. 5.1c, two mode operation is observed over some range of frequencies $\delta\upsilon$ about the symmetric condition. That is when υ_{lc} is the frequency at line centre, the frequency of the n^{th} mode is given by

$$\upsilon_n = \upsilon_{lc} \pm \frac{c}{4L} \pm \frac{\delta\upsilon}{2} . \qquad (5.1)$$

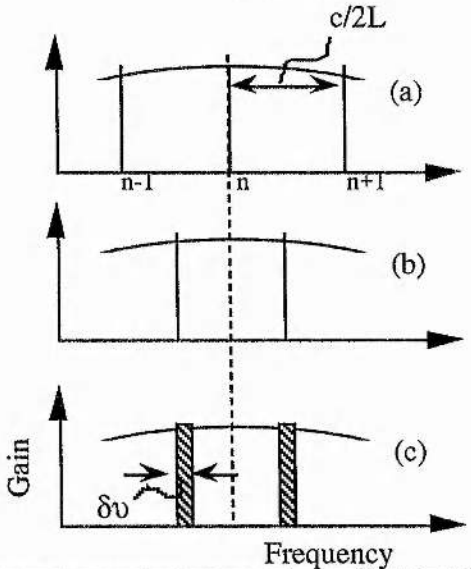

Figure 5.1: Resonator frequency selectivity; (a) An optimum condition where a resonator mode lies central in the gain profile, (b) A worst case condition with 2 modes symmetric, (c) A range over which 2 mode operation is observed.

If the range $\delta\upsilon$ over which mode beating is observed is sufficiently narrow, it should then be possible to adjust the resonator length and consequently the mode positions away from this operating point, to a point at which SLM operation will be observed. To do so a technique has been developed which, using a pre-lase Q-switch, allows the formation of a train of at least two pre-lase pulses at the end of the diode-laser pump pulse. The first of these pulses is interrogated for the presence of mode beating and if detected the resonator length is adjusted before the appearance of the second oscillation. On detection of the second oscillation the Q-switch is triggered and the Q-switch pulse builds up from what is now always an SLM low level pulse.

As the time taken for the resonator length to be altered must be less than the inter-pulse spacing of the relaxation oscillations, and will be seen in Section 5.2 to have to be less than 10 μsec, a method of length control must be used which has a modulation rate of > 100 kHz. A novel approach has been adopted here, in the use of an identical lithium niobate based Pockels cell to that used in the Q-switch, but orientated differently. By rotating the Pockels cell through 45° about the resonator axis and then applying a voltage to it, the linearly polarised intra-cavity mode, which is polarised along one of the electro-optically induced birefringence axes, will see only a voltage dependent phase delay and zero birefringence, as depicted in Fig. 5.2. In this way the effective optical length of the resonator is changed through a refractive index variation rather than the more usual means of a physical displacement of a mirror.

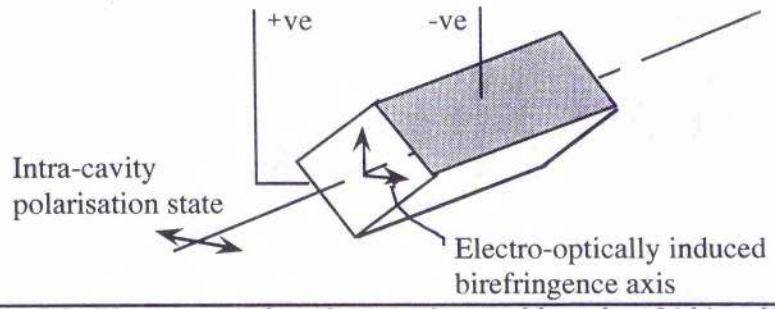

Figure 5.2: Electro-optic length control crystal based on Lithium Niobate.

In Fig. 5.1, it is evident that if mode beating is detected then a change in resonator length, which provides a change in mode frequency of c/4L, will place a longitudinal mode of the resonator near to line centre. This is equivalent to adding or removing a

quarter-wavelength to or from the resonator length, which in this case requires the introduction of a phase-change of $\pi/2$ radians along the length of the crystal.

The voltage dependent phase-delay introduced between the orthogonally polarised components, resolved along the electro-optically induced birefringence axes, in the case of using lithium niobate as a Q-switch element was described in Section 4.1.6. In such a geometry, it is the relative phasing between the resolved components that is of interest, as essentially one resolved component is advanced while the other is retarded by the initially circular index ellipsoid being made elliptical, one axis being stretched while the other is squeezed. In the geometry described here for an electro-optical resonator length control element the polarisation of the intra-cavity mode is wholly along one electro-optically induced birefringence axis and it is the absolute phase-change imparted on this one component alone which is of interest. Consequently, the phase-change induced is now described by;

$$\delta = \left(\frac{2\pi}{\lambda}\right)\frac{n_0^3 r_{22} V_x l}{2d} . \qquad (5.2)$$

For then an induced phase-change of $\pi/2$ radians, a voltage of 2.6 kV must be applied to a crystal of dimension 9 mm aperture (d) and 25 mm length (l).

The incorporation of this type of length control element with its associated electronics is shown in block form in Fig. 5.3 and described briefly here. A more detailed description of each of the elements follows in the ensuing sections, the electronic development of which was carried out with the kind assistance of Dr. W. Sleat.

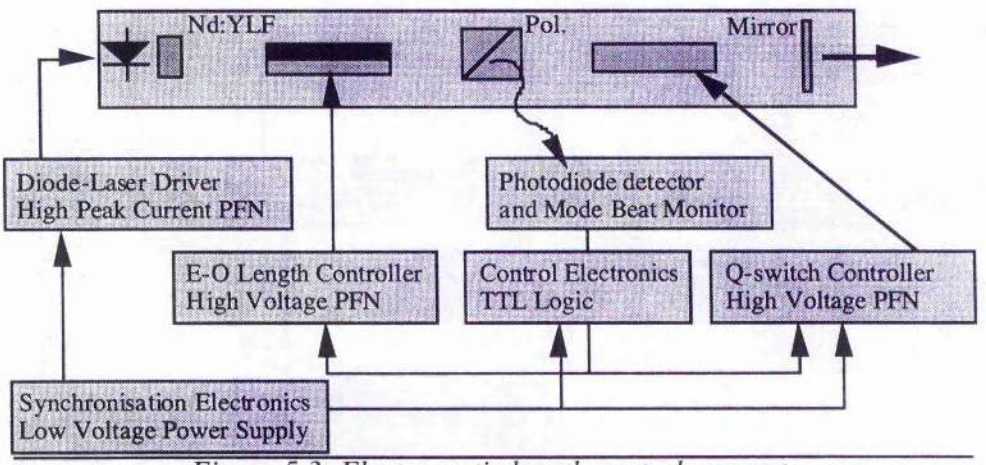

Figure 5.3: Electro-optic length control concept.

The resonator Q-factor, shown in Fig. 5.4b, is set at such a level that toward the end of the diode-laser pump pulse, shown in Fig. 5.4a, a train of low level pre-lase pulses are allowed to form, as illustrated in Fig. 5.4c. The first of these oscillations is monitored, via leakage from the intra-cavity polariser, by a fast photodiode which is connected in turn to a tuned stripline filter. The Q-factor of the filter is maximised for the mode beat frequency and provides a synchronous rf signal with any mode beating detected. The rf signal is then fed into a cascaded series of counter IC's, so that if sufficient beating is detected the logic state of the output of the final counter stage switches, and via the control electronics provides a trigger pulse to the EO phase modulator (EOPM) high voltage pulse forming network (HV PFN). The PFN in turn places a HV pulse on the EOPM, illustrated in Fig. 5.4d, which encompasses the second pre-lase pulse thus ensuring it to be beat-free.

Meanwhile, a dc signal is also extracted from the monitor photodiode which, via a comparator IC to reject noise, provides a synchronous TTL signal which is again counted to provide a trigger pulse for the Q-switch HV PFN, which is coincident with the peak of the second relaxation oscillation. As the resonator Q increases, a giant pulse, Fig. 5.4e, builds up from the low level SLM circulating field. It is to be noted that at the start of each diode-laser pump pulse the synchronisation electronics provide a reset signal for all counters and additionally a noise rejection signal which is removed only toward the expected time of appearance of the pre-lase pulses.

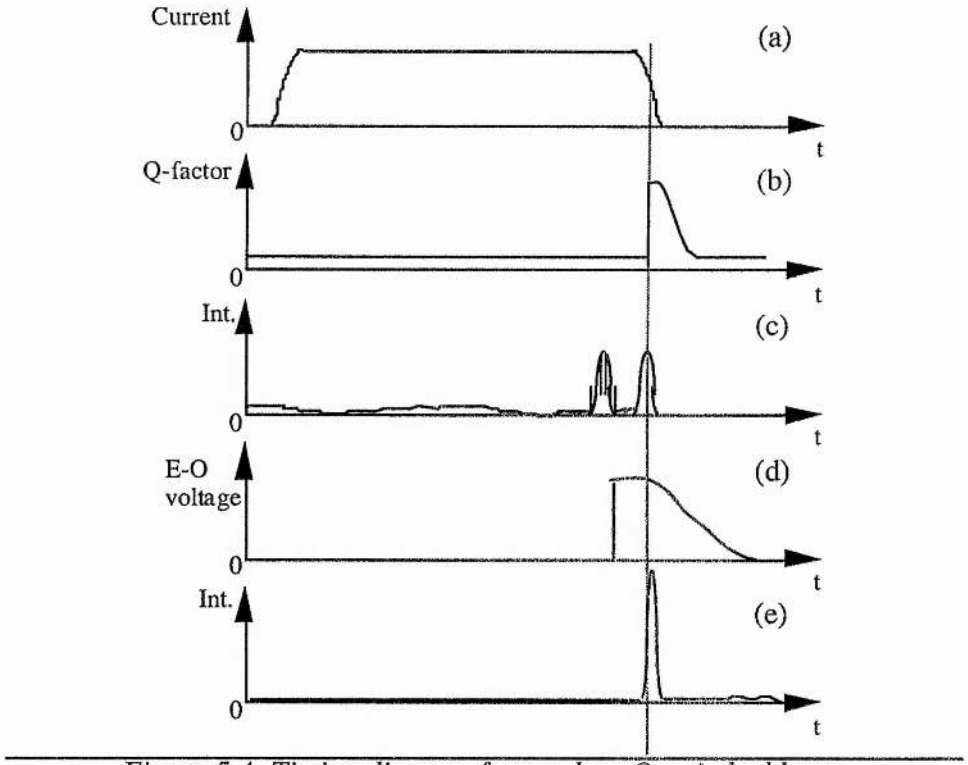

Figure 5.4: Timing diagram for pre-lase Q-switched laser.

5.1.2: Logic Board Description

Functionality of the logic control circuit is illustrated in Fig. 5.5. This logic part of the pre-lase Q-switch electronics controls the timing and form of the various trigger pulses sent to the Q-switch, and EOPM devices.

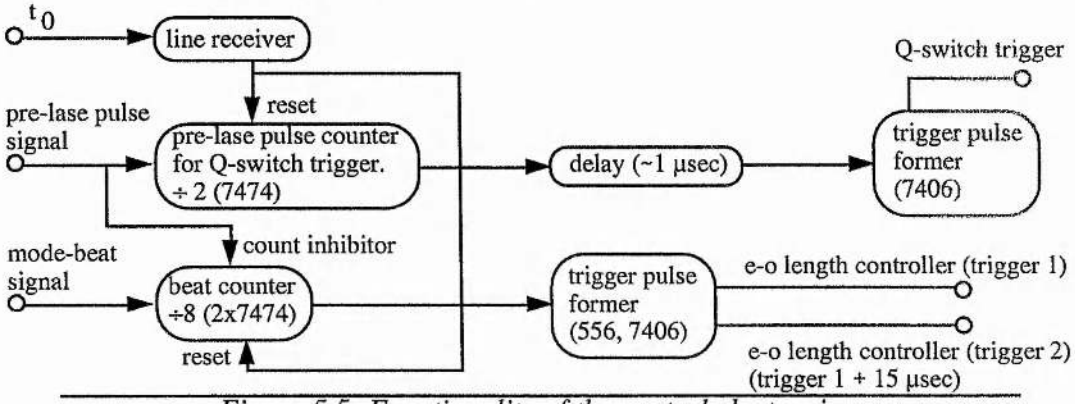

Figure 5.5: Functionality of the control electronics.

There are primarily two inputs; firstly a TTL pulse derived from the comparator IC in the mode-beat detector, which is synchronous with the pre-lase pulses, and secondly a ~20 MHz beat signal, this having been divided down on-board the mode-beat detector card from the ~400 MHz detected beat frequency. With reference to Fig's.

5.5 and. 5.6, the 20 MHz beat signal, if present, is divided down further by two of the 7474 ICs (IC1 and IC2) and if sufficient beating is present there is a change in state of the output of IC2. This in turn leads to a trigger pulse being generated by the 7406 IC (IC3) and used to toggle the EOPM. A second trigger pulse to the EOPM is generated 15 μsec later, by the 556 and 7406 ICs (IC4 and IC3), to reset the EOPM for reasons which are described in Section 5.2.4.

The comparator output pulse is fed into another 7474 (IC5), the output of which changes state when the second pre-lase pulse appears, generating a Q-switch trigger pulse via again the 7406 (IC3). The Q-switch trigger is delayed by IC6a,b so as to open the Q-switch at the peak of the second pre-lase pulse for optimum seeding.

Additionally, the control electronics provide noise rejection by way of the 7474 counters being inhibited, via the 7400 ICs (IC8 and IC9), except when a signal is present from the comparator IC. Also, a t_0 signal is accepted from the primary diode-laser driver trigger circuit, which is received by a line receiver (IC7), and as previously noted resets all counters. A DC-DC convertor is also included to generate the bias voltage (30 V) for the photodiode in the mode-beat detector.

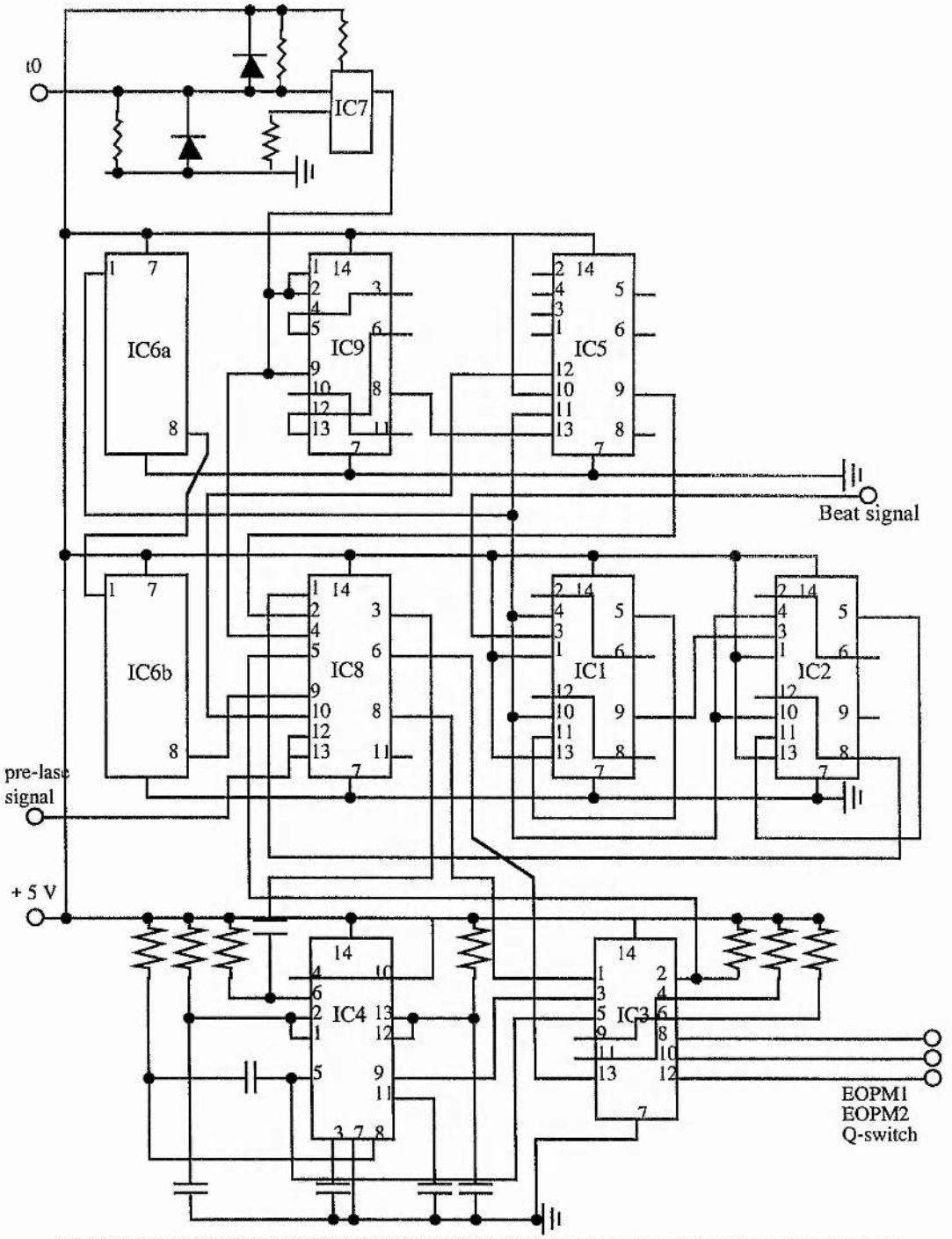

Figure 5.6: Circuit diagram - Q-switch control electronics.

5.1.3: Mode Beat Detector Design

The functionality of the mode-beat detector electronics is illustrated in Fig. 5.7.

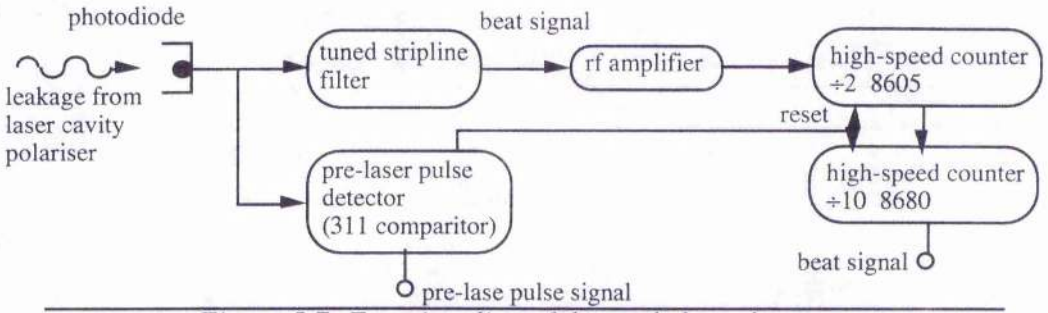

Figure 5.7: Functionality of the mode beat detector.

The design is based on a stripline filter, tuned to match the beat-note frequency (υ_b) of the laser resonator. The filter is formed by laying down, on a printed circuit board, track of appropriate dimensions to be resonant at the beat-note frequency, as illustrated in Fig. 5.8; an optimised response being obtained by including a tuning capacitor at one end of the filter, which has the effect of extending the length of the track.

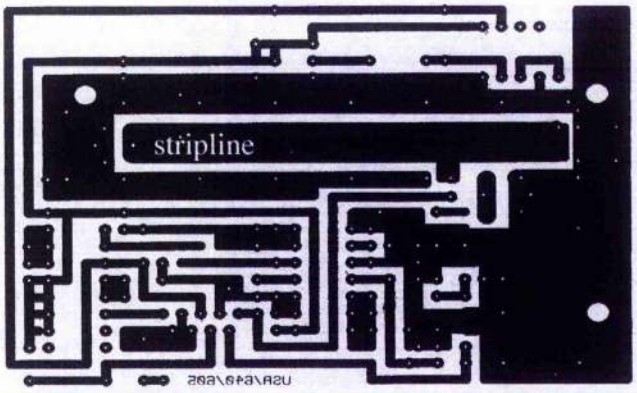

Figure 5.8: PCB board for the mode-beat detector stripline filter.

The length of stripline used is such that it is one half the wavelength of the rf signal on the board, this being determined by the dielectric constant (K) of the PCB at the beat-note frequency. The stripline length (l_{sl}) is then given by

$$l_{sl} = \frac{1}{2}\frac{c}{\sqrt{K}\upsilon_b}, \qquad (5.3)$$

which for K = 34 and υ_b = 417 MHz gives a length of 62 mm.

With reference to Fig's. 5.10 and 5.12, the optical interface to the resonator is via a reverse biased fast response photodiode (BPW28,). The filtered signal is fed into an rf amplifier (IC1) and the amplified signal then input to the cascaded divider ICs (IC2 and IC3) which divide down the rf signal by a factor of 20. It is notable that a minimum depth of modulation has to present on the pre-lase pulses before any beats are

counted, as determined by the trigger input level of the first of the dividers (IC2), which is a high-speed ecl logic device. Advantageously, the level of mode-beating which may be tolerated can then be varied optically, by attenuating the optical signal through the use of neutral density filters located between the intra-cavity polariser and photodiode.

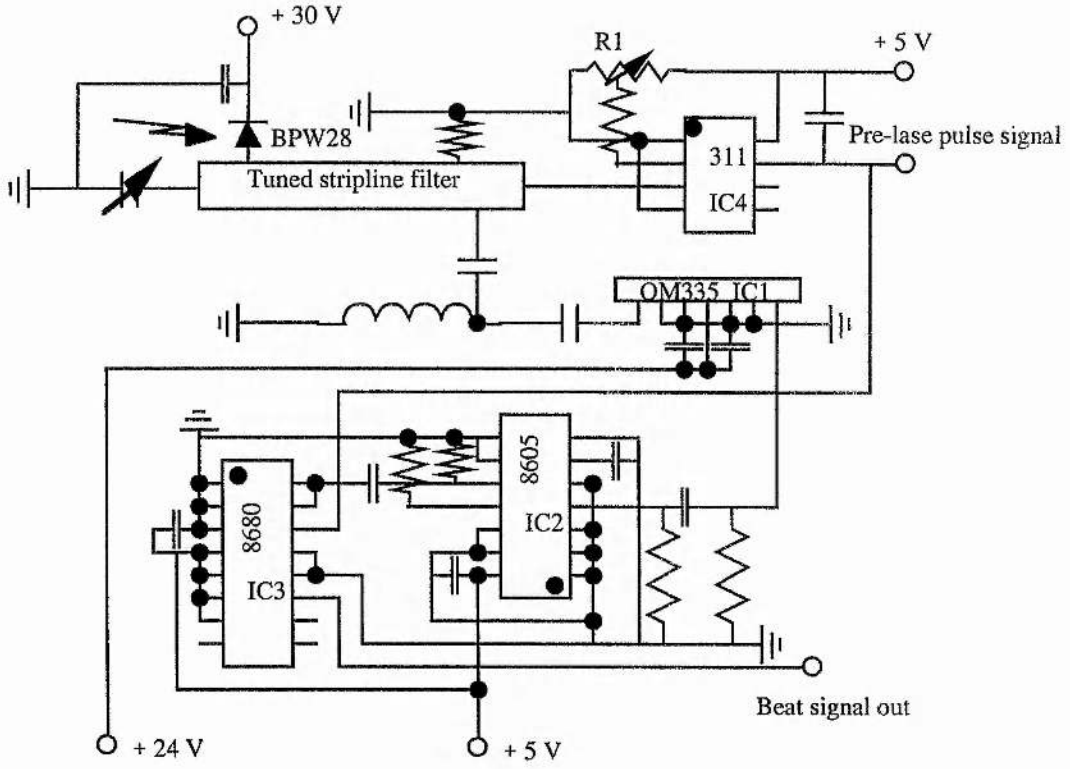

Figure 5.9: Circuit diagram - mode beat detector.

As previously noted a pseudo-dc, or pulse envelope signal, is also extracted from the photodiode, which serves to; (1) inhibit operation of the dividers in the absence of a pre-lase pulse, and (2) provide a trigger signal for the Q-switch. The synchronous TTL logic form of the pre-lase pulses is generated by the comparator IC (IC4), the detection threshold level for which is set by a variable resistor (R1).

5.1.4: High Voltage Pulse Former Design for Q-switch and EOPM

The EOPM HV PFN and Q-switch HV PFN are generically similar, both being based on a series of combined FET and capacitor stages which form a voltage adder network.

EO Phase Modulator

Functionality of the HV PFN for the EOPM is illustrated in Fig. 5.10, while the detailed circuit diagram is shown in Fig. 5.11.

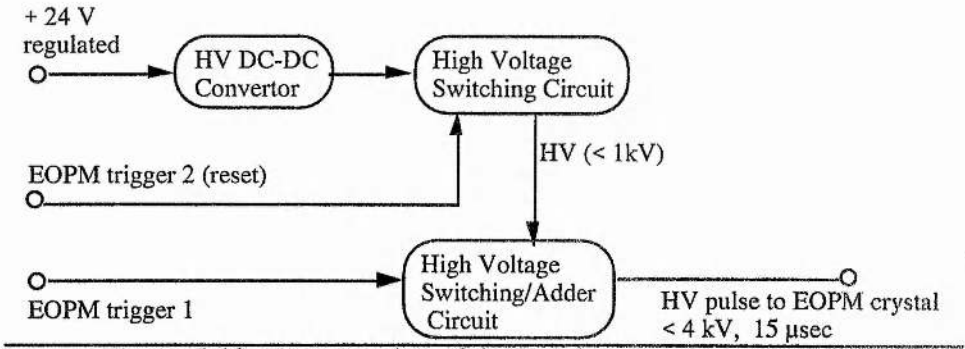

Figure 5.10: Functionality of the E-O length control HV PFN.

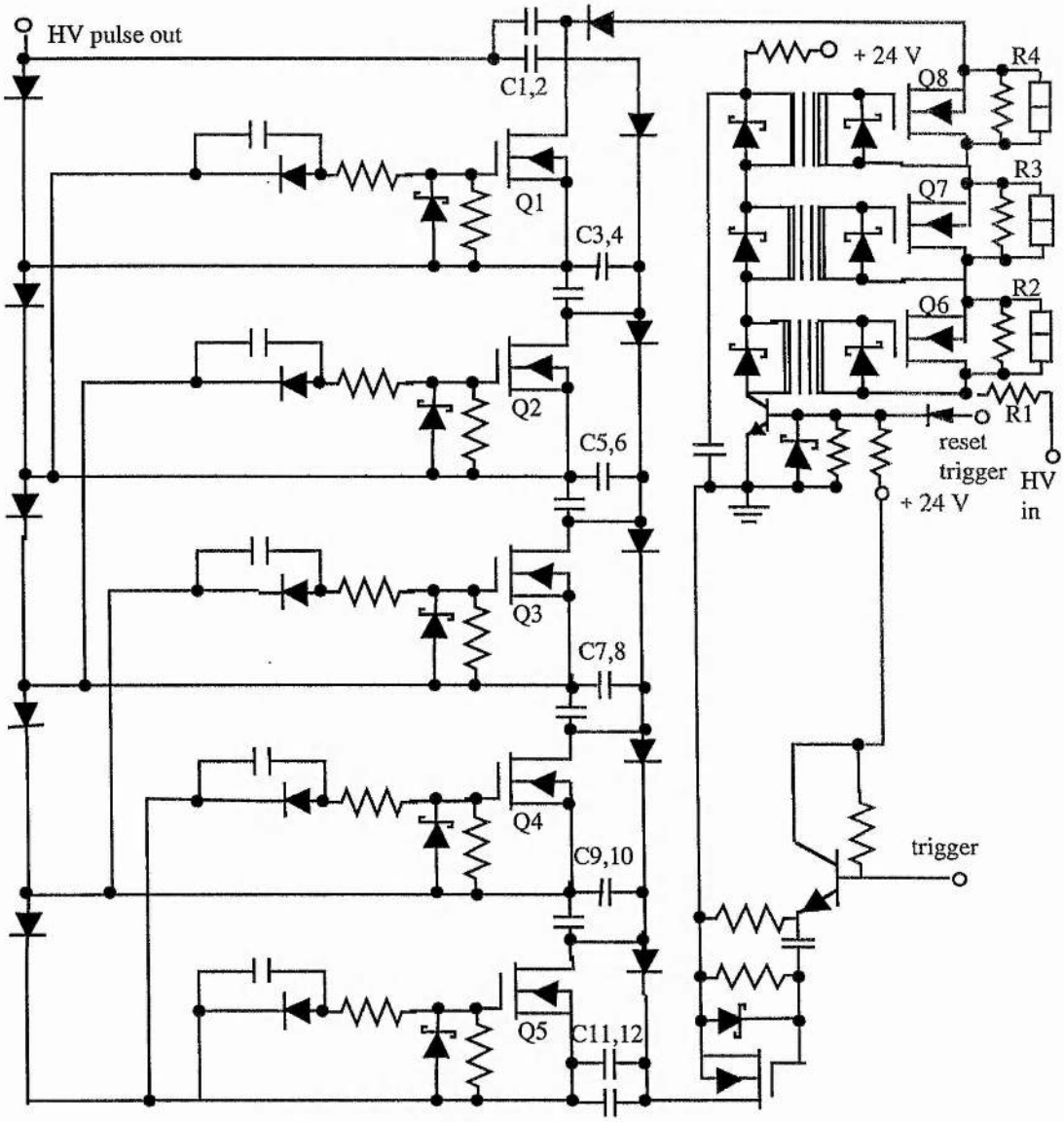

Figure 5.11: Circuit diagram - E-O length control HV PFN.

With reference to Fig. 5.11, a number of capacitors (C1 - C12) are charged in parallel and then, via triggering of the FETs (Q1 - Q5), are rapidly reconfigured in series, this resulting in the formation of a voltage pulse which increases by the charge voltage of the capacitors at each stage in the adder network. This is well illustrated by the represention of the voltage adder network,as shown in Fig. 5.15, where the FETs are depicted by the open switches. In practice the circuit is not 100% efficient and the voltage pulse generated is around 85% of that obtained by taking the product of the charge voltage and number of adder stages.

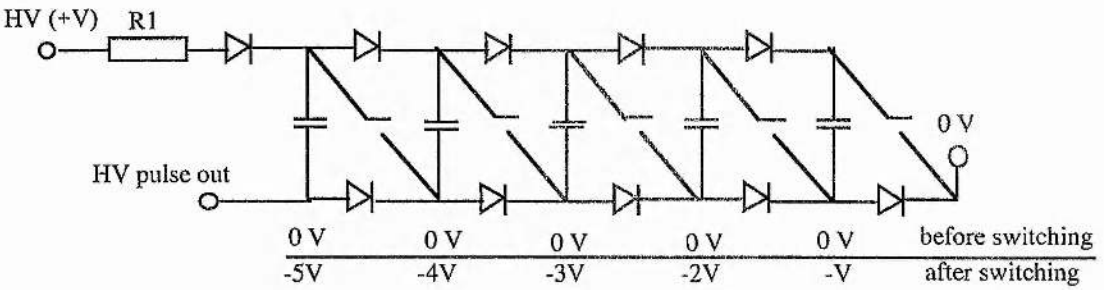

Figure 5.12: Voltage adder network.

It is desirable that the voltage applied to the crystal is constant during the build up and emission of the laser pulse, and so the voltage pulse must be maintained for a relatively long period of time (> 15 μsec). This is achieved by making the resistance through which the capacitors are charged (R1 in Fig. 5.12, R1- R4 in Fig. 5.11) particularly large (4 MΩ). A consequence of this, however, is that the EOPM Pockels cell takes several seconds to fully recover to a passive state. To reset the Pockels cell more quickly, after a time determined by the laser pulse having been emitted (20 μsec), the high value charging resistors are effectively shorted by a second FET chain (Q6 - Q8), so allowing the charge voltage on the capacitors to be rapidly re-established.

Q-switch

The Q-switch PFN is identical in operation to the core of the EOPM PFN, however, uses one less stage in the voltage adder network, as the required switching voltages are lower. Further, a secondary FET stack is not required as the series charging resistor need not be made large. The circuit diagram for the Q-switch PFN is shown in Fig. 5.13.

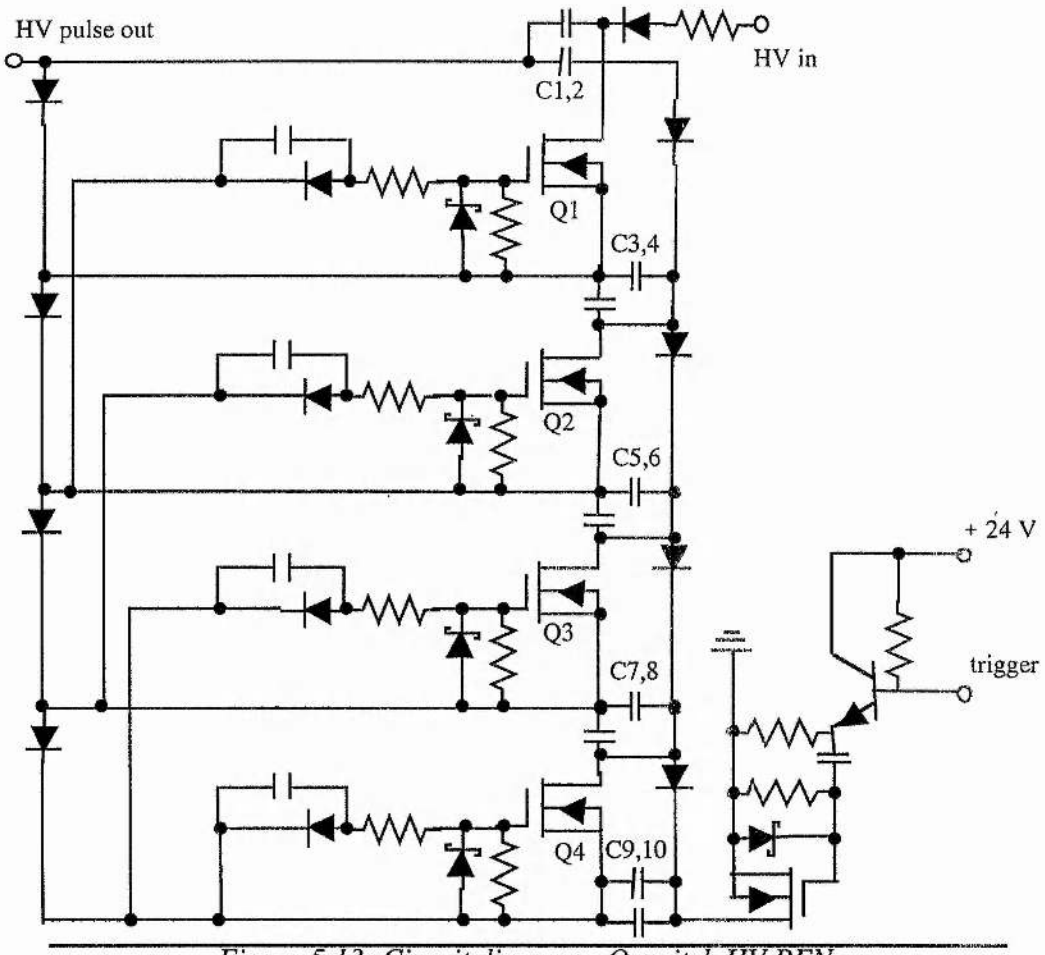

Figure 5.13: Circuit diagram - Q-switch HV PFN.

Additionally, the Q-switch electronics include a HV dc supply to provide a reverse bias voltage to the Q-switch Pockels cell, used to increase the Q-factor of the resonator during the pump pulse to allow pre-lasing.

5.2: Single Longitudinal Mode Results

5.2.1: Experimental Set-up

The laser resonator design for single longitudinal mode operation is identical to that described in Section 4.1.6, for normal Q-switched operation, except that a second Pockels cell for EOPM is inserted between the intra-cavity telescope and Nd:YLF gain element, as shown in Fig. 5.14, and additionally the resonator length has been shortened, so that the optical length of the resonator is the same as before, giving similar mode spacing.

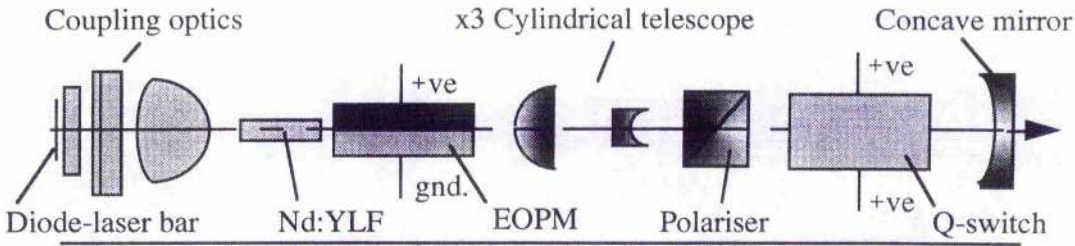

Figure 5.14: Schematic of the slow-Q-switched Nd:YLF laser resonator.

To obtain pre-lase pulses the Q-factor of the resonator during the pump pulse is increased by adjusting the bias voltages applied to the Q-switch Pockels cell. It was found that in order to obtain 3-4 pre-lase pulses at the end of the pump pulse, as shown in Fig. 5.15, the net bias applied across the crystal had to be reduced to around 650 V. This is done by decreasing the forward bias to 1.65 kV and increasing the reverse bias to 1 kV. In this way the net bias is reduced, but at the same time a large switching voltage is maintained, to circumvent elasto-optic relaxation effects described previously in Section 4.1.6, and thus obtain optimum optical switching of the Q-switch Pockels cell.

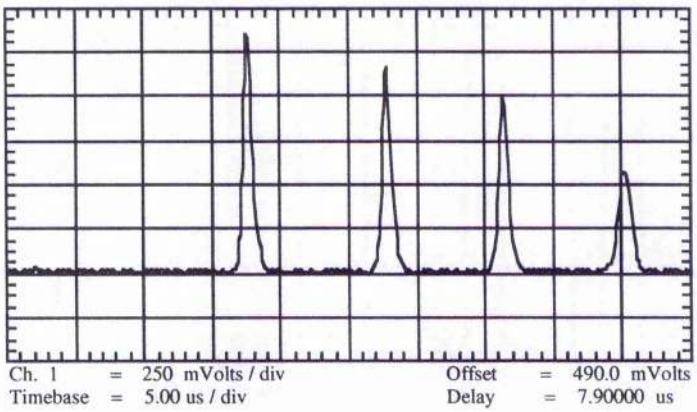

Figure 5.15: Pre-lase relaxation oscillation pulses.

The pre-lase pulses are seen to have a duration of 1 μsec and be separated by around 9 μsec. Given a mode beat frequency of 417 MHz, then over the 1 μsec pulse duration up to 417 beats are possible. As previously described, the mode beat detection electronics are designed to toggle the resonator length if greater than 160 beats are counted on the first pre-lase pulse. As also previously noted, once toggled the high voltage pulse is held on the EO length control Pockels cell for greater than 10 μsec. This is now seen to be the duration required to encompass the second pre-lase pulse,

which is used to seed the Q-switched pulse. The energy contained in each pre-lase pulse, measured using a sensitive energy probe (Molectron J25-09), was found to be less than 15 μJ. Consequently, the reduction in stored energy due to the first pre-lase pulse, which is essentially a loss mechanism, is negligible.

It should be noted that alignment of the EOPM crystal relative to the polarisation vector of the circulating field is particularly important. If the field is not polarised parallel to one of the EO-induced birefringence axes of the crystal, then when a voltage is applied to the crystal the field will experience a degree of birefringence. This results in depolarisation of the field and an increased resonator loss, which can result in the non-appearance of a second pre-lase pulse and missing pulses in the laser output. It is for this reason that the Q-switch biasing is set-up to allow the formation of 3-4 pre-lase pulses, in order that a small amount of additional loss can be tolerated. In this case alignment of the crystal was by retro-reflection of a visible He-Ne laser aligned to the resonator axis.

5.2.2: Spectral and Temporal Observations

The spectral content of the output from the laser is monitored by illuminating a fast silicon photodiode (BPX65) and observing the diode signal on an rf spectrum analyser. The spectral content of the laser output initially without the EOPM operating and then with has been observed as follows.

EO Phase Modulator Inhibited

The output from the laser was monitored over a prolonged period of time for the appearance of mode beating. With the rf spectrum analyser centre frequency set to 417 MHz, the frequency span set to 0 Hz and with a long sweep time, it is observed that the output of the laser is SLM for most of the time, with mode beating being observed at periodic intervals, as shown in Fig. 5.16. The period of this cycle is dependent upon the thermal stability of the ambient surroundings, however, could readily exceed 15 mins.

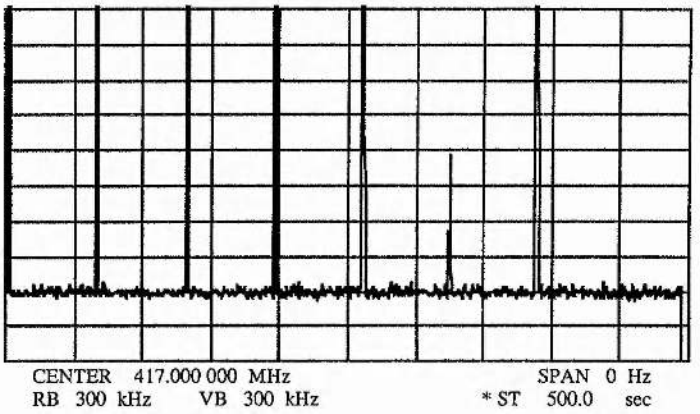

Figure 5.16: Periodic mode beating at the inter-mode frequency spacing (scan time > 8 mins).

Given the periodicity of the beating shown in Fig. 5.16, it is readily established over what frequency range ($\delta\upsilon$) about the symmetric two mode condition, as depicted in Fig. 5.1c, that mode beating is observed. This is done by ratioing the time for which beating is observed to the time between periods of beating, remembering that this time is the time taken for the resonator to scan one free spectral range (417 MHz). This then results in a value of $\delta\upsilon$ = 16.7 MHz. It is also the case then that the voltage applied to the EO length control Pockels cell need only be sufficient to displace the resonator outwith this near symmetric range, however, for the purpose of this work the voltage applied is that required to displace the resonator modes to the near optimum condition of a mode at gain centre.

Of further note is the fact that beating is only observed between two adjacent resonator modes, indicating no more distant modes to be present and an absence of spatial hole burning effects. To ensure that this observation is not a limitation in the response time of the photodiode or rf spectrum analyser, the spectral content was also observed on a Fabry-Perot interferometer which again showed no more distantly spaced resonator modes to be present. Such effects are attributable to the gain being located within a few millimetres of one end of the linear resonator.

EO Phase Modulator Active

With the EOPM active, i.e. the resonator length toggled on the detection of mode beating on the first pre-lase pulse, it is observed that each Q-switched laser pulse is now SLM. A flat line trace is observed on the rf spectrum analyser and confirmed by a only single mode being observed in the transmission rings of a Fabry-Perot interferometer (FSR - 3 GHz, Finesse - 20), as shown in Fig. 5.17.

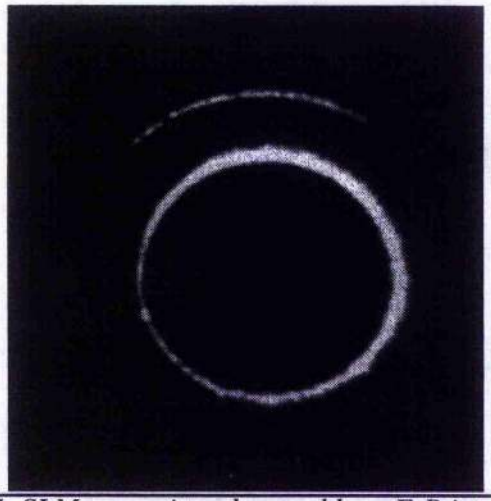

Figure 5.17: SLM operation observed by a F-P interferometer.

As well as SLM operation providing a narrow-linewidth source, it is of course also the case that a temporally smooth pulse is generated, this also being desirable for a number of applications. The temporal profile of the SLM output for the laser operating at 1.053 μm is shown in Fig. 5.18, which shows an accumulation of 200 pulses.

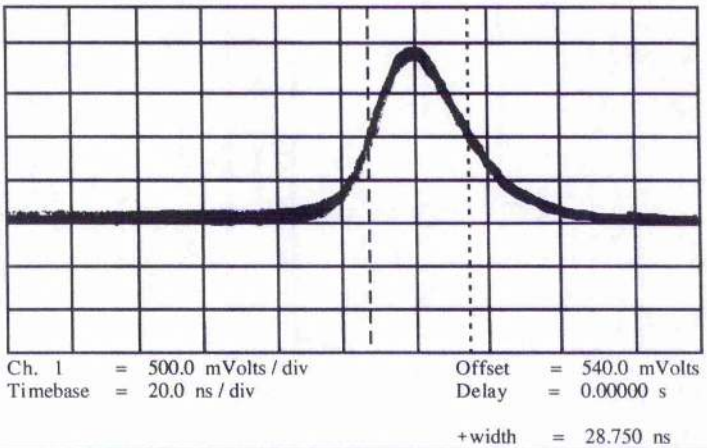

Figure 5.18: Temporal profile for SLM operation (1.053 μm, 20 sec. persistence).

It is clear that pulse to pulse stability is good and no mode beating is evident. The measured pulse duration for 1.053 μm operation is ~ 28 nsec (FWHM). Similar results are observed for 1.047 μm operation when the measured pulse duration is 17 nsec.

5.2.3: Threshold and Conversion Efficiency

The useful output energy as a function of the pump pulse energy for this Q-switched and SLM mode of operation is shown in Fig. 5.19.

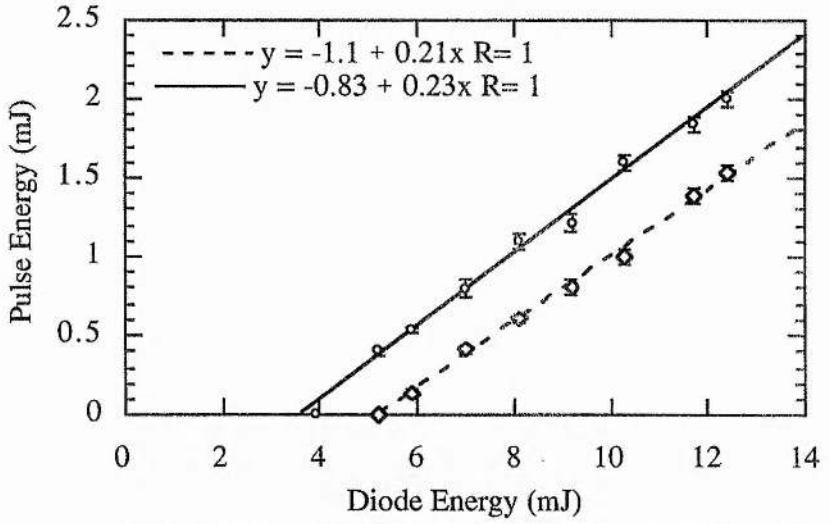

Figure 5.19: Single longitudinal mode pulse energy (o - 1.047 μm, ◊ - 1.053 μm).

These results equate to peak optical-optical conversion efficiencies of 16.2% and 12.6% for 1.047 μm and 1.053 μm operation respectively. Corresponding slope efficiencies are 23% and 21%. Taking into account the pump coupling efficiency, the laser output to pump light absorbed conversion efficiencies for 1.047 μm and 1.053 μm operation are 19.5% and 15.2% respectively, with corresponding slope efficiencies of 27.7% and 25.3%. The above and additionally wall plug efficiencies are summarised in Table 5.1.

Wavelength	Optical to Optical conversion efficiency	Absorbed pump light to Optical efficiency	Wall plug efficiency	Optical to Optical slope efficiency
1.047 μm	0.162	0.195	0.065	0.230
1.053 μm	0.126	0.152	0.050	0.210

Table 5.1: Summary of SLM operating characteristics. (Coupling optic efficiency - 83%, Diode efficiency - 40%).

Chapter 5 References:

1. D. C. Hanna and Y. W. J. Koo *"Stable single-mode operation of a Q-switched laser by a simple resonator length control technique"* Opt. Comm. 43 (6) pp.414-418, 1982.

2. D. J. Kuizenga *"Short-pulse oscillator development for the Nd-glass laser fusion systems"* IEEE J. Quant. Elect. QE-17 (9) pp.1694-1708, 1981.

Chapter 6
Theoretical Background to Nonlinear Optics and Parametric Interactions

In the preceding chapters the development of all-solid-state, diode-laser pumped Nd lasers has been discussed, and have been shown to be efficient and controllable sources of coherent radiation. While the spectral properties of these lasers are in many cases well suited to particular applications, the usefulness of the source can often be enhanced by the introduction of frequency agility. Nonlinear optical devices, such as harmonic generators and optical parametric oscillators, are means of introducing this agility.

In then a second part to this work, the application of the diode-laser pumped solid-state lasers previously developed as pump sources for nonlinear optical devices is described. In this Chapter, those aspects of nonlinear optical theory are introduced which are relevant to the devices studied, particularly frequency up-conversion, in the form of frequency doubling and tripling, and frequency down-conversion, by way of optical parametric oscillators. It is not the intention to present a highly detailed construction of the nonlinear optical theory of parametric wave interactions, this having been done previouslyby Armstrong *et al.* [1] and many authors since [2, 3], but to present the practical relationships between crystal parameters and device geometries, which will be demonstrated as useful in the results discussed in Chapters 7 and 8.

6.1: Wave Propagation in Dielectric Media

6.1.1: The Nonlinear Polarisation Wave

Nonlinear optical effects arise through the response of a dielectric media at the atomic level to the electric field of any applied and sufficiently intense beam of light. As the wave propagates through the media, the spatial and temporal distributions of the electric charge are modified, due in particular to a displacement of the valence electrons.

This displacement manifests itself in a macroscopic way in the introduction of a polarisation through the creation of electric dipoles, the amplitudes and consequential re-radiation of which do not necessarily follow the sinusoidal electro-magnetic fields which created them.

The magnitude of the polarisation per unit volume, or so called *dipole moment*, **P** is dependent upon the intensity of the applied field **E**, and linked by *susceptibility tensors* (χ) of the second, third, fourth and higher rank, and can be written in the form of a power series;

$$\begin{aligned}\mathbf{P_l}(z,t) = \varepsilon_0[&\chi^{(1)}_{lm}\mathbf{E}(z,t) + \chi^{(2)}_{lmn}\mathbf{E_m}(z,t)\mathbf{E_n}(z,t) \\ &+\chi^{(3)}_{lmn}\mathbf{E_m}(z,t)\mathbf{E_n}(z,t)\mathbf{E_p}(z,t)+.....]\end{aligned} \quad , \qquad (6.1)$$

where l,m,n and p are Cartesian co-ordinates, ε_0 the permittivity of free space, and has been separated from $\chi^{(i)}$ the units of which become metres.Volt^{-1}, and a plane wave propagating in the z-direction is assumed. In the case where the applied electric field is small and less than the intra-atomic field strengths, the response of the medium will be linear and can be approximated by the term in $\chi^{(1)}$ only. The term $\chi^{(1)}$ being related to the index of refraction (n) through $\chi^{(1)} = n^2 - 1$, and gives rise to such linear optical effects as reflection and refraction. Of interest here is the first nonlinear optical term in $\chi^{(2)}$, the second order nonlinearity, which is a third rank tensor with 27 components, although many of these components may be zero or equal due to symmetry considerations [4]. This quadratic term is responsible for such elastic effects as sum-frequency and difference-frequency generation and also the Pockels effect, and exists only in non-centrosymmetric anisotropic media. The cubic term $\chi^{(3)}$ is responsible for inelastic effects including stimulated Raman scattering, Brillouin scattering and the Kerr effect.

Considering the form of the polarisation wave which is generated by the interaction of two electro-magnetic (em) waves of frequencies ω_1 and ω_2, and where the em-waves propagation's are described by

$$\mathbf{E}_i(z,t) = E_i\cos(k_i z + \omega_i t + \phi_i) \ , \qquad (6.2)$$

where k is the wavevector, ϕ the wave-phasing and i = 1 or 2, then substituting equ. (6.2) into (6.1) and considering only the nonlinear term in $\chi^{(2)}$, the second order nonlinear polarisation becomes

$$\begin{aligned}\mathbf{P}_{\mathbf{nl}}^{(2)} = \varepsilon_0\chi^{(2)}\left[E_1^2\cos^2(k_1z+\omega_1t)+E_2^2\cos^2(k_2z+\omega_2t)\right] \\ +2E_1E_2\cos(k_1z+\omega_1t)\cos(k_2z+\omega_2t)\end{aligned}, \tag{6.3}$$

when presently the phasing terms have been neglected.

By re-expressing equ. (6.3), using the identities $\cos^2(A) = \cos(2A) - 1$ and $\cos(A)\cos(B) = 1/2[\cos(A+B) = \cos(A-B)]$, then it is readily seen that the polarisation wave consists of a number of different terms in different frequencies. These are;

$$P_{2\omega_1} = \frac{\varepsilon_0}{2}\chi^{(2)}E_1^2\cos\left[2(k_1z+\omega_1t)\right], \tag{6.4a}$$

$$P_{2\omega_2} = \frac{\varepsilon_0}{2}\chi^{(2)}E_2^2\cos\left[2(k_2z+\omega_2t)\right], \tag{6.4b}$$

$$P_{\omega_1+\omega_2} = \varepsilon_0\chi^{(2)}E_1E_2\cos\left[(k_1+k_2)z+(\omega_1+\omega_2)t\right], \tag{6.4c}$$

$$P_{\omega_1-\omega_2} = \varepsilon_0\chi^{(2)}E_1E_2\cos\left[(k_1-k_2)z+(\omega_1-\omega_2)t\right], \tag{6.4d}$$

and a frequency independent term,

$$P_0 = \frac{\varepsilon_0}{2}\chi^{(2)}\left(E_1^2+E_2^2\right). \tag{6.4e}$$

Clearly the polarisation wave contains terms in the second harmonics of E_1 and E_2, equ's. (6.4a,b), and also terms in the sum and difference frequencies, equ's. (6.4c,d). This then is the origin of the parametric wave interaction. The frequency independent term describes optical rectification and is not of interest here.

6.1.2: The Coupled Wave Equations

Having considered the formation of a nonlinear polarisation wave, it is now of concern to address how energy is coupled from one em-wave to another via this polarisation wave. The starting point is Maxwell's wave equation describing the propagation of em-waves within an anisotropic and non-conducting dielectric medium, namely;

$$\nabla^2\mathbf{E} = \mu\sigma\frac{\partial\mathbf{E}}{\partial t} + \mu\varepsilon\frac{\partial^2\mathbf{E}}{\partial t^2} + \mu\frac{\partial^2\mathbf{P}_{nl}}{\partial t^2}\ , \qquad (6.5)$$

where μ and ε are the magnetic and electric permeabilities, σ is a coefficient of absorption and $\varepsilon = \varepsilon_0(1 + \chi^{(1)})$. Where it can be assumed that higher order terms than $\chi^{(2)}$ can be neglected, then for **P** parallel to **E**, $\mathbf{P}_{nl}$ given by equ. (6.3) can be substituted for the nonlinear polarisation and equ. (6.5) becomes the general equation describing the propagation of an em-wave in a nonlinear medium with quadratic nonlinearity.

In respect of a second order nonlinear process, it is usual to consider the interaction of three em-waves of frequencies ω_1, ω_2 and ω_3. Restricting the analysis to a plane-wave situation and where all the waves propagate in the z-direction, then the individual wave propagations can be described by

$$\mathbf{E}_j(z,t) = \frac{1}{2}\left\{E_j(z)\exp\left[i(k_j z - \omega_j t)\right] + c.c.\right\}\ , \qquad (6.6)$$

where j takes the value 1, 2 and 3.

As the three waves propagate through the nonlinear medium an energy transfer takes place, via the nonlinear polarisation, and thus the respective field amplitudes are non-uniform. Consequently, the field amplitudes are expressed explicitly as a function of z, i.e. $E_j(z)$. Combining equ's (6.6) for all values of j gives the total instantaneous field as

$$\begin{aligned}\mathbf{E} = &\frac{1}{2}\left\{E_1(z)\exp\left[i(k_1 z - \omega_1 t)\right] + c.c.\right\} \\ &+ \frac{1}{2}\left\{E_2(z)\exp\left[i(k_2 z - \omega_2 t)\right] + c.c.\right\} \\ &+ \frac{1}{2}\left\{E_3(z)\exp\left[i(k_3 z - \omega_3 t)\right] + c.c.\right\}\end{aligned}\ . \qquad (6.7)$$

As noted above, consideration is restricted to the plane-wave case and propagation in the z-direction, hence, equ. (6.5) may be rewritten in the form

$$\frac{\partial^2\mathbf{E}}{\partial z^2} = \mu\sigma\frac{\partial\mathbf{E}}{\partial t} + \mu\varepsilon\frac{\partial^2\mathbf{E}}{\partial t^2} + \mu\frac{\partial^2}{\partial t^2}\left(\varepsilon_0\chi^{(2)}\mathbf{E}^2\right)\ , \qquad (6.8)$$

where ∇^2 has been replaced by the one dimensional operator $\partial^2/\partial z^2$. Substituting for **E** in equ. (6.8) using equ. (6.7) gives an expression which may be separated into three parts, each containing terms which oscillate at only one of the three frequencies.

Assuming that ω_3 is related to ω_1 and ω_2 through the relationship $\omega_3 = \omega_1 + \omega_2$, then that part of the expression oscillating in ω_1 may be written in the form [5]

$$\frac{\partial^2 \mathbf{E}^{(\omega_1)}}{\partial z^2} = -\frac{1}{2}\left(i\omega_1\mu\sigma_1 + \omega_1^2\mu\varepsilon\right)\left\{E_1(z)\exp\left[i\left(k_1 z - \omega_1 t\right)\right]\right\} + c.c. \\ -\frac{1}{2}\omega_1^2\mu\varepsilon_0\chi^{(2)}E_3(z)E_2^*(z)\exp\left[i\left(k_1 z - \omega_1 t\right) + c.c.\right] \qquad (6.9)$$

Next, observing that in view of equ. (6.6),

$$\frac{\partial^2 \mathbf{E}^{(\omega_1)}}{\partial z^2} = \frac{1}{2}\left[2ik_1\frac{dE_1(z)}{dz} - k_1^2 E_1(z)\right]\exp\left[i\left(k_1 z - \omega_1 t\right)\right] + c.c. \ , \qquad (6.10)$$

where the *slowly-varying amplitude approximation* has been made namely;

$$\left|k_1\frac{dE_1(z)}{dz}\right| >> \left|\frac{d^2E_1(z)}{dz^2}\right| , \qquad (6.11)$$

then by equating equ's. (6.10) and (6.9), recognising that $k_1 = \sqrt{(\omega_1\mu\varepsilon)}$, and then after multiplying all terms by

$$\frac{i}{k_1}\exp\left[-i\left(k_1 z - \omega_1 t\right)\right] ,$$

the spatial rate of change of the field amplitude $E_1(z)$, can be written as

$$\frac{dE_1(z)}{dz} = -\frac{\sigma_1}{2}\left(\frac{\mu}{\varepsilon_1}\right)^{\frac{1}{2}}E_1(z) - \frac{i\omega_1}{2}\left(\frac{\mu}{\varepsilon_1}\right)^{\frac{1}{2}}\varepsilon_0\chi^{(2)}{}_{(\omega_1 = \omega_3 - \omega_2)}E_3(z)E_2^*(z)\exp\left(i\Delta kz\right) \qquad (6.12a)$$

and similarly for E_2 and E_3, the oscillatory fields at ω_2 and ω_3;

$$\frac{dE_2(z)}{dz} = -\frac{\sigma_2}{2}\left(\frac{\mu}{\varepsilon_2}\right)^{\frac{1}{2}}E_2^*(z) + \frac{i\omega_2}{2}\left(\frac{\mu}{\varepsilon_2}\right)^{\frac{1}{2}}\varepsilon_0\chi^{(2)}{}_{(\omega_2 = \omega_3 - \omega_1)}E_3^*(z)E_1(z)\exp\left(i\Delta kz\right) , \qquad (6.12b)$$

$$\frac{dE_3(z)}{dz} = -\frac{\sigma_3}{2}\left(\frac{\mu}{\varepsilon_3}\right)^{\frac{1}{2}}E_3(z) - \frac{i\omega_3}{2}\left(\frac{\mu}{\varepsilon_3}\right)^{\frac{1}{2}}\varepsilon_0\chi^{(2)}{}_{(\omega_3 = \omega_1 + \omega_2)}E_1(z)E_2(z)\exp\left(i\Delta kz\right) , \qquad (6.12c)$$

where $\Delta k = k_3 - k_2 - k_1$ is the *momentum mismatch*. These then are the basic equations describing the nonlinear parametric interaction and are coupled to one another via the nonlinear constant $\chi^{(2)}$.

Before going on to discuss further the coupled wave equations in the applications of sum-frequency generation and optical parametric generation, it is useful at this point to introduce some further nonlinear preliminaries, namely; the nonlinear coefficient *d*-effective and some simple crystal optics.

6.1.3: The *d*-effective Coefficient

The nonlinear susceptibility $\chi^{(2)}$ is as previously noted a third rank tensor with 27 components, written in the form $\chi^{(2)}_{lmn}(\omega_3 = \omega_1 + \omega_2)$ when an interaction of the kind denoted in parenthesis is considered, and where l,m and n are indices referring to the Cartesian components of the fields. It is intrinsic that the second-order nonlinear susceptibility displays the symmetry properties of the crystalline material. A consequence of this is that in centrosymmetric crystals, the nonlinear coefficients must vanish. This can be seen by writing the second-order nonlinear polarisation given in equ. (6.1) in the abbreviated form

$$\mathbf{P}_l(z,t) = \varepsilon_0 \sum_{lmn} \chi^{(2)}_{lmn} \mathbf{E}_m(z,t)\mathbf{E}_n(z,t) \ . \qquad (6.13)$$

If the direction of the electric field is reversed, i.e. $\mathbf{E}_m$ becomes $-\mathbf{E}_m$ and $\mathbf{E}_n$ becomes $-\mathbf{E}_n$, then because the crystal possesses inversion symmetry the reversed field sees an identical crystal to the original and consequently the new polarisation is $-\mathbf{P}_l$. The new polarisation and the electric field causing it are still related through the same identity as equ. (6.13), that is

$$-\mathbf{P}_l(z,t) = \varepsilon_0 \sum_{lmn} \chi^{(2)}_{lmn} (-\mathbf{E}_m(z,t))(-\mathbf{E}_n(z,t)) \ . \qquad (6.14)$$

For both equ's. (6.13) and (6.14) to hold simultaneously, the nonlinear susceptibility coefficients χ_{lmn} must vanish and so it is concluded that second-order nonlinear processes are restricted to non-centrosymmetric crystals.

Substituting for the fields in equ. (6.13) using equ. (6.6) gives

$$P_l(-\omega_3) = \varepsilon_0 \sum_{lmn} \frac{\chi^{(2)}_{lmn}}{2} (\omega_3 = \omega_2 + \omega_1) E_m(\omega_2) E_n(\omega_1) \exp(i\Delta kz) \ . \qquad (6.15)$$

It is customary however, to write the driving polarisation in terms of the *nonlinear susceptibility tensor* **d** defined by

$$P_l(-\omega_3) = \varepsilon_0 \sum_{lmn} d_{lmn}(\omega_3 = \omega_2 + \omega_1) E_m(\omega_2) E_n(\omega_1) \exp(i\Delta kz) \ . \qquad (6.16)$$

Comparison of equ's. (6.15) and (6.16) then shows that the definition of d_{lmn} is just;

$$2d_{lmn} = \chi^{(2)}_{lmn} \ . \qquad (6.17)$$

In addition to conforming to crystal symmetry conditions, $\chi^{(2)}$ satisfies two further symmetry relations which restricts the number of essential, frequency independent components. Under the assumptions of a lossless media which has negligible dispersion over the range of frequencies ω_1, ω_2 and ω_3, the first relation states that $\chi^{(2)}_{lmn}(\omega_3 = \omega_1 + \omega_2)$ is invariant under permutation of the three pairs of indices (ω_3, l), (ω_1, m), (ω_2, n) [1, 6]; while the second based on Kleinman's conjecture [4] states that $\chi^{(2)}_{lmn}$ is symmetric under any permutation of its indices. $\chi^{(2)}$ can then be represented in the form

$$\chi^{(2)}_{lmn}(\omega_3 = \omega_1 + \omega_2) = \mathbf{d}_{lq} \ , \qquad (6.18)$$

where q takes the values 1 through 6 with the correspondence to mn as;

mn:	11	22	33	23,32	13,31	12,21
q:	1	2	3	4	5	6

and where $\mathbf{d}_{lq}$ becomes a tensor represented by a 3 x 6 matrix.

For convenience, it is not the susceptibility tensor components but an *effective nonlinear coefficient* d_{eff}, derivable from the **d** tensor components, that is introduced into the coupled wave equations in place of the nonlinear susceptibility $\chi^{(2)}$. The derivation of d_{eff} is rigorous and outwith the scope of this thesis, but may be found in for example the work of Boyd and Kleinman [7] or Smith [8]. In general it is given by the mathematical expression for the three wave interaction process, written as;

$$\begin{aligned} d_{eff} &= \mathbf{U}_3 \bullet \mathbf{d}(\omega_1 + \omega_2) : \mathbf{U}_1\mathbf{U}_2 \\ &= \sum_{i\varsigma} U_{3i} d_{i\varsigma}(\omega_1 + \omega_2)(\mathbf{U}_1\mathbf{U}_2)_\varsigma \ , \end{aligned} \qquad (6.19)$$

where U_{3i} is the *i* th component of the $\mathbf{U}_j$ unit vector which denotes the polarisation direction of the electric fields $\mathbf{E}_j$ at frequencies ω_j, $d_{i\varsigma}$ are the components of the nonlinear coefficient tensor and $(\mathbf{U}_1\mathbf{U}_2)_\varsigma$ is the ςth component of a column vector. The cosine vectors of the electric fields $\mathbf{E}_{m,i}$ propagating in the crystal, where m denotes the

three interacting fields at ω_1, ω_2 and ω_3, and i = 1 or 2 denotes the two possible values of refractive index in the propagation direction **K**, are written

$$\mathbf{U}_{m,i}: \cos\alpha_{m,i}, \cos\beta_{m,i}, \cos\gamma_{m,i} \ , \tag{6.20}$$

and calculated using [9];

$$\begin{aligned}
\cos\alpha &= \frac{k_x}{n^2 - n_x^2}\left[\left(\frac{k_x}{n^2 - n_x^2}\right)^2 + \left(\frac{k_y}{n^2 - n_y^2}\right)^2 + \left(\frac{k_z}{n^2 - n_z^2}\right)^2\right]^{-\frac{1}{2}} \\
\cos\beta &= \frac{k_y}{n^2 - n_y^2}\left[\left(\frac{k_x}{n^2 - n_x^2}\right)^2 + \left(\frac{k_y}{n^2 - n_y^2}\right)^2 + \left(\frac{k_z}{n^2 - n_z^2}\right)^2\right]^{-\frac{1}{2}} \\
\cos\gamma &= \frac{k_z}{n^2 - n_z^2}\left[\left(\frac{k_x}{n^2 - n_x^2}\right)^2 + \left(\frac{k_y}{n^2 - n_y^2}\right)^2 + \left(\frac{k_z}{n^2 - n_z^2}\right)^2\right]^{-\frac{1}{2}}
\end{aligned} \ . \tag{6.21}$$

The column vector for the type I phase-match geometry where the ω_1 and ω_2 waves are parallel polarised is then;

$$(\mathbf{U}_{\omega_1}\mathbf{U}_{\omega_2}) = \begin{vmatrix} \cos(\alpha_{\omega_1,2})\cos(\alpha_{\omega_2,2}) \\ \cos(\beta_{\omega_1,2})\cos(\beta_{\omega_2,2}) \\ \cos(\gamma_{\omega_1,2})\cos(\gamma_{\omega_2,2}) \\ \cos(\gamma_{\omega_1,2})\cos(\beta_{\omega_2,2}) + \cos(\gamma_{\omega_2,2})\cos(\beta_{\omega_1,2}) \\ \cos(\gamma_{\omega_1,2})\cos(\alpha_{\omega_2,2}) + \cos(\gamma_{\omega_2,2})\cos(\alpha_{\omega_1,2}) \\ \cos(\alpha_{\omega_1,2})\cos(\beta_{\omega_2,2}) + \cos(\alpha_{\omega_2,2})\cos(\beta_{\omega_1,2}) \end{vmatrix} . \tag{6.22}$$

For type II phase-matching where the fields ω_1 and ω_2 are orthogonally polarised the column vector becomes;

$$(\mathbf{U}_{\omega_1}\mathbf{U}_{\omega_2}) = \begin{vmatrix} \cos(\alpha_{\omega_1,1})\cos(\alpha_{\omega_2,2}) \\ \cos(\beta_{\omega_1,1})\cos(\beta_{\omega_2,2}) \\ \cos(\gamma_{\omega_1,1})\cos(\gamma_{\omega_2,2}) \\ \cos(\gamma_{\omega_1,2})\cos(\beta_{\omega_2,2}) + \cos(\gamma_{\omega_2,2})\cos(\beta_{\omega_1,1}) \\ \cos(\gamma_{\omega_1,2})\cos(\alpha_{\omega_2,2}) + \cos(\gamma_{\omega_2,2})\cos(\alpha_{\omega_1,1}) \\ \cos(\beta_{\omega_1,2})\cos(\alpha_{\omega_2,2}) + \cos(\beta_{\omega_2,2})\cos(\alpha_{\omega_1,1}) \end{vmatrix} . \tag{6.23}$$

And finally for both type I and type II geometries

$$\mathbf{U}_{\omega_3} = \begin{vmatrix} \cos(\alpha_{\omega_3,1}) \\ \cos(\beta_{\omega_3,1}) \\ \cos(\gamma_{\omega_3,1}) \end{vmatrix} . \tag{6.24}$$

6.1.4: Crystal Optics

In general birefringent crystals can be divided into two categories; uniaxial and biaxial. In a uniaxial crystal the index of refraction depends on a simple ellipsoid, the major axis of which is called the *optic axis* or z-axis, and about which the index ellipsoid then possesses circular symmetry. The index of refraction dependence on propagation direction in a biaxial crystal has a more complex structure, all three crystallographic axes having different indices of refraction. Consequently, propagation will be seen to be generally restricted to be in one of the principal crystallographic planes. The nature of uniaxial and biaxial crystals is now further discussed and the effect of double-refraction or walk-off introduced.

Uniaxial crystal

The index ellipsoid construction for a uniaxial crystal is shown in Fig. 6.1.

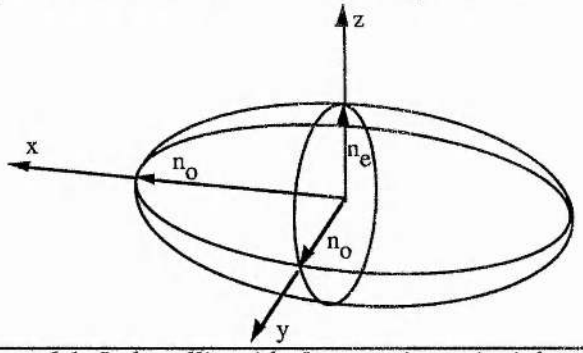

Figure 6.1: Index ellipsoid of a negative uniaxial crystal.

For any general propagation direction described by the wavevector **k**, the plane containing the z-axis and **k** is denoted the *principal plane*. Any wave whose polarisation is normal to this plane is defined as the *ordinary wave (o-wave)*, while a wave polarised within the principal plane is the *extraordinary wave (e-wave)*. In Fig. 6.1 it can be readily seen that a wave propagating in the z-direction will see no birefringence, while maximum birefringence is observed for any propagation direction perpendicular to this.

The refractive index of the o-wave will, in the case of a uniaxial crystal, be independent of the azimuth angle Ø, measured from the x-axis toward the y-axis. In contrast the e-wave refractive index will be dependent upon the polar angle θ, and may be determined from [10]

$$n_e(\theta) = \frac{n_o n_e}{\left[n_0^2 \sin^2\theta + n_e^2 \cos^2\theta\right]^{1/2}} . \qquad (6.25)$$

If the index of refraction of the e-wave is greater than that of the o-wave the crystal is termed positive uniaxial, while conversely if $n_o > n_e$ the crystal is negative uniaxial.

Biaxial crystal

The more complex index ellipsoid construction for a biaxial crystal is shown in Fig. 6.2.

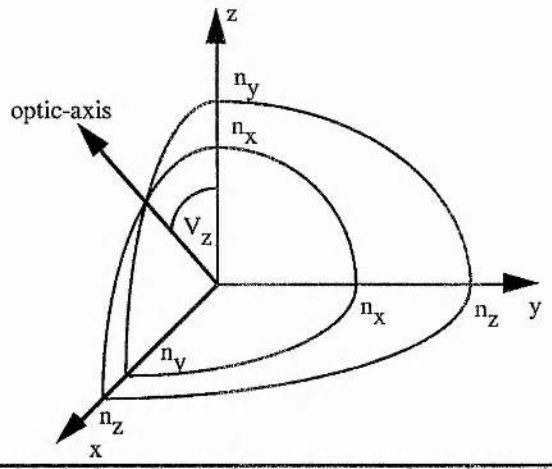

Figure 6.2: Index ellipsoid construction for a biaxial crystal.

The arcs in the index ellipsoid describe the refractive index seen by the orthogonally polarised components of the wave, perpendicular to the wave propagation direction, where propagation is in one of the principal planes x - z, y - z and x - y. In the case where the index order is restricted to the form $n_x < n_y < n_z$, then the optic-axis will be in the x - z plane as shown in Fig. 6.2, where the angle V_z subtended by the optic-axis and z-axis is given by

$$\sin V_z = \frac{n_z}{n_y}\left(\frac{n_y^2 - n_x^2}{n_z^2 - n_x^2}\right)^{\frac{1}{2}} . \qquad (6.26)$$

Again considering propagation in the principal planes, then for any given plane evaluation of the refractive indices can be performed in a similar way as for a uniaxial crystal. For example, in the y - z plane the refractive index of the wave polarised normal to this plane is independent of θ and just equals n_x. The refractive index for the wave

orthogonally polarised is, in a similar way to n_e in the case of the uniaxial crystal, given by

$$n_e(\theta) = \frac{n_y n_z}{\left[n_y^2 \sin^2\theta + n_z^2 \cos^2\theta\right]^{1/2}} \ . \tag{6.27}$$

This is just analogous to the case of a positive uniaxial crystal where $n_o = n_x$. Similarly, in the x - z plane, $n_e(\theta)$ is given by

$$n_e(\theta) = \frac{n_x n_z}{\left[n_x^2 \sin^2\theta + n_z^2 \cos^2\theta\right]^{1/2}} \ , \tag{6.28}$$

where now for $V_z > \theta$ the crystal behaves as a negative uniaxial with $n_o = n_y$ and for $V_z < \theta$ a positive uniaxial. For the x - y plane a similar construction again applies but now $n_o = n_z$ and it is the azimuth angle Ø which is varied. The expression for $n_e(Ø)$ then becomes

$$n_e(\phi) = \frac{n_x n_y}{\left[n_y^2 \sin^2\phi + n_x^2 \cos^2\phi\right]^{1/2}} \ . \tag{6.29}$$

Double-refraction

As an extraordinary wave propagates through a birefringent medium, its power flow direction differs from that of the wavevector direction **k** by the double-refraction angle ρ. Consequently, this effect, known as Poynting vector walk-off, leads to a walk-off and spatial separation of the extraordinary wave energy from the ordinary wave at the angle ρ. It is found that the direction of power flow, or the Poynting vector direction **S**, is the normal to the tangent of the index ellipsoid at the point of intersection of the wavevector **k**, as depicted in Fig. 6.3 for the case of a negative uniaxial crystal. By simple geometry, the double-refraction angle can be shown to be given by [11]

$$\rho(\theta) = \pm \arctan\left[\left(\frac{n_o}{n_e}\right)^2 \tan\theta\right] \mp \theta \ , \tag{6.30}$$

where the upper operators correspond to the negative uniaxial case and the lower operators to the positive uniaxial case.

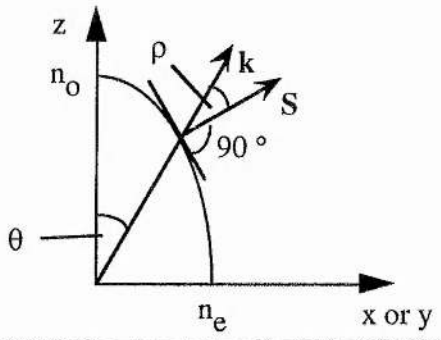

Figure 6.3: Poynting vector walk-off in a negative uniaxial crystal.

It is to be noted in Fig. 6.3 that the difference between n_o and n_e is highly exaggerated, resulting in what appears to be a large double refraction angle. In practice the difference in refractive indices is small and is often no more than 10%, resulting in a double-refraction angle of usually no more than 5°. It is also noteworthy that maximum walk-off occurs for propagation along $\theta = 45°$, while there is no double-refraction when propagation is along a principal axis.

For the case of double refraction in biaxial crystals consider the vectors **E** and **D** to represent the electric field and displacement, **k** and **S** are the wavevector and Poynting vector and **H** the magnetic field. Maxwell's equations require that **D**, **E**, and **k** are all orthogonal to the magnetic field and consequently coplanar, while $\mathbf{S} = \mathbf{E} \times \mathbf{H}$ requires that the Poynting vector lies in this plane also and consequently the angle between **E** and **D** to be the same as the double refraction angle, as shown in Fig. 6.4.

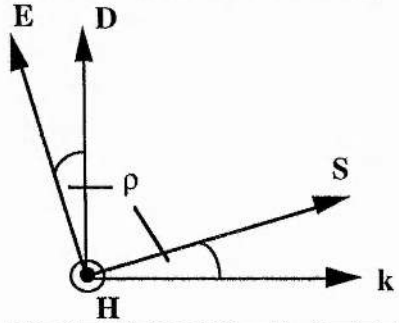

Figure 6.4: The field and displacement vectors in a birefringent medium.

By applying a scalar product to the unit vectors of **E**,**k** and **E**,**D**, it is straightforward to show that

$$\tan\rho = \frac{\mathbf{e} \bullet \mathbf{k}}{\mathbf{e} \bullet \mathbf{d}}, \tag{6.31}$$

where **e** and **d** are the unit vectors denoting **E** an **D**. The solution to this has been presented by for example Brehat [12] to be

$$\rho = \arctan\left\{ n^2 \left[\left(\frac{k_x}{n^{-2} - n_x^{-2}} \right)^2 + \left(\frac{k_y}{n^{-2} - n_y^{-2}} \right)^2 + \left(\frac{k_z}{n^{-2} - n_z^{-2}} \right)^2 \right]^{-\frac{1}{2}} \right\}, \qquad (6.32)$$

where n is the refractive index along the propagation direction. For a three wave mixing process, the walk-off angle is defined as the largest double-refraction angle associated with any of the three waves.

The spatial separation of the ordinary and extraordinary waves in either the uniaxial or biaxial cases leads then to an effective *aperture length* (l_a), which is the length over which some spatial overlap of the electric fields exists.

6.2: Optical Sum-Frequency Generation

Sum-frequency generation ($\omega_3 = \omega_2 + \omega_1$) was first demonstrated in its special form of second harmonic generation ($\omega_2 = \omega_1$) by Franken and co-workers [13], in generating the second harmonic ($\lambda = 0.347$ μm) of the output of a ruby laser ($\lambda = 0.694$ μm), when the fundamental was focused into a block of quartz. While conversion efficiencies were very small (~10^{-8}), this was the dawn of modern second order nonlinear optics which now sees conversion efficiencies in excess of 70%.

6.2.1: Small Signal Approximation

In the case of sum-frequency generation where $\omega_3 = \omega_1 + \omega_2$ and where the conversion efficiency from the waves at frequencies ω_1 and ω_2 to the wave at ω_3 is small, so that the assumption may be made that the amplitudes of the summing frequencies are constant over the length of the interaction, then the field amplitude of wave ω_3 at some point z = l may be found by integrating equ. (6.12c). Making the further assumptions that the scatter and absorption losses within the nonlinear crystal are small, i.e. $\sigma_i = 0$, and that the initial field at ω_3 is negligible, then the solution takes the form

$$E_3|_{z=l} = -i\omega_3 \frac{d_{eff}}{cn_3} E_1 E_2 \frac{\exp(i\Delta kl) - 1}{i\Delta k} , \qquad (6.33)$$

where it has been recognised that $\varepsilon_0\sqrt{(\mu_0/\varepsilon_i)} = 1/(cn_i)$.

Noting that the intensity of the wave E_i is given by

$$I_i = \frac{n_i c \varepsilon_0}{2} |\mathbf{E_i}|^2 ,$$

then the output intensity in the low conversion limit is

$$I_3|_{z=l} = \frac{2}{\varepsilon_0} \frac{(\omega_3 d_{eff} l)^2}{c^3 n_1 n_2 n_3} I_1 I_2 \frac{\sin^2(\Delta kl/2)}{(\Delta kl/2)^2} . \qquad (6.34)$$

In the special case of second harmonic generation (SHG) where $\omega_3 = 2\omega_1 = 2\omega_2$ and $n_1 = n_2 = n_3$ when the interaction is suitably phase-matched, as will be discussed later, then equ. (6.34) may be simplified somewhat and the conversion efficiency for SHG, again noting in the low conversion limit, expressed as

$$\frac{I_3}{I_1} = \Gamma^2 l^2 [E_1]^2 \mathrm{sinc}^2\left(\frac{\Delta kl}{2}\right) , \qquad (6.35)$$

where $\omega = \omega_1$, $\Gamma = (\omega d_{eff})/(nc)$ and it is recognised that $\sin(\theta)/\theta = \mathrm{sinc}\ (\theta)$.

It is notable in the above expressions for the sum-frequency generated wave intensities that phase-matching enters the nonlinear conversion process through the phase synchronism factor $\mathrm{sinc}^2(\Delta kl/2)$. Further, the conversion efficiency is seen to be dependent upon the square of both the nonlinear coefficient d_{eff} and the interaction length and, as is to be expected, the intensity of the mixed waves. It should also be borne in mind that the above analysis is for the plane-wave case.

6.2.2: Phase-Matching in Sum-Frequency Generation

Equations (6.34) and (6.35) demonstrate that the generated wave intensity is dependent upon the phase-matching parameter $\mathrm{sinc}^2(\Delta kl/2)$, where the phase-mismatch is described by $\Delta k = k_3 - k_2 - k_1$. As indicated in Fig. 6.5, for $\Delta k = 0$, the sinc^2 term becomes unity and phase-matching is optimised, while for $\Delta kl/2 = \pi$ the sinc^2 term becomes zero and therefore the generated wave intensity I_3 must also be zero.

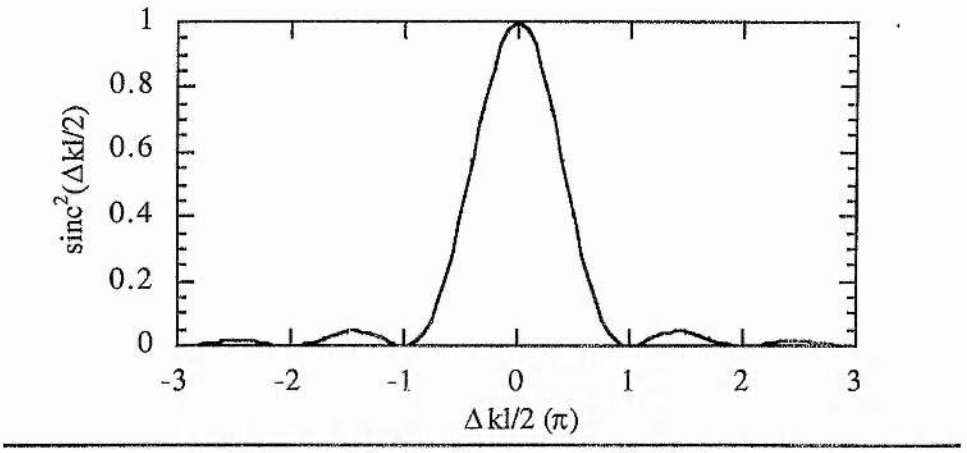

Figure 6.5: The function $sinc^2(\Delta kl/2)$.

It is possible to look upon the phase-mismatch in one of two ways; firstly, for a crystal of fixed length, the generated wave intensity output from the crystal will fluctuate depending on the degree of phase-mismatch. A phase-mismatch may for example be induced by a change in one of the phase-match acceptance parameters such as angle or temperature. One criterion for defining the *angular* or *temperature acceptance bandwidths* is to consider the point at which $\Delta kl/2 = \pi/2$, at this point the generated wave intensity falling to approximately 0.4 times its peak value. Alternatively, for a fixed value of phase-mismatch, the generated wave intensity will be seen to be a function of distance l along the crystal, as the field grows and decays with a period of $\Delta kl/2 = \pi$. Considered in this way, half of this period distance is termed the *coherence length* (l_c), this being the distance from the entrance face of the crystal to the point at which the generated wave intensity is a maximum.

Clearly, if the crystal is not perfectly phase-matched then the maximum generated signal that can be obtained is that after propagating one coherence length in the crystal, no matter how long the crystal actually is. Beyond this length and as far as a second coherence length power will flow backwards from the generated em-wave into the polarisation wave and consequently the input waves. As propagation continues an oscillatory behaviour is then observed as power fluctuates between the input and generated waves.

The means by which an ideal phase-match can be achieved have been alluded to above, by mention of angle tuning or temperature tuning the nonlinear crystal. Phase-matching will be discussed in greater detail is Section 6.4.

6.2.3: Sum-Frequency Generation with a Depleted Input

The expression (6.34) for the power of the generated wave in sum-frequency generation, and in its special form of equ. (6.35) for second harmonic generation, was derived under the assumption that there was negligible depletion of the input waves. It is the case however, that for a well phase-matched interaction and long crystal length, conversion efficiencies can begin to approach unity, in which case there is of course appreciable depletion of the input waves. To consider this regime the coupled wave equations are again considered, but now the fields $E_1(z)$ and $E_2(z)$ are allowed to vary with propagation distance. To begin, the field variables are transformed by the introduction of a new field variable, defined by

$$A_l \equiv \sqrt{\frac{n_l}{\omega_l}} E_l \qquad l = 1,2,3 \ , \tag{6.36}$$

where n_l is the refractive index of the medium at ω_l. Writing again the power flow per unit area or intensity as

$$\frac{P_l}{A} = \frac{1}{2}\sqrt{\frac{\varepsilon_0}{\mu}} n_l |E_l|^2 = \frac{1}{2}\sqrt{\frac{\varepsilon_0}{\mu}} \omega_l |A_l|^2 \ , \tag{6.37}$$

then the photon flux Θ (the number of photons passing through a square meter per second) is related to the power flow per unit area through the relationship

$$\Theta_l \hbar\omega_l = \frac{P_l}{A} = \frac{1}{2}\sqrt{\frac{\varepsilon_0}{\mu}} \omega_l |A_l|^2 \ , \tag{6.38}$$

and it becomes immediately obvious that $|A_l|^2$ is proportional to the photon flux at ω_l.

The coupled wave equations, equ. (6.12), after transformation then become;

$$\begin{aligned}
\frac{dA_1}{dz} &= \frac{-\alpha_1}{2} A_1 - \frac{i}{2}\kappa A_2^* A_3 \exp(-i\Delta k z) \\
\frac{dA_2}{dz} &= \frac{-\alpha_2}{2} A_2^* + \frac{i}{2}\kappa A_1 A_3^* \exp(i\Delta k z) \ , \\
\frac{dA_3}{dz} &= \frac{-\alpha_3}{2} A_3 - \frac{i}{2}\kappa A_1 A_2 \exp(i\Delta k z)
\end{aligned} \tag{6.39}$$

where

$$\alpha_1 = \sqrt{\frac{\mu}{\varepsilon_1}}\sigma_1$$

$$\kappa = \varepsilon_0 d_{eff}\sqrt{\frac{\mu}{\varepsilon_0}\frac{\omega_1\omega_2\omega_3}{n_1n_2n_3}}\,.$$

With this transformation the relations (6.39) now conveniently involve only a single coupling parameter κ.

Considering again the special case of second harmonic generation, then $A_1 = A_2$ and equ. (6.39) reduces to a pair of coupled equations written in the form;

$$\begin{aligned}\frac{dA_1}{dz} &= -\frac{\kappa}{2}A_3'A_1 \\ \frac{dA_3'}{dz} &= \frac{\kappa}{2}A_1^2\end{aligned}\quad , \tag{6.40}$$

where the substitution $A_3 = -iA_3'$ has been made and it has been assumed that the medium is lossless, phase-matching is ideal and that $A_1(0)$ and consequently $A_1(z)$ are real. It follows then from equ. (6.40) that

$$\frac{d}{dz}\left(A_1^2 + A_3'^2\right) = 0\ , \tag{6.41}$$

or that is to say, since as demonstrated above A^2 is proportional to the photon flux, for each photon removed from the input wave, one photon is added to the generated wave; energy being conserved through the simultaneous removal of a photon from the input wave 2.

To solve equ. (6.40) the assumption is made that there is no input wave at ω_3 and so $A_1^2 + A_3'^2 = A_1^2(0)$. The second expression of equ. (6.40) can then be written as

$$\frac{dA_3'}{dz} = \frac{\kappa}{2}(A_1^2(0) - A_3'^2)\ , \tag{6.42}$$

which has a solution of the form

$$A_3'(z) = A_1(0)\tanh\left[\frac{\kappa}{2}A_1(0)z\right]\ . \tag{6.43}$$

It is to be noted that the form of this solution means that as the term in parenthesis tends to infinity then A_3' tends to $A_1(0)$ so that all the input photons at ω are converted into half as many photons at 2ω. That is to say the conversion efficiency approaches

unity. In general the conversion efficiency can be expressed as the ratio of the squares of A, i.e.

$$\eta_{SHG} = \frac{|A_3(z)|^2}{|A_1(0)|^2} = \tanh^2\left[\frac{\kappa}{2}A_1(0)z\right] . \qquad (6.44)$$

It must also be remembered that the above analysis continues to be for a plane-wave interaction. In practice the mixing beams are likely to have a pseudo-Gaussian type intensity profile which will reduce the maximum achievable conversion efficiency.

6.2.4: Sum-Frequency Generation with Focused Gaussian Beams

Tight focusing of Gaussian beams is often employed to increase the intensity of the beams involved in the mixing process and hence the efficiency of the nonlinear process. Numerous authors have studied this regime with a view to optimising the conversion efficiency, notably Boyd and Kleinman [7] who demonstrated there to be optimum ratios of beam confocal parameter to crystal length and wavevector mis-match to crystal length. Other optimisation factors also apply which are more intuitive, such as choosing an interaction where walk-off is negligible, important when the beams have only a small cross section, and having similar confocal parameters for all the mixing beams to maintain a good spatial overlap. Various rigorous numerical models have also been developed for modelling the three wave mixing process in the presence of tight focusing, such as those of Smith [14, 15] for modelling both sum- and difference-frequency mixing and optical parametric oscillation. These models generally invoke the use of fast-Fourier-transform techniques to progress the three waves through the nonlinear crystal, assuming a non-uniform Gaussian spatial profile.

Taking a more simplistic approach, consider a focused Gaussian beam characterised by a confocal parameter b, which is that distance over which the beam must propagate for its area ($\pi\omega^2$) to become twice that at its waist ($\pi\omega_0^2$). If b is considerably greater than the crystal length l, then the beam radius may be regarded as being constant and the plane-wave result discussed earlier may be applied. In this case the solution to the generated wave intensity equ. (6.34) can be rewritten as

$$I_3(r)\big|_{z=l} = \frac{2}{\varepsilon_0}\frac{\left(\omega_3 d_{eff} l\right)^2}{c^3 n_1 n_2 n_3} I_1(r) I_2(r) \frac{\sin^2(\Delta kl/2)}{(\Delta kl/2)}\,, \qquad (6.45)$$

where it is taken that the intensity distribution is described by $I(r) = I_0(r)\exp(-2r^2/\omega^2)$, as normally so for the lowest order Gaussian beam. By making the appropriate substitutions to re-express equ. (6.45) in terms of power and the field E(r), and further recognising that

$$P_i = \frac{1}{2}\sqrt{\frac{\varepsilon_i}{\mu}}\int |E_i|^2\, dxdy \cong \sqrt{\frac{\varepsilon_i}{\mu}} E_0^2 \left(\frac{\pi\omega_0^2}{4}\right),$$

then equ. (6.45) can be integrated to give

$$\frac{P_3}{P_1} = 2\left(\frac{\mu}{\varepsilon_0}\right)^{\frac{3}{2}} \frac{\varepsilon_0^2 d_{eff}^2 \omega_1^{\,2} l^2}{n^3} \frac{P_1}{\pi\omega_0^2} \operatorname{sinc}^2\left(\frac{\Delta kl}{2}\right). \qquad (6.46)$$

With the substitution of Γ as defined previously and expressing $P^{(\omega)}$ in terms of E, this result is found to be just the same solution as was obtained before for the plane-wave case, equ. (6.35), indicative of the fact that for a near collimated or softly focused Gaussian beam, the spatial profile has little impact on the conversion efficiency achievable. It is noticeable that within the limits of soft focusing, as the beam waist size is reduced the conversion efficiency will increase. However, once the confocal parameter becomes comparable to the crystal length, significant spreading of the beam becomes evident within the crystal, so reducing the beam intensity and consequently the second harmonic power. It is therefore reasonable to focus the beam until $l \sim 2b$. At this point the beam size is given by $\omega_0^2 = \lambda l/2\pi n$, this being the point of *confocal focusing*, and on substitution equ. (6.46) becomes

$$\frac{P_3}{P_1} = 2\left(\frac{\mu}{\varepsilon_0}\right)^{\frac{3}{2}} \frac{\varepsilon_0^2 d_{eff}^2 \omega_1^{\,3} l}{\pi c n^2} P_1 \operatorname{sinc}^2\left(\frac{\Delta kl}{2}\right), \qquad (6.47)$$

where the substitution $\lambda = (2\pi c)/\omega$ has been used. Of particular note in this result is that the conversion efficiency now depends on the crystal length l and not l^2. For effective conversion over the entire length of a longer crystal focusing must be relaxed so reducing the beam intensity.

6.3: Optical Parametric Amplification and Oscillation

Optical parametric amplification involves the transfer of energy from a *pump* wave at ω_3 (or ω_p) to two waves at frequencies ω_1 and ω_2 (or the so called *signal* - and *idler* -waves ω_s and ω_i), where, as with sum-frequency mixing, energy is conserved in the interaction and thus $\omega_p = \omega_s + \omega_i$. Fundamentally, the interaction is similar to that of sum-frequency mixing except that the power flow is in the reverse direction, being fed from the high frequency wave to the two lower frequency waves. In the special case of $\omega_s = \omega_i$ it is easily identifiable that this is just the reverse of the special case of sum-frequency mixing called second harmonic generation, in the terminology of parametric amplification it being known as *degenerate* operation.

A physical picture of parametric amplification can be developed by considering a strong pump field at ω_p mixing with an initially weaker field at ω_s through the nonlinear response of the medium. As the pump and signal propagate, a polarisation wave is established at $\omega_i = \omega_p - \omega_s$. This oscillating polarisation will then re-radiate an em-wave δE_i, which mixes with the pump-wave to generate in a similar fashion an incremental field δE_s. Providing the fields are phase-matched, this process will continue over the length of the nonlinear crystal, resulting in simultaneous amplification of the signal and idler fields and a corresponding depletion of the pump field.

6.3.1: Small Signal Approximation

To analyse the case of optical parametric amplification, consider again the transformed wave equations (6.39);

$$\begin{aligned}
\frac{dA_s}{dz} &= \frac{-\alpha_s}{2}A_s - i\frac{\kappa}{2}A_i^* A_p \exp(-i\Delta kz) \\
\frac{dA_i}{dz} &= \frac{-\alpha_i}{2}A_i^* + i\frac{\kappa}{2}A_s A_p^* \exp(i\Delta kz) \quad , \\
\frac{dA_p}{dz} &= \frac{-\alpha_p}{2}A_p - i\frac{\kappa}{2}A_s A_i \exp(i\Delta kz)
\end{aligned} \tag{6.48}$$

where again

$$\alpha_j = \sqrt{\frac{\mu}{\varepsilon_j}}\sigma_j$$

$$\kappa = \varepsilon_0 d_{eff}\sqrt{\frac{\mu}{\varepsilon_0}\frac{\omega_s\omega_i\omega_p}{n_s n_i n_p}}$$

While the exact solution to equ. (6.48) has been given by Armstrong [1], the essential features of parametric amplification can, as with sum-frequency mixing, be demonstrated by initially considering the case of small signal gain. In this case, the pump wave at ω_p is considered to undergo negligible depletion as it propagates through the nonlinear crystal, so that $A_p(z) = A_p(0) =$ constant. With this approximation and assuming that scatter losses may also be ignored and that phase-matching is ideal, then the field variables A_s and A_i can be solved as a pair of coupled linear differential equations, namely;

$$\begin{aligned}\frac{dA_s}{dz} &= -\frac{i}{2}gA_i^* \\ \frac{dA_i}{dz} &= \frac{i}{2}gA_s^*\end{aligned} \quad , \tag{6.49}$$

where

$$g \equiv \kappa A_p(0) = \sqrt{\frac{\mu}{\varepsilon_0}\frac{\omega_s\omega_i}{n_s n_i}}\varepsilon_0 d_{eff}E_p(0) \ . \tag{6.50}$$

Subject to the initial conditions $A_s(z=0) = A_s(0)$, $A_i(z=0) = A_i(0)$ and $A_p(0) = A_p^*(0)$, then the solution to the coupled wave equations (6.49) is;

$$\begin{aligned}A_s(z) &= A_s(0)\cosh\left(\frac{g}{2}z\right) - iA_i^*(0)\sinh\left(\frac{g}{2}z\right) \\ A_i(z) &= A_i(0)\cosh\left(\frac{g}{2}z\right) + iA_s^*(0)\sinh\left(\frac{g}{2}z\right)\end{aligned} \ . \tag{6.51}$$

The solution (6.51) describes the exponential growth of the signal and idler fields under the restrictive conditions noted previously. In the case of parametric amplification it is usual that the input will consist of a strong pump wave at ω_p and one of the other two waves, say ω_s. Noting that the field variable A is related to the photon flux through equ. (6.38), then for $A_i(0) = 0$ equ. (6.51) gives for the photon flux;

$$\Theta_s(z) = K|A_s(0)|^2 \cosh^2\left(\frac{gz}{2}\right) \xrightarrow[gz>>1]{} K\frac{|A_s(0)|^2}{4}\exp(gz)$$
$$\Theta_i(z) = K|A_s(0)|^2 \sinh^2\left(\frac{gz}{2}\right) \xrightarrow[gz>>1]{} K\frac{|A_s(0)|^2}{4}\exp(gz) \quad , \tag{6.52}$$

where K from equ. (6.38) is given by

$$K = \frac{1}{2\hbar}\left(\frac{\varepsilon_0}{\mu}\right)^{\frac{1}{2}} .$$

In the limit gz>>1, equ. (6.52) demonstrates that the photon fluxes undergo exponential growth, while in consideration of A_s alone the signal wave sees an amplification factor of exp(gz)/4.

6.3.2: Phase-Matching in Parametric Amplification

So far consideration has been restricted to the case of ideal phase-matching, however, it is important to assess the effect of a non-zero momentum mismatch between the three waves. Where again the pump field is assumed to constant, the pair of coupled equations describing the rate of change of signal and idler fields can be written as;

$$\frac{dA_s}{dz} = -\frac{i}{2}gA_i^* \exp(-i\Delta kz)$$
$$\frac{dA_i^*}{dz} = \frac{i}{2}gA_s \exp(i\Delta kz) \quad . \tag{6.53}$$

For some finite signal and idler-wave input, described by $A_s(z=0) = A_s(0)$ and $A_i(z=0) = A_i(0)$, then the solution to equ. (6.53) can be shown to be [5];

$$A_s(z)\exp\left(\frac{i\Delta kz}{2}\right) = A_s(0)\left[\cosh(\beta z) - \left(\frac{i\Delta k}{2\beta}\right)\sinh(\beta z)\right] - \left(\frac{ig}{2\beta}\right)A_i^*(0)\sinh(\beta z)$$
$$A_i^*(z)\exp\left(\frac{-i\Delta kz}{2}\right) = A_i^*(0)\left[\cosh(\beta z) + \left(\frac{i\Delta k}{2\beta}\right)\sinh(\beta z)\right] + \left(\frac{ig}{2\beta}\right)A_s(0)\sinh(\beta z) \quad , \tag{6.54}$$

where

$$\beta = \frac{1}{2}\left[g^2 - (\Delta k)^2\right]^{1/2} . \qquad (6.55)$$

Notice that if Δk is set equal to zero in equ's. (6.54) and (6.55), then (6.54) reduces to the result (6.51) for the ideal phase-matched case considered earlier, as it should. Of greater note however, is that the exponential gain function determined by equ. (6.55) is now dependent on the phase-mismatch Δk. To assess the effect Δk has on the parametric gain, the impact three particular values of Δk has on the signal wave amplification factor can be considered; when $\Delta k < g$, $\Delta k > g$ and when $\Delta k = 0$. Firstly, note that in a similar way as to equ. (6.52), the field variable A can be re-expressed in terms of photon flux, which leads to a signal-wave amplification factor given by

$$G_s = \frac{\Theta_s(z)}{\Theta_s(0)} = \cosh^2(\beta z) + \left(\frac{\Delta k}{2\beta}\right)^2 \sinh^2(\beta z) . \qquad (6.56)$$

<u>$\Delta k = 0$</u>

When $\Delta k = 0$, the gain function becomes $\beta = g/2$ and the signal-wave amplification factor is optimised, appearing in the form

$$G_s = \cosh^2\left(\frac{gz}{2}\right) . \qquad (6.57)$$

In the high gain regime where $gz >> 1$, then equ. (6.57) can be approximated to the exponential growth term $G_s \sim (1/4)\exp(gz)$. In the low gain regime ($gz << 1$) the gain factor takes the form $G_s \sim 1 + (1/4)g^2z^2$.

<u>$\Delta k < g$</u>

For $\Delta k < g$, the exponential gain function (6.55) is seen to be always real and consequently the signal wave undergoes amplification as it propagates through the gain medium. Again considering the two regimes of high and low gains, i.e. $\beta z >> 1$ and $\beta z << 1$, then signal wave amplification factor takes the forms;

$$G_s \approx \frac{1}{4}\left[1 + \left(\frac{\Delta k}{2\beta}\right)^2\right]\exp(-2\beta z) , \qquad (\beta z >> 1)$$

$$G_s \approx 1 + \frac{1}{4}g^2z^2 . \qquad (\beta z << 1)$$

$\underline{\Delta k > g}$

With $\Delta k > g$, it is seen from equ. (6.55) that the exponential gain function β becomes imaginary and the cosh and sinh functions in equ. (6.54) take the form of oscillatory sinusoidal functions;

$$\sin\left\{\frac{1}{2}\left[(\Delta k)^2 - g^2\right]^{\frac{1}{2}} z\right\}$$

$$\cos\left\{\frac{1}{2}\left[(\Delta k)^2 - g^2\right]^{\frac{1}{2}} z\right\}$$

Consequently, the signal gain oscillates along the length of the crystal and no sustained growth is experienced by the signal-wave. In contrast, when $\Delta k < g$ the gain was seen to take the form of a hyperbolic function which allowed sustained growth. The transition point from the hyperbolic function to the sinusoidal form in the case of $\Delta k > g$, clearly occurs when $\Delta k = g$, this point being termed *gain threshold* for a parametric device.

6.3.3: Optical Parametric Oscillation

If a nonlinear crystal providing parametric gain similar to that described in the preceding sections is located within an optical resonator, which is resonant at one or both of the signal and idler frequencies, then there will be some threshold pumping intensity which causes simultaneous oscillation at one or both of the signal and idler frequencies. In so doing, the efficiency of the parametric conversion process can be significantly enhanced, the need for which can be adequately demonstrated by a numerical example.

Consider the case of a β-barium borate (BBO) crystal, pumped at an angle $\theta = 30°$ to the optic axis by a frequency tripled and Q-switched Nd:YLF laser operating at 0.349 μm, and where operation is near degenerate. In such a geometry the relevant nonlinear and linear optical parameters are;

nonlinear coefficient (d_{eff})	-	2.1 pm.V^{-1},
signal/idler frequency ($\omega_s \sim \omega_i$)	-	4.3 x 10^{14} Hz,
refractive index of the medium	-	~1.7 for all waves.

A typical diode-laser pumped Nd:YLF laser will produce pulses of around 0.5 MW after frequency tripling, which may be focused typically to a spot of 0.5 mm radius. This then gives a pump power intensity of ~ 65 $MW.cm^{-2}$. Using equ. (6.32) to convert the intensity into the field variable E, and then substituting these values into equ. (6.45) gives a value for the gain coefficient g of 0.3 cm^{-1}.

The signal-wave amplification factor, assuming $\Delta k = 0$, is then given by equ. (6.57) to be only 2.3% for a 1 cm long crystal. This then demonstrates that travelling wave parametric amplification is not expected to give large conversion efficiencies, except where the pump intensity is very high or a very long crystal is used. Consequently, the use of optical parametric oscillators (OPOs) is considered.

An OPO is schematically represented, as in Fig. 6.6, by a nonlinear crystal located within an optical resonator formed by mirrors M1 and M2.

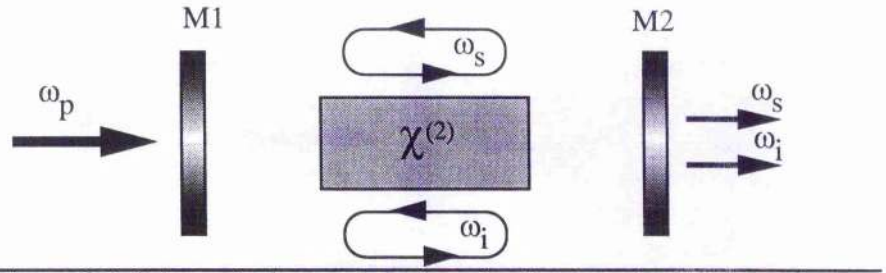

Figure 6.6: Schematical representation of a simple optical parametric oscillator.

The nonlinear crystal when pumped, via the pump transparent mirror M1, provides gain at the signal and idler frequencies ω_s and ω_i. When this gain level exceeds the resonator loss the device reaches threshold and the signal and idler wave powers increase dramatically. The generated output, like that of a laser, is spatially coherent and collinear with the resonator axis, but may be either collinear or noncollinear with the pump axis depending on the phase-match geometry.

6.4: Singly Resonant Optical Parametric Oscillators

Numerous configurations of OPO have been investigated, a particular distinction being made between singly-resonant oscillators (SRO), in which only one of the

parametric waves is resonated, and doubly- or triply-resonant oscillators (DRO, TRO) in which either both the generated parametric waves (DRO) or a combination of the generated parametric waves and pump wave (DRO, TRO) are resonated. Considered here are only singly resonant OPOs, this configuration being well suited to pumping by typical diode-laser pumped and Q-switched Nd lasers.

6.4.1: Pump Threshold and Parametric Gain

The physical process involved in parametric amplification was outlined in the introduction to Section 6.3, where it was noted that a strong pump field will interact with an initially small signal field via the nonlinear polarisation wave to create an incremental field at the idler wave frequency. This in turn creates a further incremental field at the signal frequency and so on, resulting in parametric amplification of both the signal and idler fields at the expense of the pump field. Effective amplification of the signal (and idler field) is only achieved when the parametric oscillator is above threshold, that is when the round trip parametric gain exceeds the resonator loss.

Below threshold there continues to be a parametric interaction in which a pump photon is spontaneously annihilated and a signal and idler photon pair generated. This emission is referred to as *spontaneous parametric emission* or *parametric fluorescence*, the power of which is proportional to the parametric gain. Consequently, the fluorescence observed has a spectral width determined by the sinc^2 phase-match parameter and results in a lineshape centred spectrally about the point where $\Delta k = 0$, or is minimised. Above threshold, the signal and idler fields are amplified at the expense of the pump which then suffers significant depletion. Saturation occurs when the pump intensity has been depleted as far as the threshold level.

Two particular types of SRO are of interest in this work; single-pass and double-pass pumped. Consider firstly a single-pass pumped SRO where the plane-wave approximation is valid.

Single-pass pumped OPO - Pump threshold

As the pump wave propagates through the nonlinear crystal, the generated signal- and pump-waves grow according to equ's. (6.54). Following reflection from the resonator mirror the backward travelling signal- and idler-waves experience no further gain until reflected by the second resonator mirror and are again travelling with the pump wave. The gain is thus single-pass, while the loss is a cumulative round trip loss.

By definition, the parametric amplification factor G for the signal-wave is given by

$$G = \frac{I_s(l) - I_s(0)}{I_s(0)} .$$

Using the intensity to field relationship given in equ. (6.37) this can be re-written as

$$G = \left(\frac{g}{2\beta}\right)^2 \sinh^2(2\beta l) \quad , \tag{6.58}$$

where β and g are as defined previously. For then the case where $(\Delta kl)^2 \gg (gl)^2$ and where gl is small, the amplification factor can be approximated by

$$G \approx \left(\frac{gl}{2}\right)^2 \frac{\sin^2(\Delta kl/2)}{(\Delta kl/2)^2} . \tag{6.59}$$

It is evident then that the gain dependence upon the phase-mismatch is the same as that previously noted for the case of SFG in equ. (6.34). This dependence can be shown by plotting the normalised gain $(G/(gl/2)^2)$ as a function of $\Delta kl/2$ [16], as shown in Fig. 6.7.

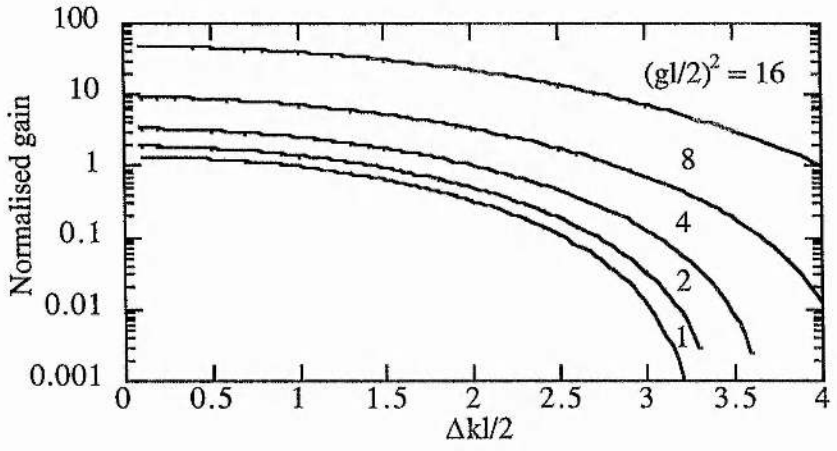

Figure 6.7: Normalised gain as a function of Δk, for various gl products.

For values of $(gl/2)^2$ ranging from 1 to 16, it is evident that the value of $\Delta kl/2$ at which the normalised gain falls to around one half its maximum value is roughly constant

and has a value of ~ $\pi/2$ ($\Delta k = \pi/l$). As for SFG, the value of $\Delta k = \pi/l$ is therefore taken to be the maximum allowable phase-mismatch when calculating such parameters as angular and temperature acceptance bandwidths, as will be discussed in Section 6.5.

Returning to equ. (6.59), for the amplification factor to be maximised the case of $dG/d(\Delta k) = 0$ can be considered. The maximum value of G is then

$$G_{max} = \sinh^2(gl/2) \xrightarrow[gl<<1]{} g^2l^2 = \frac{1}{2}\frac{\omega_s\omega_i}{n_s n_i n_p \varepsilon_0 c^3} d_{eff}^2 l^2 I_p(0) \ . \qquad (6.60)$$

The result shows that the small signal gain for parametric amplification is proportional to the square of the nonlinear coefficient and the crystal length, and varies linearly with the pump intensity. It is useful to note that if the parameter δ is introduced as a detuning parameter from degeneracy, then with

$$\omega_s = \frac{\omega_p}{2}(1+\delta) \quad \text{and} \quad \omega_i = \frac{\omega_p}{2}(1-\delta) \ ,$$

the gain amplification factor may be written as

$$G = \frac{\omega_p^2}{8 n_s n_i n_p \varepsilon_0 c^3} d_{eff}^2 l^2 I_p(0)\left(1-\delta^2\right) . \qquad (6.61)$$

To establish the threshold pump intensity of the OPO it is necessary that the point at which the single pass parametric amplification offsets the resonator loss be considered. For then signal-wave and idler-wave losses described by modified reflectivity coefficients r_s and r_i, the relationship (6.62) has to be satisfied.

$$(gl)^2 = \frac{2\left(1-r_s^2\right)\left(1-r_i^2\right)}{r_s^2 + r_i^2} \qquad (6.62)$$

In the case of a singly resonant OPO where r_s ~ 1 and r_i ~ 0, and using equ. (6.61) with the restriction that gl « 1, the pump threshold intensity is then given by

$$\left[I_p^{th}\right]_{SRO} = \frac{4 n_i n_s n_p \varepsilon_0 c^3}{\omega_i \omega_s d_{eff}^2 l^2}\left(1-r_s^2\right) . \qquad (6.63)$$

A similar analysis for the doubly-resonant OPO shows that the threshold of the SRO is approximately a factor of $2/(1-r_i)$ higher. Compared to a DRO with a parasitic 2% idler-wave loss, the singly resonant OPO has then a threshold some 100 times higher. The DRO however, imposes difficult stability constraints and mirror

requirements, problems which are not fully offset by the reduced threshold in the case of pulsed devices.

Double-pass pumped OPO - Pump threshold

It is possible to reduce the pump threshold of an OPO by non-resonantly reflecting the pump wave back through the nonlinear crystal, in this way providing gain for the parametric waves in both directions of travel in the standing-wave resonator. The reflecting element may be one of the resonator mirrors which is also made highly reflecting at ω_p or may be a separate reflecting element for the pump wave only which has high transparency at the resonated wave frequency ω_s or ω_i. It has been noted, originally by Bjorkholm *et al.* [17], that the phase of the non-resonant parametric wave at the entrance face of the nonlinear crystal is determined by the pump and resonant parametric waves, and so the relative phasing between these latter two waves as they enter the nonlinear crystal on the backward going transit is not important in considering the parametric gain.

For the plane-wave case, the pump threshold of the double-pass pumped SRO can be expressed in terms of the single-pass pumped SRO through the relationship [17];

$$\left[I_p^{th}(R_p)\right]_{SRO} = \frac{\left[I_p^{th}\right]_{SRO}}{\left(1+R_p\right)}, \qquad (6.64)$$

where R_p is the reflectivity of the pump reflector at ω_p. For a perfect pump reflector, the pump threshold can therefore be reduced by a factor of 2. Tang *et al.* [18] have, however, shown that this reduction may be more significant when the effects of Gaussian beam focusing and double-refraction are included.

Optical parametric oscillators with focused Gaussian beams

It should be noted that the analysis presented above is specifically for the case of OPO geometries where the pump and generated parametric waves are plane-waves. The analysis of parametric amplification and oscillation in the case of Gaussian beams requires a rigorous theoretical derivation and has been considered successively by many authors. For a chronological development of the model the reader is referred to the work

of for example; Boyd and Kleinman [7], Bjorkholm [19], Fischer *et al.* [20], Brosnan and Byer [3] and Guha *et al.* [21].

The contribution of these workers included in 1968 the first study by Boyd and Kleinman [7] of the effects of beam focusing and double-refraction on a doubly-resonant OPO. This saw the introduction of a beam focusing parameter ξ, which is defined as the ratio of the coherence length, as defined in Section 6.2.2, to the confocal parameter, and the parameter B which describes the effect of beam walk-off due to double-refraction and is defined by

$$B = \frac{\rho}{2}\left(l_c k_0 n_p / n_0\right)^{1/2}, \tag{6.65}$$

where ρ is the double-refraction angle for an extra-ordinary pump-wave, l_c is the coherence length, and k_0 and n_0 are the wave propagation constant and refractive index at degeneracy. The parameter $h_m(\xi, B)$ was then introduced as an optimisable function dependent upon the power of focusing and double-refraction.

Later, Fischer *et al.* [20] addressed the effects of tight focusing on SRO's, where the pump and resonated waves had the same confocal parameter. This analysis was then extended by Guha *et al.* [21] who derived threshold formulae for both SRO's and DRO's where diffraction, walk-off and beam focusing were unrestricted, but where only a type I phase-match condition (e:o+o) was considered. Most recently this model has been extended further by Tang [18] by allowing for the more general case of any type of phase-matching and additionally double-pass pumping. In this case the general solution for the pump threshold is derived to be;

$$P_{pt} = \frac{\alpha_s}{K_3\left(h_s^+ + R_p h_s^-\right)}, \tag{6.66}$$

where α_s is the round trip signal-wave loss and K_3 and h_s are as described in ref. [18]. The notable feature in this result is that the h_s^- function may be larger than h_s^+, and consequently a greater than factor of 2 reduction in threshold may be achieved.

6.4.2: Spectral Linewidth

The spectral linewidth of the singly resonant OPO is determined by fundamentally three parameters; the gain bandwidth of the OPO itself, the angular divergence of the pump beam and the spectral bandwidth of the pump beam. The primary contribution toward the OPO bandwidth normally comes from the first of these parameters which is in turn dependent upon the dispersive characteristics of the nonlinear crystal and its length. It was shown in Fig. 6.7 that the full-width half-maximum gain bandwidth for the OPO may, in the regime of $(\kappa l)^2 < \sim 15$, be defined by the condition $|\Delta k| < \pi/l$. Through a Taylors series expansion of Δk, it can then be shown that the full-width signal gain bandwidth determined by this condition is then

$$\Delta\omega_{sig} = \frac{2\pi c}{l}\left[n_i - n_s + \lambda_s \frac{dn_s}{d\lambda_s} - \lambda_i \frac{dn_i}{d\lambda_i}\right]^{-1} . \qquad (6.67)$$

6.5: Phase-Matching Methods

In the preceding discussion a phase-mismatch term Δk has been introduced, describing the difference in phase velocity between the fundamental and parametric waves and for the three-frequency process is defined by;

$$\Delta k = k(\omega_3) - k(\omega_2) - k(\omega_1) , \qquad (6.68)$$

$$\Delta k = \sqrt{\left[k(\omega_3)^2 + k(\omega_1)^2 - 2k(\omega_3)k(\omega_1)\cos\alpha\right]} - k(\omega_2) , \qquad (6.69)$$

where equ. (6.68) describes the case of a collinear phase-matching process and equ. (6.69) the noncollinear case with a noncollinear angle α. It has been seen that only if Δk can be made substantially equal to zero, and thus for some gain length l then Δkl remains less than π, will the parametric process become efficient. However, for typical dispersion values in many crystals this constraint is only satisfied over a coherence length of a few tens of microns.

To overcome this difficulty an effective way of obtaining near equal phase velocities is to offset the materials dispersion by natural birefringence in uniaxial or biaxial crystals. In such crystals there are two refractive indices for a given direction of

propagation, corresponding to the two allowed orthogonally polarised modes. In this way, with a suitable choice of propagation direction and polarisation states it is often possible to approach the condition $\Delta k = 0$. This is known as *phase-matching* or *index-matching*.

Where the birefringence properties of the crystal are exploited by choosing a particular direction of propagation, the type of phase-matching is known as *critical phase-matching*. The birefringence of a crystal may also, however, be altered by changing the crystal temperature. In this case the choice of propagation direction is chosen to be along one of the principal crystallographic axes and the temperature varied until for some given set of polarisation states the condition $\Delta k = 0$ is again satisfied. This is known as *non-critical phase-matching*.

Critical and non-critical phase-matching are now described in more detail, followed by a discussion of limiting acceptance parameters, as for example; maximum allowable fundamental wave divergence and crystal temperature fluctuation.

6.5.1: Critical Phase-Matching

For some wave described by a wavevector **k**, propagating through a birefringent medium, the index of refraction experienced is determined by the Fresnel equation;

$$\frac{1}{n^2} = \frac{k_x^2}{n^2 - n_x^2} + \frac{k_y^2}{n^2 - n_y^2} + \frac{k_z^2}{n^2 - n_z^2} , \qquad (6.70)$$

where k_i are the cosine vectors of **k** measured relative to the principal optical axes and n_i are the refractive indices along the principal axes. Using then θ to denote the angle between the wavevector **k** and the principal axis z, and $\emptyset$ to denote the azimuth angle in the x-y plane, then the cosine vectors are given by;

$$\begin{aligned} k_x &= \sin\theta\cos\phi \\ k_y &= \sin\theta\sin\phi \\ k_z &= \cos\theta \end{aligned} \quad . \qquad (6.71)$$

In the general case of a biaxial crystal and where n_a and n_b are used to represent the refractive indices of the allowed eigen-polarisations, then from equ. (6.70) one obtains, for the case $n_x < n_y < n_z$, the solution [22];

$$n_a = \left[\frac{2}{-B+\sqrt{B^2-4C}}\right]^{\frac{1}{2}}, \qquad n_b = \left[\frac{2}{-B-\sqrt{B^2-4C}}\right]^{\frac{1}{2}} \tag{6.72}$$

where

$$B = \left[-k_x^2(n_y^{-2}+n_z^{-2}) - k_y^2(n_x^{-2}+n_z^{-2}) - k_z^2(n_x^{-2}+n_y^{-2})\right]$$

$$C = \left(\frac{k_x}{n_y n_z}\right)^2 + \left(\frac{k_y}{n_x n_z}\right)^2 + \left(\frac{k_z}{n_x n_y}\right)^2$$

In the simplified case of a uniaxial crystal, where $n_x = n_y = n_0$ and $n_z = n_e$, then the two solutions reduce to the simpler form previously given in equ. (6.25)

$$n_a' = n_o$$

$$n_b' = n_e(\theta) = \frac{n_o n_e}{\left[n_o^2 \sin^2(\theta) + n_e^2 \cos^2(\theta)\right]^{1/2}} . \tag{6.73}$$

It is obvious in equ. (6.72) that for some given frequency then $n_b > n_a$. As dispersion results in an increasing index of refraction with frequency it is apparent that the high frequency wave index of refraction must be described by n_a while at least one of the low frequency waves must be described by n_b. There are then three possible phase-matched processes, which on setting $\Delta k = 0$ and re-expressing equ. (6.68) can be written in the form;

$$n(\omega_3)_a \omega_3 = n(\omega_1)_b \omega_1 + n(\omega_2)_b \omega_2 , \tag{6.74}$$

$$n(\omega_3)_a \omega_3 = n(\omega_1)_a \omega_1 + n(\omega_2)_b \omega_2 , \tag{6.75}$$

$$n(\omega_3)_a \omega_3 = n(\omega_1)_b \omega_1 + n(\omega_2)_a \omega_2 . \tag{6.76}$$

The three phase-matching conditions described by equ's. (6.74-76) are generally referred to as *type I, type II* and *type III* phase-matching respectively. Phase-matching curves can then be generated by substituting equ. (6.72) or (6.73) into (6.74-76).

6.5.2: Non-critical Phase-Matching

It has been observed in Section 6.1 that when wave propagation is at some angle to the principal optical axis, the extraordinary wave in the parametric interaction experiences Poynting vector walk-off, so reducing interaction lengths and impacting efficiency. Provided that the difference in refractive index between the interacting waves is small and that the dn/dT coefficients of the crystal are non-zero, then it is possible to change the birefringence of the crystal by varying the crystal temperature and thus achieve non-critical phase-matching.

Other methods exist also for attaining non-critical phase-match conditions, but an in-depth discussion of these lies outwith the scope of this thesis. Notably, two such methods are crystal doping and quasi-phase-matching. Through the introduction of dopants into a crystal lattice, the crystal birefringence can be altered resulting in a spectral shift in its phase-match properties [23]. One such application of this technique has been the introduction of various dopants into potassium titanyl phosphate (KTP), so allowing second harmonic generation at wavelengths as low as 0.9 μm compared to the normal short wavelength cut-off of 0.98 μm in a non-critical geometry [24]. This is of particular significance as KTP has near zero dn/dT coefficients and therefore cannot be effectively temperature tuned.

Quasi-phase-matching (QPM) is a technique by which the relative phase-mismatch in a parametric process, normally a non-critically phase-matched geometry, is circumvented by introducing a periodic correction at regular intervals along the crystal length. First suggested independently by Armstrong *et al.* [1] and Franken and Ward [25], QPM may be implemented in a number of ways. Early experiments were based on domain reversal by stacking up thin plates of suitable materials [26, 27], however, more recently periodically alternating domain structures have been created in bulk material by applying a periodic electric field [28-30]. The periodic domain structure has associated with it a grating wavevector

$$K_m = \frac{2\pi m}{\Lambda}, \qquad (6.77)$$

where m is the grating order and Λ the grating period. The grating period is then chosen so that the grating wavevector equals the phase-mismatch Δk in the bulk material. In the simple case of second harmonic generation this is readily seen to be just

$$\Lambda = \frac{\lambda_\omega}{2(n_{2\omega} - n_\omega)} . \tag{6.78}$$

6.5.3: Acceptance Parameters

The achievable efficiency in a parametric process depends on various parameters related to the pump source, such as; intensity, beam divergence and spectral linewidth, and on crystal parameters such as nonlinear coefficient, interaction length and the deviation in crystal temperature and orientation from the optimum operating point. A number of these parameters are obviously included in the expressions derived previously for threshold and efficiency, however, others including spectral linewidth, angular acceptance bandwidth and temperature acceptance bandwidth should also be considered.

To determine the allowable bandwidths, Δk is expanded in a Taylors series, normally to the second order only, and as a function of the parameter of interest. This results in a quadratic equation of the form [31]

$$\Delta k = \Delta k_0 + \frac{\partial \Delta k}{\partial \Omega}\Delta\Omega + \frac{1}{2}\frac{\partial^2 \Delta k}{\partial \Omega^2}(\Delta\Omega)^2 + \ldots\ldots , \tag{6.79}$$

where Ω denotes one of the parameters of wavelength, temperature or angle, and the equation is solved for ΔΩ which is the maximum allowable variation in this parameter to satisfy the expression for some given Δk.

It should be noted that several conventions are used in defining Δk. One of these defines the width of the half maximum point of the $sinc^2$ parametric gain profile discussed earlier, so that in this case Δkl/2 ~ 1.39. In a second case, the bandwidth is determined from the point at which the first zero is reached in the $sinc^2$ gain curve, in which case Δkl/2 = π. The convention used here is as noted previously that in which Δkl/2 = π/2, this being the point at which the gain has dropped to ~0.4 times its optimum value. Substituting this value into equ. (6.79) and making the approximation $\Delta k_0 = 0$, then the Taylors series expansion becomes

$$\frac{\partial \Delta k}{\partial \Omega}\Delta\Omega + \frac{1}{2}\frac{\partial^2 \Delta k}{\partial \Omega^2}(\Delta\Omega)^2 \approx \frac{\pi}{l} \,. \tag{6.80}$$

Equ. (6.80) is then a simple quadratic expression in $\Delta\Omega$ and has solutions of the form;

$$\Delta\Omega = \frac{-\frac{\partial \Delta k}{\partial \Omega} \pm \left[\left(\frac{\partial \Delta k}{\partial \Omega}\right)^2 + \frac{2\pi}{l}\frac{\partial^2 \Delta k}{\partial \Omega^2}\right]^{\frac{1}{2}}}{\frac{\partial^2 \Delta k}{\partial \Omega^2}} \,. \tag{6.81}$$

It should be noted that the range of values taken by the acceptance parameter is $2\Delta\Omega$, as Δk can take on values over the range $\pm \pi/l$.

Chapter 6 References:

1. J. A. Armstrong, N. Bloembergen, J. Ducuing and P. S. Pershan *"Interaction between light waves in a nonlinear dielectric"* Phys. Rev. 127 (6) pp.1918-1939, 1962.

2. R. L. Byer *"Parametric oscillators and nonlinear materials"* Proc. of the sixteenth Scottish Universities Summer School in Physics, (Academic Press, London), 1977.

3. S. J. Brosnan and R. L. Byer *"Optical parametric oscillator threshold and linewidth studies"* IEEE J. Quant. Elect. QE-15 (6) pp.415-431, 1979.

4. D. A. Kleinman *"Nonlinear dielectric polarisation in optical media"* Phys. Rev. 126 (6) pp.1977-1979, 1962.

5. A. Yariv: *"Optical Electronics - Fourth Edition"* (Harcourt Brace Jovanovich College Publishers, Orlando), 1991.

6. P. S. Pershan *"Nonlinear optical properties of solids: Energy considerations"* Phys. Rev. 130 (3) pp.919-929, 1963.

7. G. D. Boyd and D. A. Kleinman *"Parametric interaction of focused Gaussian light beam"* J. Appl. Phys. 39 (8) pp.3597-3639, 1968.

8. R. G. Smith: *"Optical Parametric Oscillators* in *Lasers"* (Dekker Publishers, New York), 1976.

9. B. Wyncke and F. Brehat *"Calculation of the effective second-order non-linear coefficients along the phase matching directions in accentric orthorhombic biaxial crystals"* J. Phys. B: At. Mol. Opt. Phys. 22 (2) pp-363-376, 1989.

10. W. Koechner: *"Solid-state laser engineering - Second Edition"* (Springer-Verlag Series in Optical Sciences, New York), 1985.

11. V. G. Dmitriev *"Handbook of nonlinear optical crystals"* (Springer-Verlag, Berlin), 1991.

12. F. Brehat and B. Wyncke *"Calculation of double-refraction walk-off angle along the phase-matching directions in non-linear biaxial crystals"* J. Phys. B. At. Mol. Opt. 22 (11) pp1891-1898, 1989.

13. P. A. Franken, A. E. Hill, C. W. Peters and G. Weinreich *"Generation of optical harmonics"* Phys. Rev. Lett. 7 (4) pp118-119, 1961.

14. A. V. Smith, W. J. Alford and T. D. Raymond *"Comparison of a numerical model with measured performance of a seeded, nanosecond KTP optical parametric oscillator"* J. Opt. Soc. Am. B 12 (11) pp.2253-2267, 1995.

15. A. V. Smith and M. S. Bowers *"Phase distortions in sum-frequency and difference-frequency mixing in crystals"* J. Opt. Soc. Am. B 12 (1) pp.49-57, 1995.

16. S. E. Harris *"Tunable optical parametric oscillators"* Proc. of the IEEE 57 (12) pp.2096-2113, 1969.

17. J. E. Bjorkholm, A. Ashkin and R. G. Smith *"Improvement of optical parametric oscillators by nonresonant pump reflection"* IEEE J. Quant. Elect. QE-6 (12) pp.797-799, 1970.

18. Y. Tang, C. F. Rae, C. P. Rahlff and M. H. Dunn *"Low threshold, high efficiency and widely tunable infrared source from a KTP based OPO"* accepted for publication in J. Opt. Soc. B. 14 (12), (1997).

19. J. E. Bjorkholm *"Some effects of spatially nonuniform pumping in pulsed optical parametric oscillators"* IEEE J. Quant. Elect. QE-7 (3) pp.109-118, 1971.

20. R. Fischer, C. Tramba and L. W. Wieczorek *"Optical focusing in a singly resonant optical parametric oscillator"* Sov. J. Quant. Elect. 7 (12) pp.1455-1458, 1977.

21. S. Guha, F. J. Wu and J. Falk *"The effects of focusing on parametric oscillation"* IEEE J. Quant Elect. QE-18 (5) pp.907-912, 1982.

22. J. Q. Yao and T. S. Fahlen *"Calculations of optimum phase match parameters for the biaxial crystal $KTiOPO_4$"* J. Appl. Phys. 55 (1) pp.65-68, 1984.

23. J. Y. Wang, Y. G. Liu, J. Q. Wei, M. H. Jiang, Z. S. Shao, W. J. Liu and S. S. Jiang *"Growth, characterization and non-critical phase-matching of niobium-doped KTP crystals"* Cryst. Research and Technology 32 (2) pp.319-327, 1997.

24. K. Hutton, R. Ward, P. Thomas, C. F. Rae and M. H. Dunn *"Growth and Characterisation of tantalum and niobium doped KTP"* in preparation - Clarendon Laboratory, Oxford, 1997.

25. P. A. Franken and J. F. Ward *"Optical harmonics and nonlinear phenomena"* Rev. Mod. Phys. 35 (1) pp.23-29, 1963.

26. C. F. Dewey, Jr. and L. O. Hocker *"Enhanced nonlinear optical effects in rotationally twinned crystal"* Appl. Phys. Lett. 26 (8) pp.442-444, 1975.

27. M. Okada, K. Takizawa and S. Ieiri *"Second harmonic generation by periodic laminar structure of nonlinear optical crystal"* Opt. Comm. 18 (3) pp.331-334, 1976.

28. G. A. Magel, M. M. Fejer and R. L. Byer *"Quasi-phase-matched second harmonic generation of blue light in periodically poled $LiNbO_3$"* Appl. Phys. Lett. 56 (2) pp.108-110, 1990.

29. M. M. Fejer, G. A. Megel, D. H. Jundt and R. L. Byer *"Quasi-phase-matched second harmonic generation: tuning and tolerances"* IEEE J. Quant. Elect. 28 (11) pp.2631-2654, 1992.

30. J.-P. Meyn and M. M. Fejer *"Tunable ultraviolet radiation by second-harmonic generation in periodically poled lithium tantalate"* Opt. Lett. 22 (16) pp.1214-1216, 1997.

31. N. P. Barnes and V. J. Corcoran *"Parametric generation processes: spectral bandwidth and acceptance angles"* Appl. Opt. 15 (3) pp.696-699, 1976.

Chapter 7
All-Solid-State LBO and Narrow Linewidth β-BBO, Pulsed OPOs

In this chapter, the design and characterisation of pulsed optical parametric oscillators (OPO's) is discussed, which are pumped by frequency up-converted, diode-laser pumped solid-state lasers, including the 144 mJ-diode-laser pumped Nd:YLF laser discussed in Chapter 4. A second pump laser based on Nd:YAG, which has been previously developed with co-workers in this School [1], and which is also diode-laser pumped but in a side-pumped geometry is also used.

While pulsed OPO's based on the materials beta-barium borate (β-BBO) and lithium triborate (LBO) have in recent years become well developed devices, previous studies in all-solid-state configurations have concentrated on using either the fundamental or frequency-doubled output of the Nd laser, see for example ref. [2], so providing a tunable output in the red and near-infrared, or the use of high energy flashlamp pumped and frequency tripled Nd lasers for UV pumped devices, as for example described in ref's [3, 4]. In particular, less attention has been given to the operation of this type of OPO at low pump pulse energies (< 10 mJ) in the UV, more suited to the moderate powers readily available from diode-laser pumped solid-state lasers. This school was the first to demonstrate an all-solid-state configuration [5], in which a low threshold (<0.5 mJ) LBO based OPO was developed, which was tunable over the range 0.45 μm to 1.68 μm when pumped at 0.355 μm. Now, the further development of this device is presented, where: (i) the frequency tripled Nd:YAG laser used previously has been replaced by the frequency tripled 144 mJ-diode-laser pumped Nd:YLF laser, previously discussed in Chapter 4, (ii) the threshold has been further reduced and (iii) the tuning range extended.

With only modest pump energies involved, a compact reliable and widely tunable source is promised through the realisation of this approach. However, for such a source to exploit fully a potentially wide-range of applications, such as in spectroscopy,

linewidth control is vital. Narrow-linewidth operation to the point of obtaining single longitudinal mode output from the OPO must therefore be considered. Again previous studies have tended to concentrate on IR or green pumped OPOs and non-diode-laser pumped sources [6, 7, 8]. Now, the development of line-narrowed, UV pumped β-BBO OPOs is presented, which are pumped by all-solid-state diode-laser pumped Nd lasers and have thresholds of just a few millijoules.

7.1: Frequency Doubling and Tripling of the Nd Pump Lasers

7.1.1: Experimental Set-up

The OPO's discussed in this chapter are all pumped by frequency tripled Nd lasers. The tripling scheme adopted follows one of the standard techniques for generating the third harmonic of a Nd laser, by way of frequency doubling the fundamental Nd laser output in potassium titanyl phosphate (KTP) and then sum-frequency mixing the generated second harmonic wave and residual fundamental wave in lithium triborate (LBO). The generic experimental set-up is shown schematically in Fig. 7.1.

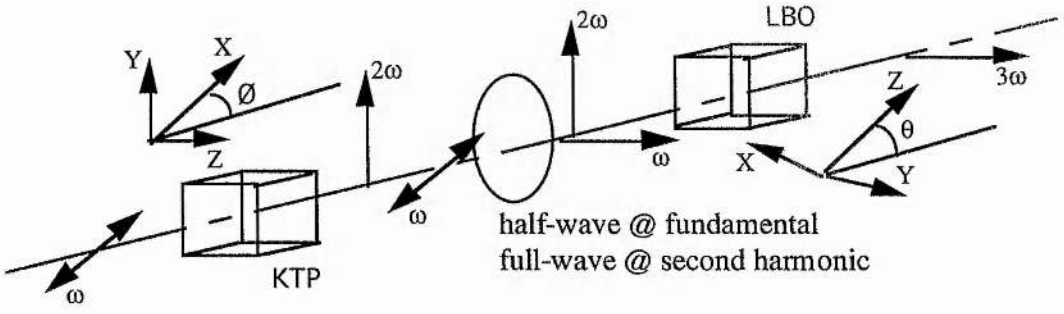

Figure 7.1: Experimental set-up for frequency up-conversion of the Nd pump lasers.

As will be described later, the peak power and consequently field intensity of the output of the Nd lasers used to pump the optical parametric oscillators is sufficiently high as to not to have to focus the fundamental wave into the nonlinear crystals used in the frequency up-conversion process. Some reduction in waist size is however desirable and so the fundamental beam first impinges a beam compression telescope which is set afocal. The KTP frequency doubling crystal and LBO sum-frequency mixing crystals are

both cut for type II critical phase-match (CPM) interactions. The linear and nonlinear parameters associated with these interactions are summarised in Table 7.1.

Process	Material	theta	phi	d_{eff} (pm.V^{-1})	Walk-off (mrad)	δ(θ,Ø) (mrad)
SHG	KTP	90	24.8†	3.175	4.7	47.4, 19.7
		90	37.1#	3.042	6.0	47.5, 15.3
SFM	LBO	43.1†	90	0.655	9.3	3.5, 50.6
		47.0#	90	0.613	9.3	3.5, 47.9

† - 1064 nm fundamental (Nd:YAG), # - 1047 nm fundamental (Nd:YLF)
δ - angular acceptance bandwidth for 5 mm KTP crystal and 10 mm LBO crystal

Table 7.1: Second and third harmonic generation design parameters.

It is apparent that in this arrangement , i.e. the type II SHG interaction being followed by a type II SFM interaction, only one half of the residual fundamental beam after the SHG stage will be in the correct polarisation state for the SFM stage. Means are available by which this difficulty may be overcome, for example; (i) a dual wavelength retardation plate may be incorporated between the SHG and SFM stages, which acts as a half-wave retardation plate at the fundamental wavelength and full-wave retardation plate at the second harmonic, so that, without affecting the second harmonic polarisation state, the plane of polarisation of the fundamental wave can be rotated to be orthogonal to it and so optimised for mixing, or (ii) launching the fundamental wave into the KTP frequency doubling crystal such that the field polarisation is at an angle $\theta_p = \tan^{-1}(1/\sqrt{2})$ to the KTP z-axis. This arrangement ensures that two o-photons at ω are input for every e-photon, resulting in the creation of an e-photon at 2ω and a residual o-photon at ω for combining in the tripling stage. Craxton *et al.* [9] have proposed that in excess of 90% efficiencies are attainable using this technique, however, only 80% has been demonstrated [10]. In this work the UV pulse energies available without incorporating such techniques are sufficient for carrying out the nonlinear optical studies and so no polarisation correction is incorporated.

7.1.2: Up-converted 144 mJ-Diode-Laser Pumped Nd:YLF Laser

As the pump source for the LBO OPO, which will be discussed in Section 7.2, the 144-mJ-diode-laser pumped Nd:YLF laser discussed in Chapter 4 has been frequency

tripled using the methods described here. A x2 reduction telescope is used to compress the fundamental beam prior to the KTP frequency doubling crystal, giving a spot size of 0.46 mm ($1/e^2$ radius), whereafter the fundamental propagates as a collimated beam through both the frequency doubling and frequency tripling stages. Design parameters and resulting pulse energies at the maximum pump level are summarised in Table 7.2.

KTP size (w x h x l)	Pulse energy (0.523 μm)	Pulse duration (0.523 μm)	LBO size (w x h x l)	Pulse energy (0.349 μm)	Pulse duration (0.349μm)
5 x 5 x 5 mm	5.3 mJ	8.5 nsec	5 x 5 x 14 mm	2.1 mJ	6.0 nsec

Table 7.2: Frequency up-conversion parameters.

The maximum conversion efficiencies observed for each frequency up-conversion process are then 46% for SHG (ω:2ω) and 18.3% for SFM (ω:3ω). For a fundamental pulse energy of 10 mJ, 11 nsec duration and 0.46 mm spot size, the average pump intensity impinging the frequency doubling crystal is 137 $MW.cm^{-2}$. For this type of laser the overall conversion efficiency from the fundamental to third harmonic can be shown to saturate at around 30% for a fundamental beam intensity of ~ 300 $MW.cm^{-2}$ [11] . Further optimisation is then possible, however, is not necessary for this work.

The spatial profile of the generated third harmonic wave is near Gaussian with a spot size of 0.4 mm ($1/e^2$ radius). The M^2 value is calculated to be 1.5 (0.67 mm.mrad).

7.1.3: Up-converted 144-mJ Diode-Laser Pumped Nd:YAG Laser

As the pump source for the β-BBO OPO, which will be discussed in Section 7.3, a 144-mJ-diode-laser pumped Nd:YAG laser developed in-house [5] has been used as the basis, the laser having been upgraded in terms of; (i) spectral quality when necessary, by the addition of the slow-Q-switching technique described in Chapter 5, and (ii) pulse energy, by the addition of an amplifier stage. The laser and amplifier are depicted schematically in Fig. 7.2.

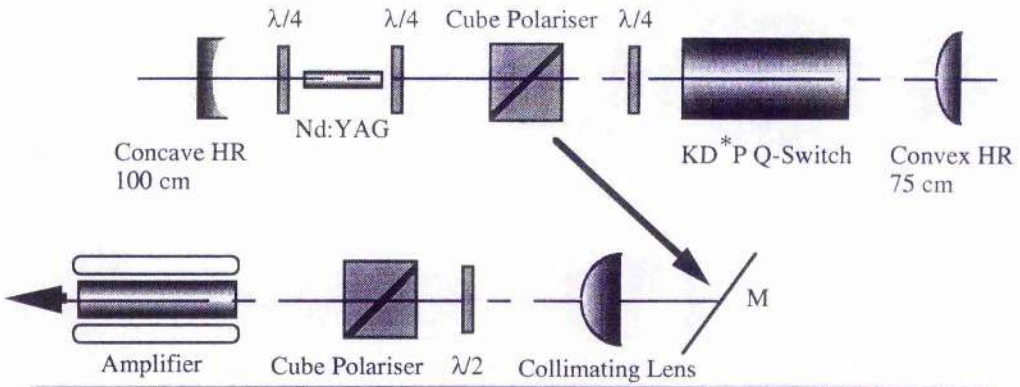

Figure 7.2: Diode-laser pumped Nd:YAG laser and amplifier.

The Nd:YAG oscillator is based on a 20 mm long x 3 mm diameter Nd:YAG (Nd 1.1%) rod, which is side pumped by 6, 2-bar stacked diode-laser arrays (SDL-3230-TA). The arrays are arranged in a three-fold symmetrical pattern about the Nd:YAG rod in a close coupled geometry, resulting in a circularly symmetric gain profile which is well matched to the lowest order transverse mode of the resonator. The quasi-CW diode-laser arrays each emit pulses of 200 μsec duration and 24 mJ energy, providing a total of 144 mJ of pump radiation. The resonator is of a convex-concave design (100 cm radius of curvature concave mirror and 75 cm radius of curvature convex mirror, separated by an optical distance of 34 cm). With a conventional Q-switching geometry, based on a KD*P Pockels cell, pulses of 10 mJ energy at 1.064 μm and in a TEM_{00} mode ($M^2 = 1.3$) are obtained. The pulse duration is 14 nsec and the laser is typically operated at 10 Hz.

As the laser is to be used in the study of line-narrowed OPOs pumped by its third harmonic, where thresholds are likely to be a few millijoules, it is necessary to increase the available pulse energy. To the laser then has been added a flashlamp pumped amplifier stage. This is the pump chamber from a Quantel YG481 laser and is based on a 1% Nd doped Nd:YAG rod which is 115 mm long and 7 mm diameter. The rod is located between 2 krypton flashlamps in a diffuse reflector type chamber. At the maximum lamp discharge voltage of 1.825 kV (25 J per lamp), the amplifier provides a single pass gain of 10, increasing the IR pulse energy to 75 mJ. The beam quality is reduced slightly, the M^2 value of the amplified beam being measured to be 1.7.

For use in the future at higher pulse energies, double-pass amplifier geometries have also been considered. In the first of these, shown in Fig. 7.3, a quarter-waveplate and mirror are located after the amplifier, so as to reflect the amplified beam from the first

pass back along the same optical path to be amplified again on a second pass. The beam is then decoupled from the original optical path by the polariser, the plane of polarisation of the amplified beam having been rotated 90° by a double pass of the quarter-waveplate.

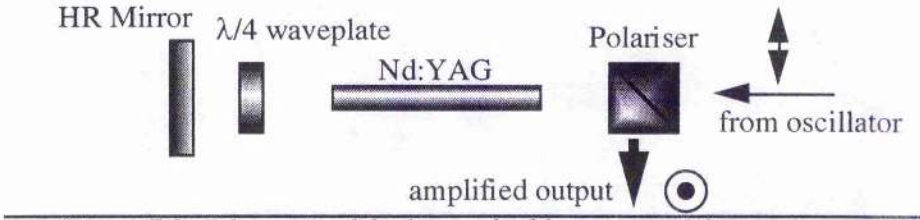

Figure 7.3: Schematic of the linear double pass amplifier arrangement.

While providing a further amplification factor of around 3, this linear scheme has the disadvantage of some feed-back leaking through the polariser back into the oscillator. This leakage is found to be tolerable when operating the laser multi-longitudinal mode, however, even with the insertion of an optical isolator is found to upset the pre-lase pulse formation when operating the laser SLM, using the technique described in Chapter 5. To circumvent this difficulty a ring amplifier arrangement has also been assessed.

In the arrangement shown in Fig. 7.4, light is never reflected back along its incident path toward the oscillator, so eliminating feed-back effects. By following the optical path in Fig. 7.4, it can be seen that after a first pass through the amplifier, the radiation is reflected by a second polariser (pol-2), now located after the amplifier, around a loop and then coupled back along the original optical path and in the same direction of propagation as the first amplification pass, by the first polariser (pol-1). For the second pass of the amplifier the plane of polarisation is orthogonal to the first, so that the further amplified light is now transmitted by pol-2 and used as the useful output. In this arrangement amplification factors of greater than 3 have again been observed, but now as expected with no feed-back being observed.

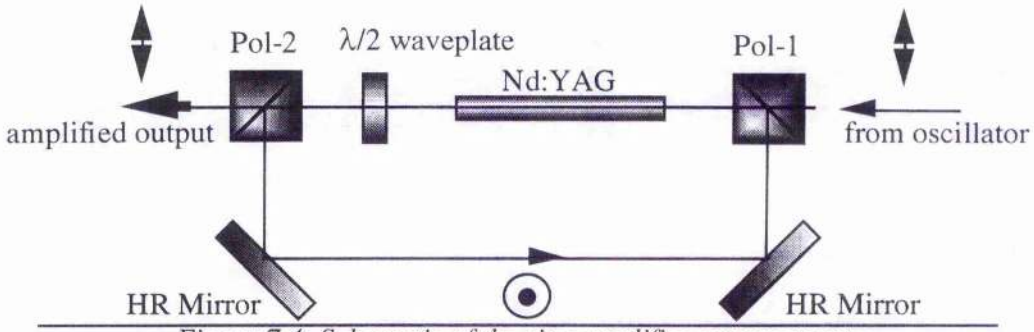

Figure 7.4: Schematic of the ring amplifier arrangement.

During the nonlinear optical studies described in Section 7.3, it is necessary at times to address the use of a line-narrowed pump source. To this end the slow-Q-switching technique described in Chapter 5 has also been applied to this laser. It is found, however, that slow-Q-switching alone does not in this case result in reliable SLM operation, due to spatial hole burning effects. To circumvent this problem the Nd:YAG resonator is made to be of a twisted mode type, by the introduction of suitably orientated λ/4 waveplates at each end of the gain element. In so doing SLM operation is observed for around 90% of the time.

With the introduction of the frequency up-conversion methods described in Section 7.1.1 the laser output has been frequency tripled to 0.355 μm. A x2 reduction telescope is used to compress the fundamental beam prior to the KTP frequency doubling crystal, giving a spot size of 1.2 mm ($1/e^2$, radius), whereafter the fundamental propagates as a collimated beam through both the frequency doubling and frequency tripling stages. Design parameters and resulting pulse energies at the maximum pump level are summarised in Table 7.2.

KTP size (w x h x l)	Pulse energy (0.532 μm)	Pulse duration (0.532 μm)	LBO size (w x h x l)	Pulse energy (0.355 μm)	Pulse duration (0.355 μm)
5 x 5 x 5 mm	42 mJ	9.8 nsec	5 x 5 x 14 mm	18 mJ	8.0 nsec

Table 7.2: Frequency up-conversion parameters.

The maximum conversion efficiencies observed for each frequency up-conversion process are then 56% for SHG (ω:2ω) and 24% for SFM (ω:3ω).

The spatial profile of the generated third harmonic wave is near Gaussian with a spot size of 0.87 mm ($1/e^2$ radius), measured at the position at which the optical parametric oscillator will be located. The M^2 value is calculated to be 1.8 (0.81 mm.mrad).

7.2: All Solid-State Lithium Triborate OPO

In this section, the development of a low-threshold OPO based on the nonlinear material lithium triborate (LBO) is described. The principal aim is to develop a device which has a low threshold (preferably less than 0.5 mJ) and consequently is suited to pumping by moderate power diode-laser pumped solid-state lasers, and which can fully exploit the broad tuning ranges known to be associated with UV pumped LBO OPOs. The device is pumped by the frequency up-converted 144-mJ-diode-laser pumped Nd:YLF described in Section 7.1.2.

7.2.1: Design Parameters

A schematical representation of the type I (e:o+o) critically phase-matched LBO OPO is shown in Fig. 7.5.

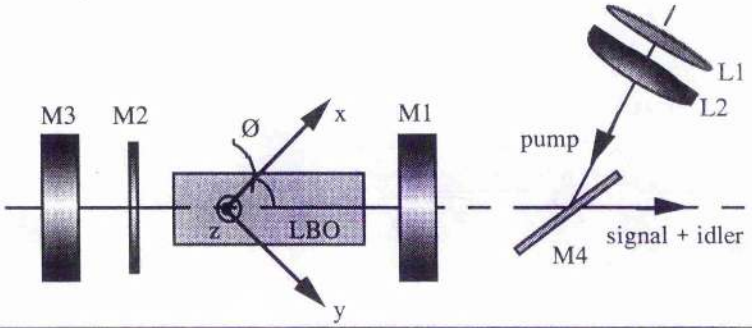

Figure 7.5: Type I critically phase-matched LBO OPO.

The OPO consists of a single crystal of LBO located within a resonator, which in this case is designed to resonate the short-wavelength signal-wave. The UV pump-wave is linearly polarised in the x-y plane (e-wave) and the generated signal- and idler-waves are orthogonally polarised to the pump and parallel to the z-axis (o-waves). The OPO is tuned by rotating the LBO crystal about the z-axis (in the x-y or Ø-plane). The expected

tuning behaviour is shown in Fig. 7.6, which has been calculated using the Sellmeier data of Lin *et al.* [12] as given in equ. (7.1).

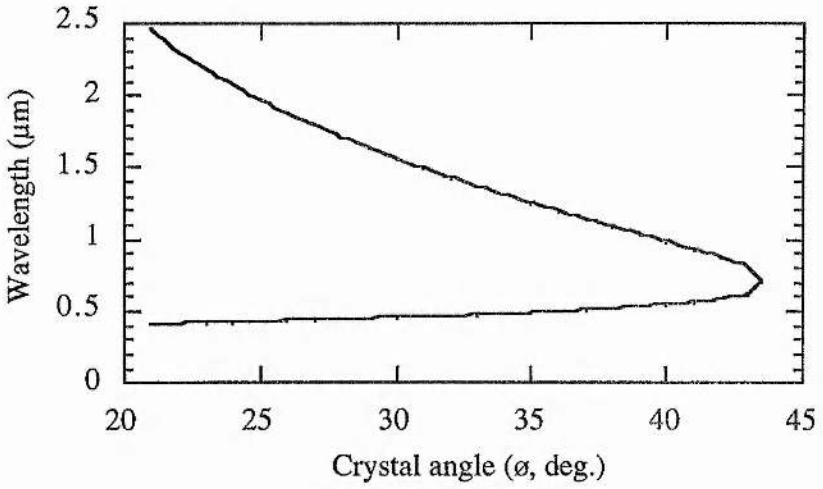

Figure 7.6: Tuning behaviour of the 0.349 μm pumped LBO OPO in the x-y plane.

It is seen that tuning is over the range 21° to 44° in the Ø-plane and thus a crystal cut for propagation along Ø = 31° at normal incidence is used. The crystal dimensions are 6 x 3 x 15 mm^3 and it is polished but uncoated. The 6 mm dimension is in the Ø-plane to allow angular rotation without aperturing the beams.

With reference to Fig. 7.5, the resonator mirrors are located in close proximity to the LBO crystal in order to minimise the resonator length in this low-threshold device. The UV pump light is transmitted by the OPO partial reflector (M1), passes through the nonlinear crystal and is reflected by the intra-cavity UV reflector (M2), either back along its original path, forming a double-pass pump geometry, or slightly off-axis, forming a single-pass pump geometry. The OPO resonator is formed by the broadband partial reflector (M1) and broadband high reflector (M3), separated by 25 mm (physical length not allowing for the index of refraction of the LBO). A partially reflecting mirror coating was not available at the time which had a sufficiently broad bandwidth to cover the entire signal-wave range while having with a sufficiently high damage threshold to withstand the intense UV pump field. Consequently, for optimum performance two different output couplers have then to be used, although, threshold could be reached across the entire tuning range with a single mirror set. A combination of the two partial reflectors provides a nominal 95% reflectivity across the signal-wave tuning range. The pump

wave and generated parametric waves are separated outside the OPO resonator by a Brewster angled dichroic separator (M4).

The pump light is focused into the OPO using a spherical (+400 mm) / cylindrical (+150 mm) lens combination (L1 and L2), both of which are fabricated from UV grade fused silica and uncoated. In this type I geometry the pump-wave, which is the e-wave, will walk-away from the signal and idler o-waves due to Poynting vector walk-off. In a low-threshold device employing a tight focusing geometry, the effects of walk-off can significantly reduce the effective interaction length in the nonlinear crystal and thus increase threshold and reduce efficiency. For this reason a cylindrical focusing geómetry is adopted, where the beam is loosely focused in the plane containing the walk-off direction and tightly focused in the orthogonal plane. The pump beam walk-off in this case is calculated using equ. (6.32), where the refractive indices for LBO are again given by equ. (7.1).

$$\begin{aligned} n_x^2 &= 2.45316 + 0.01150/(\lambda^2 - 0.01058) - 0.01123 * \lambda^2 \\ n_y^2 &= 2.53969 + 0.01249/(\lambda^2 - 0.01339) - 0.02029 * \lambda^2 \\ n_z^2 &= 2.58515 + 0.01412/(\lambda^2 - 0.00467) - 0.01850 * \lambda^2 \end{aligned} \quad . \qquad (7.1)$$

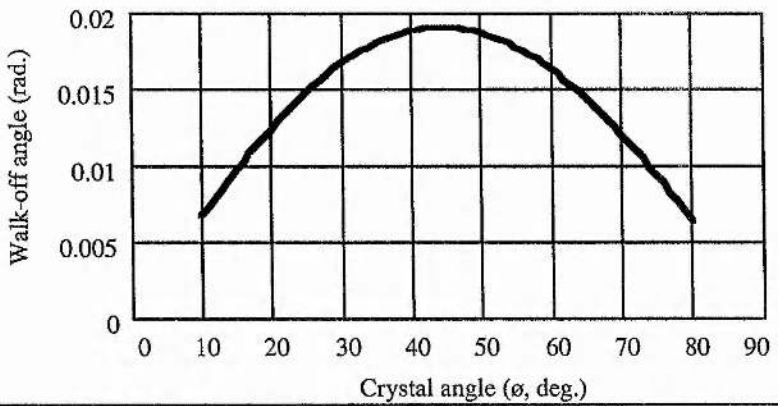

Figure 7.7: Pump-wave Poynting vector walk-off in LBO.

The pump coupling geometry used results in a spot size in the nonlinear crystal of 0.055 mm x 0.38 mm ($1/e^2$ radius). The large pump dimension in the walk-off plane defines a maximum allowable double refraction angle, for the entire crystal length to contribute toward the parametric interaction, of 25 mrad, assuming a similar sized signal-

beam spot size. Over the angular tuning range, walk-off is seen in Fig 7.7 to increase from 12.5 mrad to 18.4 mrad, and thus satisfy this criteria.

The effective nonlinear coefficient for LBO OPO can be calculated using the simplified expression for propagation in the x-y plane

$$d_{eff} = d_{32}\cos(\phi) \ , \qquad (7.2)$$

where d_{32} = 1.05 pm.V^{-1} [12]. The resulting curve is shown in Fig. 7.8.

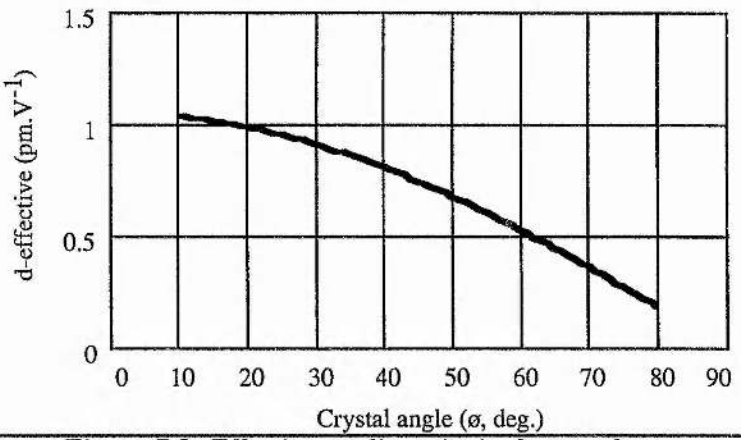

Figure 7.8: Effective nonlinearity in the x-y plane.

While the effective nonlinearity of LBO is only around one half that of β-BBO (see Fig. 7.16), due to its smaller walk-off angle it remains the preferred choice for low threshold devices [13]. In this case, due to pump coupling optic losses, arising from the uncoated focusing lenses, OPO mirror coating transmission and the uncoated crystal surface, the maximum available pump pulse energy is 1.5 mJ.

7.2.2: Experimental Results

Tuning Behaviour

In Fig. 7.9 the experimentally determined tuning behaviour of the LBO OPO is shown in comparison with the theoretical tuning curve (solid line).

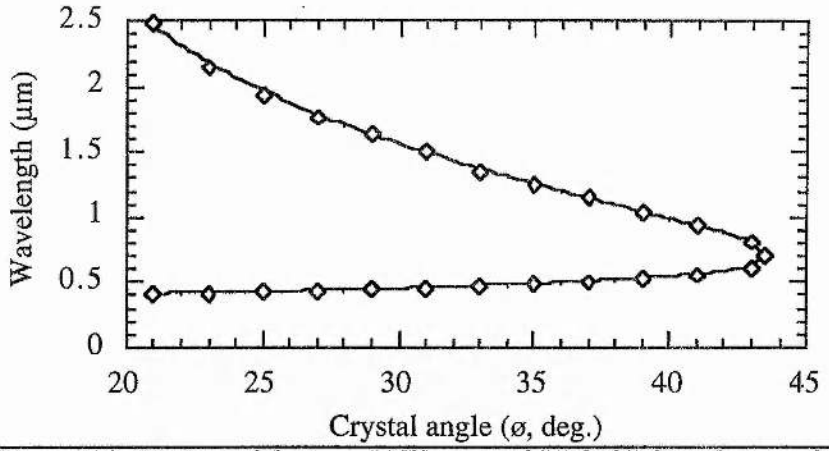

Figure 7.9: Tuning of the type I UV pumped LBO OPO in the x-y plane.

Clearly, agreement with the predicted tuning curve is good. The OPO can be tuned over a signal-wave range extending from 0.698 μm (degeneracy) to a lower wavelength cut-off of 0.406 μm. The corresponding idler-wave range is from 0.698 μm to 2.486 μm.

Pump Threshold

The pump threshold of the LBO OPO has been investigated across the signal-wave tuning range. A single high reflector has been used in conjunction with two different output couplers, one designed for resonating toward the blue-end of the signal-wave spectrum and the other toward the red-end. The blue mirror has a nominal 95% reflectivity in the range 0.44 μm to 0.54 μm, decreasing to 80 % at 410 nm. The red mirror is also nominally 95% reflecting but in the range 0.53 μm to 0.63 μm, decreasing to 70 % at 0.7 μm. The results are shown in Fig. 7.10.

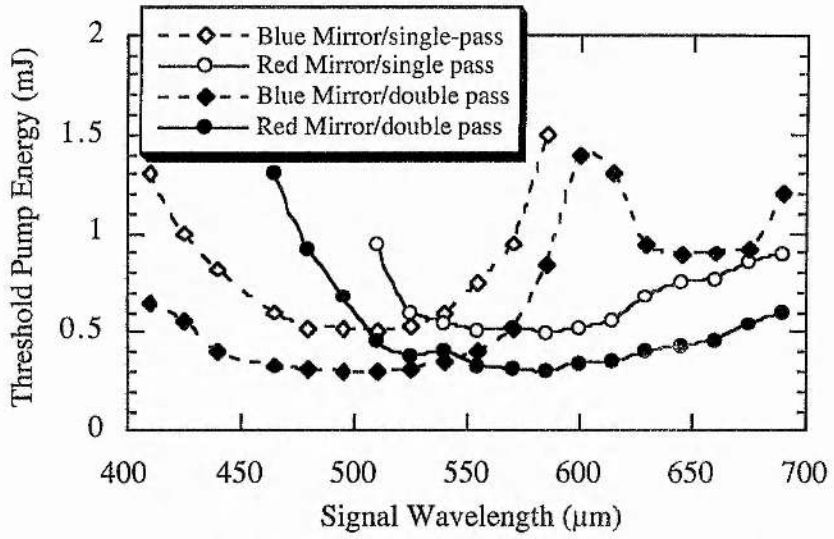

Figure 7.10: Pump threshold as a function of the signal wavelength (open symbols - single-pass pump, filled symbols - double-pass pump).

In a single-pass pump geometry, threshold could be achieved over the entire signal-wave tuning range by using the two mirror sets, although operation was near to threshold at the extremes of tuning. In this case pump threshold was in the range 0.5 mJ to 1.3 mJ, corresponding to a pump fluence of 0.84 J.cm^{-2} to 2.2 J.cm^{-2}. This to be compared with a threshold achieved by co-workers [13] of 0.6 mJ for a similar plane-plane OPO resonator, but with a circular pump spot. This slight reduction in threshold is attributable to the larger pump dimension in the walk-off plane in this case. As the OPO is tuned away from degeneracy it is expected that threshold will increase, as indicated by the $(1 - \delta^2)$ term in equ. (6.61). In this case however, both the factors of walk-off and d_{eff} tend to favour operation at smaller angles of Ø so compensating for this term. Consequently, threshold appears in Fig. 7.10 substantially constant across much of the tuning range.

In a double-pass pump geometry threshold could be readily achieved across the entire tuning range using the two mirror sets, and indeed also using only the blue mirror set, although the device operates very near to threshold at around 600 nm due to a decrease in mirror reflectivity at this point. Pump pulse threshold energies are seen in Fig. 7.10 to be in the range 0.3 mJ to 0.65 mJ, corresponding to a pump fluence of 0.5 J.cm^{-2} to 1.09 J.cm^{-2}. This then represents a near factor of 2 reduction in the pump threshold compared to the single-pass pump case. While a greater than factor of 2 reduction is possible in the case of a double-passed focused pump beam, as described

previously in Section 6.4.1, in this case the pump beam has expanded significantly on the return pass, the spot size being approximately 0.1 mm x 0.32 mm ($1/e^2$ radius).

Conversion Efficiency

The internal conversion efficiency of the double-pass pumped OPO has been extracted from measurements of the pulse energy of the depleted pump beam and compared to the input pump pulse energy. Firstly, the conversion efficiency has been measured as a function of the signal wavelength, at the maximum pump level, as shown in Fig. 7.11.

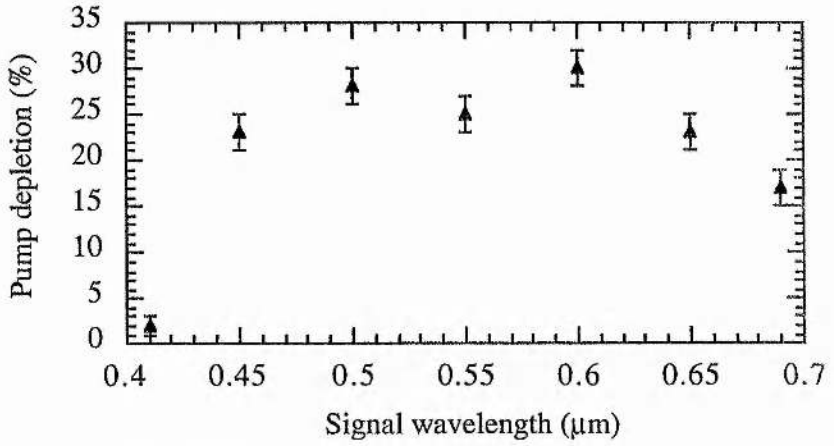

Figure 7.11: Pump depletion as a function of the signal wavelength for the double-pass, UV pumped, type I LBO OPO.

As threshold for the OPO is less than 0.5 mJ over a large part of the tuning range, it is possible to pump the OPO at levels in excess of 3 times threshold in this region. This results in conversion efficiencies of ~30% over most of the tuning range, and consequently combined signal- and idler-wave pulse energies in excess of 0.5 mJ. This represents an overall conversion efficiency from the infrared into the fully tunable output of almost 5%. As is to be expected, the conversion efficiency falls to much lesser values as operation at the maximum input level of 1.5 mJ becomes closer to threshold.

The conversion efficiency as a function of pump pulse energy has also been measured, and is shown in Fig. 7.12 for operation at 0.58 μm.

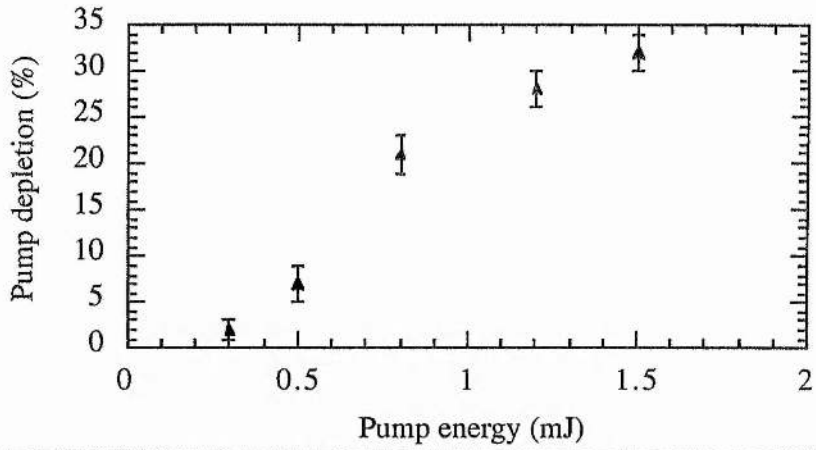

Figure 7.12: Pump depletion as a function of number of times above threshold for the type I LBO OPO at a signal wavelength of 0.58 μm.

Threshold at this signal wavelength is 0.31 mJ and at the maximum pump level of 1.5 mJ (~5 times threshold), the conversion efficiency is 32%, corresponding to 0.18 mJ at 0.955 μm in the idler-wave and 0.3 mJ in the signal-wave.

Spectral Linewidth

The spectral linewidth of the type I LBO OPO has been measured across its tuning range using a 1 m monochromator which has a spectral resolution of less than 0.05 nm. Results are shown in Fig. 7.13, where for clarity a logarithmic y-ordinate is adopted and the linewidth expressed in units of nanometres.

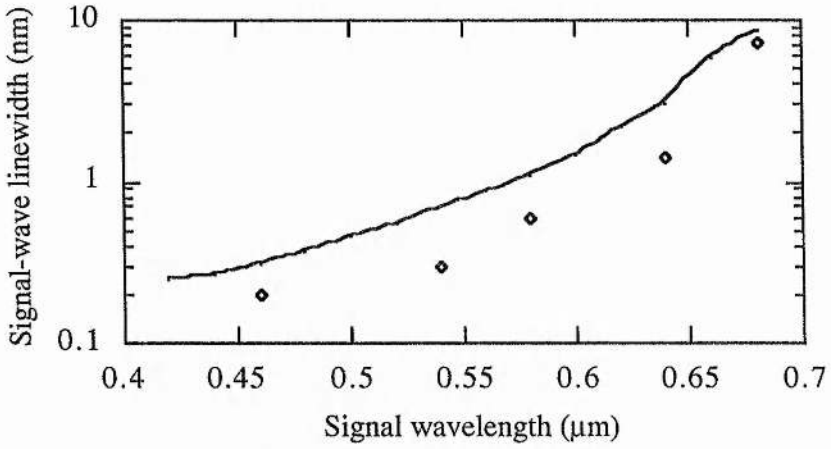

Figure 7.13: Spectral linewidth as a function of the signal wavelength for the type I UV pumped LBO OPO.

The maximum spectral linewidth of the OPO is dependent primarily upon the crystal birefringence $(n_i - n_s)$ and the crystal length l, such that the phase-match

conditions are satisfied, and can be calculated using equ. (6.81) where Ω is replaced by ω_s. The theoretical linewidth of the type I LBO OPO, where a crystal length of 15 mm has been assumed and the Sellmeier data described by equ. (7.1) is used, has been calculated including the effects of pump divergence and is as indicated by the solid line also shown in Fig. 7.13. Agreement with experimentally determined values is relatively good, the experimental linewidth increasing from around 0.18 nm far from degeneracy, to a value of 7.5 nm as degenerate operation is approached. It is noted that the measured linewidth is unexpectedly narrower than that predicted, for reasons which are at this time not fully understood. Possible causes may be that (i) a narrower than expected pump beam divergence is prevalent or (ii) linewidth narrowing effects in the OPO exist due for example to an étaloning effect.

Spatial and Temporal Characteristics

The signal-wave output from the OPO has a pseudo-Gaussian profile and a measured M^2 value of around 6 (4.2 mm.mrad) at 0.55 μm. No attempt has been made to improve the beam quality but could probably be so by for example the use of resonators designed to be more stable.

The pulse duration of the signal-wave is measured to be 5 nsec near to threshold, compared to the pump pulse duration of 6 nsec. The pulse duration is shorter than the pump as only the intense central area of the pump pulse is frequency-down-converted while additionally the short decay time of the OPO resonator (τ_{cav}~1.4 nsec for a 16% round trip loss and 0.23 nsec round trip time) does not serve to increase the pulse width substantially. Above threshold the signal-wave pulse duration approaches the pump pulse duration as threshold is reached sooner and more of the pump pulse is down-converted. The temporal profiles of the pump pulse, depleted pump and signal-wave are shown in Fig. 7.14.

A photograph of the LBO OPO integrated with the Nd:YLF pump laser and frequency up-conversion optics was shown previously in Fig. 4.43.

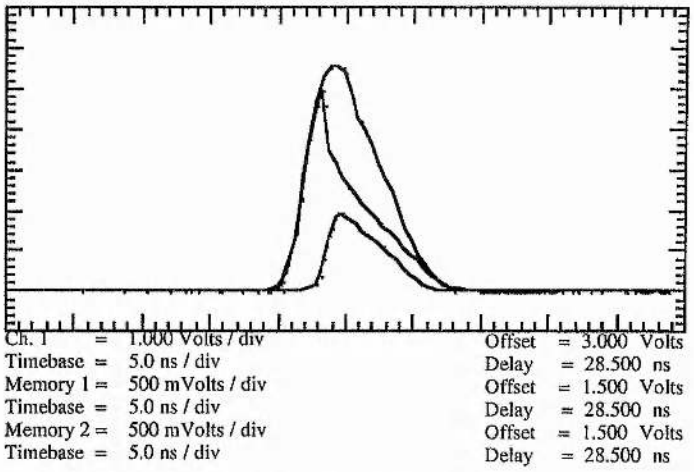

Figure 7.14: Temporal profiles of the pump, depleted pump and signal-wave pulses for the type I LBO OPO.

7.3: Line-Narrowed, Low-Threshold β-Barium Borate OPOs

In this section, the development of line-narrowed OPOs based on the nonlinear material β-barium borate (β-BBO) is described. Initially, a description is given of the design and operating parameters of the free-running device, so providing a benchmark against which the effectiveness of the various frequency control techniques employed may be measured. It will be demonstrated that effective control can be obtained by a variety of techniques, including; spectral dispersion, interferometric and injection seeding, with the potential for obtaining single frequency output from the OPO over its entire tuning range and where modest pump power thresholds are maintained. The pump laser used is that described in Section 7.1.3.

7.3.1: Design Parameters

The basic β-BBO OPO consists of a single crystal of β-BBO located within a plane-parallel resonator, with additionally a pair of 45° dichroic reflectors to couple the UV pump light into and out of the OPO, as shown schematically in Fig. 7.15.

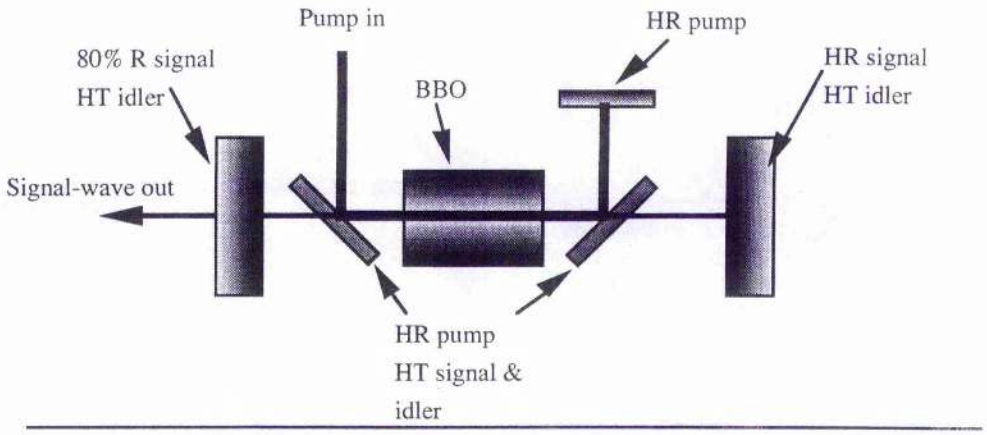

Figure 7.15: Schematic of the basic type I β-BBO OPO resonator.

Both type I and type II phase-match geometries are possible in the case of the frequency tripled Nd:YAG-pumped (0.355 μm) β-BBO OPO, however, the type I interaction is usually preferred. After some early confusion over the assignation of a point group to BBO [14,15], which led to varying expressions for the effective nonlinear coefficient, it has been finally ascertained that β-BBO belongs to the point group 3m and space group R 3c [15] and thus the expressions for d_{eff} for each of the interaction types are found to be;

$$\text{(type I)}\ d_{eff} = d_{31}\sin(\theta) - d_{22}\sin(3\phi)\cos(\theta) + d_{11}\cos(3\phi)\cos(\theta)\ , \qquad (7.3)$$

$$\text{(type II)}\ d_{eff} = d_{22}\cos(3\phi)\cos^2(\theta) + d_{11}\sin(3\phi)\cos^2(\theta)\ , \qquad (7.4)$$

where θ is the phase-match angle measured from the optic axis and Ø is the azimuthal angle. The definition of the azimuth angle is dependent upon the co-ordinate system used. Following the convention of Eimerl [15], the abc co-ordinate system is chosen in which c lies along the crystal optic axis and a is perpendicular to the crystallographic mirror plane. The azimuth angle Ø is then given by the projection of the wavevector k_p onto the a-b plane. For this convention, it is found that $d_{22} \approx d_{31}$ and $d_{22} < 0.05 \times d_{11}$ and thus equ's (7.3) and (7.4) can be reduced to functions of d_{11} alone. It is then apparent that in the case of the type II interaction d_{eff}, given by equ. (7.4), is maximum for Ø = 30° (sin3Ø = 1), while in the case of the type I interaction d_{eff}, given by equ. (7.3), is maximum for Ø = 0° (cos3Ø = 1). It is also apparent that the main contribution toward the relative difference between d_{eff} in the two cases arises through the linear cos(θ) dependence in the case of type I, while in the type II case this dependence is quadratic. Consequently, as θ is increased d_{eff} drops off more rapidly in the case of type

II phase-matching. This dependence is illustrated graphically in Fig. 7.16, which shows d_{eff} as a function of θ in the case of type I phase-matching with Ø = 0° and type II phase-matching with Ø = 30°, and where $d_{11} = 2.6$ pm.V^{-1} [16].

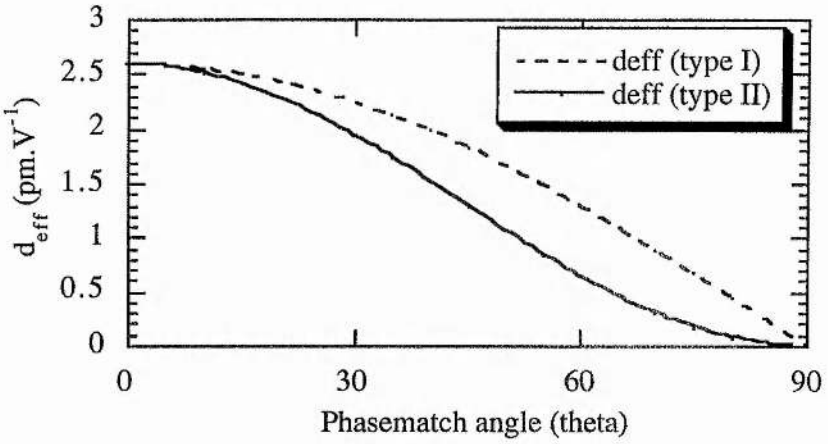

Figure 7.16: Effective nonlinear coefficient for type I and type II phase-matching in β-BBO (type I - Ø=90°, type II - Ø=0°).

The theoretical tuning range for the type I (e:o+o) and type II (e:o+e) geometries can be calculated using the Sellmeier data of Kato [14];

$$n_o^2 = 2.7359 + 0.01878/(\lambda^2 - 0.01822) - 0.01354*\lambda^2$$
$$n_e^2 = 2.3753 + 0.01224/(\lambda^2 - 0.01667) - 0.01516*\lambda^2 \quad . \qquad (7.5)$$

This results in a possible tuning range for the combined signal and idler wavelengths of <0.4 μm to >3.1 μm, where the tuning curve is centred about θ = 28° in the case of the type I interaction and 35° in the case of the type II interaction, as shown in Fig. 7.17.

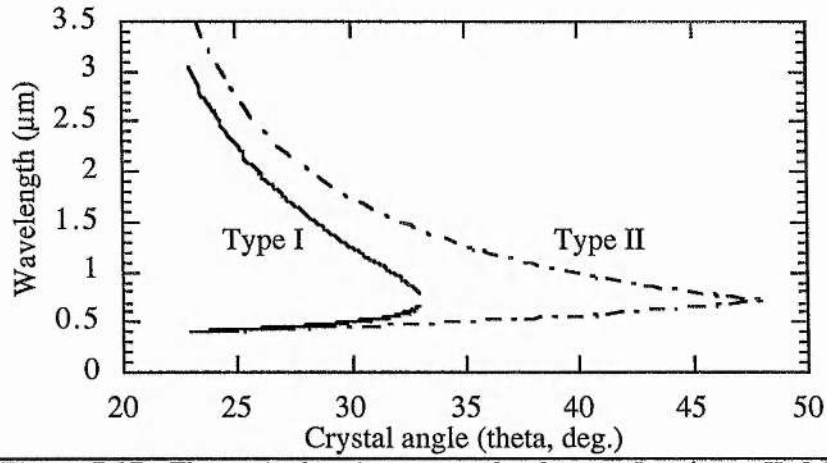

Figure 7.17: Theoretical tuning curves for the type I and type II, 0.355 μm pumped β-BBO OPO.

The type I phase-match geometry being preferred, the extra-ordinary pump wave is brought into the OPO via the 45° dichroic reflector, shown in Fig. 7.15, which is >95%

transmitting for the ordinary signal and idler waves over the wavelength range 0.4 μm to 2.7 μm. The β-BBO crystal used has dimensions 8 x 5 mm aperture and 16 mm length. The 8 mm dimension is chosen to be in the θ-plane to allow angular rotation of the crystal without incurring aperturing difficulties. The crystal is cut for propagation at 29° (θ) to the optic axis at normal incidence and the aperture faces are polished but uncoated. After passing through the β-BBO crystal, the pump beam is coupled out of the OPO resonator by a second dichroic reflector, and may then be reflected back along its initial path by a high reflector, in a double pass pump geometry if desired. Coupling the pump in this way serves additionally to remove the intense UV beam from the OPO resonator mirrors, or as will be seen later dispersive gratings and étalons, so avoiding potential damage problems. A single set of OPO resonator mirrors are used to resonate the entire signal wavelength range (0.4 μm to 0.71 μm), one being highly reflecting and the other, the output coupler, having a nominal 80% reflectivity from 0.42 μm to 0.71 μm. Both mirrors have high transmission across the idler wavelength range (0.72 to 2.7 μm), thus ensuring singly resonant operation.

As demonstrated in Chapter 6, the OPO threshold is dependent upon the resonator length and consequently the OPO is designed to be as short as possible, typically around 75 mm. A further factor noted in Chapter 6 affecting the OPO performance is that of Poynting vector walk-off, which takes place in the plane of the pump wavevector $\mathbf{k}_p$ and the optic axis. It is desirable to choose a pump geometry in which the entire length of the nonlinear crystal can be exploited, in this case 16 mm, prior to the complete spatial separation of the e-wave pump beam energy and o-wave parametric waves. The calculated double refraction angle (ρ), obtained using equ. (6.25) and the same Sellmeier data as before, and the corresponding aperture length (l_a), where a 0.5 mm radius beam spot size is assumed, are shown in Fig. 7.18.

It is seen that providing the beam sizes are not less than the assumed 0.5 mm ($1/e^2$ radius), then the majority of the 16 mm crystal length can be exploited.

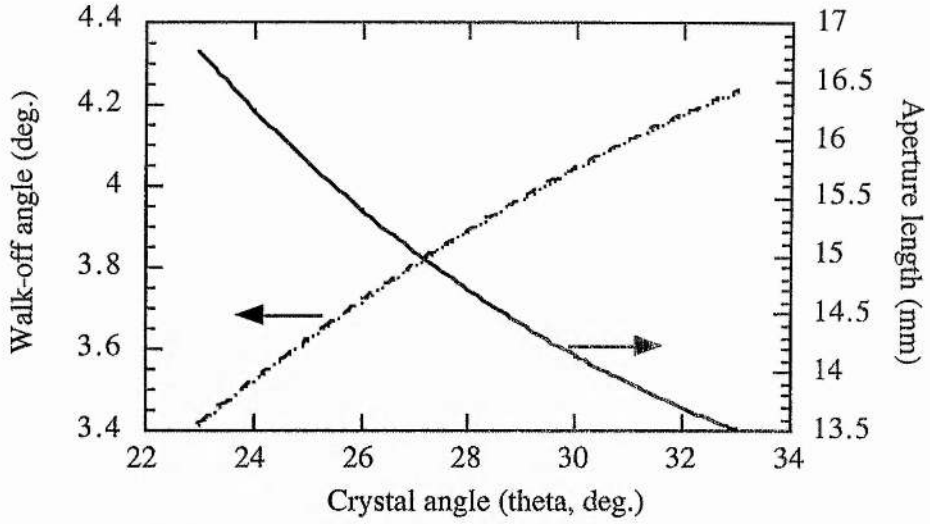

Figure 7.18: Double refraction angle and effective aperture length for the 0.355 μm pumped β-BBO OPO.

7.3.2: Free-Running β-BBO OPO Characterisation

Tuning Behaviour

In Fig. 7.19 the experimentally determined tuning behaviour of the basic β-BBO OPO is shown in comparison with the theoretical tuning curve, previously shown in Fig. 7.17.

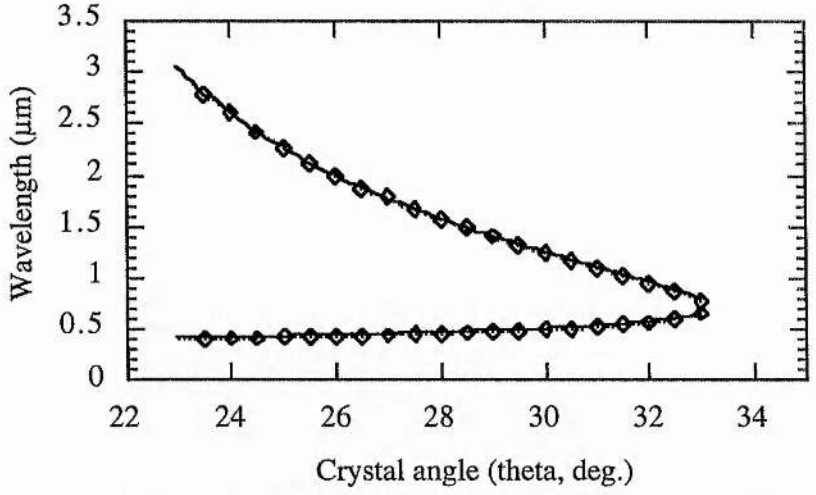

Figure 7.19: Angle-tuning curves for the type I β-BBO OPO pumped at 0.355 μm.

Agreement with the expected tuning curve is seen to be good. The measured signal wavelength range was from 0.406 μm to 0.71 μm (degeneracy), with a corresponding idler wavelength range of 2.75 μm to 0.71 μm. The lower wavelength cut-off is due to a

combination of factors, including; a decreasing reflectivity of the OPO resonator mirrors below 420 nm and an increasing parasitic loss due the rotation of the crystal resulting in an increasing Fresnel loss, noting that the turning angle is somewhat greater than the change in internal angle shown in the figures.

Pump Threshold

Pump threshold was shown in Chapter 6 to be influenced by the combined effects of Poynting vector walk-off, effective nonlinear coefficient, resonator loss (being the combined parasitic and output coupling loss) and the point of operation relative to degeneracy. For an otherwise fixed resonator geometry, Fig's. 7.16 and 7.18, show that the two former parameters will tend to favour a low threshold at the high frequency end of the signal wave spectrum. More significantly, however, the latter two favour operation nearer to degeneracy. The pump threshold for the basic β-BBO OPO has been experimentally measured as a function of crystal angle, as is shown in Fig. 7.20, where initially the output coupler has been replaced by a high reflector.

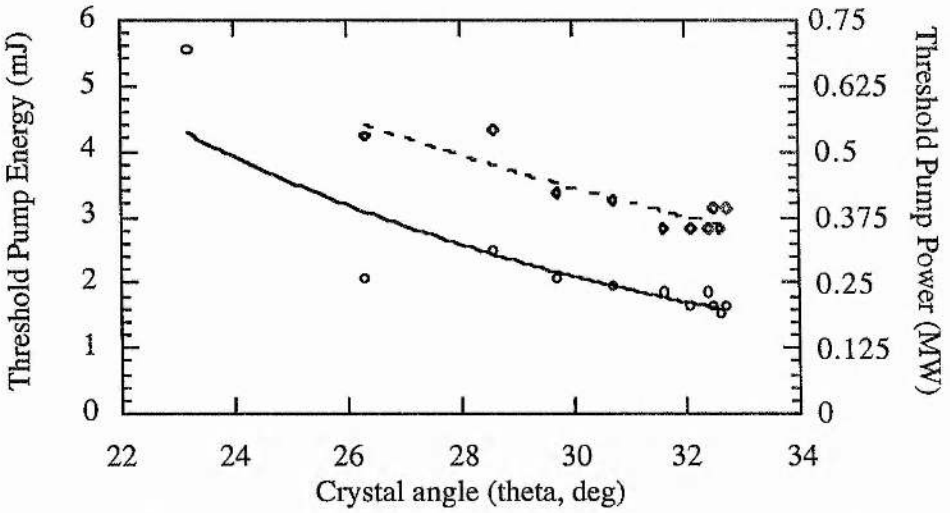

Figure 7.20: Pump threshold as a function of crystal angle for the unconstrained, type I β-BBO OPO and no output coupling (dashed line - single-pass pump, solid line - double-pass pump).

It is evident that there is a general reduction in pump threshold toward degeneracy as expected. Pump threshold in units of Watts is also shown on the second y-ordinate, where the pump pulse duration is a nominal 8 nsec. The pump pulse duration was kept constant at all pump levels by the use of a half-wave retardation plate and polariser to

attenuate the UV pump light. For a single-pass pump geometry threshold at the extreme of the tuning range is measured to be 4.6 mJ, reducing to 2.8 mJ near degeneracy. The rapid increase in threshold toward the extreme of tuning is due to a reducing reflectivity of the OPO resonator mirrors. The corresponding peak powers are shown in the figure, while pump fluences for a spot size of 0.87 mm ($1/e^2$ radius) are then in the range 0.193 $J.cm^{-2}$ to 0.117 J.cm-2.

In the presence of output coupling the pump threshold is obviously expected to increase. The measured thresholds for the output coupler previously noted are then as shown in Fig. 7.21.

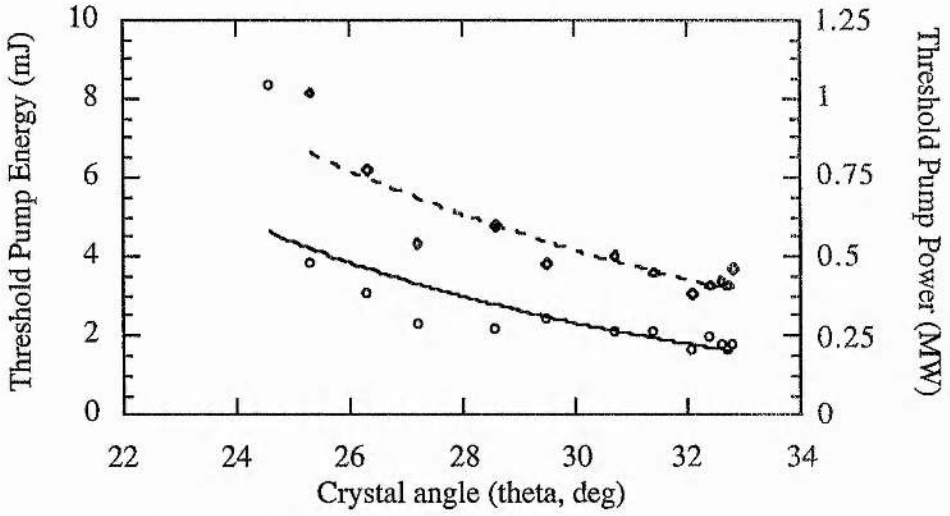

Figure 7.21: Pump threshold as a function of crystal angle for the unconstrained, type I β-BBO OPO with output coupling (dashed line - single-pass pump, solid line - double-pass pump).

Fluctuation due to the mirror reflectivity profile is clearly evident, while threshold for this nominal 20% output coupling is seen to increase generally by around a factor of 1.2 when compared to the case of no output coupling. This relatively small increase is indicative of a high parasitic loss in the OPO, arising from uncoated crystal surfaces and the intra-cavity pump beam reflectors. With output coupling pump threshold fluences are now in the range 0.336 $J.cm^{-2}$ to 0.126 $J.cm^{-2}$.

The pump threshold fluence can be compared to that expected, based on the theoretical expression, equ. (6.63), generated in Chapter 6 for the single-pass pumped and singly resonant OPO, but where the equation has been re-expressed in terms of the pump fluence by multiplying both sides by the pump pulse duration τ_p;

$$\left[J_p^{th}\right]_{SRO} = \tau_p \frac{4n_i n_s n_p \varepsilon_0 c^3}{\omega_i \omega_s d_{eff}^2 l^2}\left(1 - r_s^2\right) . \qquad (7.6)$$

Evaluating this expression over the OPO signal-wave tuning range results in the curve shown in Fig. 7.22, when; τ_p = 8 nsec, r_s = 0.82 (combined mirror and Fresnel losses) and d_{eff} is as given by equ. (7.3) and d_{22} = 2.6 pm.V^{-1}.

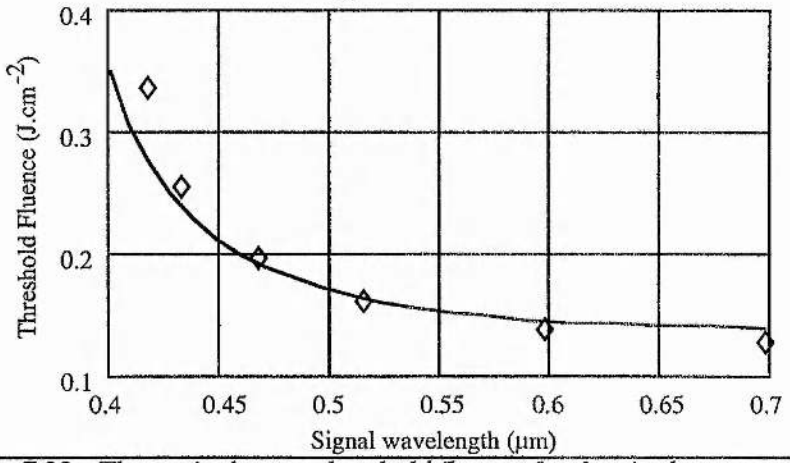

Figure 7.22: Theoretical pump threshold fluence for the singly resonant and single-pass pumped β-BBO OPO and experimental data points.

Comparing the theoretical solid curve with the experimental data, plotted also in Fig. 7.22, shows threshold values to be in good agreement with those predicted.

To reduce pump threshold, the use of a double pass pump geometry has also been explored. The result of doing so is also indicated in Fig's. 7.20 and 7.21, where it can be seen that a factor of 2 reduction in threshold has been achieved. This is good agreement with expected behaviour based on the plane-wave approximation described by equ. (6.64).

The pump threshold dependence on pump beam spot size has also been investigated by measuring, at a fixed wavelength (λ_s = 549 nm) and for the single-pass pump geometry, the threshold energy for numerous spot sizes, the pump beam spot size having been varied using a series of reduction/expansion telescopes. The observed threshold fluence dependence on pump beam spot size is then shown in Fig. 7.23, where for convenience the x-ordinate variable is made threshold pump energy.

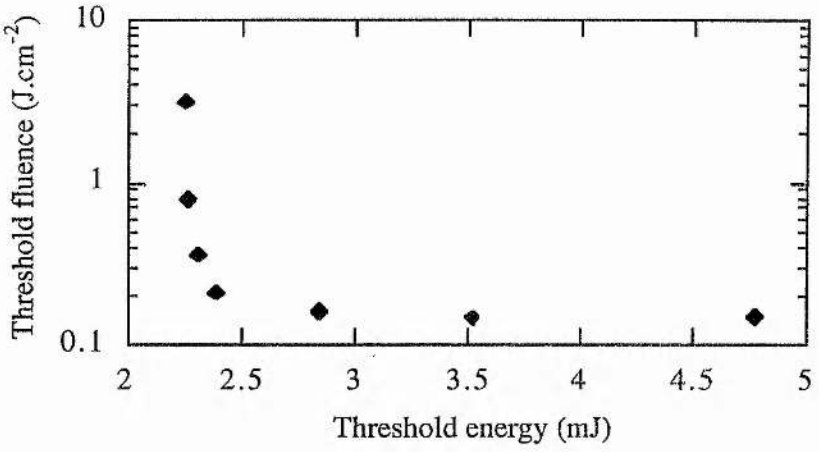

Figure 7.23: Pump threshold fluence as a function of the pump threshold energy (pump beam spot size) for the free-running, type I β-BBO OPO.

At large spot sizes, and thus high threshold energy values, the threshold fluence is largely constant at around 0.15 J.cm^{-2}. However, as the beam size is reduced the threshold fluence is observed to increase, attributable to Poynting vector walk-off, where the lateral displacement of the extraordinary pump beam becomes comparable to the beam spot size. It can be deduced from Fig. 7.23 that this is at a spot size of less than 0.5 mm, comparable to the value expected from Fig. 7.1618 Further reduction in spot size results in an ever increasing pump threshold fluence, to a point of exceeding the damage threshold of the crystal or pump steering optics.

Conversion Efficiency

The internal conversion efficiency of the double-pass pumped OPO has been extracted from measurements of the pulse energy of the depleted pump-wave compared to the input pump pulse energy. The pump depletion as a function of the pump pulse energy is then shown in Fig. 7.24 for operation at 0.549 μm.

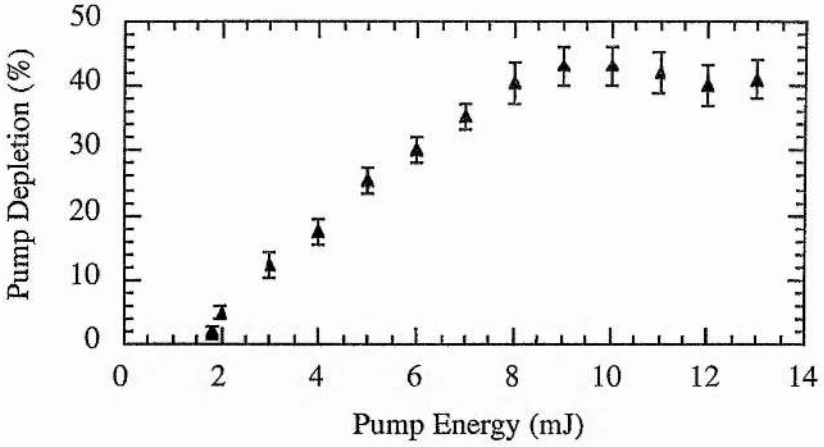

Figure 7.24: Conversion efficiency as a function of the pump pulse energy for the free-running type I β-BBO OPO.

Threshold at this signal wavelength is 1.8 mJ and at the maximum pump level of 13 mJ (7 times threshold), the conversion efficiency is 41%, corresponding to 1.9 mJ at 1.005 μm generated in the idler-wave and 3.4 mJ generated in the signal-wave.

Spectral Linewidth

The spectral linewidth of the unconstrained, type I β-BBO OPO has been measured across its tuning range using a 1 m monochromator having a spectral resolution of less than 0.05 nm. Results are shown in Fig. 7.25, where for clarity a logarithmic y-ordinate is adopted and the linewidth expressed in units of nanometres.

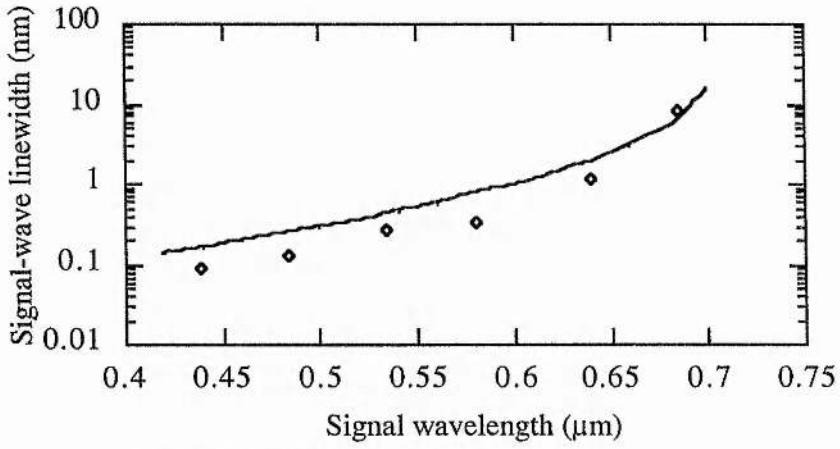

Figure 7.25: Spectral linewidth of the unconstrained, type I β-BBO OPO (◊ - measured values, solid line - theoretical).

As described in Section 6.4.3 and by equ. (6.66), the spectral linewidth of the OPO is limited primarily by the crystal birefringence $(n_i - n_s)$ and the crystal length l. The

theoretical linewidth of the type I β-BBO OPO based on this approximation, where a crystal length of 16 mm has been assumed and the Sellmeier data described by equ. (7.5) is used, has been calculated and is as indicated by the solid line also shown in Fig. 7.25. Clearly good agreement is found with experimentally determined values, the linewidth increasing from around 0.1 nm far from degeneracy, to a value some two orders of magnitude greater as degenerate operation is approached. Such large intrinsic linewidths require that for many applications some form of linewidth control is necessary.

Spatial and Temporal Quality

The signal-wave output from the OPO has a pseudo-Gaussian profile and a measured M^2 value of around 10 (7.0 mm.mrad) at 0.55 μm.

The pulse duration of the signal-wave is measured to be 6 nsec near to threshold, compared to the pump pulse duration of 8 nsec. Above threshold the signal-wave pulse duration approaches the pump pulse duration as threshold is reached sooner and more of the pump pulse is down-converted.

7.3.3: Line-Narrowing by Dispersive Gratings

In the first instance the use of dispersive gratings, with the possible addition of beam expansion elements, as shown in Fig. 7.26 has been explored, with a view to obtaining line-narrowed operation of the β-BBO OPO.

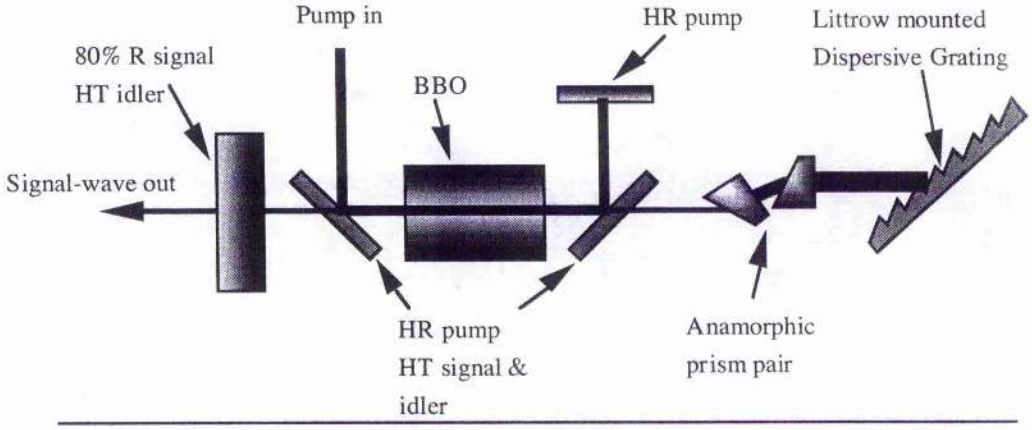

Figure 7.26: Schematic of the type I β-BBO singly resonant OPO, line-narrowed by a Littrow mounted dispersive grating and prism beam expander.

The geometry differs from that of the basic OPO in that the signal-wave high reflector has been replaced by a grating mounted in a Littrow geometry. Considering the grating equation for a Littrow mount geometry

$$m\lambda = 2d\sin\beta \ , \tag{7.7}$$

where m is the grating order, d the rule spacing and β the grating angle, then for any spectral component two grating positions exist (± β and ± m) where resonance is achieved. It is usual that one particular position will have a higher reflectivity associated with it, that being the position chosen here. The dispersive properties of the grating can be conveniently described by considering the chromatic dispersion as a function of angle, or dλ/dβ. From (7.7), this is just

$$\frac{d\lambda}{d\beta} = \frac{2d}{m}\cos\beta = \frac{\lambda}{\tan\beta} \ . \tag{7.8}$$

Immediately, it is apparent that the chromatic dispersion is a function of both the grating order and rule spacing, the higher the order and closer the rule spacing then the greater the dispersion. Three gratings have been used throughout this work; a 1200 l/mm grating blazed at 500 nm with a specified reflectivity of greater than 55% across the range 410 nm to 650 nm when used in the first order, a 2400 l/mm grating blazed at 500 nm with a specified reflectivity of greater than 60% over the same range and again used in the first order, and a 600 l/mm grating designed for use in the fifth order and having a reflectivity which increases from 22% at 510 nm to 45% at 700 nm. The corresponding chromatic dispersion for each of these gratings at 550 nm is shown in Table 7.3.

Grating	Order	AoI†	Chromatic Disp.†
1200 l/mm	1	19.3°	1.57 nm.mrad^{-1}
2400 l/mm	1	41.3°	0.63 nm.mrad^{-1}
600 l/mm	5	55.6°	0.38 nm.mrad^{-1}

† - In a Littrow geometry @ 550 nm.

Table 7.3: Chromatic dispersion and operating conditions for dispersive gratings.

Given a signal-wave wavelength of 550 nm and a diffractive angle of the signal-beam of ~2 mrad, then to a first order a linewidth in the range 0.76 nm to 3.3 nm is to be expected, depending on the grating used. However, the above simplified analysis does not take into account the benefits of the multiple reflection geometry realised in using the

grating as a resonator mirror, and further improvement which can be achieved by first expanding the beam and so reduce the beam diffractive angle. Such beam expansion then results in a reciprocal reduction in the observed linewidth, while to a first approximation the grating linewidth is reduced by a factor of $\sqrt{p}$, where p is the number of grating reflections, in a multiple reflection geometry. A full discussion of the effects of multiple pass geometries and beam expansion was given by Brosnan and Byer [17], taking into account the nature of a Gaussian beam and the effects of a limiting aperture imposed by the gain region.

As for the unconstrained device, the spectral linewidth of the now grating narrowed type I β-BBO OPO has been measured at several points across its tuning range for the various gratings used, the results being shown in Fig. 7.27. Broad linewidths have again been measured using the 1 m monochromator, however, for linewidth measurements below 0.1 nm a pulsed wavemeter has been used (Burleigh WA4500), which has a linewidth resolution of better than 1×10^{-4} nm.

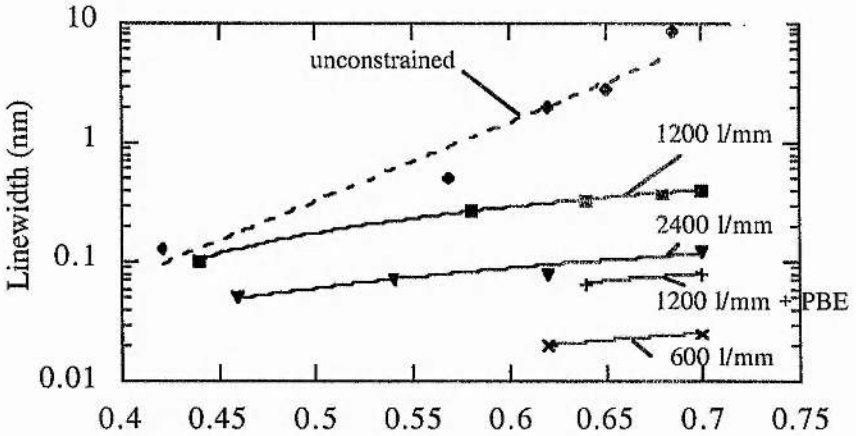

Figure 7.27: Spectral linewidth of the grating narrowed, type I β-BBO OPOs.

Considering firstly the 1200 l/mm grating, it is seen that the linewidth shows little change from the unconstrained OPO far from degeneracy, where the inherent linewidth is already comparable to or less than the grating linewidth. As the OPO is tuned toward degenerate operation the linewidth is effectively constrained, resulting in a linewidth at degeneracy of 0.4 nm (240 GHz). A prism beam expander (PBE) with a magnification of 4 has also been tried in combination with the 1200 l/mm grating, where the PBE is

formed by two prisms each having one surface orientated at near Brewsters angle to the incident beam and the second surface AR coated, and where they are orientated to provide expansion in the plane perpendicular to the grating rule. With this addition the linewidth has been further reduced to 0.085 nm at degeneracy, in good agreement with the factor of 4 reduction expected. A high loss from the AR coating precluded use of the PBE at shorter wavelengths.

The use of gratings with a higher chromatic dispersion has also been explored, as shown in Fig. 7.27 for the 2400 l/mm grating and 600 l/mm grating used in 5th order. Measured linewidths are in good agreement with those expected based on the relative chromatic dispersions of the gratings given in Table 7.3. The linewidths obtained from the 600 l/mm grating are slightly better than expected, however, this may be due to operation of the OPO at only 1.5 times pump threshold, due to a high insertion loss, compared to 2 times pump threshold for the other geometries.

Use of the 1200 l/mm and 2400 l/mm gratings resulted in a factor of 2 increase in pump threshold compared to the unconstrained OPO with output coupling. A factor of 3 increase in threshold was obtained for the 600 l/mm grating. An additional benefit derived from the use of dispersive gratings was an observed increase in the stability of the central wavelength. Without constraint, the central OPO wavelength is observed to fluctuate randomly under the gain profile, this being as much as 2 nm near to degeneracy (1.2 THz). With the addition of the 2400 l/mm grating, central wavelength stability is improved to better than ±0.01 nm (12 GHz). One notable disadvantage in the use of dispersive gratings is of course the need to accurately orientate the crystal angle with grating position. In Section 7.4, however, a novel phase-match geometry which may be used to alleviate this requirement will be described.

7.3.4: Line-narrowing with Fabry-Perot Étalons

It has been demonstrated in the preceding section that though significant linewidth reduction can be obtained through the use of dispersive gratings alone, additional linewidth narrowing elements are required to obtain SLM operation. The use of Fabry-Perot étalons has been previously introduced in Chapter 2, and seen to be a means by

which a periodic cluster of modes or single mode of the resonator may be selected from under the gain bandwidth, with a periodicity of the free-spectral range of the étalon and where the width of a cluster is approximated by the passband of the étalon. It is usual that two or more étalons of varying thickness are used, each thicker étalon selecting a limited number of the resonator modes encompassed by the thinner étalons, until only a single mode experiences any net gain.

A range of solid étalons have been used in this study, varying in thickness from 30 μm to 2 mm. All have broadband partially reflective coatings (R=75%) on both surfaces, resulting in a finesses of around 10 and are fabricated from fused silica (n~1.47). The free spectral range and passband of the étalons are summarised in Table 7.4. Like dispersive gratings, étalons have associated with them an insertion loss. The size of this loss can be estimated by considering the peak transmission of a non-ideal étalon, described by the mathematical relationship, equ. (2.108)

$$\frac{I_{t,max}}{I_i} = \left[1 - \frac{a}{(1-r)}\right]^2, \qquad (7.9)$$

where a is the combined single-pass scatter and absorption losses and r the coating reflectivity. The estimated single pass loss of each étalon is also given in Table 7.4, and accounts for the increased pulse threshold observed in the experiments.

Thickness (mm)	FSR (GHz)	Bandwidth (GHz)	Transmission
0.03†	3401	340	0.39
0.5	204	20.4	0.8
2.0	51	5.1	0.8

† - parasitic loss of 0.075 (0.02 others)

Table 7.4: Fabry-Perot étalon characteristics.

With the addition of the 30 μm étalon to the unconstrained resonator, the single shot signal-wave linewidth is reduced in the orange/red region of the tuning curve to less than 300 GHz (~0.5 nm). However, near degeneracy 2 mode clusters are periodically observed as the FSR of the étalon is not large enough to encompass the entire gain bandwidth in this region. Additionally, erratic behaviour is observed as the central wavelength of the signal-wave wanders within the gain bandwidth. Similar behaviour is observed for the thicker étalons, in each case selecting a narrower cluster bandwidth, but

a greater number of clusters as the FSR reduces with increasing thickness. For example, the 2 mm étalon resulted in clusters of < 3 GHz linewidth, but the number of clusters varied between 2 (far from degeneracy) and 15 (near degeneracy). Results are summarised in Table 7.5.

Geometry	λ_s (nm)	Linewidth (GHz) Single Cluster	Linewidth (GHz) Multiple Clusters	Pump Threshold (mJ)
Unconstrained	421	150 (0.09 nm)		4
	568	470 (0.5 nm)		2.5
	650	2130 (3 nm)		2
0.03 mm étalon	450	150		
	685	240	3000	
0.5 mm étalon	421	10		6.2
	568	10	420	4
	684	10	1440	3
2.0 mm étalon	421	3	52	8
	568	3	360	4.8
	684	3	716	3.5
0.5 + 2.0 mm étalons	421	<3		12
	568	<3	205	7.7
	684	<3	614	5.5
2400 l/mm grating + 2 mm étalon	421	<2		12
	685	<2		5

Table 7.5: Étalon narrowed type I β-BBO OPO characteristics.

It is to be noted that the results presented in Table 7.5 are for a single pulse. When a single or multiple étalons are used without a dispersive grating, considerable instability is observed in the central wavelength of the OPO, particularly toward degeneracy, resulting in multiple shot linewidths approaching the unconstrained linewidth. As before however, the addition of a dispersive grating, as in the last result noted in the table, results in a central wavelength stability of better than 12 GHz across the entire signal-wave tuning range.

Results indicate that the 2 mm thick étalon is not thick enough (or requires a higher finesse) to discriminate against adjacent OPO resonator modes reliably. Used in conjunction with the 2400 $l.mm^{-1}$ grating, spectral output varied between SLM and 2

adjacent mode operation, while a combination of the 2 mm and the 0.5 mm thick étalons results in the appearance of satellite modes separated by the FSR of the 0.5 mm étalon. An additional thinner étalon may be used to suppress these modes, however, in this case with the 30 μm étalon threshold could not be achieved.

The progress towards SLM operation through the sole use of étalons is well described by a series of CCD images of the exit slit of the 1 m monochromator shown in Fig. 7.28, where at a signal-wave wavelength of 684 nm the effect of the 0.5 mm and 2 mm thick étalons is clearly demonstrated.

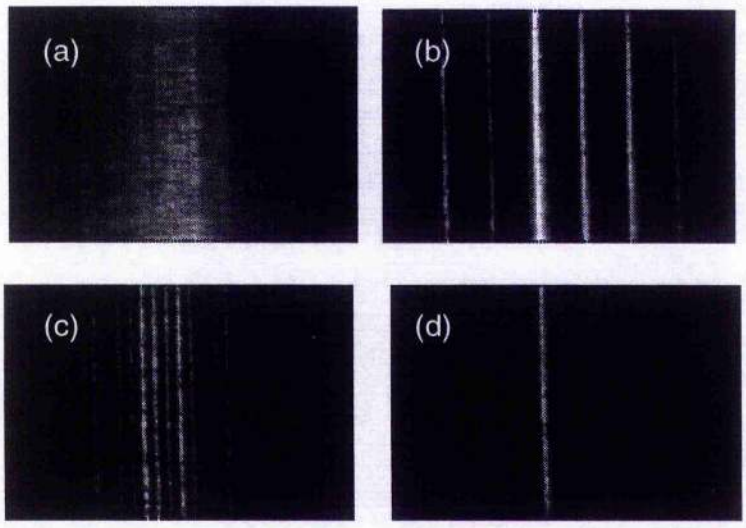

Figure 7.28: CCD images of the exit slit of the 1 m monochromator; (a) unconstrained type I β-BBO OPO @ 684 nm, (b) mode clusters generated by a 0.5 mm thick étalon, (c) mode clusters generated by a 2 mm thick étalon, (d) combined 0.5 mm and 2 mm thick étalons.

The linewidth of the single axial mode selected can be accurately measured by illuminating a Fabry-Perot interferometer and measuring the resulting ring structure. A CCD image of the ring structure observed, again at 684 nm, is shown in Fig. 7.29.

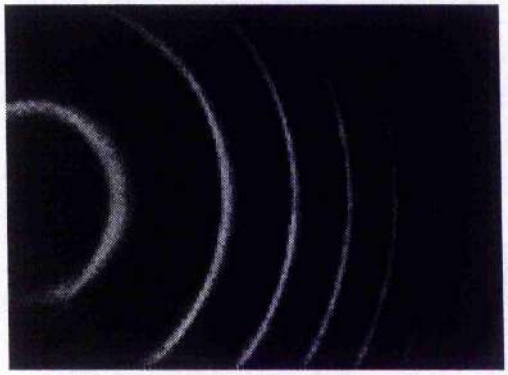

Figure 7.29: Fabry-Perot interferometer image for the étalon narrowed (0.5 mm + 2 mm) type I β-BBO OPO @ 684 nm (FSR = 1.67 GHz).

The linewidth is measured by taking a linear scan through the centre of the image as shown in Fig. 7.30 and ratioing the ring thickness to ring separation. Knowing the FSR of the interferometer to be 1.67 GHz (90 mm, air spaced), then the linewidth of the single mode OPO output is measured to be < 300 MHz.

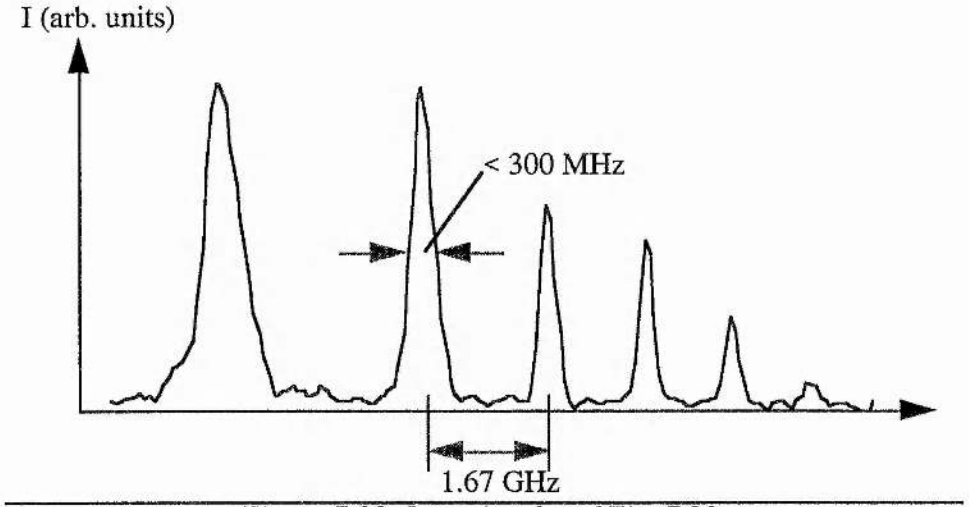

Figure 7.30: Intensity plot of Fig. 7.29.

7.3.5: Line-Narrowing by Injection Seeding

While grating and étalon techniques have been shown to be successful in controlling the linewidth of the OPO, a penalty is paid in the increasing threshold of the device and greater complexity in the resonator design. A possible means of alleviating these difficulties is to line-narrow the OPO by injection seeding. In this work a number of seeding geometries are considered, including the use of visible (red) and IR diode-lasers and a He-Ne laser as the seed source and linear and ring OPO geometries. It will also be shown that injection seeding on its own is not necessarily sufficient to control the linewidth of the OPO to only a single axial mode and that additional dispersive or interferometric elements need be added.

The two SLM diode-lasers used for seeding were obtained from LASIRIS, one having a wavelength of 670 nm at room temperature and maximum output power of 5 mW, the other a wavelength of 822 nm and maximum output power of 15 mW. Both were supplied in a 9 mm cylindrical package which includes collimation optics. The He-Ne laser has a power output of 1 mW at 632.8 nm.

7.3.5.1: Seeding with a He-Ne Laser

Linear OPO Resonator

The injection seeded linear resonator is identical to the unconstrained resonator, shown in Fig. 7.15, except that the seed signal is coupled into the resonator co-axially with the UV pump beam, by combining the two at one of the pump beam steering mirrors as shown in Fig. 7.31, and additionally one of the resonator mirrors is now mounted on a piezo-ceramic so that the seed wave may be resonantly enhanced. The intra-cavity 45° reflector has around 3% reflectivity for the seed wave.

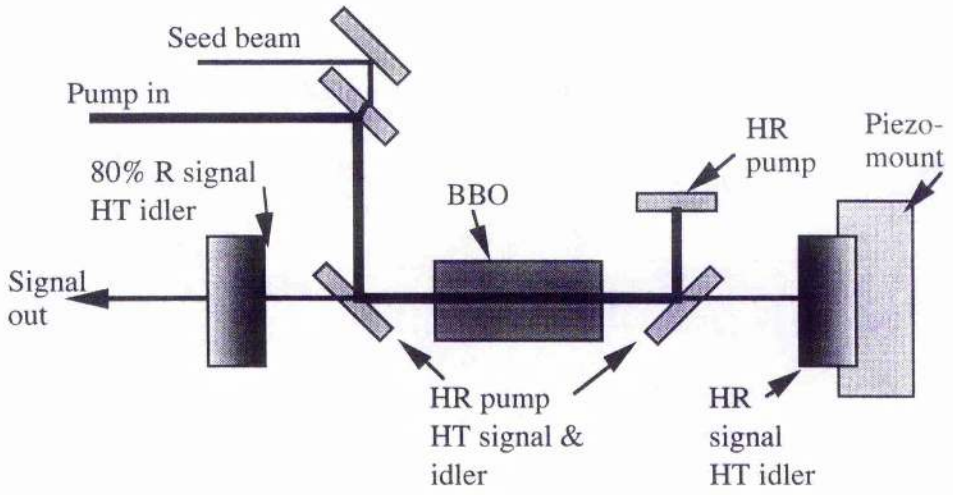

Figure 7.31: Schematic of the injection seeded, linear type I β-BBO OPO.

The output from the OPO was monitored simultaneously on the 1 m monochromator and Fabry-Perot interferometer. The wide exit slit of the monochromator was imaged onto a CCD array, which provided a 3 nm wide observation window with ~ 40 GHz resolution. The air-spaced interferometer has a finesse of 10 and FSR appropriate to the linewidths being measured for detailed analysis of the spectral output.

With the seed beam carefully aligned, then by varying the voltage to the piezo mirror mount, to bring the OPO resonator on-resonance with the seed wave, the effect of seeding the OPO can be clearly demonstrated as a sharp feature appears in the spectral profile. The seeded feature appearing in this spectral profile of the signal-wave output has a measured linewidth of < 400 MHz, demonstrated by the Fabry-Perot ring intensity profile shown in Fig. 7.32.

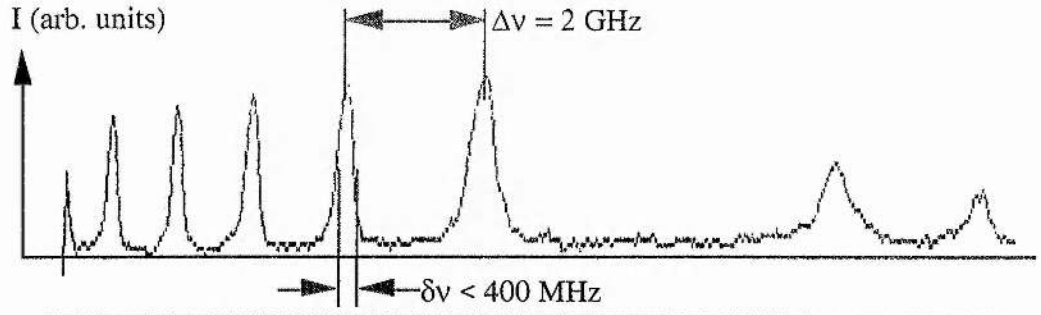

Figure 7.32: Fabry-Perot ring intensity for the He-Ne injection seeded type I β-BBO OPO.

However, in observing the spectral output on the monochromator, as shown in Fig. 7.33, it is evident that a significant pedestal is also present which is not obvious in the interferometer ring pattern. This pedestal takes the form of wings located symmetrically about the seeded peak and positioned about 1 nm distant.

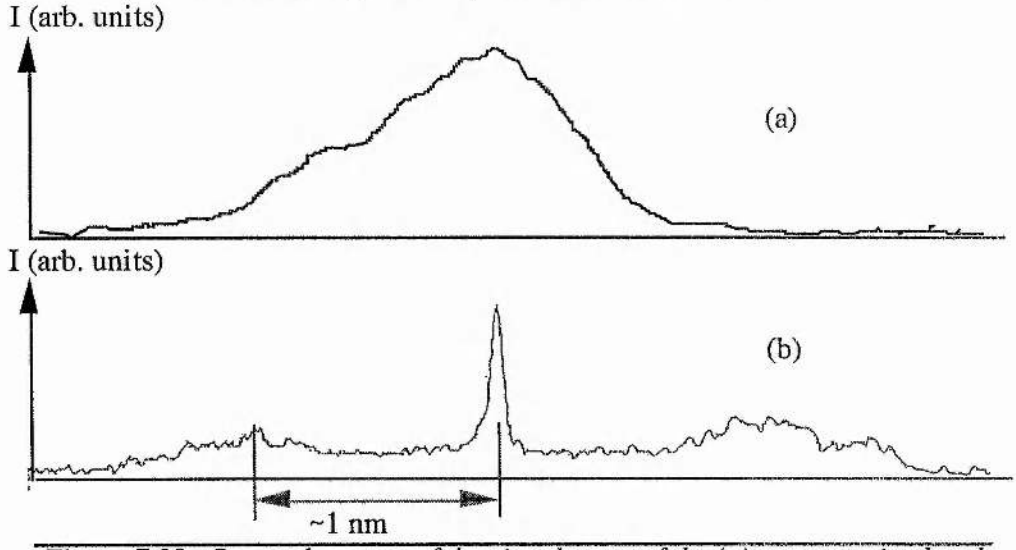

Figure 7.33: Spectral content of the signal-wave of the (a) unconstrained and (b) injection seeded type I β-BBO OPO at 632.8 nm (exit slit - 1 m monochromator).

One possible cause of this pedestal effect may be non-collinear phasematching of the pump, the divergence of which (0.7 mrad) is larger than the angular acceptance bandwidth of the OPO at this signal wavelength (0.2 mrad). No mention of this pedestal effect has been found in literature, however, this may be due to other workers operating at higher pump energy levels with larger beam sizes of lower divergence.

Additional measurements have also been made with regard to the spectral quality of the idler wave from the OPO. In so doing the pump laser has been made to operate SLM through the slow-Q-switching technique described in Chapter 5. It has been observed

that for both line-narrowed and broadband pumping the signal-wave (seeded) remains SLM with a broad pedestal, while as expected the idler-wave takes up the additional pump bandwidth. Consequently, setting aside the spectral components of the idler-wave generated by the signal-wave pedestal, by controlling the pump linewidth and signal-wave linewidth, a narrow-linewidth idler-wave is also generated. The number of idler-wave 'modes' observed, this terminology being a little arbitrary as the idler-wave is non-resonant, and their frequency spacing reflects the number of modes and spacing of the pump laser, where the signal-wave is well constrained. This effect is demonstrated clearly in the Fabry-Perot ring intensity profiles shown in Fig. 7.34, which shows in the upper trace the idler-wave with a SLM pump beam and in the lower trace the idler wave with a two-mode pump beam. The two-'mode' idler wave has a mode separation of 440 MHz, the mode spacing of the pump laser.

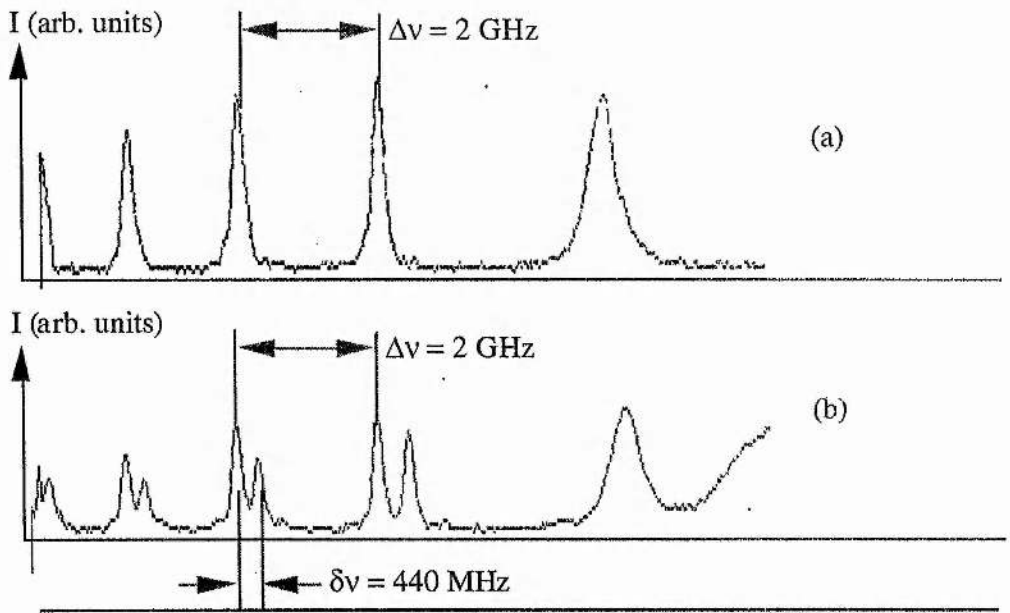

Figure 7.34: Spectral content of the idler-wave of the (a) SLM pumped and (b) 2 mode pumped type I β-BBO OPO, injection seeded at 632.8 nm.

Ring OPO Resonator

With a view to diode-laser seeding of the OPO and the potentially catastrophic effect on the diode-laser of feedback from a linear resonator, a ring OPO resonator has been developed as shown in Fig. 7.35. Prior to diode-laser seeding this resonator has also been seeded using the He-Ne laser.

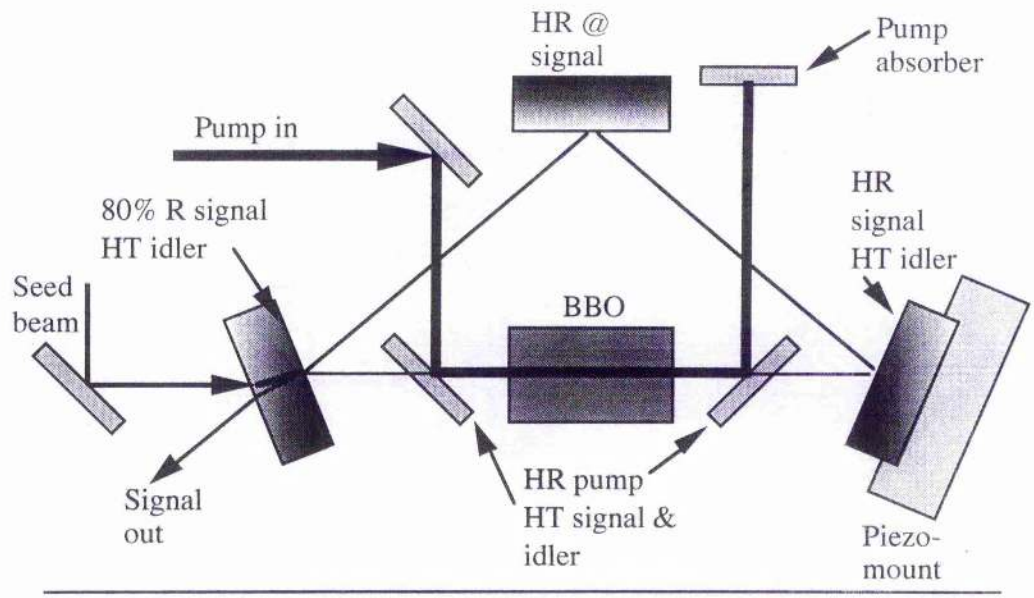

Figure 7.35: Schematic of the injection seeded, ring resonator type I β-BBO OPO.

The ring resonator is in the form of a right angled triangle, where the pump reflectors and nonlinear crystal are located in the long arm. After propagating through the nonlinear crystal, the signal-beam is turned through 135° by a broadband high reflector, which is piezo mounted for resonator length control, onto a second high reflector which turns the beam through a further 90° and onto the 80% reflecting broadband output coupler. The reflected beam is then turned back along its original path through the nonlinear crystal. The resonator mirrors used are the same as those for the linear resonator but turned off-axis and the round trip length is 144 mm. The resonator operates unidirectionally, determined by the now single-pass pump beam, which advantageously removes any feedback from the diode-laser seed device. Disadvantageously, the single-pass pump geometry reduces the parametric gain by around a factor of 2 and at the same time the resonator length is increased, resulting in the pump threshold being increased to 5 mJ.

Results for the seeded ring resonator are very similar to those previously described for the linear resonator, a single longitudinal mode of the resonator oscillating preferentially, but a broad low level background continuing to be evident.

7.3.5.2: Seeding with a Single-Mode Diode-Laser

Having addressed seeding of the OPO signal-wave using a He-Ne laser, this technique although convenient offers no tunability. Consequently, the He-Ne source has been replaced by single-mode diode-lasers operating in the visible (red) and infra-red regions of the spectrum around 670 nm and 822 nm respectively. Extending the signal-wave seed wavelength to 670 nm also allows seeding to be studied nearer to degenerate operation, while the IR diode-laser addresses seeding of the non-resonant idler-wave. A ring resonator geometry identical to that described above has been used, with the sole addition of an optical isolator between the OPO and seed source.

Signal-Wave Diode-Laser Seeding

Seeding of the signal-wave by the red diode-laser was carried out as for the He-Ne source. No significant differences were observed, with preferential oscillation being consistently observed at the seed wavelength but with the attendant broad background pedestal. Seeding was found to be successful at powers of < 300 μW, there being no improvement, particularly with regard to the observed pedestal, when seed powers were increased to greater than 5 mW. The seeded peak has a linewidth of < 400 MHz.

With the broad gain bandwidth associated with diode-lasers, it was possible to tune the seed frequency over ± 3 nm about the 670 nm central wavelength. It was found that from an optimised position the OPO could be tuned in pace with the seed wavelength over ± 0.25 nm without having to re-orientate the β-BBO crystal, larger wavelength excursions requiring the crystal to be re-orientated. The resonator length was continually varied for optimum seed resonance.

IR Diode-Laser Seeding

Given the limited spectral coverage of single mode diode-lasers in the visible region of the spectrum, it would be advantageous if the signal-wave linewidth could be controlled by seeding the non-resonant idler-wave in the IR. Single mode diode-laser coverage now extends from ~670 nm to > 2μm and thus, with the implementation of idler-wave seeding, linewidth control could be facilitated over almost the entire OPO

tuning range. As noted previously however, this does place additional frequency constraints on the pump laser.

In the same ring configuration as before, the red diode-laser was replaced by the IR diode-laser and seeding observations made. With a seeded idler-wave and SLM pump beam, the signal-wave linewidth was measured to be less than 570 MHz, as shown in Fig. 7.36.

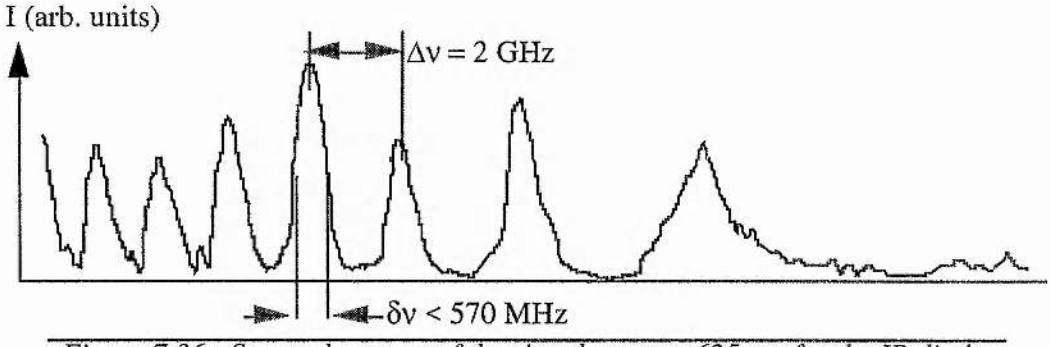

Figure 7.36: Spectral content of the signal-wave at 625 nm for the IR diode-laser seeded idler-wave at 822 nm.

It was again found that successful seeding could be obtained for seed powers of less than 300 μm, even though the seed wave is now non-resonant. The mirror through which the seed wave is launched is however, highly transmitting at the seed wavelength allowing all the seed power to enter the resonator.

7.3.5.3: Control of Pedestal Effect

The broad pedestal or wings observed in all the diode-laser seeding experiment results can contain a significant proportion of the pulse energy, evident from considering the area under the curve in for example Fig. 7.33. To remove this pedestal it is possible to employ either interferometric or dispersive techniques similar to those discussed previously.

Use of Étalon

An étalon of sufficiently large free spectral range and finesse may be used to select that portion of the spectral content which contains the seeded mode, while discriminating against the spectral regions containing the wings. It has been shown that at a central

wavelength of 632.8 nm, the pedestal extends over a range of ± 2 nm about this wavelength, requiring then an étalon of similar FSR (1.5 THz). This FSR corresponds to a solid étalon of ~ 70 μm thickness. Such an étalon not being available, an air spaced étalon formed by two 40% reflectors separated by 100 μm, was located in the resonator, so providing an FSR of 1.5 THz with a finesse of around 3.2.

With the étalon inserted into the ring resonator and the OPO injection seeded by the 670 nm red diode-laser as before, reliable SLM operation was observed with no pedestal on either the signal-wave or idler-wave spectral traces, as shown in Fig.7.37.

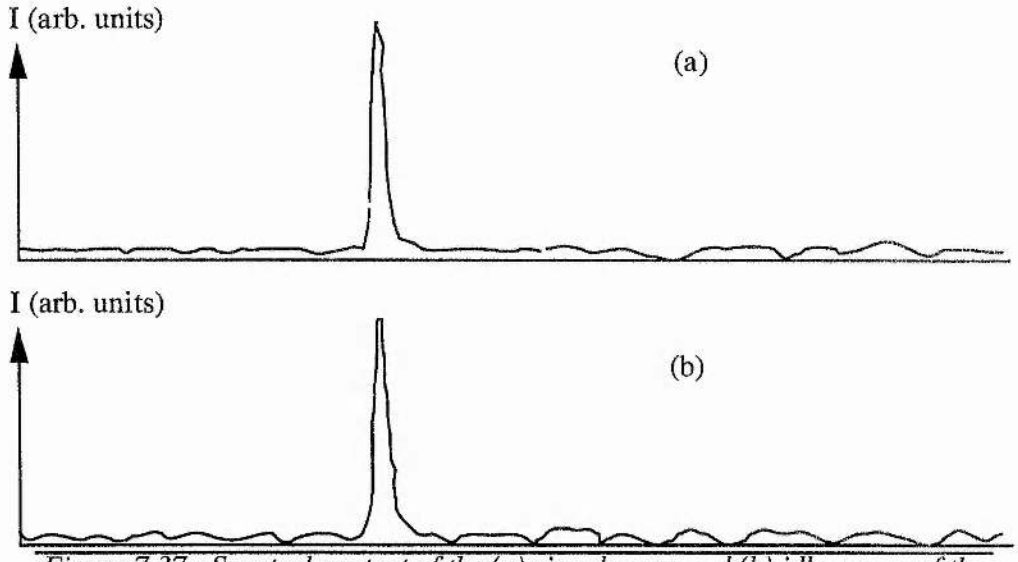

Figure 7.37: Spectral content of the (a) signal-wave and (b) idler-wave of the type I BBO OPO injection seeded by a diode-laser at 670 nm and including a 100 μm air-spaced étalon (monochromator exit slit - 3 nm wide).

The signal-wave linewidth is measured to be <240 MHz at three times pump threshold, which was measured to be 5.5 mJ.

Use of Dispersive Grating

In the linear resonator configuration injection seeded by the He-Ne laser, the 1200 l/mm dispersive grating described previously has also been successfully used to eliminate the observed pedestal. As the linewidth of the output is determined by the seeding process rather than the grating (or étalon used in the preceding geometry) the linewidth is again measured to be < 240 MHz. Threshold is now 6 mJ, the grating having a higher insertion loss than the étalon.

Chapter 7 References:

1. Y. Cui, C. J. Norrie, C. F. Rae, C. P. Rahlff, Y. Tang, J. A. C. Terry, D. E. Withers, M. H. Dunn, B. D. Sinclair and W. Sibbett *"Diode laser pumped solid-state lasers"* (RARDE Progress Report, Univ. of St Andrews, Scotland, UK), March 1992.

2. S. J. Lin, J. Y. Huang, J. W. Ling, C. T. Chen and Y. R. Shen *"Optical parametric amplification in a lithium triborate crystal tunable from 0.65 to 2.5 μm"* Appl. Phys. Lett. 59 (22) pp.2805-2807, 1991.

3. Z. Xu, D. Deng, Y. Wang, B. Wu and C. Chen *"Optical parametric oscillation from LiB_3O_5 pumped at 355 nm"* Conference on Lasers and Electro-Optics, (1990 Technical Digest Series 7, Optical Society of America, Washington, USA), Paper CWE6, 1990.

4. Y. Wang, Z. Xu, D. Deng, W. Zheng, B, Wu and C. Chen *"Visible optical parametric oscillation in LiB_3O_5"* Appl. Phys. Lett. 59 (3) pp.531-533, 1991.

5. Y. Cui, M. H. Dunn, C. J. Norrie, W. Sibbett, B. D. Sinclair, Y. Tang and J. A. C. Terry *"All-solid-state optical parametric oscillator for the visible"* Opt. Lett. 17 (9) pp.646-648, 1991.

6. Y. X. Fan, R. C. Eckardt and R. L. Byer *"Visible BaB_2O_4 optical parametric oscillator pumped at 355 nm by a single-axial-mode pulsed source"* Appl. Phys. Lett. 53 (21) pp.2014-2016, 1988.

7. J. M. Boon-Engering, W. E. van der Veer and J. W. Gerritsen *"Bandwidth studies of an injection-seeded β-barium borate optical parametric oscillator"* Opt. Lett. 20 (4) pp.380-382, 1994.

8. P. Bourdon, M. Péalat and V. I. Fabelinsky *"Continuous-wave diode-laser injection-seeded β-barium borate optical parametric oscillator: a reliable source for spectroscopic studies"* Opt. Lett. 20 (5) pp.474-476, 1995.

9. R. S. Craxton *"Theory of high efficiency third harmonic generation of high power Nd-glass laser radiation"* Opt. Comm. 34 (3) pp.474-478, 1980.

10. W. Seka, S. D. Jacobs, J. E. Rizzo, R. Boni and R. S. Craxton *"Demonstration of high efficiency third harmonic conversion of high power Nd-glass laser radiation"* Opt. Comm. 34 (3) pp.469-473, 1980.

11. Y. Cui *"UV pumped holosteric optical parametric oscillator"* (Ph.D. Thesis, Univ. of St Andrews, Scotland, UK), 1993.

12. S. J. Lin, Z. Y. Sun, B. C. Wu and C. T. Chen *"The nonlinear optical characteristics of a LiB_3O_5 crystal"* J. Appl. Phys. 67 (2) pp.634-638, 1990.

13. D. E. Withers, G. Robertson, a. J. Henderson, Y. Tang, Y. Cui, W. Sibbett, B. D. Sinclair and M. H. Dunn *"Comparison of lithium triborate and β-barium borate as nonlinear media for optical parametric oscillators"* J. Opt. Soc. B. 10 (9) pp.1737-1743, 1993.

14. K. Kato *"Second-harmonic generation to 2048 Å in β-BaB_2O_4"* IEEE J. Quant. Elect. QE-22 (7) pp.1013-1014, 1986.

15. D. Eimerl, L. Davis, S. Velsko, E. K. Graham and A. Zalkin *"Optical, mechanical, and thermal-prperties of barium borate"* J. Appl. Phys. 62 (5) pp.1968-1983, 1987.

16. Casix Optronics Inc. *"Crystal Guide 97/98"* (Casix Optronics Inc., Fuzhou, P. R. China), 1997.

17. S. J. Brosnan and R. L. Byer *"Optical parametric oscillator threshold and linewidth studies"* IEEE J. Quant. Elect. QE-15 (6) pp.415-431, 1979.

Chapter 8
Polychromatic β-Barium Borate Optical Parametric Oscillator

It has now been well established that optical parametric oscillators (OPOs) can be used to generate laser-like output over a certain spectral range, constrained by the pump wavelength, the nonlinear material used and the relevant geometry-type implemented. However, while the tuning range can be large, the instantaneous bandwidth is typically much less. Normally, for a certain orientation of the crystal and for some given temperature, only a narrow range of signal and idler wavelength pairs simultaneously satisfy the phase-match constraints, resulting in spectral bandwidths of typically no more than a few nanometres, and often much less, as demonstrated in Chapter 7. Although narrow spectral bandwidths are desirable for a number of applications, such as high resolution spectroscopy and differential absorption lidar (DIAL), considerable interest also exists in the development of broadband sources, where linewidths are typically tens or hundreds of nanometres.

The development of broad-bandwidth parametric generators has several advantages over conventional broadband sources, which include; solid-state and solution dye lasers, Ti:Sapphire, Cr:LiSAF and other vibronic gain media. Notably, dyes are usually harmful and awkward to handle, while vibronic laser systems have bandwidths of typically less than 50 nm when free-running in the nanosecond pulsewidth regime [1]. Furthermore, the exceptionally broad tuning ranges observed for conventional OPOs holds potential for accessing spectral regions not accessible by other gain media.

It is possible to attain relatively broadband output from collinearly phase-matched OPOs by operating some devices near to degeneracy, pumping with broadband radiation, or developing resonator and pump geometries which allow simultaneous parametric oscillation over a range of different phase-match directions. However, near degenerate operation restricts the spectral regions which may be accessed, while broadband pumping is limited to only a few pump laser types. Modified resonator and pump geometries may

be possible, however, increases complexity in the system, require high energy pump lasers and can result in both signal- and idler-waves being spatially dispersed or fanned-out .

In this chapter the identification and demonstration of noncollinear geometries for parametric generation are described, which allow the simultaneous phase-matching of a broad spectral range of signal and idler wavelength pairs (polychromatic), even when using a fixed frequency and collimated pump, and where all the spectral components of one of the generated parametric waves are also coaxial. Such sources could have applications in for example; ultrafast technologies including broadband parametric amplification, 'white-light' interferometric fringe devices, and spectroscopic studies where the high spatial coherence may be exploited in remote-sensing type uses.

8.1: Polychromatic Phase-match Geometry

Numerical studies of noncollinear phase-matching in various nonlinear materials, notably β-barium borate (β-BBO), as a function of both signal and pump direction within the nonlinear crystal have revealed that there exist particular configurations which allow a continuous range of signal and idler wavelength pairs to satisfy simultaneously the phase-matching constraints.

Fig.8.1 shows schematically the situation for a noncollinear type I (e:o+o) phase-match geometry in a negative uniaxial crystal.

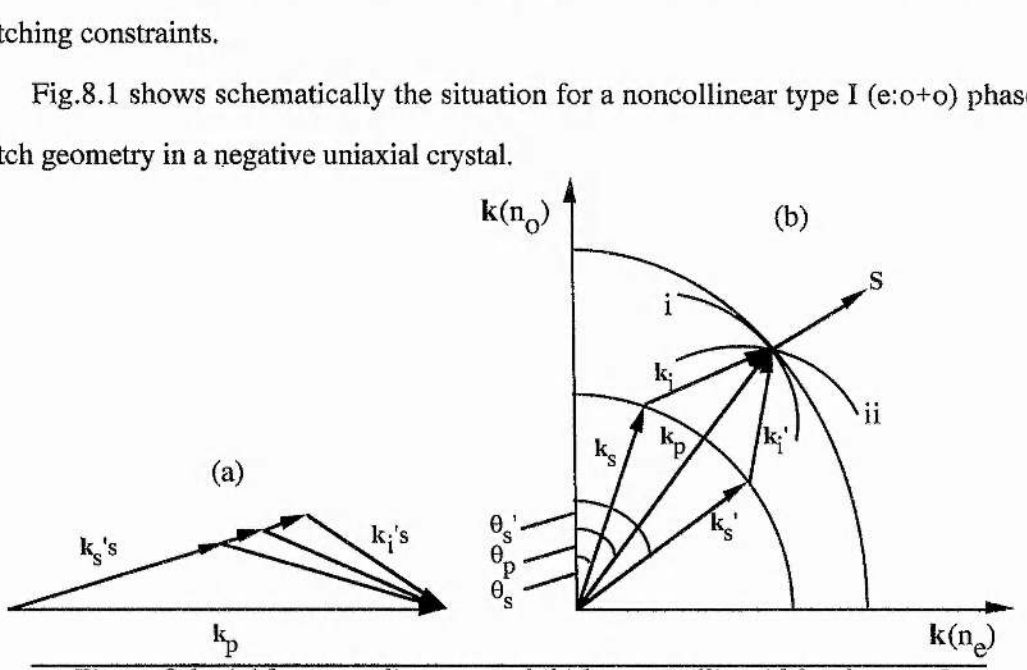

Figure 8.1: (a) k-vector diagram and (b) k-space ellipsoid for the type I (e:o+o) noncollinear phase-matching geometry in a uniaxial crystal.

If $\mathbf{k}_p$, the pump wavevector and in this case an extraordinary wave, is fixed in both magnitude and direction and $\mathbf{k}_s$ is also fixed in direction only, but allowed to vary in length (frequency), then for an appropriate choice of angles θ_p and θ_s, polychromatic phase-matching can be observed where, over some spectral range of $\mathbf{k}_s$'s, the necessary $\mathbf{k}_i$'s are found to exist to satisfy phase-matching constraints. It is to be noted that the spectrally-broad idler-wave will, as indicated in Fig. 8.1(a), be spatially dispersed, however, this need not be detrimental. Further, there will exist, as indicated in Fig. 8.1(b), for an appropriate θ_p, two noncollinear solutions $\theta_s, \theta_s' = \theta_p \pm \alpha$, where α is the noncollinear angle, due to the symmetry of the type I interaction.

Considering specifically the above phase-matching geometry within β-BBO and where the OPO is pumped by the third harmonic (0.3547 μm) of an Nd:YAG laser, then it is found using the Sellmeier data of Chen *et al.* [2] and the usual phase-mismatch expression for Δk;

$$\Delta k = \sqrt{k_p^2 + k_s^2 - 2k_p k_s \cos(\theta_s - \theta_p)} - k_i \qquad (8.1)$$

that the particular conditions for polychromatic phase-matching exist when the pump wavevector direction relative to the optical axis (θ_p) is near to 35.9° and the two possible signal wavevector directions (θ_s, θ_s') are 31.5° and 40.3°. This is shown graphically in Fig. 8.2 and Fig. 8.3.

In Fig. 8.2 the tuning behaviour of the noncollinear phase-matched β-BBO OPO around the polychromatic condition is demonstrated for various signal-wave directions, where the plot variable is the pump direction. In Fig. 8.3 the converse is shown where phase-matched operation is depicted for various pump directions and the plot variable is now the signal-wave direction. It is apparent that at the polychromatic phase-match condition, the phase-matchable bandwidth exceeds 100 nm, centred about a wavelength of ~ 0.55 μm. Similar broadening of the spectral bandwidth of the noncollinear β-BBO OPO has also been observed by Gloster *et al.* [3], however, in their work particular interest lay in the increased efficiency of this noncollinear geometry and not the potential for polychromatic operation.

In practice, the spectral width of the output need not be limited to the vertical portions of the phase-match curves, representing the plane-wave solution, but is further broadened due to the spectral width of the pump source and the divergence of the pump and signal waves. Fig. 8.4 explores in greater detail the phase-mismatch for the case of $\theta_s = 31.5°$, where the shaded areas represent the regions in which Δk is less than 0.5 mm^{-1}, this value being chosen as, as will be demonstrated later, the effective interaction length (l_{eff}) in later experiments is around 6 mm, so then $\Delta k l_{eff}$ is less than π.

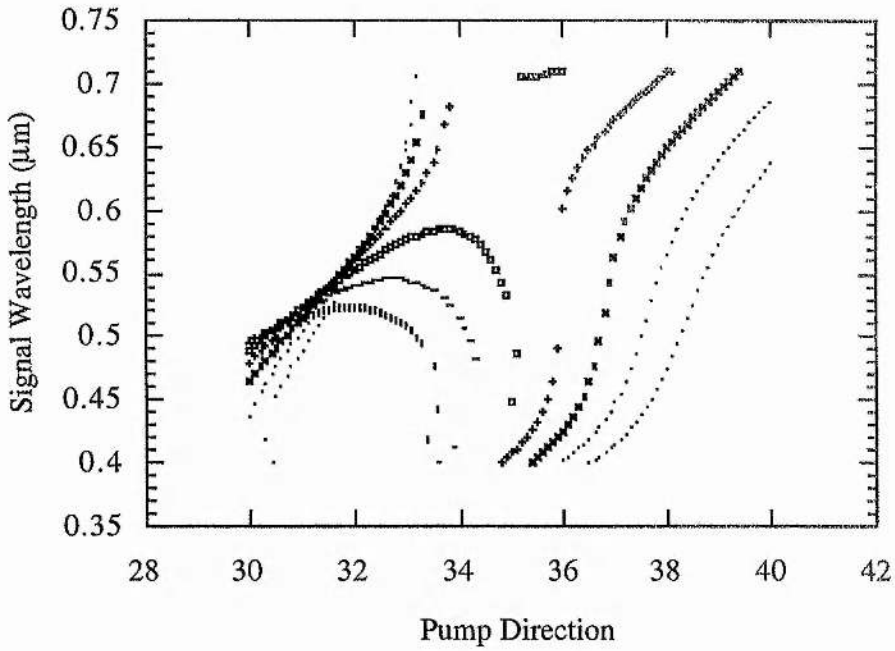

Figure 8.2: Tuning curves for the type I noncollinear β-BBO OPO around the polychromatic condition (plots are at 0.5° intervals in θ_s, in the main part of the diagram, ranging from 33°(.) to 30°(\|) right to left).

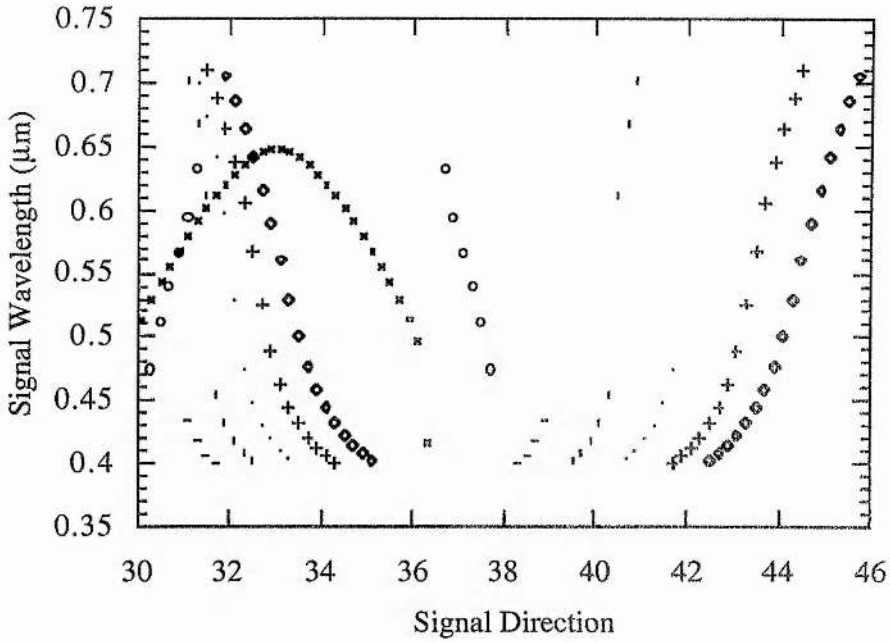

Figure 8.3: Tuning curves for the type I noncollinear β-BBO OPO around the polychromatic condition (plots are at 1° intervals in θ_p, ranging from 39° (◊) to 33° (o) right to left).

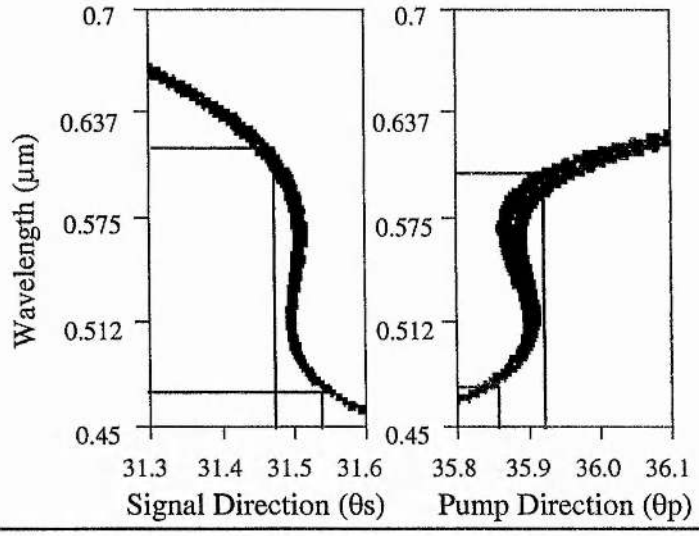

Figure 8.4: Detailed phase-mismatching curves for the $\theta_s = 31.5°$ solution in β-BBO, showing the comparative effects of signal beam divergence and pump beam divergence on the spectral bandwidth.

In comparing the two curves, it is clear that the spectral bandwidth is more sensitive to divergence in the signal-wave, the horizontal cursors indicating the phase-matchable bandwidth achievable when assuming a 1 mrad divergence in either the pump or signal

waves respectively. This difference is due to a tangential phase-matching effect which will be discussed later [4], but is evident from inspection of Fig. 8.1(b). It is seen that the phase-matchable bandwidth is extended from around 100 nm in the case of the plane-wave solution to > 150 nm, when only a 1 mrad divergence is considered.

8.2: Experimental Set-up for the Polychromatic β-BBO OPO

The experimental set-up used in studying the 0.355 μm pumped noncollinear β-BBO OPO is depicted schematically in Fig. 8.5. The OPO is pumped by the third harmonic of a diode-laser-pumped and Q-switched Nd:YAG laser, the same as that described in Section 7.1. UV pump pulse energies are up to 9 mJ, in a pulse duration of 10 nsec and with a spot size in the OPO crystal of 0.54 mm ($1/e^2$, radius). The pump beam divergence x diameter product is measured to be 0.75 mm.mrad, or around x1.7 diffraction limited.

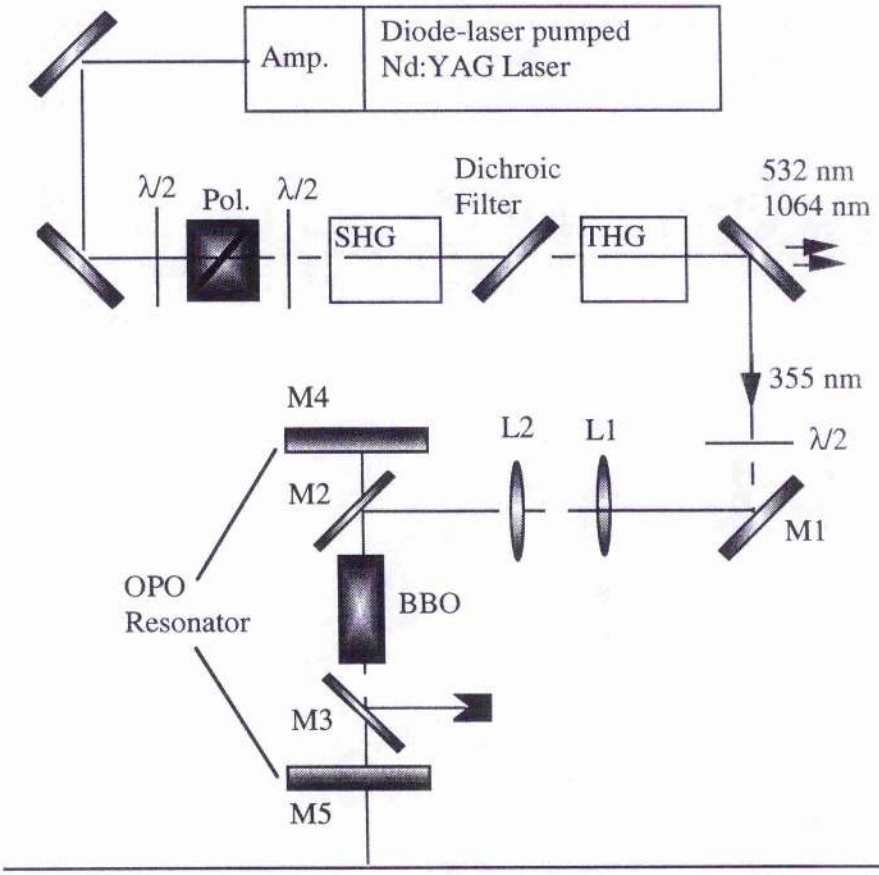

Figure 8.5: Schematic of the experimental set-up for the noncollinear β-BBO OPO; M1-M3, pump steering mirrors; M4, M5, OPO resonator mirrors.

The pump beam is steered into the OPO via mirrors M1, M2 and M3 and a conjugate lens pair L1 and L2. The conjugate lenses form a 1:1 image magnification ratio of conjugate points located on M1 and at the centre of the OPO nonlinear gain element, so facilitating fine tuning of the pump beam direction without displacing the beam from the crystal centre. M2 and M3 are dichroic to allow high transmission of the signal and idler waves within the OPO resonator. The β-BBO OPO crystal was cut at $\theta = 40°$ relative to its optic axis and has dimensions 8 x 4 x 18 mm^3. The polished faces were broadband AR coated with a single layer MgF_2 coating to reduce Fresnel reflections and protect the crystal from hygroscopic effects. The OPO resonator is formed by mirrors M4 and M5; M4 being highly reflecting from 0.4 - 0.7 μm and M5 partially reflecting (R~75%) over the same spectral range, both mirrors having high transparency for the idler wave (0.72 μm - 3 μm).

8.3: Experimental Results

8.3.1: Parametric Fluorescence Observations

Initially, with the OPO resonator mirrors removed, observations were made of the parametric fluorescence seen to emanate from the crystal. Predictably, for some general pump angle spatially dispersed parametric fluorescence is observed in noncollinear directions above and below the pump direction (in the plane of θ), as shown in Fig. 8.6, at angles corresponding to those at which strongest parametric gain is to be expected. However, as the pump angle is tuned toward the predicted polychromatic condition, the spatially dispersed spectral components of the signal-wave are observed to converge to a pair of common emission directions, as now shown in Fig. 8.7. As the pump angle is tuned beyond this polychromatic condition the spectral components are observed to once again become fanned out, but now in the reverse order to before, behaviour which is understandable from consideration of Fig. 8.3. Note also in Fig's 8.6 and 8.7 the blue central spot due to residual pump light at 0.355 μm which has walked-off in the β-BBO crystal from residual second harmonic light at 0.532 μm leaking through the system (green central spot).

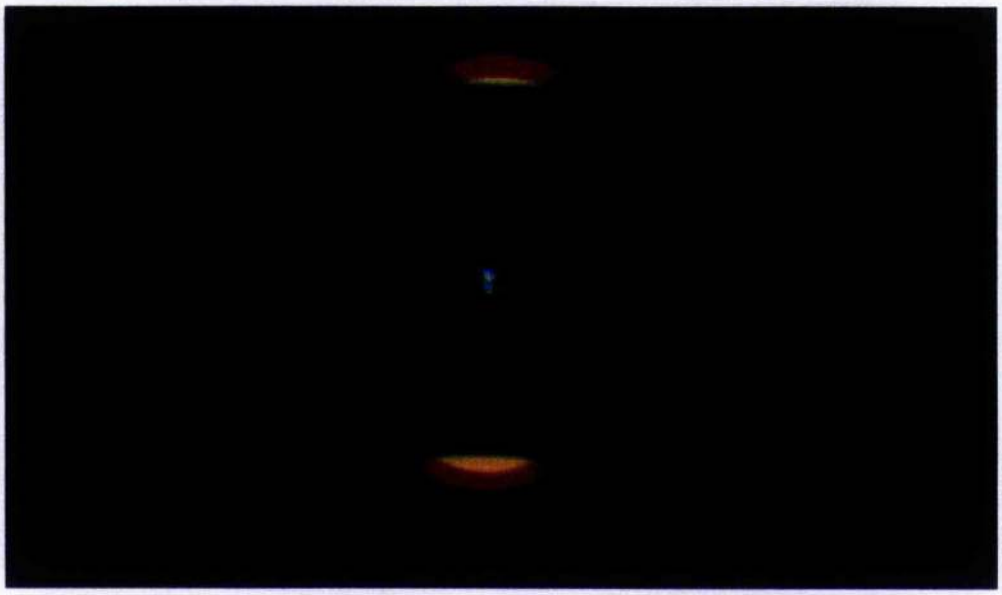

Figure 8.6: Parametric fluorescence observed in the directions θ_s and θ_s', for θ_p less than the polychromatic pump condition.

Figure 8.7: Parametric fluorescence observed in the directions θ_s and θ_s', for θ_p at the polychromatic pump condition. Brighter fluorescence in the $\theta_s = 31.5°$ direction.

The measured noncollinear angles for the polychromatic condition are in good agreement with those predicted and shown in Fig. 8.3. The simultaneous spectral content of the parametric fluorescence is measured to extend from ~0.5 μm to ~0.7 μm in the signal-wave (1.225 μm to 0.72 μm in the idler-wave).

It is observed that stronger parametric fluorescence exists along the $\theta_s = 31.5°$ direction. To understand this, consideration has to be given to a number of factors, including; Poynting vector walk-off, associated with which is an effective interaction length, and angular acceptance bandwidth due to tangential phase-matching. A discussion of these effects is given in the next section.

8.3.2: Parametric Oscillation Results

Spectral Profile and Threshold

Replacing the OPO resonator mirrors and aligning the resonator axis along the signal-wave direction $\theta_s = 31.5°$, the spectral content of the resonant OPO is recorded using a scanning monochromator, and is as illustrated in Fig's. 8.8 and 8.9. The spectrum is seen to be consistent with bandwidths predicted from phase-matching calculations, although appears displaced from the expected central wavelength of 0.55 μm.

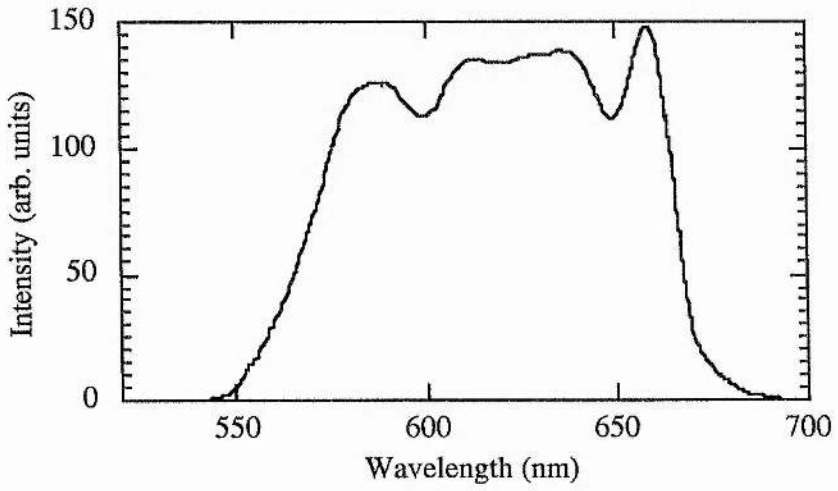

Figure 8.8: Spectral content of a single pulse from the polychromatic phase-matched β-BBO OPO.

Operation at $\theta_s' = 40.3°$, while keeping $\theta_p = 35.9°$, has also been addressed and similar spectral profiles to that shown in Fig. 8.8 are generated. In both geometries a pump threshold of 33 MW.cm^{-2} (0.33 J.cm^{-2}) is measured, with the pump threshold for > 100 nm bandwidth (FWHM) operation being measured to be 70 MW.cm^{-2} (0.7 J.cm^{-2}). Pump depletions of up to 50% have been achieved.

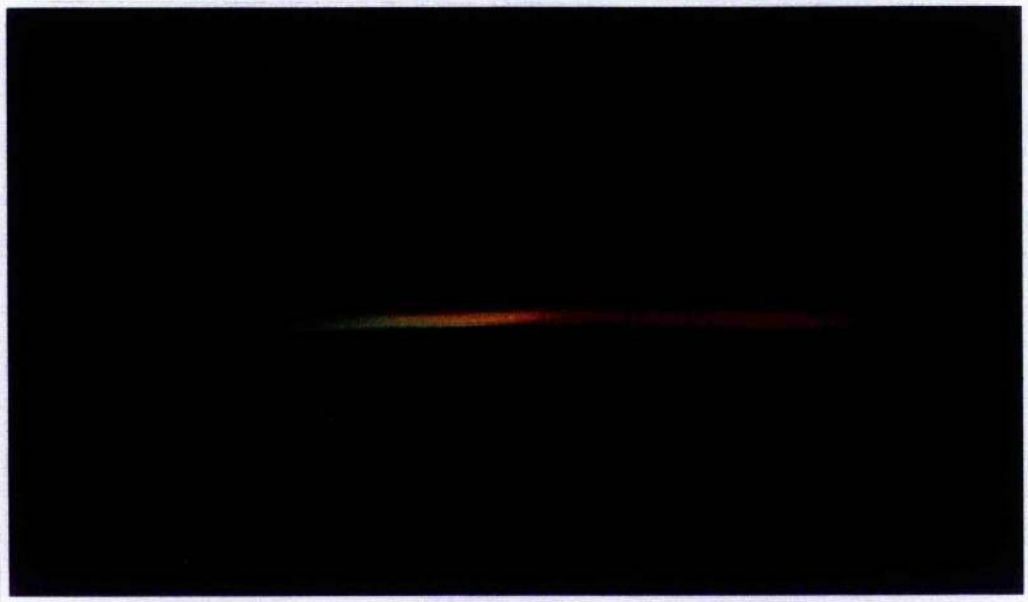

Figure 8.9: Chromatically dispersed spectral content of the coaxial spectral components of the signal-wave of the polychromatic β-BBO OPO (dispersed by a 1200 l/mm grating)

While then some degree of preference is apparent in the observed parametric fluorescence, under resonance conditions there is little to choose, in terms of the efficiency of the device, between the two signal directions. This is considered in relation to the combined effects of tangential phase-matching and effective interaction length.

Where the signal wave direction is constrained by the OPO resonator mirrors, then with reference to Fig. 8.1(b), it is apparent that for the $\theta_s' = 40.3°$ solution the idler wavevector direction is such that the arc it scribes (ii) cuts the pump ellipsoid at an acute angle. In contrast, for the $\theta_s = 31.5°$ solution the idler wavevector now scribes an arc (i) which is near tangential to the pump ellipsoid, representing a greater angular acceptance for the pump wave. Indeed, by evaluating the walk-off angle for the extraordinary pump

at the wavevector direction $\theta_p = 35.9°$, using equ. (6.25), it is found to be 4.55°, which is almost exactly equal to the noncollinear angle between the pump and idler **k**-vectors, so providing near perfect tangential phase-matching. An increased angular acceptance is, however, only beneficial where the pump beam divergence is of a similar magnitude to or greater than the acceptance bandwidth. As described in Section 6.5, the angular acceptance for the type I β-BBO OPO has been calculated around the polychromatic crystal orientation of $\theta_p = 35.9°$, as shown in Fig. 8.10, for a collinear and near tangential noncollinear phase-matching geometry.

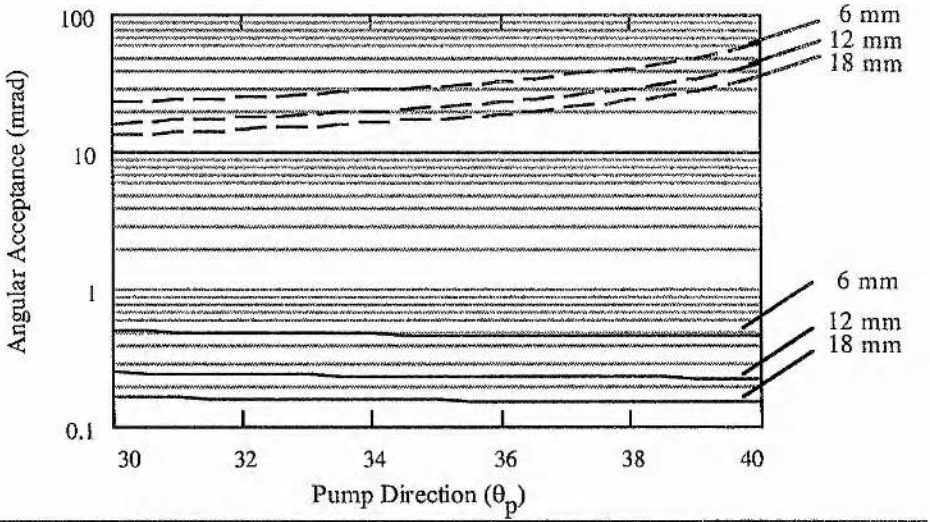

Figure 8.10: Angular acceptance bandwidths for the pump beam in a collinear (lower curve set) and near tangential noncollinear (upper curve set) phase-match geometry, for 6 mm, 12 mm and 18 mm interaction lengths.

It is apparent then that given a pump divergence in this case of 0.7 mrad, angular acceptance bandwidth is likely to be a significant factor and consequently the affects of tangential phase-matching for the $\theta_s = 31.5°$ solution will be beneficial.

Additionally, however, it has also to be noted that the $\theta_s' = 40.3°$ solution benefits more from Poynting vector walk-off compensation in the effective interaction length. For the $\theta_s = 31.5°$ solution, the noncollinearity of the idler wavevector direction (which is also the Poynting vector direction for this o-wave) partially compensates for Poynting vector walk-off of the extraordinary pump wave. However, the effective interaction length remains only that length it takes the pump beam energy (Poynting vector) to walk through the resonant signal beam (≈ 6 mm). In contrast, for the $\theta_s' = 40.3°$ solution, where the signal and pump Poynting wavevectors are near coaxial, the parametric process

continues over the entire length of the crystal, although some reduction in efficiency is to be expected, due to a loss in the idler-wave as it effectively walks away from the pump and signal. The combination of these two effects apparently leads to as equally good operation for either signal direction under the operating conditions described here.

Recent work by Oien *et al.* [5] has also addressed these issues in some detail, and provides quantitative examples of the best choice of phase-match geometry, for different pump beam characteristics, in a noncollinear β-BBO OPO operating near to the polychromatic condition. Their conclusions are the same as those drawn here, in that no particular geometry can be generally regarded as superior, but dependent upon the mode size and pump beam divergence.

Spatial Quality

The OPO resonator design is in no way optimised for a high quality spatial output, being based on a plane-parallel design with a large Fresnel number, determined by [6]

$$N = \frac{a^2}{\lambda L}, \tag{8.2}$$

to be 6.9, where a is a limiting aperture imposed by the pump spot size , λ is taken to be nominally 0.6 μm and the resonator length L is 70 mm. Consequently, the diffraction losses for higher order modes are small and a poor spatial quality is to be expected.

The spatial quality for an optimally aligned resonator has been measured to be around 10, although it should be noted that this increases rapidly (>40) for small misalignments of the resonator mirrors. Improved stability is likely to be achieved by for example the use of plano-concave resonators.

8.3.3: Tunable Broadband Operation

Noted in the previous section is an apparent discrepancy between the calculated and observed central wavelength of the broadband output from the polychromatic β-BBO OPO. In fact, a rigorous study of the theoretical tuning characteristics of the OPO, confirmed by experimental analysis, has revealed that when the linewidth broadening effects of pump beam and signal-wave divergence are considered in conjunction with an allowable Δk of π/l, then it is possible to tune the central wavelength of the broadband

output in such a way that the entire visible spectrum may be covered. The more easily observed broadband output biased toward the red end of the spectrum can however, be understood by considering the single-pass, signal-wave power gain.

The single-pass, signal-wave power gain was shown in Chapter 6 to be given by equ. (6.53)

$$G = \left(\frac{g}{\beta}\right)^2 \sinh^2(\beta l) \ . \qquad (8.3)$$

Clearly, the gain is dependent on both the effective interaction length (l) and the detuning parameter δ which is implicit in g through the substitution $\omega_s \omega_i = \omega_p^2(1 - \delta^2)$. Simple geometry shows that due to the noncollinearity in the phase-match geometry a longer interaction length is obtained for near degenerate operation, while the $(1-\delta^2)$ term clearly reduces the power gain as the signal-wave moves progressively further away from degeneracy. This is demonstrated in Fig. 8.11, which shows the solution to equ. (8.3) for a number of pump directions. By adjusting either the pump or signal-wave direction broadband operation at the blue end of the visible spectrum has indeed been observed, but with a much lower conversion efficiency.

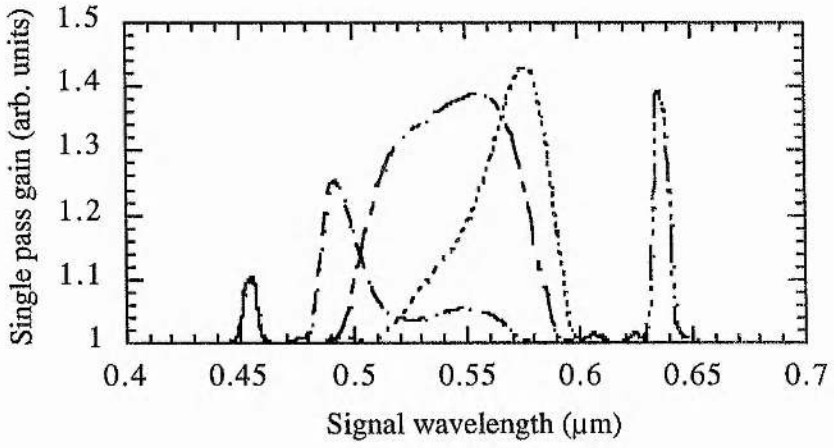

Figure 8.11: Theoretical single-pass, signal-wave power gain as a function of pump direction and wavelength (Pump-wave directions are from left to right - 35.8°, 35.98°, 36.02°, 36.05° and 36.5°).

8.3.4: Tunable Narrowband Operation

In addition to broadband operation, the polychromatic phase-match geometry may also be exploited in narrowband devices where a narrowband signal/idler wavelength pair may be selected by for example; seeding, grating tuning or the introduction of a tunable

filter into the OPO. The advantage of this geometry is that a static crystal and pump configuration can be employed, so relaxing the need to track crystal orientation or temperature with wavelength.

Grating Tuning

Tunable operation has been demonstrated by replacing the OPO output coupler with a dispersive grating (1200 l/mm, blazed at 0.5 μm), which has a nominal 55% reflectivity from 0.45 μm to 0.65 μm in a 1st order Littrow geometry, as shown in Fig. 8.12.

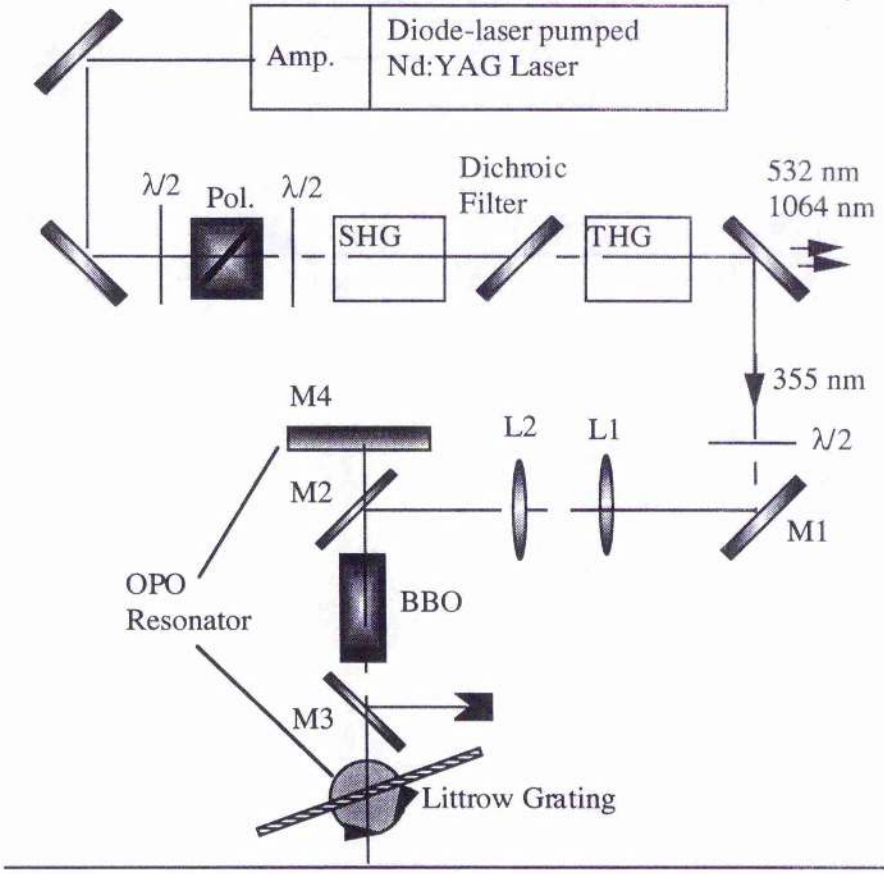

Figure 8.12: Schematic of the experimental set-up for the noncollinear β-BBO OPO with additional grating tuning.

The OPO has been successfully tuned over a spectral range comparable to the broadband operation, with observable spectral coverage from 0.510 nm to 0.698 μm (FWHM intensity range 0.554 to 0.677 μm), without the need to alter the crystal or pump orientation. The typical spectral linewidth is measured to be 75 GHz using a pulsed wavemeter, however, this could be made narrower by employing additional techniques such as those discussed in Chapter 7.

Injection Seeding

With the experimental set-up shown in Fig. 8.5 and additionally one of the resonator mirrors mounted on a piezo transducer, to provide fine adjustment of the resonator length, an attempt has been made to injection seed the β-BBO OPO otherwise arranged for polychromatic operation.

The OPO resonator is brought on resonance with the seed-wave, derived in this case from a 1 mW He-Ne laser operating at 0.6328 μm, which is injected into the resonator through the high reflector. Under such conditions a degree of seeding has been achieved, as shown in Fig. 8.13, which clearly demonstrates preferential operation at the seed wavelength, although a substantial pedestal remains evident.

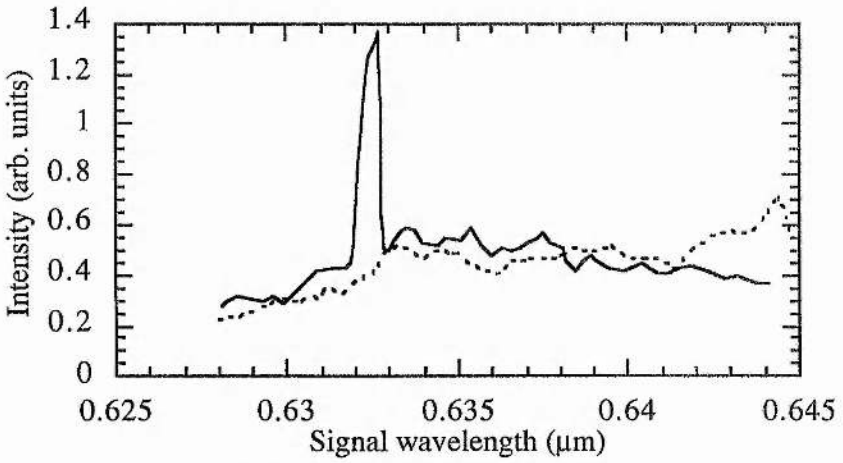

Figure 8.13: Spectral content of the injection seeded polychromatic β-BBO OPO.

8.4: Other Polychromatic OPO Geometries

While concentrating on the study of one particular polychromatic OPO, this type of phase-matching is more general, although not necessarily with the attributes of either Poynting vector walk-off compensation and tangential phase-matching associated with the UV pumped β-BBO device. Considering mainly alternative geometries for broadband IR operation, the possibilities noted in Table 8.1 have been identified through rigorous numerical simulation.

Crystal	λ_p (μm)	θ_p	θ_s	$\varnothing_p$	$\varnothing_s$	Wavelength range (μm)
BBO	0.532	23.9	21.5, 26.3	90	90	0.76-0.92
LBO	0.355	90	90	49.0	45.5,52.5	0.47-0.64
LBO	0.532	90	90	11.4	11.0	0.95-1.19
$AgGaSe_2$	2.1	51.6	49.8, 53.4	90	90	2.85-3.92
$KNbO_3$	1.064	40.9	36.8, 45.0	0	0	2.8-3.2

Table 8.1: Alternative broadband operating conditions.

This is by no means an exhaustive list but is intended to demonstrate the potential which exists for broadband parametric generation in this type of noncollinear geometry.

Chapter 8 References:

1. P. Brockman, C. H. Bair, J. C. Barnes, R. V. Hess and E. V. Browell *"Pulsed injection control of a titanium-doped sapphire lasers"* Opt. Lett. 11 (11) pp.712-714, 1986

2. C. Chen, B. Wu, A. Jiang and G. You *"A new-type ultraviolet SHG crystal - beta-Ba_2O_4"* Sci. Sin. Ser. B 28 (3) pp.235-243, 1985.

3. L. A. W. Gloster, Z. X. Jiang and T. A. King *"Characterization of an Nd:YAG-Pumped β-BaB_2O_4 Optical Parametric Oscillator in Collinear and Noncollinear Phase-Matched Configurations"* IEEE J. Quant. Elect. 30 (12) pp.2961-2969, 1994.

4. J. Wang, M. H. Dunn and C. F. Rae *"Polychromatic optical parametric generation by simultaneous phase matching over a large spectral bandwidth"* Opt. Lett. 22 (11) pp.763-765, 1997.

5. A. L. Oien, I. T. McKinnie, P. Jain, N. A. Russell, D. M. Warrington and L. A. W. Gloster *"Efficient, Low-Threshold Collinear and Noncollinear β-Barium Borate Optical Parametric Oscillators"* Opt. Lett. 22 (12) pp.859-861, 1997.

6. W. Koechner *"Solid state laser engineering - second edition"* (Springer Verlag series in optical sciences, New York), 1988.

Chapter 9
Conclusions and Discussion

9.1: Conclusions

In this work the feasibility of longitudinally pumped, high-peak-power, diode-laser pumped Nd:YLF lasers has been demonstrated, which utilise a 1 cm wide diode-laser bar or 2-dimensional arrays as conventionally used in transverse pump geometries. It has been shown that by carefully matching the shape and size of the pumped volume established in the Nd laser to the lowest order transverse mode of the laser resonator, exceptionally high spatial quality beams ($M^2 < 1.1$) can be generated in a device which has a low oscillation threshold (as low as 3.5 mJ for the low peak power device and 25 mJ for the high peak power device) and remains highly efficient (up to 27 % slope efficiency). As a consequence of the high pump light absorption coefficient found in Nd:YLF, and consequential short absorption depth, this type of laser has been found to lack many of the difficulties associated with spatial hole burning effects and possess a high degree of inherent spectral purity. This feature has been exploited in the development of single axial mode devices which utilise the technique of slow-Q-switching or self-injection-seeding. It has been found that by employing this technique it is possible to obtain oscillation on at most two axial modes of the laser resonator. A novel technique has been developed to detect this condition and when necessary disrupt it, by modifying the laser resonator length through an electro-optic phase modulation derived from a suitably oriented Pockels cell. The technique has been shown to be successful in generating consistent near transform limited single axial mode laser pulses. As the technique involves only the insertion of a second Pockels cell, which may be made low-loss, no significant drop in efficiency has been observed compared to normal Q-switched operation.

The high power Nd:YLF laser developed in this work has been shown to be a useful source in pumping OPOs. The pump laser was efficiently frequency up-converted to its third harmonic and used to pump a visible/near infrared OPO based on the nonlinear

material LBO. Extensive tuning has been demonstrated from 0.406 μm to 0.698 μm (degeneracy) in the visible signal-wave, with a corresponding idler-wave range of 0.698 μm to 2.486 μm, when using a single crystal and mirror set. Pump depletions as high as 30 % have been measured in a 15 mm long crystal, while pump threshold is typically 0.5 to 1.1 $J.cm^{-2}$ over most of the tuning range in a double pass pump geometry.

If such a source is to find wide ranging applications, in for example spectroscopy, linewidth control to the level of single-frequency, near transform limited operation is vital. Using the nonlinear material β-BBO, a number of line-narrowed OPO geometries have been presented. Linewidths of less than 400 MHz for the controlled parametric wave have been measured, this being either the resonant or non-resonant wave. Similar linewidths have been measured for the uncontrolled parametric wave when the OPO is pumped by a single longitudinal mode laser, which utilises the slow-Q-switch line-narrowing technique described in this work. The line-narrowed device continues to be broadly tunable in the case of using dispersive and/or interferometric techniques, and is limited only by the availability of suitable single mode diode-lasers when injection seeded. However, as linewidth control of the resonant signal-wave has been successfully demonstrated when seeding the non-resonant idler-wave, in the near-infrared, spectral coverage remains large even for this option, although does require a line-narrowed pump source.

Complementing line-narrowing studies of the β-BBO OPO has been the successful development of broadband devices. A previously unidentified phase-match condition in β-BBO has been exploited to generate broad-bandwidth or polychromatic radiation. More than 100 nm (FWHM intensity points) of simultaneous bandwidth was generated in a collimated signal-wave in the visible. The device was shown to be efficient and operate at relatively low pump powers by serendipidously operating near to a tangential phase-match condition. With the addition of dispersive tuning elements the phase-match condition has been demonstrated to be advantageous in tunable and potentially narrow-band devices also.

9.2: Future Studies

9.2.1: Longitudinally pumped solid-state lasers

It is likely that the rapid progress in the development of diode-laser pumped solid-state lasers during the last few years will continue for the foreseeable future. Of major benefit to their continued development is the reduction in cost of diode-lasers, making such systems competitive with traditional flashlamp pumped lasers. This is demonstrated in the recent introduction of commercial devices such as the Spectra-Physics 'Millennia' range, Coherent 'Verdi' and Uniphase 'Daylight', and also encourages the development of more powerful devices utilising greater numbers of diode-laser arrays.

Due to the significant advantages offered by longitudinally pumped lasers compared to transversely pumped lasers it is of interest to continue to develop ways in which the output powers achievable can be further increased in such a geometry. As the brightness of diode-laser arrays is likely to continue to increase there will be a consequential enhancement in solid-state laser powers, however, more significant increases may come in the short-term from the development of novel coupling techniques which allow more diode-laser bars/arrays to be efficiently coupled into the gain medium. Such schemes are for example being developed by Clarkson and Hanna [1], where beam shapers are used to segment and recombine the output of diode-laser arrays to form more circularly symmetric and compact pump profiles, or by the use of fibre-coupled devices [2] which although inefficient are becoming more cost effective as again diode-laser costs fall. In coupling geometries more analogous to that used here, it is possible that larger 2-dimensional arrays could be similarly coupled through cylindrical/spherical lens combinations. Such schemes will undoubtedly benefit from the recent development of microlens arrays for individually collimating the output of diode-laser bars within a 2-dimensional array [3]. In this way the stripe structure in the cross-section of the pumped volume may be alleviated and the overall size of the pumped volume reduced, even with greater numbers of bars in each array, leading to higher gains. A further enhancement in pump power can come from exploiting the polarised nature of diode-laser arrays by way of polarisation coupling schemes. Again such schemes would benefit from improved collimation of the diode-laser output by microlenses and could in relevance to the work

described here also alleviate the need for a double-ended pumping scheme, resulting in a simplified optical resonator arrangement.

9.2.2: Pulsed optical parametric oscillators

While nanosecond pulsed optical parametric oscillators based on β-BBO and LBO are becoming a mature technology, there remains specific areas of interest for further development.

Firstly, it has been demonstrated in this work that through the use of high spatial quality pump lasers and tight focusing geometries the pump threshold, and particularly in the case of LBO, can be made very low. In fact, the thresholds observed are close to the UV pulse energies/powers now capable of being generated in CW pumped, repetitively Q-switched solid-state lasers [4], and thus opens up the possibility of developing new high average power, broadly tunable OPOs for the visible and near-infrared. In realising such a device, it is likely for example that the pump threshold can be reduced further by optimising the pump focusing parameter and improving the OPO resonator design to optimise the pump/mode spatial overlap.

Secondly, through recent advances in the growth of β-BBO (so called super-BBO) and also in the use of dopants in β-BBO, particularly strontium (SBBO), the transparency of this material has been further extended into the UV. This brings about the possibility of more practical devices for the generation of tunable radiation deeper into the UV through either pumping with the fourth harmonic of Nd:YAG or Nd:YLF lasers [5] or sum frequency mixing the OPO output with the fundamental or residual higher harmonics of the pump laser.

Thirdly, and in respect of polychromatic type OPOs, in this work the ability to tune such a phase-matched device has as previously noted been demonstrated through the use of dispersive elements. A number of applications could benefit from more rapid tuning of the OPO and to this end a variety of techniques can be considered. One of the most interesting identified to date is the use of an acousto-optic tuning filter (AOTF). This is essentially a high diffraction efficiency acousto-optic Bragg cell which is designed to have a narrow frequency selection band, tunable through a modulation of the rf drive

frequency. Such devices have for example been demonstrated previously in dye lasers [6] and vibronic lasers [7], however, this would be the first demonstration of such a device for tuning an OPO.

Although having presented the details of only one particular polychromatic OPO geometry based on β-BBO, this type of phase-matching is found to be more general. Similar polychromatic operation is predicted in other nonlinear materials and for other pump wavelengths, such as; LBO, $\theta_s = 52.2°$ and $\theta_p = 48.6°$, $\lambda_p = 355$ nm ($\lambda_s = 470$-640 nm); BBO, $\theta_s = 21.5°$ and $\theta_p = 23.9°$, $\lambda_p = 532$ nm ($\lambda_s = 760$-920 nm); and $AgGaSe_2$, $\theta_s = 49.8°$ and $\theta_p = 51.6°$, $\lambda_p = 2.1$ μm ($\lambda_s = 2.85$ - 3.92 μm). These and other polychromatic conditions are expected to be of interest in a number of applications in the future.

Interest also lies in the further development of pulsed OPOs pumped by diode-laser pumped solid-state lasers but based on other nonlinear materials. In particular, much recent interest has arisen in the use of periodically poled materials. For a nonlinear process to be efficient, it is imperative that the interaction be closely phase-matched. This is a most demanding criterion and in this work has been demonstrated by the most widely practised means of using birefringence to offset dispersion in the refractive index. Such means however, do not allow the full potential of a nonlinear material to be exploited, either in regard to the requisite birefringence not being present to allow phase-matching across the crystals entire transparency range or due to the specific polarisation states required not allowing access to the highest nonlinear coefficients. An alternative approach to phase-matching which can alleviate both these difficulties is quasi-phase-matching (QPM); that is to alternate the sign of the nonlinear coefficient after each coherence length in order to maintain phase-synchronism for the nonlinear interaction. QPM then allows the nonlinear crystal to be chosen which best fits the application independent of the dispersion of the material. First proposed by Armstrong *et al.* [8] in 1962, QPM was first, and near simultaneously, demonstrated in practical arrangements in late 1988 by Magel *et al.* [9] in bulk $LiNbO_3$ and Lim *et al.* [10] in waveguide $LiNbO_3$. Since then many new opportunities have been exploited, particularly in the development of low threshold and efficient CW nonlinear devices, a comprehensive

review of which can be found in for example ref. [11]. However, interest also lies in the use of such phase-matching techniques in the nanosecond pulsed regime.

Much recent interest has been shown in the development of high average power, low peak power, pulsed sources in the 2 - 5 μm region, typically pumped by CW pumped and repetitively Q-switched diode-laser pumped lasers. While devices based on for example potassium titanyl phosphate (KTP) have been shown to be practical in both NCPM and CPM geometries [12], potential exists for improvement through the use of QPM and particularly in the case of the CPM tunable device. It is of immediate interest to us to explore the possibilities of QPM in both the phosphate and arsenate crystal series, with a view to developing low threshold, high efficiency and high average power 2 - 5 μm sources.

Chapter 9 References:

1. W. A. Clarkson and D. Hanna *"2-mirror beam-shaping technique for high-power diode bars"* Opt. Lett. 21 (6) pp.375-377, 1996.

2. J. Zhang, M. Quade, K. M. Du, Y. Liao, S. Falter, H. Baumann, P. Loosen and R. Poprawe *"Efficient TEM_{00} operation of a Nd:YVO_4 laser end pumped by fibre-coupled diode laser "* Elect. Lett. 33 (9) pp.775-777, 1997.

3. Z. L. Liau, D. Z. Tsang and J. N. Walpole *"Simple compact diode-laser/microlens packaging"* IEEE J. Quant Elect. QE-33 (3) pp.457-461, 1997.

4. C. Rahlff, M. H. Dunn, B. D. Sinclair and W. Sibbett *"High-power , end-pumped effects and applications in Nd:YLF at 1047 and 1053 nm"* Conference on Lasers and Electro-Optics, (1994 Technical Digest Series 8, Optical Society of America, Washington, USA), Paper CThG4, 1994.

5. Y. Tang, Y. Cui and M. H. Dunn *"Lithium triborate optical parametric oscillator pumped at 266 nm"* Opt. Lett. 17 (3) pp.192-194, 1992.

6. D. J. Taylor, S. E. Harris and S. T. K. Nieh *"Electronic tuning of a dye laser using the acousto-optic filter"* Appl. Phys. Lett. 19 (8) pp.269-271, 1971.

7. S. Wada, K. Akagawa and H. Tahiro *"Electronically tuned Ti:sapphire laser"* Opt. Lett. 21 (10) pp.731-733, 1996.

8. J. A. Armstrong, N. Bloembergen, J. Dicuing and P. S. Pershan *"Interactions between light waves in a nonlinear dielectric"* Phys. Rev. 127 (6) pp.1918-1939, 1962.

9. G. A. Magel, M. M. Fejer and R. L. Byer *"Quasi-phasematched second-harmonic generation of blue light in periodically poled $LiNbO_3$"* Appl. Phys. Lett. 56 (2) pp.108-110, 1990.

10. E. J. Lim, M. M. Fejer and R. L. Byer *"Second harmonic generation of green light in periodically poled planar lithium niobate waveguide"* Elect. Lett. 25 (3) pp.174-175, 1989.

11. L. E. Myers and W. R. Bosenberg *"Periodically poled lithium niobate and quasi-phase-matched optical parametric oscillators"* IEEE J. Quant. Elect. 33 (10) pp.1663-1672, 1997.

12. Y. Tang, C. F. Rae, C. P. Rahlff and M. H. Dunn "Low-threshold, high-efficiency, widely tunable infrared source from a KTP-based optical parametric oscillator" J. Opt. Soc. B 14 (12) pp.3442-3451, 1997.